

# Pulse shaping for all-optical signal processing of ultra-high bit rate serial data signals

**Palushani, Evarist**

*Publication date:*
2012

*Document Version*
Publisher's PDF, also known as Version of record

DTU Fotonik
Department of Photonics Engineering

# Pulse shaping for all-optical signal processing of ultra-high bit rate serial data signals

Ph.D. Thesis

Evarist Palushani

DTU Fotonik, Department of Photonics Engineering
Technical University of Denmark
Building 343
Kgs. Lyngby, 2800
Denmark

*There is no harm in doubt and skepticism,*
*for it is through these that new discoveries are made.*
**Richard Feynman** (1918–1988)

*One can only see what one observes,*
*and one observes only things which are already in the mind.*
**Alphonse Bertillon** (1853–1914)

# Acknowledgements

In my opinion, there is an intrinsic risk when writing the acknowledgement part, because one easily ends up forgetting about someone (most of the time someone important), especially when one is pressed for time. In my case there are so many people I would love to thank that, in a way or another, made possible the realization of this Ph.D. thesis. My first thought goes to my family, who has always supported me in all my decisions and gave me the possibility to study abroad. Even after almost ten years of living away from home, my mother still is not used to let me go after summer vacations. But, thanks to the Internet and indirectly thanks to fiber optics, she has the chance to see me every day.

If good luck comes in finite quantities then I must have used most of it when I met Karina. I do not know what my life would be without her, but for sure I would not like to live in it. Thank you *zemer* for being with me!

I am grateful to my supervisors Leif K. Oxenløwe and Anders T. Clausen, that took the risk and chose me as part of the team in the NOSFERATU project. They guided and supported me during these three long years. However, I could not have achieved most of the results presented in this manuscript without the help and support of the High-Speed Optical Communications Group at DTU Fotonik, especially without Hans Christian, Hao, Michael, Christophe, Jana and Ji Hua. Working with them has been very instructive and enjoyable, especially the quick stop at the Friday bar, before the weekend.

The NOSFERATU project would not have been possible without the funding of the Danish Research Council. I hope its supporting will continue to help the development of new researchers for a better society.

A special thank you goes to Colja Schubert for accepting me as a guest researcher for 7 months at the Heinrich-Hertz Institute (HHI) in Berlin, and especially for the trust he put in me with the laboratory equipment. My stay in Berlin gave me the opportunity to work with some wonderful people, and part of this thesis would not have been possible without their help. I am grateful to Thomas, Carsten, Reinhold, Robert, Jochanes, Saleem, and Markus for accepting me in the group and never denying me their support. I would have never thought that in such a short time many new friends would have become such an important part of my life. I will never forget Franzi, Chris, Alex, Nikos, Mathilde, and the rum-fortified hot wine at the Christmas markets with Thomas.

With this occasion I would love to thank also the Otto Mønsted Fond, for the financial support during my stay at HHI.

I would love to thank Radan Slavík for fabricating the long–period grating filters used in this thesis. They lasted longer than initially planned.

Among the people who are not present today, to see this work, I would love to remind my grandparents. They will always be present in my life.

I can not forget my friends in Denmark: Giulio, Marco, Luigi, Kamau, Claire, Georgios,

Filippo, Sara, Silvia, Valerie, Maria, just to mention a few. Their presence made the dark Danish winter afternoons more bearable, and the long summer days more enjoyable.

To all of you that I did not mention, it is not because you are not important, but because I am pressed for time and I have to finish.

# Abstract

The following thesis concerns pulse shaping and optical waveform manipulation for all-optical signal processing of ultra-high bit rate serial data signals, including generation of optical pulses in the femtosecond regime, serial-to-parallel conversion and terabaud coherent optical time division multiplexing (OTDM). Most of the thesis is focused on the utilization of space-time dualities for temporal pulse shaping and Fourier transformation. The space-time duality led to the implementation of the optical Fourier transform (OFT) technique which was used as a crossing bridge between the temporal and spectral domain. By using the frequency-to-time OFT technique or optical temporal differentiators based on long-period gratings (LPGs), it was possible to generate narrow flat-top pulses in the picosecond regime, and use them for mitigation of timing jitter or polarization dependence effects in OTDM demultiplexing experiments. The frequency-to-time technique was deployed also for implementing an all-optical synchronizer and re-timer. By using the specular phenomenon, time-to-frequency OFT, it was possible to develop a novel scheme for serial-to-parallel conversion, implemented via four-wave mixing (FWM) between dispersed OTDM data and linearly chirped pump pulses. This resulted in spectral compression, enabling the OTDM tributaries to be converted directly onto a dense wavelength division multiplexing (DWDM) grid. The serial-to-parallel conversion was successfully demonstrated for up to 640-GBd OTDM signals, reaching DWDM grids ranging from 100 GHz down to 25 GHz spacing, compliant with ITU-T specifications in terms of wavelength spacing and allocation. The final part of this thesis presents the latest results in OTDM transmission systems in combination with digital coherent detection, which enabled record-high serial data rates on a single-wavelength channel. The experimental results demonstrate 5.1- and 10.2-Tbit/s OTDM data signals achieved by 16-ary quadrature amplitude modulation (16-QAM), polarization multiplexing and symbol rates as high as 640 GBd and 1.28 TBd. These signal were transmitted with no penalty over 80- and 29-km dispersion-managed fiber (DMF).

# Resumé på dansk

Denne afhandling omhandler pulsformning og manipulering af optiske bølge-former til optisk signal behandling af ultrahurtige serielle data signaler, herunder frembringelsen optiske pulser af femtosekunders varighed, seriel til parallel konvertering, og koherent optisk tidslig multiplexing (OTDM) ved Terabaud symbolhastigheder. En stor del af afhandlingen fokuserer på brugen af rum-tid dualiteter til manipulering af pulsformer og Fourier transformation. Denne såkaldte rum-tid dualitet er baggrunden for optisk Fourier transformations (OFT) teknikken som bruges til at skifte mellem det tidslige og det spektrale domæne. Ved at anvende OFT teknikken (fra frekvens til tid) og optisk tids differentiering baseret på long-period gratings (LPG) lykkes det at frembringe flad-top pulser af pikosekunders varighed. Disse anvendes i forbindelse med OTDM demultiplexing til at dæmpe effekten af tidslig jitter samt til at opnå polarisationsuafhængighed. OFT teknikken (frekvens til tid) anvendes også til optisk synkronisering og re-timing. Denne afhandling præsenterer også en ny metode til optisk seriel til parallel konvertering baseret på OFT teknikken (fra tid til frekvens). Denne metode er baseret på firebølgeblanding (FWM) mellem disperserede OTDM pulser og lineært chirpede pumpe pulser, hvilket resulterer i en spektral komprimering af OTDM kanalerne der således kan konverteres direkte til et dense wavelength division multiplexing (DWDM) gitter. Metoden anvendes på OTDM signaler med symbolrater op til 640 GBd som konverteres til DWDM gitre med kanalafstande fra 100 GHz og ned til 25 GHz, i overensstemmelse med ITU-T specifikationerne. Til sidst præsenteres nye resultater indenfor OTDM transmissionssystemer med digital kohærent detektion, hvor der opnås rekordhøje bit hastigheder for datasignaler på én bølgelængde. Hér demonstreres 5.1 Tbit/s (640 GBd) transmission over 80 km fiber og 10.2 Tbit/s (1.28 TBd) transmission over 29 km dispersion managed fiber (DMF).

# Contents

# Ph.D. Publication List

## Publication list

This Ph.D. project has resulted in the following publication list:

Articles in peer-reviewed journals (11):

[J–1]: **E. Palushani**, H. C. H. Mulvad, M. Galili, H. Hu, L. K. Oxenløwe, A. T. Clausen, and P. Jeppesen, "OTDM-to-WDM Conversion Based on Time-to-Frequency Mapping by Time-Domain Optical Fourier Transformation", *IEEE J. Sel. Topics Quantum Electron.*, vol. 18, no. 2, pp. 681–688, March/April 2012.

[J–2]: J. Azaña, L. K. Oxenløwe, **E. Palushani**, R. Slavík, M. Galili, H. C. H. Mulvad, H. Hu, Y. Park, A. T. Clausen, and P. Jeppesen, "In-fiber sub-picosecond pulse shaping for nonlinear optical telecommunication data processing at 640 Gbit/s", *International J. Opt.*, vol. 2012, DOI: 10.1155/2012/895281, January 2012.

[J–3]: T. Richter, **E. Palushani**, C. Schmidt-Langhorst, R. Ludwig, L. Molle, M. Nölle, J. K. Fischer, and C. Schubert, "Transmission of Single-Channel 16-QAM Data Signals at Terabaud Symbol Rates", *J. Lightw. Technol.*, vol. 30, no. 4, pp. 504–511, February 2012.

[J–4]: H. C. H. Mulvad, **E. Palushani**, H. Hu, H. Ji, M. Galili, A. T. Clausen, M. Pu, K. Yvind, J. M. Hvam, P. Jeppesen, and L. K. Oxenløwe, "Ultra-high-speed optical serial-to-parallel data conversion by time-domain optical Fourier transformation in a silicon nanowire", *Opt. Express*, vol. 19, no. 26, pp. B825–B835, December 2011.

[J–5]: H. Hu, J. L. Areal, H. C. H. Mulvad, M. Galili, K. Dalgaard, **E. Palushani**, A. Clausen, M. S. Berger, P. Jeppesen, and L. K. Oxenløwe, "Synchronization, retiming and time-division multiplexing of an asynchronous 10 Gigabit NRZ Ethernet packet to terabit Ethernet", *Opt. Express*, vol. 19, no. 26, pp. B931–B937, December 2011.

[J–6]: L. K. Oxenløwe, M. Galili, H. C. H. Mulvad, H. Hu, J. L. Areal, **E. Palushani**, H. Ji, A. T. Clausen, and P. Jeppesen, "Nonlinear Optical Signal Processing for Tbit/s Ethernet Applications", *International J. Opt.*, vol. 2012, DOI: 10.1155/2012/573843, July 2011.

[J–7]: H. Hu, J. L. Areal, **E. Palushani**, L. K. Oxenlowe, A. T. Clausen, M. S. Berger and P. Jeppesen, "Optical Synchronization of a 10-G Ethernet Packet and Time-Division Multiplexing to a 50-Gb/s Signal Using an Optical Time Lens", *IEEE Photon. Technol. Lett.*, vol. 22, no. 21, pp. 1583–1585, November 2010.

[J–8]: T. D. Vo, H. Hu, M. Galili, **E. Palushani**, J. Xu, L. K. Oxenløwe, S. J. Madden, D. Y. Choi, D. A. P. Bulla, M. D. Pelusi, J. Schröder, B. Luther-Davies, and B. Eggleton, "Photonic chip based transmitter optimization and receiver demultiplexing of a 1.28 Tbit/s OTDM signal", *Opt. Express*, vol. 18, no. 16, pp. 17252–17261, July 2010.

[J–9]: H. Hu, H. C. H. Mulvad, M. Galili, **E. Palushani**, J. Xu, A. T. Clausen, L. K. Oxenløwe, and P. Jeppesen, "Polarization-Insensitive 640 Gb/s Demultiplexing Based on Four Wave Mixing in a Polarization-Maintaining Fibre Loop", *J. Lightw. Technol.*, vol. 28, no. 12, pp. 1789–1795, June 2010.

[J–10]: H. Hu, **E. Palushani**, M. Galili, H. C. H. Mulvad, A. T. Clausen, L. K. Oxenløwe, and P. Jeppesen, "640 Gbit/s and 1.28 Tbit/s polarisation insensitive all optical wavelength conversion", *Opt. Express*, vol. 18, no. 10, pp. 9961–9966, April 2010.

[J–11]: **E. Palushani**, L. K. Oxenløwe, M. Galili, H. C. H. Mulvad, A. T. Clausen, and P. Jeppesen, "Flat-top Pulse Generation by the Optical Fourier Transform Technique for Ultra-High-Speed Signal Processing", *IEEE J. Quantum Electron.*, vol. 45, no. 11, pp. 1317–1324, November 2009.

Articles in peer–reviewed conferences (33):

[C–1]: **E. Palushani**, T. Richter, R. Ludwig, C. Schubert, H. C. H. Mulvad, A. T. Clausen, and L.K. Oxenløwe, "OTDM-to-WDM Conversion of Complex Modulation Formats by Time-Domain Optical Fourier Transformation", in *Optical Fiber Communication Conference, OFC/NFOEC 2012*, Los Angeles, California, USA, 4–8 March, 2012, Paper OTh3H.2.

[C–2]: H. Hu, P. Münster, **E. Palushani**, M. Galili, K. Dalgaard, H. C. H. Mulvad, P. Jeppesen, and L.K. Oxenløwe, "640 Gbaud NRZ-OOK data signal generation and 1.19 Tbit/s PDM-NRZ-OOK field trial transmission", in *Optical Fiber Communication Conference, OFC/NFOEC 2012*, Los Angeles, California, USA, 4–8 March, 2012, Paper PDP5C.7 (postdeadline).

[C–3]: L. K. Oxenløwe, H. C. H. Mulvad, H. Hu, H. Ji, M. Galili, M. Pu, **E. Palushani**, K. Yvind, J. M. Hvam, A. T. Clausen, and P. Jeppesen, "Ultrafast Nonlinear Signal Processing in Silicon Waveguides", in *Optical Fiber Communication Conference, OFC/NFOEC 2012*, Los Angeles, California, USA, 4–8 March, 2012, Paper OTh3H.5.

[C–4]: H. C. H. Mulvad, **E. Palushani**, M. Galili, H. Hu, H. Ji, J. Xu, A. T. Clausen, P. Jeppesen, and L. K. Oxenløwe, "Time-Domain Optical Fourier Transformation for OTDM–DWDM and DWDM–OTDM Conversion", in *International Conference in Information Photonics & Optical Communications, IPOC 2011*, Singapore, 21–23 October, 2011.

[C–5]: H. C. H. Mulvad, **E. Palushani**, H. Hu, H. Ji, M. Galili, A. T. Clausen, M. Pu, K. Yvind, J.M. Hvam, P. Jeppesen, and L. K. Oxenløwe, "Ultra-High-Speed Optical Serial-to-Parallel Data Conversion in a Silicon Nanowire", in *European Conference on Optical Communication, ECOC 2011*, Geneva, Switzerland, 18–22 September, 2011, Paper Th.13.A.2 (postdeadline).

[C–6]: **E. Palushani**, C. Schmidt-Langhorst, T. Richter, M. Nölle, R. Ludwig, and C. Schubert, "Transmission of Serial 5.1-Tb/s Data Signal Using 16-QAM and Coherent Detection", in *European Conference on Optical Communication, ECOC 2011*, Geneva, Switzerland, 18–22 September, 2011, Paper We.8.B.5.

[C–7]: H. C. H. Mulvad, H. Hu, M. Galili, H. Ji, **E. Palushani**, A. T. Clausen, L. K. Oxenløwe, and P. Jeppesen, "DWDM–OTDM Conversion by Time-Domain Optical Fourier Transformation", in *European Conference on Optical Communication, ECOC 2011*, Geneva, Switzerland, 18–22 September, 2011, Paper Mo.1.A.5.

[C–8]: H. Hu, J. L. Areal, H. C. H. Mulvad, M. Galili, K. Dalgaard, **E. Palushani**, A. T. Clausen, M. S. Berger, P. Jeppesen, and L. K. Oxenløwe, "Synchronization, retiming and OTDM of an asynchronous 10 Gigabit Ethernet NRZ packet using a time lens for Terabit Ethernet", in *European Conference on Optical Communication, ECOC 2011*, Geneva, Switzerland, 18–22 September, 2011, Paper Tu.3.K.4.

[C–9]: L. K. Oxenløwe, M. Galili, M. Pu, H. Ji, H. Hu, K. Yvind, J. M. Hvam, H. C. H. Mulvad, **E. Palushani**, J. L. Areal, A. T. Clausen, and P. Jeppesen, "Ultrafast Optical Signal Processing in Nonlinear Silicon Waveguides", in *8th International Conference on Group IV Photonics, GFP 2011*, 14–16 September, 2011, Paper FB1, pp. 335–337.

[C–10]: R. Ludwig, T. Richter, **E. Palushani**, C. Schmidt-Langhorst, L. Molle, J. K. Fischer, M. Nölle, R. Elschner, and C. Schubert, "Ultrafast Transmission Systems using Coherent Technology", in *The 16th Opto–Electronics And Communications Conference, OECC 2011*, Kaohsiung, Taiwan, 4–8 July, 2011, pp. 808–811.

[C–11]: L. K. Oxenløwe, H. C. H. Mulvad, M. Galili, H. Hu, H. Ji, **E. Palushani**, J. L. Areal, A. T. Clausen, and P. Jeppesen, "Ultra-fast Optical Signal Processing using Optical Time Lenses and Highly Nonlinear Silicon Nanowires", in *Conference on Lasers and Electro-Optics, CLEO 2011*, Baltimore, Maryland, USA, 1–6 May, 2011, Paper CThA5.

[C–12]: T. Richter, **E. Palushani**, C. Schmidt-Langhorst, M. Nölle, R. Ludwig, J. K. Fischer, and C. Schubert, "Single Wavelength Channel 10.2 Tb/s TDM-Data Capacity using 16-QAM and Coherent Detection", in *Optical Fiber Communication Conference, OFC/NFOEC 2011*, Los Angeles, California, USA, Paper PDPA9 (postdeadline).

[C–13]: H. C. H. Mulvad, **E. Palushani**, M. Galili, J. Xu, H. Hu, A. T. Clausen, L. K. Oxenløwe, and P. Jeppesen, "OTDM–WDM Conversion Based on Time-Domain Optical Fourier Transformation with Spectral Compression", in *Optical Fiber Communication Conference, OFC/NFOEC 2011*, Los Angeles, California, USA, Paper OThN2.

[C–14]: J. L. Areal, H. Hu , **E. Palushani**, H. C. H. Mulvad, A. T. Clausen, M. S. Berger, L. K. Oxenløwe, and P. Jeppesen, "Synchronization and NRZ-to-RZ conversion of 10 Gbit/s Ethernet-like data packets and subsequent optical TDM multiplexing to 330 Gbit/s", in *Optical Fiber Communication Conference, OFC/NFOEC 2011*, Los Angeles, California, USA, Paper OThN5.

[C–15]: **E. Palushani**, H, Hu, M. Galili, H. C. H. Mulvad, R. Slavík, L. K. Oxenløwe, A. T. Clausen, and P. Jeppesen, "640 Gbit/s Polarisation-Independent Demultiplexing in a Standard Nonlinear-Optical-Loop-Mirror Using a Cascaded Long-Period Grating Pulse Shaper", in *IEEE Photonics Society 23rd Annual Meeting*, Denver, Colorado, USA, 7–11 November, 2010, pp. 203–204, Paper TuM2.

[C–16]: J. L. Areal, H. Hu, **E. Palushani**, H. Ji, A. T. Clausen, M. S. Berger, P. Jeppesen, and L. K. Oxenløwe, "Conversion of Asynchronous 10 Gbit/s Ethernet NRZ Frame into a Synchronous RZ Frame and Multiplexing to 170 Gbit/s", in *IEEE Photonics Society 23rd Annual Meeting*, Denver, Colorado, USA, 7–11 November, 2010, pp. 211–212, Paper TuM6.

[C–17]: L. K. Oxenløwe, M. Galili, H. Hu, H. Ji, **E. Palushani**, J. L. Areal, J. Xu, H. C. H. Mulvad, A. Clausen, and P. Jeppesen, "Serial Optical Communications and Ultra-Fast Optical Signal Processing of Tbit/s Data Signals", in *2010 IEEE International Topical Meeting on Microwave Photonics, MWP 2010*, Montreal, Canada, 5–8 October, 2010, pp. 361–364.

[C–18]: L. K. Oxenløwe, M. Galili, H. C. H. Mulvad, H. Hu, H. Ji, J. Xu, **E. Palushani**, J. L. Areal, A. T. Clausen, and P. Jeppesen, "Ultra-High-Speed Optical Signal Processing of Tbaud Data Signals", in *European Conference on Optical Communication, ECOC 2010*, Torino, Italy, 19–23 September, 2010, Paper Mo.1.A.1 (Invited).

[C–19]: H. Hu, J. L. Areal, **E. Palushani**, M. Galili, A. T. Clausen, M. S. Berger, L. K. Oxenløwe, and P. Jeppesen, "Synchronization and NRZ-to-RZ format conversion of 10 G Ethernet Packet based on a time lens", in *International Conference on Photonics in Switching, PS 2010*, Monterey, California, USA, 25–28 July, 2010, Paper PMD2.

[C–20]: T. D. Vo, H. Hu, M. Galili, **E. Palushani**, J. Xu, L. K. Oxenløwe, S. J. Madden, D.-Y. Choi, D. A. P. Bulla, B. Luther-Davis, J. Schröder, M. D. Pelusi, and B. J. Eggleton, "All-Optical Demultiplexing of 1.28 Tb/s to 10 Gb/s Using a Chalcogenide photonic chip", in *OSA Optics & Photonics Congress*, Karlsruhe, Germany, 21–24 June, 2010, Paper SPTuB2.

[C–21]: T. D. Vo, M. D. Pelusi, J. Schröder, B. J. Eggleton, H. Hu, M. Galili, **E. Palushani**, J. Xu, L. K. Oxenløwe, S. J. Madden, D.-Y. Choi, D. A. P. Bulla, and B. Luther-Davis, "Photonics chip based transmitter optimization and error-free receiver demultiplexing of 1.28 Tbit/s data", in *1st International Workshop on Nonlinear Systems and Advanced Signal Processing, IWNSASP 2010*, Ho Chi Min City, Vietnam, 15–17 September, 2010, pp. 98–102.

[C–22]: J. L. Areal, H. Hu, **E. Palushani**, L. K. Oxenløwe, A. T. Clausen, M. S. Berger, and P. Jeppesen, "Time-lens based Synchronizer and Retimer for 10 Gb/s Ethernet packets with up to ±1 MHz frequency offset", in *Conference on Lasers and Electro–Optics, CLEO 2010*, San Jose, California, USA, 16–21 May, 2010, Paper CThBB7.

[C–23]: H. Hu, **E. Palushani**, M. Galili, H. C. H. Mulvad, A. T. Clausen, L. K. Oxenløwe, and P. Jeppesen, "1.28 Tb/s Wavelength Conversion for Polarisation Multiplexed RZ-DPSK Signals", in *Optical Fiber Communication Conference, OFC/NFOEC 2010*, San Diego, California, USA, 21–25 March, 2010, Paper OWP1.

[C–24]: H. Hu, **E. Palushani**, J. L. Areal, M. Galili, A. T. Clausen, M. S. Berger, C. Peucheret, L. K. Oxenløwe, and P. Jeppesen, "Optical Frame Synchronizer for 10G Ethernet Packets aiming at 1 Tb/s OTDM Ethernet", in *Optical Fiber Communication Conference, OFC/NFOEC 2010*, San Diego, California, USA, 21–25 March, 2010, Poster JWA46.

[C–25]: M. Galili, H. C. H. Mulvad, L. K. Oxenløwe, H. Hu, **E. Palushani**, A. T. Clausen, and P. Jeppesen, "Generation and Detection of 2.56 Tbit/s OTDM Data Using DPSK and Polarisation Multiplexing", in *Optical Fiber Communication Conference, OFC/NFOEC 2010*, San Diego, California, USA, 21–25 March, 2010, Paper OThV2.

[C–26]: T. D. Vo, H. Hu, M. Galili, **E. Palushani**, J. Xu, L. K. Oxenløwe, S. J. Madden, D. Y. Choi, D. A. P. Bulla, M. D. Pelusi, J. Schröder, B. L.-Davies, and B. J. Eggleton, "Photonic Chip based 1.28 Tbaud Transmitter Optimization and Receiver OTDM Demultiplexing", in *Optical Fiber Communication Conference, OFC/NFOEC 2010*, San Diego, California, USA, 21–25 March, 2010, Paper PDPC5 (postdeadline).

[C–27]: J. L. Areal, H. Hu, C. Peucheret, **E. Palushani**, R. S. Puttini, A. T. Clausen, M. S. Berger, A. V. Osadchiy, and L. K. Oxenløwe, "Analysis of a Time-lens based Optical Frame Synchronizer and Retimer for 10G Ethernet Aiming at a Tb/s Optical Router/Switch Design", in *2010 14th conference on Optical Network Design and Modelling, ONDM 2010*, Kyoto, Japan, 31 January– 03 February, 2010, Poster P.3.

[C–28]: J. L. Areal, H. Hu, **E. Palushani**, A. T. Clausen, M. S. Berger, and L. K. Oxenløwe, "Time-lens based optical packet pulse compression and retiming", Proceedings of *SPIE, Nonlinear Optics and Applications IV*, vol. 7728, 2010.

[C–29]: **E. Palushani**, H, Hu, L. K. Oxenløwe, R. Slavík, M. Galili, H. C. H. Mulvad, A. T. Clausen, and P. Jeppesen, "640 Gb/s timing tolerant demultiplexing using a cascaded long-period fiber grating pulse shaper", in *European Conference on Optical Communication, ECOC 2009*, Vienna, Austria, 20–24 September, 2009, Paper Tu.4.3.3.

[C–30]: H. Hu, H. C. H. Mulvad, M. Galili, **E. Palushani**, A. T. Clausen, L. K. Oxenløwe, and P. Jeppesen, "Polarisation-insensitive 640 Gbit/s demultiplexing using a polarisation maintaining highly non-linear fibre", in *International Conference on Photonics in Switching, PS 2009*, Pisa, Italy, 19–23 September, 2009, Paper FrI1–2.

[C–31]: C. Peucheret, L. K. Oxenløwe, H. C. H. Mulvad, M. Galili, J. B. Jensen, J. Seoane, **E. Palushani**, H. Hu, J. Xu, A. T. Clausen, K. Rottwitt, N. Kang, J. L. Areal, H. Ji, B. Zsigri, and P. Jeppesen, "High-Speed Signal Processing Using Highly Nonlinear Optical Fibres", in *International Conference on Optical Communication And Networks, ICOCN 2009*, Beijing, China, 15–17 September, 2009.

[C–32]: H. C. H. Mulvad, L. K. Oxenløwe, M. Galili, A. T. Clausen, J. Xu, **E. Palushani**, H. Ji, and P. Jeppesen, "Optical Signal Processing up to 1.28 Tbit/s ", in *The 14th Opto -Electronics and Communications Conference, OECC 2009*, Hong Kong, China, 13–17 July, 2009, Paper WD1.

[C–33]: **E. Palushani**, L. K. Oxenløwe, M. Galili, H. C. H. Mulvad, A. T. Clausen, and P. Jeppesen, "Pulse shaping using the Optical Fourier Transform Technique for ultra-high speed signal processing", in *IEEE Lasers and Electro–Optics Society Winter Topicals, LEOS 2009*, Innsbruck, Austria, 12–14 January, 2009, pp. 272–273, Paper WC4.4.

# Chapter 1

# Introduction

Increasing bandwidth needs [1] driven by high-definition video on demand, video sharing, cloud computing, data centric applications, etc., request the refinement of actual techniques and the research of new ones in order to improve signal generation, transmission and detection. Increased Internet traffic growth is forcing carriers to provide more bandwidth to meet new market demands. This can be seen in Fig. 1.1, where it is shown the data traffic for the German internet exchange DE-CIX in Frankfurt [2] for the period July 2008–August 2010. As it can be seen the average traffic has increased by almost 100% every year, and its growths has not been influenced by the latest economic crisis. In these scenarios, research in optical communication systems has an important role due to the high capacity bandwidth that fibers can provide.

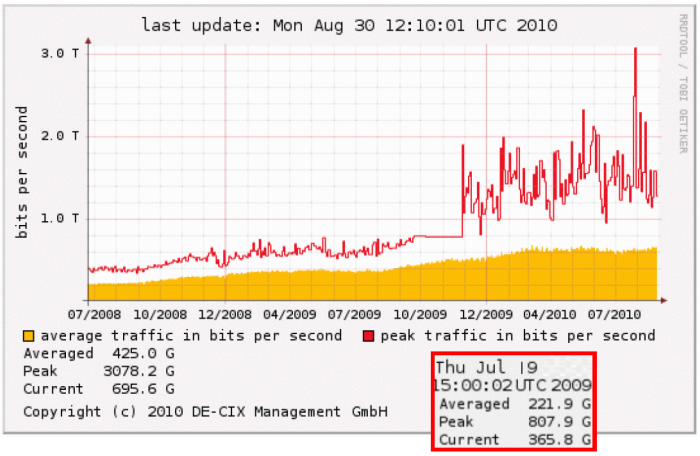


**Figure 1.1:** German internet exchange DE-CIX, Frankfurt (2010). Inset for comparison: average, peak and current traffic data on a specific date in July 2009.

Different technologies have been developed in order to face the increasing bandwidth requests: wavelength division multiplexing (WDM) [3], orthogonal frequency division multiplexing (OFDM) [4,5], space division multiplexing [6], multicore fiber technology [7], or even a combination of space-, wavelength- and polarization-division multiplexing [8,9]. At the same time, the increase of the serial channel bit rate has always been an active research topic. This is reflected in commercial systems which have steadily adopted the fastest electrical time division multiplexing technology (ETDM), whose symbol rates have reached the 100 GBd regime. The optical counterpart of ETDM is optical time division multiplexing (OTDM), whose deve-

lopment started more than 20 year ago [10], having as a target the realization of a technology that would fit the demands of future optical networks. These would be all-photonic networks, in which ultra-fast optical signals of any bit rate and modulation format are transmitted and processed end-to-end in the optical domain, with optical-electrical-optical (O/E/O) conversions necessary only in the end terminals. Today OTDM has succeeded in the transmission of optical data signals at TDM rates of up to 10.2 Tbit/s over a single wavelength [11–13], [C-12]. This is related to the advantageous combination of OTDM technology with coherent detection [12,14], [C-12] which is compatible with spectrally efficient modulation formats and allows for simultaneous demultiplexing and demodulation of ultrahigh speed data signals as well as mitigation of transmission impairments in the receiver.

High-speed serial data may be particularly beneficial e.g., in metropolitan area networks or for serial connections between super-computers. At such high bit-rates, all-optical realization of multiplexing, demultiplexing and processing must be considered, in order to avoid the limitation caused by the electronic bottleneck. All-optical signal processing, acting as a bridge between low-bit-rate electrical signals and high-bit-rate OTDM signals, relies on optical effects with intrinsic response times down to a few femtoseconds, which allow for operation speeds of several Tbit/s without an associated increase in energy consumption as seen in electronics. This Ph.D. thesis concentrates on optical waveform manipulation for all-optical signal processing of ultra-high bit rate serial data signals, including generation of optical pulses in the femtosecond regime, serial-to-parallel conversion and terabaud coherent OTDM.

## 1.1 Project description and objectives

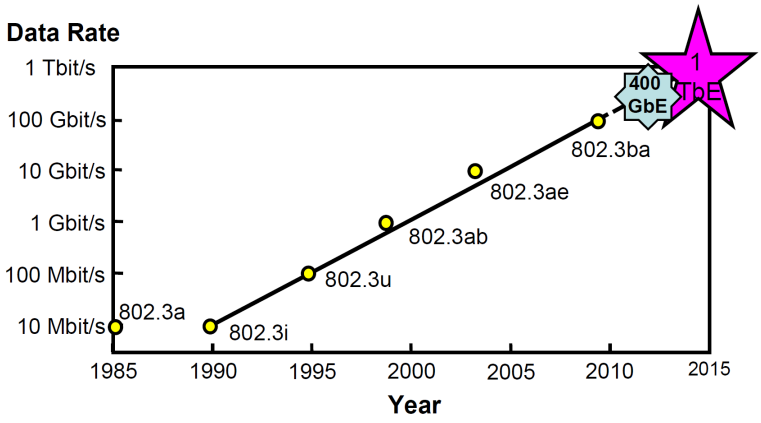


**Figure 1.2:** Published Ethernet standards by IEEE.

This Ph.D. is part of a larger three-year project called NOSFERATU (**N**onlinear **O**ptical **S**witching **F**or **E**xtremely High Data **Rat**e Comm**u**nications), which started in January 2009 and was funded by the Danish Research Council (*Danmarks Forskningsrådet for Teknologi og Production*).

Figure 1.2 can be considered as the motivational point of the NOSFERATU project. It shows the Ethernet standards defined over the years by the IEEE and ITU-T. At the time when the NOSFERATU project started the P802.3ba Task Force was trying to define the standards for 40 Gbit/s (40 GE) and 100 Gbit/s Ethernet (100 GE), whose ratification in

June 2010 was a major result in the long run of Ethernet as a consolidated protocol [15]. In fact, some of the Task Force's objectives, among others, were: 1) preservation of the 802.3 Ethernet frame structure; 2) preservation of the minimum and maximum frame size for the current 802.3 standard; 3) provide appropriate support for optical transport network (OTN); 4) support a media access control (MAC) data rate of 40- and 100-Gbit/s; and 5) provide 40- and 100-Gbit/s operations over at least 40 km single-mode fiber (SMF) [16]. While on one side the development of 100 GE is seen as a way to relieve the congested network, it is also supposed to introduce new ways of electrical and optical signaling that will increase the port density integration while reducing the cost and energy consumption.

The development of 100 GE was justified from observing that the bandwidth requirement for core networks is doubling every 18 months [17]. This means that by 2015 core networks will need Terabit Ethernet (TE), and that next generation Ethernet standards will need a greater focus and research on electrical and optical signaling. With this in mind, the NOSFEARTU project was started in order to investigate the potentiality of the OTDM technique for the realization of the first serial TE. In a certain way, NOSFERATU followed the path of other projects conducted at DTU Fotonik, such as HECTO (High-Speed Electro-Optical Components for Integrated Transmitter and Receiver in Optical Communication) [18] and GIBON (Opto-electronic integration for 100 Gigabit Ethernet Optical Networks) [19], aiming at the realization of the first serial 100 GE. NOSFERATU's goal was to propose a network scenario allowing for current standard 10 Gbit/s Ethernet (10 GE) lines to be time-multiplexed up to 1 TE, and develop techniques to add intelligence to the network allowing for efficient switching/routing. Traditionally, when the Ethernet data rate has been increased to boost efficiency, it has been in factors of 10×. For this reason the project tried to propose an optical Ethernet upgrade from future 100 GE lines to serial 1 Tbit/s. Some of the functionalities addressed in the project were: 1) investigation, in collaboration with the Networks group at DTU Fotonik, of OTDM networking issues for optical Ethernet solutions leading to 1 TE, starting from 100 GE or from 10 GE; 2) investigation of a stable multiplexer for 1 TE; 3) pulse shaping for 1 Tbit/s data rates; 4) exploration and selection, based on stable operation, of various nonlinear switches based on the ultra-fast third order optical Kerr effect, such as fiber switches, chalcogenite ($As_2S_3$-based) glass waveguides, etc.

As part of NOSFERATU, this Ph.D. project focuses its attention on the physical layer of the network. More specifically, it concentrates on the generation, transmission, reception and processing of the ultra-high-speed optical waveforms involved with Tbit/s OTDM signals.

## 1.2 Optical time division multiplexing

Figure 1.3 shows a typical OTDM transmitter. Differently from WDM systems, OTDM systems require only one laser source, able to generate short pulses at a certain base rate ($B$). This is much lower compared to the OTDM signal rate, and sources at 10- or 40-GHz are commercially available. Some of the pulsed light sources that can be used for OTDM are: 1) electro-absorption modulator (EAM) based [20, 21], semiconductor mode-locked lasers (SMLL) [22] and erbium glass oscillator pulse generating lasers (ERGO-PGL) [23]. Some of the main requirements on the pulse source are low or absent ghost pulses and a low timing jitter, as these deteriorate the system's performance resulting in inter-channel crosstalk. As typically the pulses' width is too broad to reach ultra-high serial data communication in the terabaud (TBd) regime, a compression stage can be employed

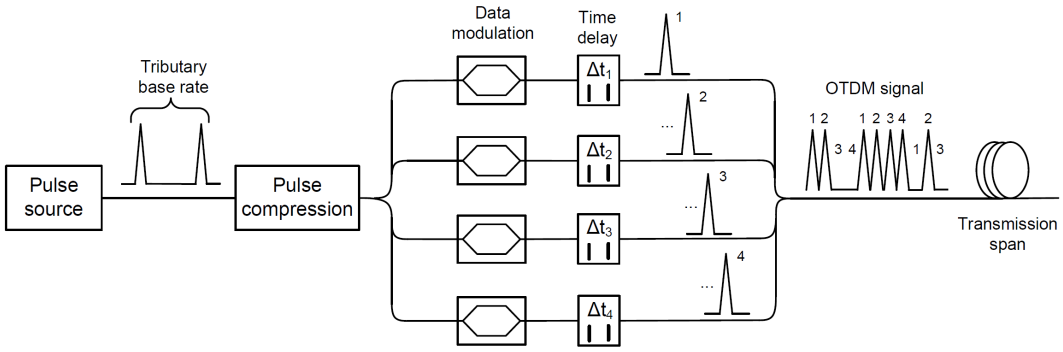


**Figure 1.3:** A conventional OTDM transmitter: A pulse source generates narrow pulses at the *tributary base rate* ($B$). The pulses are split into $N$ branches (4 in this case) which are separately modulated with individual data streams. The data-modulated channels are then bit-interleaved, by using appropriate time-delays $\Delta t_{1,2,3,4}$, and are combined into the OTDM data signal having a bit rate equal to $N \times B$.

to generate narrow pulses with femtosecond widths. Usually, the compression stage consists of a nonlinear medium, such as highly-nonlinear fiber (HNLF) in which due to self-phase modulation (SPM) a broad supercontinuum is generated. After the compression stage, the laser pulses are injected into an optical multiplexer, where they are split in $N$ different branches, each equipped with a modulator and a time delay. Typically, on-off keying (OOK) data modulation is the most used format for OTDM. However, in order to improve spectral efficiency, advance modulation formats such as quadrature phase shift keying (QPSK) or 16-ary quadrature-amplitude modulation (16-QAM) [C-12] can be deployed as well. In this case a coherent receiver would be necessary in order to retrieve the data information (see App.1). After modulation, the lower speed tributary channels are time-delayed and combined into a higher speed OTDM signal. The width of the pulses should be narrow enough to allow bit-interleaving without inter-channel interference caused from overlapping of neighboring pulses. The resulting aggregated rate of the OTDM signal is given from the number of branches in the multiplexing stage multiplied by the base rate of the tributaries ($N$x$B$). In the following work the aggregated symbol rate of the OTDM signal will be 320-, 640- and 1280-GBd, derived from time-multiplexing 10 GBd channels. It has to be noticed that under laboratory investigations, usually in order to minimize the number of optical components, the laser pulse train is modulated before the multiplexing stage. This results in the same data stream on all channels, but it also simplifies the set-up considerably.

The OTDM transmitter allows generation of serial data rates that go beyond the speed limits of electronic data generation and reception. For this reason, the OTDM channels have to be extracted, or demultiplexed to the base rate, before electrical detection and further processing. In fact, the receiver part is one of the more challenging parts of the OTDM system. Figure 1.4 shows the schematic of a typical OTDM receiver. A clock recovery mechanism is needed in order to synchronize the demultiplexer and the receiver. The base rate clock can be transmitted along with the OTDM signal on a different wavelength and extracted by passive filter or it can be directly extracted from the data signal itself. The OTDM demultiplexer is required to implement a switching window able to select only a single channel. This is immediately translated in terms of speed, width and shape of the switching window. In terms of response time, fibre-based switches are an ideal candidate due to the ultra fast response <10 fs of the nonlinear Kerr effect in silica [24]. Ideally, the switch should open a switching window equal to the inverse bit rate of the data signal. In all-optical

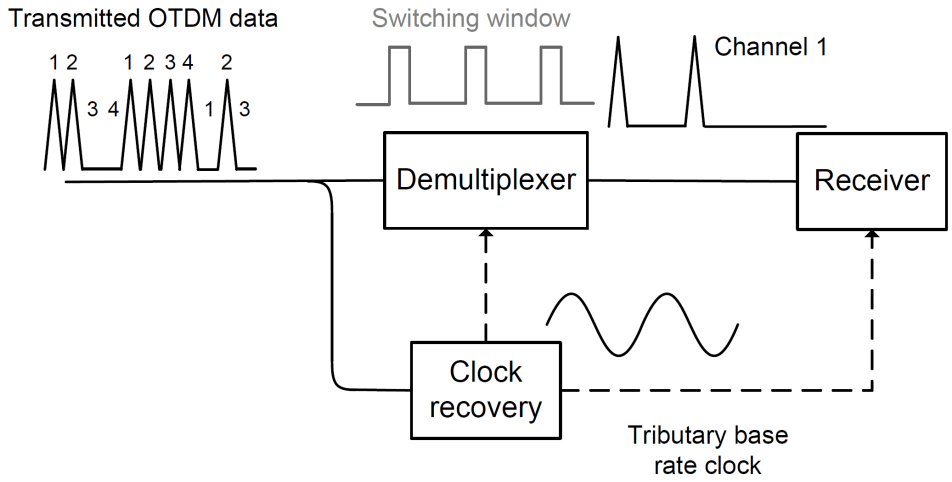


**Figure 1.4:** A conventional OTDM receiver: A clock recovery mechanism extracts the base rate clock from the transmitted OTDM data signal. The clock is used to synchronize the demultiplexer to the OTDM data. The switching window of the demultiplexer extracts one individual tributary data-channels (channel #1 in this case), which can be detected by a low-speed electronic receiver.

demultiplexing the switching window mechanism is implemented by combining the data signal with a base rate signal, called control or switching signal. In these systems the shape of the switching pulse determines the shape of the switching window. Typically, a demultiplexer extracts only a single channel at a time, as shown in Fig. 1.4, and separate (e.g., parallel) demultiplexers are needed to retrieve all channels. This means that the complexity of the receiver scales linearly with the number of tributaries. However, we report in this thesis the utilization of a new mechanism for extracting in a single shot half of the tributary channels, independently on their aggregation rate and type of modulation. Once demultiplexed, each channel runs at the low base rate, and can therefore be detected by a standard receiver, be this one direct-detection (DD) or coherent detection. It has to be noticed that chromatic dispersion (CD) and polarization mode dispersion (PMD) are two big detrimental factors for OTDM systems. This is related to the broad spectral content of the narrow OTDM pulses. For this reason full compensation of these effects is necessary before signal demultiplexing and reception.

## 1.3 Contributions of this Ph.D. thesis

The following describes some of the main results and contributions achieved during this Ph.D. project, listed in the same order as the chapters in which they appear:

- **Flat-top pulse generation for polarization-independent demultiplexing in a nonlinear optical loop mirror (NOLM).** It was experimentally demonstrated, as predicted in [25], that the utilization of flat-top control pulses can be used to increase the polarization-independence of the NOLM, even at high symbol rates such as 640 GBd. In this experiment the flat-top pulses were generated by using a cascaded pair of lon-period gratings (LPG) inscribed in a standard single-mode fiber (SMF).

- **Utilization of the optical Fourier transform (OFT) technique for all-optical signal processing.**

1. It is shown how the frequency-to-time conversion is used to generate flat-top pulses deployed in a demultiplexing experiment in order to increase the tolerance to timing jitter. The properties of the linearly chirped flat-top pulses were used also for channel equalization of time-to-frequency converted OTDM channels.
2. Time-to-frequency OFT led to the realization of a novel scheme for serial (OTDM) to parallel (WDM) signal conversion. The conversion process is based on time-to-frequency mapping implemented by a FWM process between dispersed OTDM data and linearly chirped pump pulses. This technique is shown to be independent of the OTDM symbol rate and the tributary data modulation. This technique can not only enable a significant reduction in the complexity of an OTDM receiver, but due to its simplicity and symbol-rate scalability it could permit ultra-high-speed serial data communication systems with potentially moderate energy requirements.
3. Finally, it is proven how to utilize the Fourier transformation properties of a time lens as an optical re-timer used to synchronize incoming asynchronous Ethernet packets to a local master clock.

- **Transmission of single-channel 16-QAM data signals at terabaud symbol rates.** These results were obtained during the author's external research stay at the Heinrich-Hertz Institute in Berlin. The highest serial data rate so far (10.2 Tbit/s [C-12], [J-3]), was generated by combining multi-level modulation, polarization multiplexing (PolMux), digital coherent detection, and the record symbol rate of 1.28 TBd. This signal was transmitted, with low penalty, in 29-km dispersion managed fiber (DMF). Moreover this is the first demonstration of the successful use of 16-QAM modulation on a symbol rate as high as 1.28 TBd.

Other secondary contributions in which the author has participated but are not analyzed in this thesis include: all-optical monitoring and demultiplexing of a 1.28 TBd OTDM signal performed in a photonic chalcogenite chip [C-20, 21, 26], [J-8], and polarization insensitive wavelength conversion and demultiplexing of a 640 GBd and 1.28-TBd OTDM signal [C-23, 30], [J-9, 10]. For more details please refer to the publication list.

## 1.4 Structure of the thesis

This manuscript starts with Chapter 2, which contains the background material needed to understand the experimental work in the rest of the thesis. It gives an introduction to pulse propagation in nonlinear fibers; it describes the implementation and functionality of the NOLM; and it describes the general principle of pulse compression in order to reach pulse widths suitable for terabaud serial data signals.

Chapter 3 is intended as a mathematical overview of the space-time duality and its application for realization of temporal optical systems equivalent to spatial ones. The chapter derives the conditions under which it is possible to achieve a conversion mechanism between the spectral and temporal domains by utilizing a time lens and a dispersive mechanism. The frequency-to-time conversion is analyzed at first, followed by the time-to-frequency mapping, and followed as well by the re-timing principle. Chapter 4, 5 and 6 show the experimental validation of these concepts in the same order as their theoretical foundations are analyzed

in Chapter 3.

Chapter 4 focuses on two different techniques for generation of flat-top pulses, respectively by frequency-to-time OFT mapping and long-period gratings (LPG). These pulses are used in some OTDM demultiplexing experiments aiming at improving the system's performance towards timing jitter and polarization dependence.

Chapter 5 describes the utilization of the time-to-frequency conversion OFT technique for serial-to-parallel mapping, in a single step, of an OTDM signal into a dense WDM (DWDM) grid. The OFT technique is implemented by a FWM process between dispersed OTDM data and linearly chirped pump pulses. The chapter includes both numerical and experimental results demonstrating the scalability of the technique to different symbol rates, modulation formats, and spectral compression ratios.

Chapter 6 describes the utilization of the time lens for synchronization of an incoming Ethernet packet to a certain master clock. The problem of asynchronous data arrivals is transformed into a re-timing issue between the lens and the input signal. In this case the time lens is implemented via an electro-optical phase modulator with sinusoidal phase modulation, resulting in re-timing of different packet lengths to a local clock corresponding to the base rate of an OTDM signal.

Finally, Chapter 7 presents the latest results on 5.1- and 10.2-Tbit/s serial data rates, achieved with 16-QAM modulation at symbol rates of 640 GBd and 1.28 TBd with transmission over 80- and 29-km dispersion-managed fiber (DMF). The bit error ratio (BER) of all 256 OTDM tributaries (both polarizations, 10.2 Tbit/s case) was found to be below the threshold for hard-decision forward error correction (FEC) coding. Assuming 7% FEC, this resulted in a net data rate of 9.5 Tbit/s, which is the highest serial data rate achieved up to now. The 10.2 Tbit/s signal is simultaneously demultiplexed and demodulated in a coherent homodyne receiver using a pulsed local oscillator (LO).

# Chapter 2

# Background

Techniques for the precise synthesis and control of the temporal shape of optical pulses with durations in the picosecond and sub-picosecond regimes [26] are of fundamental importance for a wide range of applications in ultrahigh-bit-rate optical communications, particularly to enhance the performance of a range of nonlinear optics-based data-processing operations [26–29].

The following chapter is intended as an introduction to pulse compression and demultiplexing techniques used with OTDM systems and deployed in the rest of this thesis. The chapter touches upon some topics which are relevant for understanding the experimental work included in the manuscript. The chapter is organized as follows: Section 2.1 gives an introduction to fiber nonlinearities[1], with a focus on nonlinear pulse propagation (Section 2.1.1), self- and cross-phase modulation (SPM, XPM) (Section 2.1.2), and four-wave mixing (Section 2.1.3); Section 2.2 focuses on the nonlinear optical loop mirror (NOLM) and its implementation as a demultiplexing device; finally Section 2.3 gives a general overview on pulse compression techniques which can be deployed for generation of 1.28 TBd OTDM data signals [C-12]. The simultaneous demultiplexing and demodulation of OTDM tributaries with advanced modulation formats performed with pulsed local oscillators (LO) in a coherent receiver will be treated in Chapter 7 (Section 7.2).

## 2.1 Fiber nonlinearities

### 2.1.1 Nonlinear pulse propagation in optical fibers

The study of most nonlinear effects in optical fibers involves the use of short pulses with widths ranging from few picoseconds to tens of femtoseconds. When such optical pulses propagate inside a fiber, both dispersive and nonlinear effects influence their temporal and spectral shapes.

By using Maxwell's equations, it is possible to obtain the wave equation describing light propagation in optical fibers [24]:

$$\nabla \times \nabla \times \mathbf{E} = -\frac{1}{c^2}\frac{\partial^2 \mathbf{E}}{\partial t^2} - \mu_0 \frac{\partial^2 \mathbf{P}}{\partial t^2}, \tag{2.1}$$

where $c$ is the speed of light, $\mu_0$ is the vacuum permeability, $\mathbf{E}$ is the electric field and $\mathbf{P}$ is the

[1] Please note that a more complete description and accurate analysis can be found in [24].

induced electric polarization. When a strong electromagnetic field is applied, the response of a dielectric material becomes nonlinear. As a result, the polarization $\mathbf{P}$ induced by the electric dipoles is related in a nonlinear fashion to the electric field $\mathbf{E}$ [24, 30–33]:

$$\mathbf{P} = \varepsilon_0\Big(\chi^{(1)} \cdot \mathbf{E} + \chi^{(2)} : \mathbf{EE} + \chi^{(3)}\vdots\mathbf{EEE} + \cdots\Big), \tag{2.2}$$

where $\varepsilon_0$ is the vacuum permittivity and $\chi^{(m)}$ is the $m$th order susceptibility.

The dominant contribution to $\mathbf{P}$ comes from the linear susceptibility term $\chi^{(1)}$. Its effects are included through the refractive index $n(\omega)$ and the field attenuation $\alpha(\omega)$:

$$n(\omega) = 1 + \frac{1}{2}\mathrm{Re}\left[\tilde{\chi}^{(1)}(\omega)\right], \tag{2.3}$$

$$\alpha(\omega) = \frac{\omega}{nc}\mathrm{Im}\left[\tilde{\chi}^{(1)}(\omega)\right]. \tag{2.4}$$

where $\tilde{\chi}^{(1)}(\omega)$ is the Fourier transform of $\chi^{(1)}(t)$, and Re and Im stand for real and imaginary part.

The second-order susceptibility $\chi^{(2)}$ is responsible for certain nonlinear effects such as: second-harmonic generation (SHG) [33, 34], sum- and difference-frequency generation (SFG, DFG) [33]. However this term vanishes for symmetric dielectric molecules, such as $SiO_2$. Hence, optical fibers do not present second-order nonlinear effects. On the other hand, third-order susceptibility $\chi^{(3)}$ is responsible for such nonlinear effect as third-harmonic generation (THG), four-wave mixing (FWM) and nonlinear refraction [24]. In case of non phase matching, unless special efforts are made, third-harmonic generation and four-wave mixing are very low in optical fibers. Hence most of the nonlinearities come from the nonlinear refraction, or the ability of the refractive index to be dependent on the intensity of the injected field.

As a result of the above argumentation, the induced electric polarization can be written as a sum of a linear polarization term ($\mathbf{P}_L$) and a nonlinear one ($\mathbf{P}_{NL}$)

$$\mathbf{P}(\mathbf{r}, t) = \mathbf{P_L}(\mathbf{r}, t) + \mathbf{P_{NL}}(\mathbf{r}, t) \tag{2.5}$$

where

$$\mathbf{P}_L(\mathbf{r}, t) = \varepsilon_0 \int_{-\infty}^{t} \chi^{(1)}(t - t')\mathbf{E}(\mathbf{r}, t')\,\mathrm{d}t', \tag{2.6}$$

and

$$\begin{aligned}\mathbf{P}_{NL}(\mathbf{r}, t) = &\varepsilon_0 \int_{-\infty}^{t} \mathrm{d}t_1 \int_{-\infty}^{t} \mathrm{d}t_2 \int_{-\infty}^{t} \mathrm{d}t_3 \\ &\times \chi^{(3)}(t - t_1, t - t_2, t - t_3)\vdots\mathbf{E}(\mathbf{r}, t_1)\mathbf{E}(\mathbf{r}, t_2)\mathbf{E}(\mathbf{r}, t_3).\end{aligned} \tag{2.7}$$

Due to the fact that the attenuation $\alpha(\omega)$ (Eq. (2.4)) of optical fibers is very small, at least in the 1500–1600 nm range of interest, the dielectric constant $\varepsilon(\omega) = 1 + \chi^{(1)}(\omega) = (n + i\alpha c/2\omega)^2$ can be substituted by $n^2(\omega)$. This, combined with the fact that the refractive index $n(\omega)$ is independent on the spatial distribution, results in the following wave equation

$$\nabla^2\mathbf{E} - \frac{1}{c^2}\frac{\partial^2\mathbf{E}}{\partial t^2} = \mu_0\frac{\partial^2\mathbf{P}_L}{\partial t^2} + \mu_0\frac{\partial^2\mathbf{P}_{NL}}{\partial t^2}. \tag{2.8}$$

In the slowly varying envelope approximation the electric field $\mathbf{E}$(r,t) can be written as

$$\mathbf{E}(\mathbf{r},t) = \frac{1}{2}\hat{x}\left[E(\mathbf{r},t)\exp(-i\omega_0 t) + \text{c.c.}\right], \tag{2.9}$$

where $\hat{x}$ is the polarization unit vector, $E(\mathbf{r},t)$ is a slowly varying function of time, and *c.c.* stands for complex conjugate. Considering the nonlinear response as instantaneous[2], meaning that the time dependence of $\chi^{(3)}$ in Eq. (2.7) is given by a product of three delta functions, then Eq. (2.7) is rewritten as

$$\mathbf{P}_{NL}(\mathbf{r},t) = \varepsilon_0\chi^{(3)}\vdots\mathbf{E}(\mathbf{r},t)\mathbf{E}(\mathbf{r},t)\mathbf{E}(\mathbf{r},t). \tag{2.10}$$

By eliminating the third-harmonic terms resulting from the above equation, then $\mathbf{P}_{NL}$ is given by

$$P_{NL}(\mathbf{r},t) \approx \varepsilon_0\varepsilon_{NL}E(\mathbf{r},t), \tag{2.11}$$

where the power dependent nonlinear contribution to the dielectric constant is

$$\varepsilon_{NL} = \frac{3}{4}\chi^{(3)}_{xxxx}|E(\mathbf{r},t)|^2. \tag{2.12}$$

In the slowly varying envelope approximation, the Fourier transform ($\tilde{E}(\omega-\omega_0)$) of the slowly varying function $E(\mathbf{r},t)$ satisfies the Helmholtz equation:

$$\nabla^2\tilde{E} + \varepsilon(\omega)k_0^2\tilde{E} = 0, \qquad \text{with} \qquad k_0 = \frac{\omega}{c}, \tag{2.13}$$

and

$$\varepsilon(\omega) = \underbrace{1+\tilde{\chi}^{(1)}(\omega)}_{\text{linear part}} + \varepsilon_{NL}. \tag{2.14}$$

The new refractive index ($\tilde{n}$) and absorption coefficient ($\tilde{\alpha}$) can be related to the new dielectric constant via $\varepsilon = (\tilde{n} + i\tilde{\alpha}/2k_0)^2$ or

$$\tilde{n} = n + n_2|E|^2 = \frac{3}{8n}\text{Re}(\chi^3_{xxxx}), \quad \tilde{\alpha} = \alpha + \alpha_2|E|^2 = \frac{3\omega_0}{4nc}\text{Im}(\chi^3_{xxxx}), \tag{2.15}$$

where $n$ and $\alpha$ are related to the linear part of $\varepsilon(\omega)$. The last equation shows that the refractive index is dependent on the intensity of the field ($|E|^2$) inside the fiber.

Under the slowly varying envelope approximation it is possible to write

$$\tilde{E}(\mathbf{r},\omega-\omega_0) = F(x,y)\tilde{A}(z,\omega-\omega_0)\exp[i\beta(\omega)z], \tag{2.16}$$

where

$$\tilde{E}(\mathbf{r},\omega-\omega_0) = \int_{-\infty}^{\infty} E(\mathbf{r},t)\exp\left[i(\omega-\omega_0)t\right]\mathrm{d}t, \tag{2.17}$$

[2]No Raman effect was taken into consideration.

and $\tilde{A}(z, \omega - \omega_0)$ is a slowly varying function of $z$, $\beta(\omega)$ is the propagation constant, and $F(x, y)$ is the modal distribution, which for a single-mode fiber corresponds to the modal distribution of the fundamental fiber mode $HE_{11}$, or to its Gaussian approximation. In the time domain the linearly polarized electric field can be expressed as

$$\mathbf{E}(\mathbf{r}, t) = \frac{1}{2}\hat{x}\left[F(x, y)A(z, t)\exp\left[i(\beta_0 z - \omega_0 t)\right] + \text{c.c.}\right] \tag{2.18}$$

where $A(z, t)$ is the slowly varying complex envelope. The nonlinear evolution of the field can be described by the evolution of $A(z, t)$, governed by the nonlinear Schrödinger equation

$$\frac{\partial A}{\partial z} + \beta_1 \frac{\partial A}{\partial t} + i\frac{\beta_2}{2}\frac{\partial^2 A}{\partial t^2} + \frac{\alpha}{2}A = i\gamma|A|^2 A, \tag{2.19}$$

where $\gamma$ is the nonlinear coefficient expressed as

$$\gamma(\omega_0) = \frac{n_2\omega_0}{cA_{eff}}, \qquad \text{with} \qquad A_{eff} = \frac{\left(\iint_{-\infty}^{+\infty} |F(x, y)|^2 \,\mathrm{d}x\,\mathrm{d}y\right)^2}{\iint_{-\infty}^{+\infty} |F(x, y)|^4 \,\mathrm{d}x\,\mathrm{d}y}. \tag{2.20}$$

$A_{eff}$ is the effective core area, and as it can be seen, it is dependent on the modal distribution $F(x, y)$. The propagation constant $\beta(\omega)$ can be written in a Taylor expansion around the carrier frequency $\omega_0$ as

$$\beta(\omega) = n(\omega)\frac{\omega}{c} = \beta_0 + \sum_{m=1} \frac{(\omega - \omega_0)^m}{m!}\beta_m, \quad \text{with} \quad \beta_m = \frac{\mathrm{d}^m \beta}{\mathrm{d}\,\omega^m}\Big|_{\omega=\omega_0} \tag{2.21}$$

where $\beta_0 \equiv \beta(\omega_0)$. The coefficient $\beta_1 \equiv 1/v_g$ is related to the group velocity $v_g$ of the pulse envelope, and the second term $\beta_2$ is related to the derivative $\mathrm{d}\beta_1/\mathrm{d}\omega$, which can be positive (normal dispersion regime) or negative (anomalous dispersion regime). To be noticed the fact that the Taylor expansion of $\beta(\omega)$ in Eq. (2.19) was stopped at the second term. However, higher-order terms should still be included if their influence is relevant during pulse propagation.

### 2.1.2 Self- and cross-phase modulation

The two most widely known nonlinear effects that result form the dependence of the refractive index on the intensity of the optical field, are self-phase modulation (SPM) and cross-phase modulation (XPM). Self-phase modulation is related to the phase shift ($\phi_{NL}^{(SPM)}$) that an optical field induces upon itself during propagation and can be written as

$$\phi_{NL}^{(SPM)}(z, t) = n_2|E|^2 kz = \gamma P(t)L, \tag{2.22}$$

where $k = 2\pi/\lambda$, $z$ is the propagation length, and $P(t)$ is the pulse power envelope. Due to the SPM effect, a time-dependent phase-shift, $\Delta\phi(z, t)$, accumulates during propagation, leaving the temporal profile unaltered. The temporal profile of $\Delta\phi$ is proportional to that of the pulse's power $P(t)$. This time-dependent nonlinear phase shift leads to dynamic shifts in the instantaneous frequency, given by

$$\omega_{inst}(z, t) = \omega_0 + \Delta\omega(z, t), \tag{2.23}$$

where

$$\Delta\omega(z,t) = -\frac{\partial}{\partial t}(\Delta\phi) = -\frac{\partial}{\partial t}\left(\gamma P z\right). \tag{2.24}$$

Thus, the instantaneous frequency is modulated according to the time derivative of the intensity, and its magnitude scales with the magnitude of the nonlinear phase shift. For the normal dispersion case (media with positive nonlinear refractive index ($n_2 > 0$)) [34], the frequency modulation assumes the form of an approximately linear up-chirp in the central, most intense region of the pulse. The spectral broadening connected with this chirp can be exploited successfully for optical pulse compression (see Section 2.3). In fact, in the rest of this project we will deploy the ability of SMP to broaden the spectrum of narrow optical pulses for generation of supercontinuua.

In case two optical fields $\mathbf{E}_1$ and $\mathbf{E}_2$, with respective frequencies $\omega_1$ and $\omega_2$, and polarization along the $x$-axis co-propagate simultaneously inside a fiber, then the total electrical field can be written as

$$\mathbf{E} = \frac{1}{2}\hat{x}[E_1 \exp(-i\omega_1 t) + E_2 \exp(-i\omega_2 t) + \text{c.c.}]. \tag{2.25}$$

These fields will interact with each other through the fiber nonlinearity, which will result in a nonlinear polarization component:

$$P_{NL}(\omega_1) = \frac{3\varepsilon_0}{4}\chi^{(3)}_{xxxx}\left(|E_1|^2 + 2|E_2|^2\right)E_1, \tag{2.26}$$

$$P_{NL}(\omega_2) = \frac{3\varepsilon_0}{4}\chi^{(3)}_{xxxx}\left(|E_2|^2 + 2|E_1|^2\right)E_2, \tag{2.27}$$

$$P_{NL}(2\omega_1 - \omega_2) = \frac{3\varepsilon_0}{4}\chi^{(3)}_{xxxx}E_1^2E_2^*, \tag{2.28}$$

$$P_{NL}(2\omega_2 - \omega_1) = \frac{3\varepsilon_0}{4}\chi^{(3)}_{xxxx}E_2^2E_1^*. \tag{2.29}$$

The above expressions were derived by substituting Eq. (2.25) into Eq. (2.10). The last two terms ($P_{NL}(2\omega_1-\omega_2)$ and $P_{NL}(2\omega_2-\omega_1)$) are responsible for the generation of new frequency components and we will deal with them in the next section. Instead, the first two equations indicate the fact that the effective refractive index seen by an optical field in a nonlinear medium depends not only on the intensity of that field itself but also on the intensity of other co-propagating fields. In fact, the total nonlinear phase shift for the field $\mathbf{E}_1$is given as

$$\phi_{NL}(z) = n_2 k z(|E_1|^2 + 2|E_2|^2). \tag{2.30}$$

.

The last equation includes both SPM and XPM terms. As it can be seen, the contribution of XPM is twice as much compared to the one of SPM. The XPM-effect will be used in this thesis only in conjunction with the nonlinear optical loop mirror (NOLM), which will be explained in Section 2.2, and further used in Chapter 4.

### 2.1.3 Four-wave mixing

The four-wave mixing (FWM) effect has been extensively used for all optical signal processing, such as mid-span inversion [35], wavelength conversion [C-10], demultiplexing [C-9],

multicasting [36], time lens implementation [37], parametric amplification [38], phase restoration [39], etc. As mentioned earlier, FWM is one of the nonlinear processes that result from third-order susceptibility $\chi^{(3)}$, and is related to the third-order polarization term:

$$\mathbf{P_{NL}} = \varepsilon_0 \chi^{(3)} \vdots \mathbf{EEE}. \tag{2.31}$$

Lets consider four different electrical fields, linearly polarized along the $x$-axis, and having respective frequencies $\omega_1$, $\omega_2$, $\omega_3$ and $\omega_4$. The co-propagating field, expressed as a linear superposition of the aforementioned fields, can be written as

$$\mathbf{E} = \frac{1}{2}\hat{x}\sum_{m=1}^{4} E_m \exp\left[i(\beta_m z - \omega_m t)\right] + \text{c.c.}, \tag{2.32}$$

where $\beta_m$ are the respective propagation constants. By substituting Eq. (2.32) in Eq. (2.31) the nonlinear polarization term can be expressed as

$$\mathbf{P_{NL}} = \frac{1}{2}\hat{x}\sum_{m=1}^{4} P_m \exp\left[i(\beta_m z - \omega_m t)\right] + \text{c.c.}, \tag{2.33}$$

where the polarization components $P_m$ consist of a number of terms involving the products of three electric fields. As an example the $P_4$ can be written as

$$\begin{aligned} P_4 = \frac{3\varepsilon_0}{4}\chi^{(3)}_{xxxx}\Big[&|E_4|^2 E_4 + 2(|E_1|^2 + |E_2|^2 + |E_3|^2)E_4 + \\ &+ 2E_1E_2E_3\exp(i\theta_+) + 2E_1E_2E_3^*\exp(i\theta_-) + \cdots\Big], \end{aligned} \tag{2.34}$$

where $\theta_+$ and $\theta_-$ are equal to

$$\theta_+ = (\beta_1 + \beta_2 + \beta_3 - \beta_4)z - (\omega_1 + \omega_2 + \omega_3 - \omega_4)t, \tag{2.35}$$

$$\theta_- = (\beta_1 + \beta_2 - \beta_3 - \beta_4)z - (\omega_1 + \omega_2 - \omega_3 - \omega_4)t. \tag{2.36}$$

The first line in Eq. (2.34), containing the term $E_4$, determine the SPM and XPM contributions of $E_4$. The other terms are responsible for the generation of new frequency components. However, the strength of these ones depends on the phase mismatch between $E_4$ and $P_4$. In order for the FWM process to occur, the phase mismatch should disappear. This requires a match of frequencies and wave vectors.

As it can be seen from Eq. (2.34), there are two types of FWM products: the ones containing the $\theta_+$ term and the ones containing $\theta_-$. In the first case the energy of three photons is annihilated in order to generate a fourth one ($\omega_4 = \omega_1 + \omega_2 + \omega_3$)[3]. In the second case, the energy of two photons at $\omega_1$ and $\omega_2$ is combined to generate two photons at $\omega_3$ and $\omega_4$ such that

$$\omega_1 + \omega_2 = \omega_3 + \omega_4. \tag{2.37}$$

[3]In case of third-harmonic generation $\omega_1 = \omega_2 = \omega_3$

The phase-matching ($\Delta k$) condition for the second case is

$$\Delta k = \beta_3 + \beta_4 - \beta_1 - \beta_2 = 0. \tag{2.38}$$

This last case is the most interesting and relevant in our discussion, and for this reason we are going to analyze the evolution of the different field envelopes.

### Coupled mode equations

The starting point is the wave equation in Eq. (3.2). By substituting Eq. (2.32) and Eq. (2.31) in the wave equation and neglecting the time dependence of the field components, then the evolution of the amplitude $A_m(z)$ inside an optical fiber is governed by the following set of coupled equations:

$$\begin{aligned}
\frac{\mathrm{d}A_1}{\mathrm{d}_z} &= \frac{in_2\omega_1}{c}\Big[\Big(f_{11}|A_1|^2 + 2\sum_{k\neq 1} f_{1k}|A_k|^2\Big)A_1 + \\
&\quad + 2f_{1234}A_2^* A_3 A_4 \exp(i\Delta k z)\Big], && (2.39)\\
\frac{\mathrm{d}A_2}{\mathrm{d}_z} &= \frac{in_2\omega_2}{c}\Big[\Big(f_{22}|A_2|^2 + 2\sum_{k\neq 2} f_{2k}|A_k|^2\Big)A_2 + \\
&\quad + 2f_{2134}A_1^* A_3 A_4 \exp(i\Delta k z)\Big], && (2.40)\\
\frac{\mathrm{d}A_3}{\mathrm{d}_z} &= \frac{in_2\omega_3}{c}\Big[\Big(f_{33}|A_3|^2 + 2\sum_{k\neq 3} f_{3k}|A_k|^2\Big)A_3 + \\
&\quad + 2f_{3412}A_1 A_2 A_4^* \exp(-i\Delta k z)\Big], && (2.41)\\
\frac{\mathrm{d}A_4}{\mathrm{d}_z} &= \frac{in_2\omega_4}{c}\Big[\Big(f_{44}|A_4|^2 + 2\sum_{k\neq 4} f_{4k}|A_k|^2\Big)A_4 + \\
&\quad + 2f_{4312}A_1 A_2 A_3^* \exp(-i\Delta k z)\Big] && (2.42)
\end{aligned}$$

where $\Delta k$ is the phase mismatch given by Eq.(2.38) and where the overlap integrals $f_{lm}$ and $f_{lmno}$, are written as

$$f_{lm} = \frac{\left(\iint_{-\infty}^{+\infty} |F_l(x,y)|^2 |F_m(x,y)|^2 \,\mathrm{d}x\,\mathrm{d}y\right)}{\left(\iint_{-\infty}^{+\infty} |F_l(x,y)|^2 \,\mathrm{d}x\,\mathrm{d}y\right)\left(\iint_{-\infty}^{+\infty} |F_m(x,y)|^2 \,\mathrm{d}x\,\mathrm{d}y\right)} = \frac{\langle |F_l|^2 |F_m|^2\rangle}{\langle |F_l|^2\rangle\langle |F_m|^2\rangle}, \tag{2.43}$$

and

$$f_{lmno} = \frac{\langle F_l^* F_m^* F_n F_o\rangle}{\sqrt{\langle |F_l|^2|F_m|^2|F_n|^2|F_o|^2\rangle}}, \qquad \text{where} \qquad \langle b\rangle = \int\!\!\int_{-\infty}^{+\infty} b(x,y)\,\mathrm{d}x\,\mathrm{d}y. \tag{2.44}$$

The overlap integral is an indicator of the degree of modal spatial superposition. The differences among the overlap integrals can be significant in multimode fibers if the two waves

propagate in different fiber modes. However, in practice the difference is small in single-mode fibers, even though $f_{11}$, $f_{22}$, and $f_{12}$ might differ from each other because of the frequency dependence of the modal distribution $F_m(x, y)$.

In case $\omega_1 = \omega_2$ then a single pump can be used to initiate the FWM process [40, 41]. This is called a *degenerate FWM*, as only three waves are involved in the nonlinear process. In case of degenerate FWM, if a weak signal at $\omega_3$ is co-propagated with the pump at $\omega_1$ then an idler signal at $\omega_4 = 2\omega_1 - \omega_3$ will be created, while the weak signal will be amplified. This is the type of FWM process that we will be dealing in the experimental work in this manuscript (Chapter 4 and extensively Chapter 5). As it can be seen form Eq. (2.39), the idler is proportional to the square of the pump, and to the complex conjugate of the probe. From an intensity point of view this information will be useful in Chapter 4, were the FWM mixing process in conjunction with flat-top probe or pump pulses will be used to mitigate the detrimental effects arising from timing jitter in OTDM systems. Instead, from a phase-transfer point of view this proportionality will become very important in Chapter 5, where we will use the FWM product to generate a time lens able to map the intensity profile of a data signal into the power spectral density of the generated idler.

## 2.2 Nonlinear optical loop mirror

The NOLM is based on a nonlinear Sagnac interferometer switch, where two interfering light beams follow the same optical path in opposite directions [42,43]. It is formed by connecting the outputs of a standard bidirectional coupler into a fiber loop with a phase-shifting element in the middle.

Fig. 2.1 shows the structure and basic operation of the NOLM [44–48]. Let $S$ be the input signal's field into the NOLM. In Fig. 2.1, $S$ is an OTDM signal consisting of four time-interleaved tributaries. The signal is coupled into the device via port (1) of the 50:50 coupler. Due to the nature of the coupler the signal with be equally split in port (3) and (4), in respectively a clockwise ($S_{cw} = \sqrt{1/2}S$) and a counterclockwise ($S_{ccw} = i\sqrt{1/2}S$) propagating signal, which defer by a $\pi/2$ phase shift compared to each other. At the recombination ports (1) and (2) the signals will accumulate and extra $\pi/2$ phase difference, which results in the output fields to be written as

$$\begin{aligned} S_r &= \sqrt{\frac{1}{2}}S_{ccw} + i\sqrt{\frac{1}{2}}S_{cw} \\ &= iS \end{aligned} \tag{2.45}$$

$$\begin{aligned} S_t &= \sqrt{\frac{1}{2}}S_{cw} + i\sqrt{\frac{1}{2}}S_{ccw} \\ &= 0 \end{aligned} \tag{2.46}$$

where $S_r$ is the reflected field through port (1) and $S_t$ is the transmitted field through port (2). The opposite traveling signals will interfere constructively in port (1) and destructively in port (2). As a result, the entire signal is reflected in the same input port. Hence, the term "mirror" in the NOLM definition. As it can be noticed, Fig. 2.1 shows also a polarization controller (PC) as part of the NOLM. This is placed in order to control the polarization state of the signals circulating in the loop, as the fiber birefringence can alter the behavior of the NOLM itself [49].

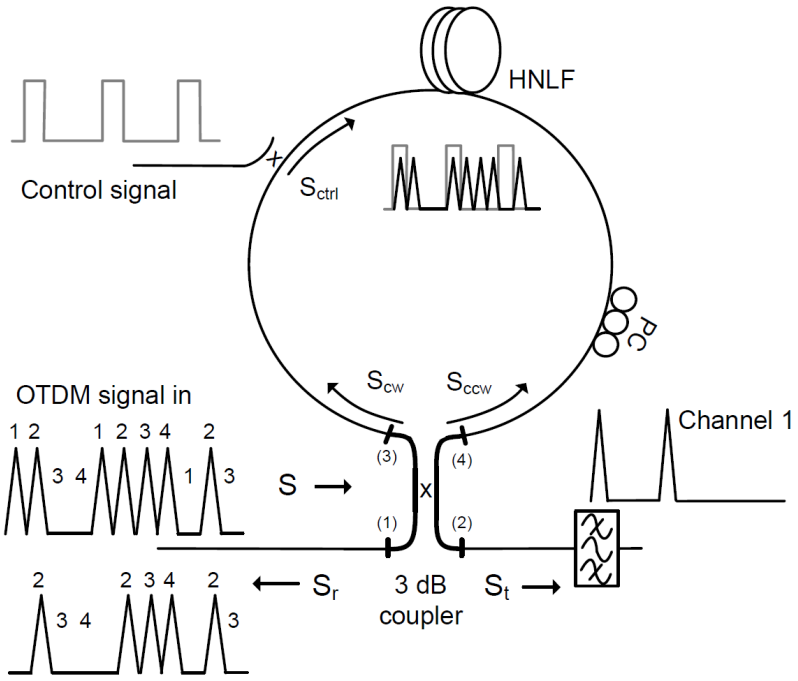


**Figure 2.1:** Basic principle of the NOLM operation as a demultiplexing device. The input $S$ (central wavelength $\lambda_s$) to the NOLM is an OTDM signal consisting of four tributaries, whose identification numbers are placed on top of their bits. The control signal $S_{ctrl}$ (central wavelength $\lambda_{ctrl}$), propagating in the same clockwise direction as $S_{cw}$ is synchronized to channel #1 of the OTDM signal. Due to the XPM-phase shift induced by $S_{ctrl}$'s presence this channel is the only one to be transmitted through port (2) of the NOLM. The rest is reflected in port (1). At the output of the device an optical bandpass filter separates the desired channel from the control signal.

In case a high-intensity signal ($S_{ctrl}$), having a different central wavelength ($\lambda_{ctrl}$) compared to the data signal ($\lambda_s$), operating at the base rate and employed as control, is unidirectionally coupled into the NOLM (clockwise direction) then the phase shift induced by its presence via XPM can be used to demultiplex one of the OTDM channels at the transmission port. In fact the NOLM validity as a demultiplexer has been demonstrated for up to 1.28-TBd OTDM data signal, being able to switch pulses as narrow as 410 fs [13].

The phase shifting element is a highly-nonlinear fiber (HNLF) with length $L$ and nonlinear coefficient $\gamma$. The data and control pulses are assumed to propagate with the same group velocity (no walk-off), and to be in the same linear polarization state. Due to its co-propagation with the control signal the $S_{cw}$ part of the signal in the loop with acquire a XPM-induced phase-shift equal to

$$\Delta\phi_{cw}(t) = 2\gamma L P_{ctrl}(t), \tag{2.47}$$

where $P_{ctrl}(t)$ is the temporal power profile of the control pulse. Also the counter-propagating field will experience the control field presence via XPM. The induced phase-shift in this case can be written as:

$$\Delta\phi_{ccw}(t) = 2\gamma L \langle P_{ctrl}(t)\rangle, \tag{2.48}$$

where $\langle P_{ctrl}(t)\rangle$ is the time-average control power, assuming that the loop transit time is much longer than the control pulse repetition period [47]. After the XPM-induced phase shift, the reflected and transmitted fields respectively in port (1) and (2) can be written as:

$$S_r = \frac{i}{2}S\left[\exp(-i\Delta\phi_{cw}) + \exp(-i\Delta\phi_{ccw})\right] \quad (2.49)$$

$$S_t = \frac{1}{2}S\left[\exp(-i\Delta\phi_{cw}) - \exp(-i\Delta\phi_{ccw})\right]. \quad (2.50)$$

If we define the transmissivity ($T$) and reflectivity ($R$) of the NOLM as:

$$T = \frac{|S_t|^2}{|S|^2}, \qquad \text{and} \qquad R = \frac{|S_r|^2}{|S|^2}, \quad (2.51)$$

then for the 50:50 coupler they result equal to

$$T = \frac{1}{2}(1 - \cos(\Delta\phi)), \quad (2.52)$$

$$R = \frac{1}{2}(1 + \cos(\Delta\phi)), \quad (2.53)$$

where $\Delta\phi = \Delta\phi_{cw} - \Delta\phi_{ccw}$ is the difference between the XPM-induced phase shift on the clockwise ($S_{cw}$) and counterclockwise ($S_{ccw}$) fields[4]. In case the control pulse is absent, the XPM phase-shift is 0, hence $\Delta\phi = 0$ ($R = 1$ and $T = 0$). As the total XPM-induced phase shift is linearly dependent on the control power, if this one is adjusted such that $\Delta\phi = \pi$ then part of the signal overlapping with the control will be switched to the transmission port ($T = 1$ and $R = 0$). Hence the NOLM operates as a temporal switching window, or demultipexing device. Fig. 2.1 shows the control pulse overlapping with channel #1 of the OTDM input signal. As this is the only channel satisfying $\Delta\phi = \pi$, then it will be the only switched to the transmission port. The rest of the channels will be reflected[5] to the input port ($R = 1$).

Due to the fact that the XPM-induced phase shift is proportional to the shape of the control, then a flat-top pulse that can entirely cover only one of the OTDM tributaries is very desirable. In this thesis, the NOLM will be used only in Chapter 4 (Section 4.3), in which a flat-top control pulse generated in a pair of long-period gradings (LPG) inscribed in a standard single-mode fiber (SSMF) is used to realize a polarization-independent NOLM (PI-NOLM). Please refer to Section 4.3 for more detayls on both the PI-NOLM operation and flat-top pulse generation.

## 2.3 Pulse compression for terabaud communications

Terabaud (TBd) return-to-zero (RZ) communications require pulses of few hundred femtosecond widths. Conventional laser sources used in OTM systems can generate pulses whose width varies between 1.5- and 2-ps. But these are too broad to be directly time multiplexed, without causing inter-channel crosstalk. The highest pulse rate employed in OTDM experiments to date is 1.28 TBd [13], [C-10, 12, 20, 21, 23, 26], [J-3, 8, 10], which requires pulse compression in order to obtain the necessary pulse width well below 500 fs. The compression stage is a challenging task due to the high requirements on the quality of the compressed

[4]Due to power conservation $T + R = 1$.

[5]It is assumed that $\Delta\phi_{ccw} \approx 0$ [50].

pulses [51], even though the required compression factor might be between 3 and 4 times, depending on the initial width of the laser pulses.

The main technique employed in this thesis for generation of narrow pulses is based on filtering of SPM-induced broad spectra and subsequent chirp elimination by propagation into a dispersive element such as single-mode fiber (SMF) (Section 2.3.1). The resulting pulses are highly suitable for 1.28 TBd applications, and no pedestal-reduction is required after the compression stage. The compression technique is suitable not only for on-off keying (OOK) modulation formats but it is proven to properly work also for advanced modulation formats allowing for the realization of the first 16-ary quadrature amplitude modulation (16-QAM) 1.28-TBd RZ-OTDM signal, as it will be seen in Chap. 7. For the sake of completeness, Section 2.3.2 revises the soliton, and adiabatic soliton pulse compression techniques, even though they were not used in the experimental work covered in this thesis.

### 2.3.1 SPM followed by anomalous dispersion

Spectral broadening accompanying SPM leads to the possibility of optical pulse compression, since the increased bandwidth can support shorter optical pulses [34]. Fig. 2.2 shows a block diagram of the entire process, where the pulse firstly propagates into a medium with nonlinear refractive index. For sufficiently high input powers, the SPM effect leads to spectral broadening in the form of an up-chirp[6]. The utilization of a dispersive element, in anomalous dispersion regime, can compensate the SPM-induced chirp, bringing the different optical frequency components into synchronism, which leads to pulse compression. The output pulse is both shorter and more intense[7] compared to the input, since the input energy is compressed into a shorter time duration.

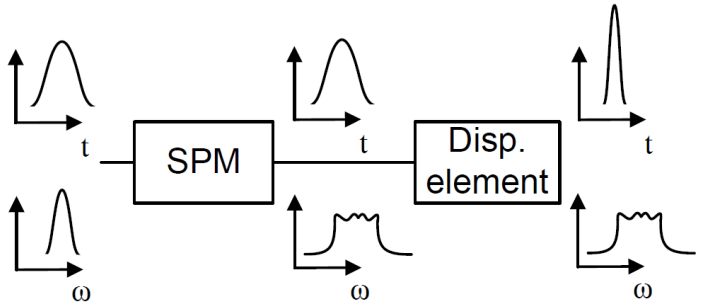


**Figure 2.2:** Block diagram of optical pulse compression based on SPM.

The field envelope $A_{SPM}(t)$, after SPM-induced spectral broadening can be written as

$$A_{SPM}(t) = \frac{1}{2\pi}\int_{-\infty}^{+\infty} A_{SPM}(\omega)\exp[-i(\omega-\omega_0)t]\exp[\phi_{SPM}(\omega)]\mathrm{d}\omega, \tag{2.54}$$

where $\phi_{SPM}(\omega)$ is the spectral phase component resulting from the SPM process. After the dispersive element, the field envelope ($A_D(t)$) acquires an extra spectral phase component $\phi_D(\omega)$ and can be written as:

$$A_D(t) = \frac{1}{2\pi}\int_{-\infty}^{+\infty} A_{SPM}(\omega)\exp[-i(\omega-\omega_0)t]\exp\left[\phi_{SPM}(\omega)+\phi_D\right]\mathrm{d}\omega. \tag{2.55}$$

[6]Dispersionless SPM does not cause modification to the pulse intensity.
[7]Lossless case.

An ideal pulse compressor, which would eliminate the extra phase information on the optical pulses, should satisfy

$$\phi_D(\omega) = -\phi_{SPM}(\omega), \tag{2.56}$$

which enables the spectral phase terms to cancel completely, sets the frequency-dependent delay $\tau(\omega)$ to a constant, and compresses the pulses to the bandwidth limit. However, in a practical compressor, it may not be possible to fully compensate the complete spectral phase. As a result, the output pulse may be compressed imperfectly, either because $\phi_{SPM}(\omega)$ contains higher-order terms or because $\phi_D(\omega)$ imparts, in addition to the desired quadratic term, undesired cubic or higher-order phase terms onto the spectrum. In fact, when only the effect of SPM is taken under consideration, the instantaneous frequency varies as the derivative of the temporal intensity profile of the pulse. Unless parabolic pulses [29] are used, SPM results in strong nonlinear chirp components (see Fig. 2.3(a)). As this nonlinear chirp component is hard to compensate then its effect can be mitigated by removing the frequency components that are afflicted from it. As seen from Fig. 2.3(b) the nonlinearly chirped frequency components reside at the edges of the broad SPM-induced spectrum, and can be eliminated by an optical bandpass filter (OBPF).

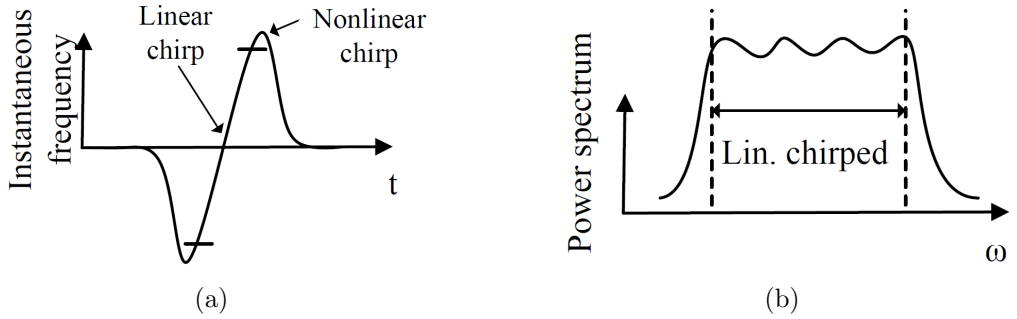


**Figure 2.3:** Filtering of the spectral extremities of an SPM-broadened spectrum removes the frequency components that contain a nonlinear chirp. (a) Instantaneous frequency of a self-phase modulated pulse, (b) the corresponding power spectrum [52].

It has to be noticed that both, normal group velocity ($\beta_2 > 0$) and SPM, lead to a frequency up-chirp, meaning that the leading edge of the pulse is red-shifted compared to the trailing edge which is blue-shifted instead. In case these phenomena act simultaneously they lead to a substantially linear chirp and hence a predominantly quadratic spectral phase. This can be explained with the fact that SPM is the dominating effect at the beginning of the propagation process, accompanied by spectral broadening. On the other hand, spectral broadening increases the effect of dispersion through temporal broadening. As the pulse broadens its peak power decreases and the SPM-effect is smoothed out. For large propagation lengths, dispersion becomes the dominating effect. Due to the dispersion and SPM interplay the power spectrum is substantially flatter compared to the dispersionless SPM case. The propagation of the pulse in the nonlinear medium leads to flat-top pulse reshaping of the original input. This leads to a stronger linear chirp and a very large fraction of the pulse energy falling within the linear chirp region [34, 53].

Because of the predominantly linear chirp, the compression technique used in this thesis is based on spectral broadening by SPM in a fiber with negative dispersion (normal group velocity dispersion), followed by propagation in single-mode fiber for chirp compensation.

In fact, as higher-order terms of the Taylor expansion of the propagation constant $\beta$ would distort the linear up-chirp applied on the pulse, dispersion-flattened highly-nonlinear fibers (DF-HNLF) are the best choice [54]. This is the case in all the experiments in this thesis. In most of the experiments the useful part of the broad SPM-induced spectrum is selected at a different central wavelength compared to the input pulse (off-carrier filtering) [55]. This is done not only to use the broad spectrum for generation of different WDM channels [56], [C-7] but also to reduce the influence of pulse pedestals and possible undesired ghost pulses of lower amplitude, present at the transmitter.

### 2.3.2 Soliton pulse compression

From the previous section it is clear that nonlinear pulse propagation in the normal and anomalous dispersion regimes result in two different outcomes. In the normal dispersion regime, SPM and group velocity dispersion reinforce each other, resulting in enhanced linear chirping and pulse flattening effects. In the case of anomalous dispersion, SPM and dispersion act in opposite directions, possibly balancing and canceling each other out. This phenomenon leads to the concept of *solitons* [57–59], pulses that can propagate without distortions in dispersive media, due to the interplay between nonlinearities and dispersion. This is the case of fundamental or first-order solitons, which propagate without distortions while maintaining their $sech^2$ shape. On the other hand, higher order solitons change their shape periodically as they propagate along the fiber. They experience a narrowing stage before they recover their initial shape. Hence, soliton pulse compression [60] is achieved for high-order solitons when they are intercepted (leave the nonlinear fiber) at their minimum width. The main drawback of this compression technique is the fact that the compressed pulse is accompanied by broad pedestal components next to the narrow central pulse, which would result in inter-channel crosstalk in case of OTDM systems. The pedestals presence is detrimental for time-interleaved systems and it needs to be removed [61, 62].

On the other hand, adiabatic soliton compression [63–67] can give a better pulse quality in terms of pedestal reduction or even elimination. In this case, instead of higher order solitons (soliton pulse compression), the fundamental soliton is launched into the fiber and pulse compression is achieved by manipulating the stability of the pulse via weak perturbation of its energy. Due to fiber losses the variation of the fiber dispersion along the pulse propagation can be used not only to prevent soliton broadening, but will result as well in pulse compression. The utilization of dispersion-decreasing fibers (DDF) has been shown to generate pedestal free pulses in the sub-picosecond regime [68]. The pulse compression factor after a DDF of length $L$ is given by the ratio between the input and output dispersion ($\beta_2(0)/\beta_2(L)$). The adiabatic soliton pulse compression technique has been extensively used in many OTDM experiments [11, 12, 14, 69]. By using this technique, the pulses from commercial lasers were compressed in order to suite 640 GBd OTDM systems. Compared to soliton pulse compression adiabatic soliton compression gives lower compression factors and has to be performed in longer nonlinear fibers. However, in case higher order solitons are used at the fiber input, then higher compression ratios can be achieved with lower fiber lengths [67].

# Chapter 3

# Space-time duality for all-optical signal processing

## 3.1 Introduction

In the spatial domain, optical data processing takes advantage of the fact that a simple lens constitutes a Fourier transform processor, capable of transforming a complex two-dimensional pattern into a two-dimensional transform at very high resolution and at the speed of light [70]. The diffraction pattern of an object formed by the lens is shown to be a two-dimensional Fourier transform of the input object itself. This pattern may be manipulated in turn, using masks or filters to modify the final image produced by a second lens in a process called spatial filtering.

It turns out that Fourier properties of spatial optical elements are present also in the temporal domain. An equivalent temporal optical system is found for a spatial optical one by exchanging spatial variables with temporal variables and spatial frequencies with spectral ones [71]. Space-time duality is based on the mathematical analogy between equations describing paraxial diffraction of space-confined beams and second order dispersion of optical pulses propagating in dispersive elements [72–82]. This duality can also be extend to lenses, where a quadratic phase modulation on a temporal optical pulse is similar to the effect of a thin lens on a spatial beam. By choosing and combining in an appropriate way time lenses and dispersive devices it is possible to create new systems for processing, controlling and generating temporal optical signals, equivalent to spatial signal processing based on thin lenses and diffraction. The space-time duality insight is a great tool to design pulse shaping systems, and has already enabled a variety of applications in fiber communication systems, such as temporal imaging [83], distortion-free pulse transmission [84], distortion-free compression or expansion of a waveform [85, 86], time-to-frequency converters [71, 81] and repetition-rate multipliers [87].

The following chapter presents a theoretical overview of the space-time dualities and their application for waveform manipulation and all-optical signal processing. In the rest of this work, the term Optical Fourier Transformation (OFT) will be used to define a process or technique which converts the time and/or frequency information into each other. The additional terms *time-to-frequency* and *frequency-to-time* will distinguish each case separately. The chapter is organized as follows: Section 3.2 gives an overview of the mathematical analogies between spatial optical systems and temporal ones; Section 3.3 concentrates on frequency-to-time mapping, implemented via quadratic phase modulation and second order

dispersion; Section 3.4 deals with the opposite phenomenon (time-to-frequency conversion), while Section 3.5 focuses on the utilization of the space-time duality applied to re-timing of optical pulses (similar to the effect of space lenses). All these topics will be experimentally investigated in the next chapters.

## 3.2 Space-time duality

In the following section we are going to derive and analyze the mathematical similarities between paraxial diffraction[1] of beams confined in space and propagation of narrow-band[2] pulses in dispersive optical elements, such as fibers, filters etc. It will become clear that both phenomena can be described by a set of similar complex parabolic differential equations. The space-time duality can also be extended to thin lenses, where quadratic phase modulation on an optical pulse is analogous to the effect of a thin lens on a spatial beam. For this reason quadratic phase modulation is also referred to as a *time lens*.

### 3.2.1 Analogy between diffraction and dispersion

#### Paraxial diffraction

For a monochromatic beam propagating along the $z$-axis, the electric field $\mathbf{E}$ can be written as [76]

$$\mathbf{E}(x,y,z,t) = E(x,y,z,t)\exp[i(\omega_0 t - k_0 z)], \tag{3.1}$$

where $E(x,y,z,t)$ is the slowly varying envelope function for the spatial beam, $\omega_0$ is the light frequency and $k_0 = 2\pi/\lambda_0$ is the wave number ($\lambda_0$ being the beam's wavelength).

The wave equation for the electric field can be written as

$$\nabla^2\mathbf{E} = \mu_0\varepsilon_0\frac{\partial^2\mathbf{E}}{\partial t^2}, \tag{3.2}$$

where the constants $\varepsilon_0$ and $\mu_0$ are respectively the permittivity and permeability of vacuum. Under the assumption that the waves are monochromatic, the Fourier transform of $\mathbf{E}$ in Eq. 3.2 can be written as

$$\tilde{E}(x,y,z,\omega) = \mathbf{E_0}\delta(\omega - \omega_0), \tag{3.3}$$

which leads to a simplified Helmholtz [70] wave equation

$$(\nabla^2 + k^2)\mathbf{E_0} = 0. \tag{3.4}$$

For paraxial rays, confined along the $z$-axis (propagation axis), the most rapidly phase variations will occur along this axis, leading to

$$\mathbf{E_0}(x,y,z) = E(x,y,z)\exp(-ikz), \tag{3.5}$$

[1] The term *diffraction* is used to express the general problem of light propagation.

[2] The term *narrow-band* is related to the spectral extension of optical pulses and to the Taylor expansion approximation of the propagation constant $\beta$ of a dispersive element.

where $E(x, y, z)$ is the slowly varying envelope function. By expanding the Laplacian operator ($\nabla^2$) and using Eq. 3.5 in Eq. 3.4 the reduced wave equation becomes:

$$\frac{\partial^2 E}{\partial x^2} + \frac{\partial^2 E}{\partial y^2} + \frac{\partial^2 E}{\partial z^2} - 2ik\frac{\partial E}{\partial z} = 0. \tag{3.6}$$

The paraxial approximation can be written as

$$\left|\frac{\partial^2 E}{\partial z^2}\right| \ll \begin{cases} |\partial^2 E/\partial x^2| \\ |\partial^2 E/\partial y^2| \\ |2k\partial E/\partial z| \end{cases} \tag{3.7}$$

This means that the curvature of the field envelope in the direction of propagation is much smaller than in the transverse profile, which leads to the following paraxial wave equation [76]:

$$\frac{\partial^2 E}{\partial x^2} + \frac{\partial^2 E}{\partial y^2} - 2ik\frac{\partial E}{\partial z} = 0 \qquad \text{or} \qquad \frac{\partial E}{\partial z} = -\frac{i}{2k}\nabla_t^2 E, \tag{3.8}$$

with $\nabla_t^2$ being the transverse Laplacian operator (applied on the transverse variables $x$ and $y$). As it can be seen, the last equation, describing the evolution of the electric field envelope of a beam during its propagation along the $z$-axis (Eq. 3.8) has a differential parabolic form.

**Dispersion**

In Chapter 2 (Section 2.1.1) we introduced the nonlinear Schrödinger equation, which describes pulse evolution in the nonlinear regime. However, if the loss ($\alpha$), and nonlinearities ($\gamma$) are not taken into consideration then Eq. (2.19) can be written as

$$\frac{\partial A}{\partial z} + i\frac{\beta_2}{2}\frac{\partial^2 A}{\partial t'^2} = 0, \tag{3.9}$$

in which we have substituted $t' = t - \beta_1 z$. Under the assumption that the pulse is narrowband, the Taylor expansion of $\beta(\omega)$ was stopped at the second order ($\beta_2$), which is defined as the group velocity dispersion (GVD) parameter or chromatic dispersion. This results in a transfer function, and impulse response of a dispersive element, with only second order dispersion $\beta_2$, equal to

$$H_{\beta_2}(\omega) = \exp(i\frac{\omega^2\beta_2 z}{2}) \qquad \text{and} \qquad h_{\beta_2}(t) = \sqrt{\frac{i}{2\pi\beta_2 z}}\exp(-\frac{it^2}{2\beta_2 z}) \tag{3.10}$$

By looking at Eq. (3.8) and (3.9), it can be deduced that they have the same complex parabolic differential structure. This means that the same phenomena related to diffraction can be seen in the time domain because of dispersion.

### 3.2.2 Analogy between thin lenses and quadratic phase modulation

As mentioned at the beginning of this chapter, space-time analogy does not hold only for optical phenomena such as diffraction and dispersion but also for optical components such as thin lenses and phase modulation processes.

The phase transformation of a lens on a space beam can be described as [70]

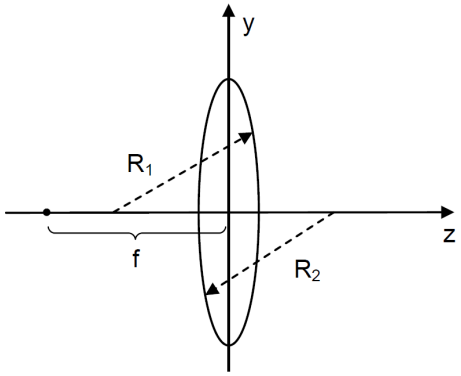


**Figure 3.1:** Conventional thin space lens, with radii of curvature $R_1$ and $R_2$, focal length $f$, refraction index $n$ and propagation axis $z$.

$$\mathbf{t}_l(x,y) = \exp(-ikn\Delta_0) \cdot \exp(i\frac{k}{2f}(x^2+y^2)), \tag{3.11}$$

where $\Delta_0$ is the maximum thickness of the lens, $k$ is the wave number and $f$ is its focal length, defined as (see Fig. 3.1):

$$f = \frac{1}{(n-1)(\frac{1}{R_1} - \frac{1}{R_2})}, \tag{3.12}$$

with $n$ being the refractive index, and $R_1$ and $R_2$ the radii of curvature.

The second factor in Eq. (3.11) is the one holding the key to the lens operation, meaning that it produces an instantaneous quadratic phase modulation in the real space [76]. This is the opposite of what happens in the paraxial diffraction case where the quadratic phase modulation is produced in the Fourier space (frequency domain). The spatial phase function of the thin lens then becomes

$$\phi(x,y) = \frac{k(x^2+y^2)}{2f}. \tag{3.13}$$

In the time domain quadratic phase modulation on the time variable $t$ for a temporal pulse is the dual version of quadratic phase modulation on the *profile variables* $(x,y)$ in the space domain. For this reason the phase information in the time domain can be written as

$$\phi(t) = \frac{Ct^2}{2}, \qquad \text{where } C \text{ is the chirp of the signal,} \tag{3.14}$$

or in an analog way with the space case equation

$$\phi(t) = \frac{\omega_0 t^2}{2f_t} \qquad \text{where} \qquad C = \frac{\omega_0}{f_t} \tag{3.15}$$

where $\omega_0$ is the carrier frequency of the time pulse and $f_t$ is called the focal time of the time lens in analogy with the focal length $f$ in Eq. (3.13). The phase information (chirping) applied on the pulse, Eq. (3.14), corresponds to multiplying the signal in the time domain with the function $h_l(t)$ or convolving its Fourier transform with $H_l(\omega)$, defined as

$$h_l(t) = \exp(\frac{iCt^2}{2}) \qquad \text{and} \qquad H_l(\omega) = \sqrt{\frac{2\pi i}{C}}\exp(\frac{-i\omega^2}{2C}). \tag{3.16}$$

From Eq. (3.16) it can be noticed that a linear chirp is imposed on the signal.

There are different mechanism by which a quadratic phase modulation, or linear chirp, can be applied on a temporal pulse. It can be implemented by using an electro-optic phase modulator driven by a sinusoidal signal [76], cross-phase modulation [82, 88] of the original pulse with an intense pump pulse in a nonlinear medium, by parametric processes such as sum- or difference-frequency generation (SFG, DFG) [80, 83, 89] or four wave mixing (FWM) [37, 90, 91]. Chapter 5 will focus on the implementation of the time lens via FWM in both highly nonlinear fiber and silicon nanowires.

### 3.2.3 Analogy between dispersion and quadratic phase modulation

In space optics it is possible to make an analogy between paraxial diffraction and thin lenses [92]. From the space-time duality argumentation this should be possible also in the time domain, respectively between dispersion and time lenses. By comparing the mechanism of dispersion and time lenses, it can be noticed that the action of a time lens on an optical pulse in the time domain is equal to the effect of dispersion in the frequency domain. From the dual nature of the Fourier transform, the action of the time lens in the frequency domain is analogous to GVD in the time domain [76, 93]. In the transform domain quadratic phase modulation (time lens) and second-order dispersion are the dual of each other. This is summarized in Table 3.1, where equations on the diagonals of the table result in having a similar structure. This analogy between these two phenomena will be explored in the next sections, and used in the next chapters to create temporal imaging systems.

**Table 3.1:** Equations describing the structural similarities between time lenses and group velocity dispersion.

| Time Domain | Frequency Domain |
|---|---|
| $h_{\beta_2}(t) = \sqrt{\frac{i}{2\pi\beta_2 z}}\exp(-\frac{it^2}{2\beta_2 z})$ | $H_{\beta_2}(\omega) = \exp(i\frac{\omega^2\beta_2 z}{2})$ |
| $h_l(t) = \exp(\frac{iCt^2}{2})$ | $H_l(\omega) = \sqrt{\frac{2\pi i}{C}}\exp(\frac{-i\omega^2}{2C})$ |

## 3.3 Frequency-to-time mapping

As demonstrated in [76], the evolution of optical pulses in dispersive media is equivalent to free-space diffractive imaging, where the far field image, by virtue of the Fraunhofer diffraction integral, simply becomes the Fourier transform of the object. For optical pulses transmitted through a dispersive medium as e.g., an optical fiber, the equivalent of the *far field image* becomes a temporal waveform which is the Fourier transform of the input temporal waveform (the *object*). The Fourier transform of the input waveform is simply the input spectrum.

### 3.3.1 Basic principle

The analogy between dispersion and time lenses (Table 3.1) leads to the implementation of the frequency-to-time OFT technique, where the energy spectral density of a given waveform (f.x., an optical pulse) is directly mapped into the time domain. Fig. 3.2 shows the basic principle and implementation of the OFT technique. It is composed of a time lens mechanism able to provide a quadratic phase modulation, and a dispersive element, such as a fiber or optical filter with the required GVD. To create a certain waveform in the time domain, e.g., flat-top pulses as sketched in Fig. 3.2, the basic idea is to create a flat-top spectrum by means of passive filtering, and then Fourier transform its temporal equivalent into a flat-top temporal waveform.

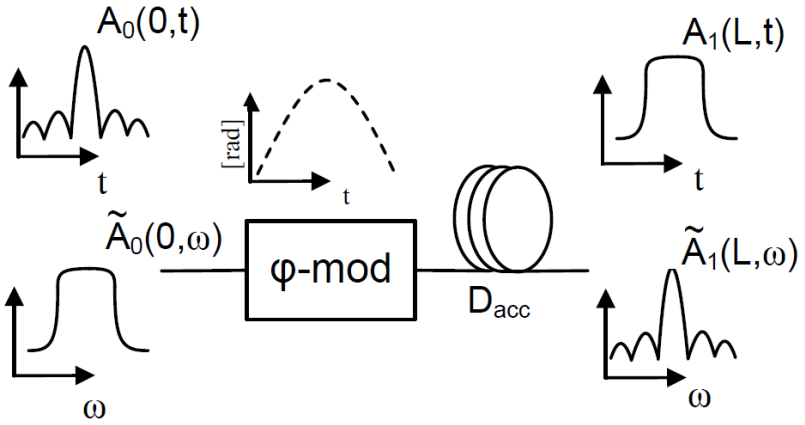


**Figure 3.2:** Schematic of the basic principle for frequency-to-time conversion OFT, implemented via quadratic phase modulation and propagation in dispersive media.

Let $A_0(0,t)$ be the electric field envelope of the pulse at the input of the OFT system, and let $A_c(0,t)$ be the envelope after the phase modulator ($\varphi$-mod). $A_c(0,t)$ will be linearly chirped (quadratically phase modulated) and can be written as

$$A_c(0,t) = A_0(0,t)\exp(\frac{iCt^2}{2}). \tag{3.17}$$

The linearly chirped pulse, $A_c(0,t)$, is further propagated through a dispersive medium of length $L$, such as a fiber with accumulated dispersion $D_{acc} = \beta_2 L$. Recalling the impulse response of a dispersive element (Eq. (3.10)) and convolving it with $A_c(0,t)$ yields the output $A_1(L,t)$ of the OFT system

$$\begin{aligned} A_1(L,t) &= A_c(0,t) * h_{\beta_2}(t) \\ &= \int_{-\infty}^{+\infty} A_c(0,\tau)h_{\beta_2}(t-\tau)d\tau \\ &= \sqrt{\frac{i}{2\pi D_{acc}}}\int_{-\infty}^{+\infty} A_c(0,\tau)\exp(-\frac{i(t-\tau)^2}{2D_{acc}})d\tau \\ &= b\int_{-\infty}^{+\infty} A_0(0,\tau)\exp(\frac{iC\tau^2}{2})\exp(i\frac{2t\tau-\tau^2}{2D_{acc}})d\tau, \end{aligned} \tag{3.18}$$

with

$$b = \sqrt{\frac{i}{2\pi D_{acc}}} \exp(-\frac{it^2}{2D_{acc}}). \tag{3.19}$$

If the condition $C = 1/D_{acc}$ is fulfilled, meaning that the accumulated dispersion is matched to the chirp imposed on the pulse, and by using the transformation $\omega = t/D_{acc}$, then the output from the OFT system can be written as

$$\begin{aligned} A_1(L,t) &= b \int_{-\infty}^{+\infty} A_0(0,\tau) \exp(i\frac{t\tau}{D_{acc}}) d\tau \\ &= b \cdot \tilde{A}_0(0,\omega)_{\omega=t/D_{acc}}, \end{aligned} \tag{3.20}$$

with $\tilde{A}_0(0,\omega)$ being the Fourier transform[3] of the input pulse envelope $A_0(0,t)$.
Finally, the power at the output of the OFT, from (3.20) becomes

$$|A_1(L,t)|^2 = \frac{1}{2\pi D_{acc}} |\tilde{A}_0(0,\omega)_{\omega=t/D_{acc}}|^2. \tag{3.21}$$

Eq. (3.21) shows that the output waveform of the OFT system is proportional to the power spectral density of the input signal ($|\tilde{A}_0(0,t/D_{acc})|^2$). This means that $D_{acc}$ (or equivalently $C$) determines the transformation ratio between the time and frequency domain. By controlling the $C$ and $D_{acc}$ parameters it is possible to control the FWHM of the resulting $A_1(L,t)$. This leads to the huge potentiality of the OFT technique: if it is possible to generate a desired spectral shape then due to frequency-to-time OFT the power spectral density can be mapped into the time domain, and by manipulating the chirp parameter $C$ and the accumulated dispersion $D_{acc}$ it is possible to change the width of the resulting pulses.

Note the fact that the OFT technique does not make any assumptions on the sign of the chirp $C$ or the accumulated dispersion $D_{acc}$. Since $\beta_2$ can be positive or negative, and by implementing $C$ with the same sign as $D_{acc}$, the temporal images can be formed by positive and negative temporal lenses.

### 3.3.2 Frequency-to-time conversion without phase modulation

The frequency-to-time conversion OFT is possible also by avoiding the linear chirping mechanism given by the time lens. It can be achieved by using the equivalent principle of the far-field Fraunhofer image plane. In this case a higher accumulated dispersion and narrower initial pulses are required.

Let again, $A_0(0,t)$ and $A_1(L,t)$ be the electric field envelopes at the input and output of a dispersive fiber of length $L$. $A_1(L,t)$ is calculated as the convolution of the input $A_0(0,t)$ and the GVD impulse response:

[3] In $\tilde{A}_0(0,\omega)$, the variable $\omega$ represents the frequency at baseband.

$$\begin{aligned} A_1(L,t) &= A_0(0,t) * h_{\beta_2}(t) \\ &= \sqrt{\frac{i}{2\pi D_{acc}}} \int_{-\infty}^{\infty} A_0(0,\tau)\exp(-\frac{i(t-\tau)^2}{2D_{acc}})d\tau \\ &= b\int_{-\infty}^{\infty} A_0(0,\tau)\exp(-\frac{i\tau^2}{2D_{acc}})\exp(\frac{it\tau}{D_{acc}})d\tau. \end{aligned} \tag{3.22}$$

Let $\delta t_0$ be the total duration of the input pulse envelope. If the pulse is very narrow and the accumulated dispersion $D_{acc}$ is large enough then

$$\left|\frac{\delta t_0^2}{2D_{acc}}\right| \ll 1. \tag{3.23}$$

If the condition in Eq. (3.23) is true then the phase factor expressed by $\exp(-i\tau^2/2D_{acc})$ in the last integral in Eq. (3.22) can be neglected, i.e., can be set to 1. This means that by making the transformation $\omega = t/D_{acc}$ the output envelope can again be written as:

$$\begin{aligned} A_1(L,t) &= b\int_{-\infty}^{\infty} A_0(0,\tau)\exp(\frac{it\tau}{D_{acc}})d\tau \\ &= b\cdot \tilde{A}_0(0,\omega)_{\omega=t/D_{acc}}. \end{aligned} \tag{3.24}$$

The power at the output of the dispersive element once again becomes[4]

$$|A_1(L,t)|^2 = \frac{1}{2\pi D_{acc}}|\tilde{A}_0(0,\omega)_{\omega=t/D_{acc}}|^2, \tag{3.25}$$

If the condition in Eq. (3.23) is satisfied the output pulse envelope is proportional to the Fourier transform of the input envelope. The only substantial difference between this case and the one with time lens relies on the fact that in order for Eq. (3.23) to be true, and for the dispersed pulse envelope ($A_1(L,t)$) to be narrow and still resemble its spectral density, then $D_{acc}$ has to be large while $\delta t_0$ should be negligible. Moreover, the condition in Eq. (3.23) is dependent on the square of $\delta t_0$ and the width of $A_1(t)$ is linearly dependent on $D_{acc}$. This means that in order for the resulting pulse power to resemble the power spectral density $|A_0(0,\omega)|^2$ and to be as narrow as possible the initial pulse $A_0(0,t)$ should be narrow and the total dispersion $D_{acc}$ should not be too large.

From the previous discussion it can be found that another similarity between diffraction and dispersion lies in the far-field Fraunhofer condition. In the space domain the far-field Fraunhofer criterion for a monochromatic beam with width $d$ can be written as:

$$\frac{d^2}{\lambda l} \ll 1 \tag{3.26}$$

where $l$ is the propagation distance and $\lambda$ is the wavelength of the beam. As it can be seen there is an analogy between the Fraunhofer far-field criteria and the inequality in Eq. 3.23. For this reason Eq. 3.23 is also called the temporal Fraunhofer condition [94]. The distance at which the condition in Eq. 3.23 is satisfied will be called the frequency-to-time OFT-plane.

[4]It has to be noticed that in both cases only the amplitude of the Fourier transform is recovered, since the output envelope $A_1(L,t)$ has extra phase information given by the term $b$.

### 3.3.3 Influence of higher-order dispersion terms

The effect of chromatic dispersion ($\beta_2$) is responsible for pulse broadening and intensity reshaping during propagation of pulses in dispersive media. But in some cases the effect of higher order dispersion terms can not be neglected and should be taken into consideration when studying pulse evolution. The higher order terms (Eq. 2.21) come mainly into play for ultrashort pulses, having a broad spectral content, and when the pulse's central wavelength is at or close to the zero dispersion wavelength of the fiber. As the space-time duality is based on chromatic dispersion, large values of $\beta_2$ are preferred, as was seen in the previous paragraphs. For wide spectra the effect of third order dispersion (TOD) has to be considered as well. TOD is expressed by the term $\beta_3 \equiv d\beta_2/d\omega$, which stems from the variation of the GVD ($\beta_2$) with frequency.

The presence of TOD can be a problem in approximating the paraxial diffraction to the dispersion phenomenon (Section 3.2). In the space-time duality context, TOD can be viewed as a factor of aberration expressed as a departure of an optical system from the predictions of paraxial optics. However, the TOD effect can be overcome in different ways, which imply fiber or filter alternatives. From a fiber perspective, dispersion-flattened fiber (DFF) is one solution. DFFs are specially designed fibers with $\beta_3$ being almost zero over a certain wavelength range and $\beta_2$ being constant. However, the flat dispersion bandwidth of these fibers should be large enough to cover the pulse bandwidth. An example of DFF is given in [95], where the proposed fiber is a negative dispersion-flattened fiber with dispersion parameter equal to –60 ps/(nm·km) and a dispersion slope of ±0.005 ps/(nm$^2$·km) at 1550 nm. This kind of fiber has also the advantage of having high GVD which is used to reduce the fiber length and still achieve the far-field condition. Shorter fibers also mean smaller effect of $\beta_3$ as the phase information given from TOD is given as:

$$H_{\beta_3}(\omega) = \exp(\frac{i\beta_3 z\omega^3}{6}). \tag{3.27}$$

A different approach used to overcome the TOD effect and apply high linear chirp is by employing a filter which works as a dispersive medium. Such devices are linearly chirped intermodal couplers (LCIC) and linearly chirped fiber Bragg gratings (LCFG) [94], [96, 97] which provide a propagation delay that is a linear function of the frequency, by coupling the energy between two modes with different group velocities. In the design of these components the bandwidth and the total dispersion can be fixed independently in order to realize the required Fraunhofer temporal condition.

## 3.4 Time-to-frequency mapping

In the previous section it was demonstrated that it is possible to map the power spectral density into the time domain (frequency-to-time mapping) by using quadratic phase modulation followed by second order dispersion. It was shown that even the utilization of only dispersion was enough to ensure frequency-to-time mapping, but the resulting waveform characteristics could not be easily controlled. In the following section we will demonstrate that the opposite effect, time-to-frequency mapping, is also possible.

### 3.4.1 Basic principle

Intuitively, time-to-frequency conversion, opposite effect compared to Section 3.3, can be achieved, if the order in which phase modulation and chromatic dispersion operating on the waveform, is inverted. In fact, in spatial optics, if the object is placed at the front focal plane of a lens, the field distribution at this point and at the output plane are related by a Fourier transform [92]. But, also the output field distribution and its spatial spectral frequency distribution are related by a Fourier transform as well. Therefore, the output spectrum and input field are related by two successive Fourier transforms, implying that measuring the output power spectrum gives the spatial shape of the input object.

The basic principle for time-to-frequency mapping is shown in Fig. 3.3, where time-interleaved pulses are transformed into frequency-interleaved channels.

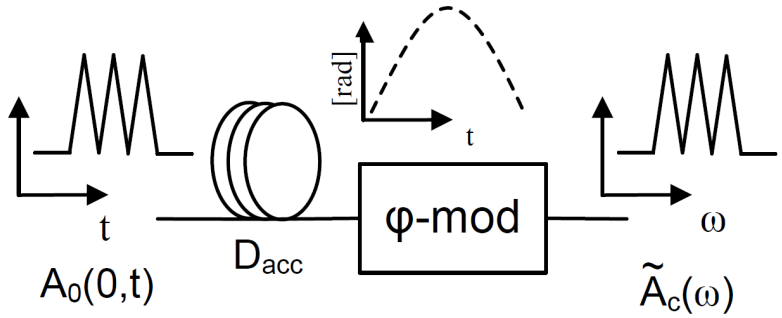


**Figure 3.3:** Schematic of the basic principle for time-to-frequency conversion OFT, implemented via propagation in dispersive media and quadratic phase modulation.

Let $A_0(0,t)$ be the electric field envelope of a waveform at the input of the time-to-frequency OFT system, propagated through a dispersive medium of length $L$ with accumulated dispersion $D_{acc} = \beta_2 L$. The Fourier transform of the waveform at the output of the dispersive medium is

$$\tilde{A}_0(L,\omega) = \tilde{A}_0(0,\omega) H_{\beta_2}(L,\omega), \tag{3.28}$$

with $\tilde{A}_0(0,\omega)$ being the Fourier transform[5] of the input. The dispersed waveform is subsequently quadratically phase modulated ($\varphi$-mod). As this process is a multiplication in the time domain, it will results in a convolution in the frequency domain. Hence, the Fourier transform of the phase modulated waveform becomes

$$\begin{aligned}
\tilde{A}_c(\omega) &= \frac{1}{2\pi}\tilde{A}_0(L,\omega) * H_l(\omega) \\
&= \frac{1}{2\pi}\int_{-\infty}^{+\infty} \tilde{A}_0(L,\omega') H_l(\omega-\omega') d\omega' \\
&= \sqrt{\frac{i}{2\pi C}}\int_{-\infty}^{+\infty} \tilde{A}_0(L,\omega') \exp(-\frac{i(\omega-\omega')^2}{2C}) d\omega' \\
&= \tilde{b}\int_{-\infty}^{+\infty} \tilde{A}_0(0,\omega') \exp(i\frac{(\beta_2 LC-1)\omega'^2 + 2\omega\omega'}{2C}) d\omega'
\end{aligned} \tag{3.29}$$

[5] In $\tilde{A}_0(0,\omega)$, the variable $\omega$ represents the frequency at baseband.

where

$$\tilde{b} = \sqrt{\frac{i}{2\pi C}}\exp(-\frac{i\omega^2}{2C}). \tag{3.30}$$

As in the previous section, if the condition $C = 1/D_{acc}$ is fulfilled then Eq. (3.29) can be written as

$$\tilde{A}_c(\omega) = \tilde{b}\int_{-\infty}^{+\infty} \tilde{A}_0(0,\omega')\exp(i\frac{\omega\omega'}{C})d\omega'. \tag{3.31}$$

By using the transformation $t = \omega/C$, the output from the OFT system (Eq. 3.31) can be written as

$$\tilde{A}_c(\omega) = 2\pi\tilde{b}A_0(0,t)_{t=\omega/C}, \tag{3.32}$$

and the power spectrum at the output of the OFT becomes

$$|\tilde{A}_c(\omega)|^2 = \frac{2\pi}{|C|}|A_0(0,t)_{t=\omega D_{acc}}|^2. \tag{3.33}$$

Eq. (3.33) shows that the power spectrum of the output waveform is proportional to the intensity of the input signal. The dispersion $D_{acc}$, or equivalently $C$, determines the scaling factor, between time and frequency domains, expressed as $t = \omega/C$. This means that a time interval $\Delta t$ will be mapped into a frequency interval $\Delta\omega = \Delta t \cdot C$. Higher $D_{acc}$ values lead to denser wavelength allocations, hence higher spectral compression rates of the transformed waveform. This information will be very useful in Chapter 5, were we will investigate the utilization of the time-to-frequency OFT for serial-to-parallel conversion.

### 3.4.2 Time-to-frequency conversion without dispersion

As it can be seen from the previous equations a true time-to-frequency conversion requires an appropriate dispersive and quadratic phase modulation mechanism. However, Section 3.3.2 showed that it is possible to have a frequency-to-time mapping even without the quadratic phase modulation part, but just by dispersing the waveform. The same should be possible also for time-to-frequency mapping, if the dispersion mechanism is omitted. For the sake of completeness we are going to derive the condition under which this is possible.

By omitting the dispersive's element transfer function, Eq. (3.29) is rewritten as

$$\begin{aligned}
\tilde{A}_c(\omega) &= \frac{1}{2\pi}\tilde{A}_0(0,\omega) * H_l(\omega) \\
&= \frac{1}{2\pi}\int_{-\infty}^{+\infty} \tilde{A}_0(0,\omega')H_l(\omega-\omega')d\omega' \\
&= \sqrt{\frac{i}{2\pi C}}\int_{-\infty}^{+\infty} \tilde{A}_0(0,\omega')\exp(-\frac{i(\omega-\omega')^2}{2C})d\omega' \\
&= \tilde{b}\int_{-\infty}^{+\infty} \tilde{A}_0(0,\omega')\exp(\frac{-i\omega'^2}{2C})\exp(\frac{i\omega\omega'}{C})d\omega'
\end{aligned} \tag{3.34}$$

Let $\delta\omega_0$ be the spectral width of the pulse. If the pulse is narrow-band and the linear chirp rate $C$ is very large then

$$\left|\frac{\delta\omega_0^2}{2C}\right| \ll 1. \tag{3.35}$$

If the last condition is true, the phase factor expressed by $\exp(-i\omega'^2/(2C))$, in the last integral in Eq. (3.34), can be set to 1. This means that after the transformation $t = \omega/C$ the power spectrum can be written as

$$|\tilde{A}_c(\omega)|^2 = \frac{2\pi}{|C|}|A_0(0,t)_{t=\omega/C}|^2. \tag{3.36}$$

which, as in the previous section's conclusion (Section 3.4.1), leads to

$$\Delta\omega = \Delta t \cdot C. \tag{3.37}$$

The only substantial difference between this case and the one where dispersion is present, resides in the fact that for Eq. (3.35) to be true, and for the Fourier transform ($\tilde{A}_c(\omega)$) to resemble the original time-domain signal ($A_0(0,t)$), then $C$ has to have a large value while $\delta\omega_0$ should be small. Moreover, the condition in Eq. (3.35) is dependent on the square of $\delta\omega_0$ and the spectral compression is linearly proportional to $1/C$. This means that in order for the resulting converted spectrum to resemble the initial time-domain waveform and to be as compressed as possible the initial spectrum $\tilde{A}_0(0,\omega)$ should be narrow and the total chirp $C$ should not be too large in order to keep $\Delta\omega$ small.

## 3.5 Re-timing by temporal lensing

In the previous sections it was show the utilization of the space-time duality for generation of optical time systems that perform frequency-to-time or time-to-frequency conversion. One of the properties that derives from frequency-to-time conversion is the ability of the time lens to align (re-time) with its temporal axis the image of an object that is displaced (time offset) compared to the lens' axis itself.

### 3.5.1 Basic principle

The realignment (*re-timing* in case of time lenses) principle can be easily explained in the space domain, as shown in Fig. 3.4. Let the object in front of the lens be displaced $\Delta y$ from the optical axis of the lens. The resulting image produced at the focal length of the lens is the Fourier transform of the input object, but without any spatial displacements. Due to the space-time duality the same should be true also in the time domain.

Let, again, $A_0(0,t)$ be the electric field envelope of a pulse at the input of the OFT system, and let $\Delta t$ be the time delay between the quadratic phase modulation imposed by the time lens and the peak of the pulse. The pulse envelope after phase modulation is

$$A_c(0,t) = A_0(0,t-\Delta t)\cdot\exp(\frac{iCt^2}{2}). \tag{3.38}$$

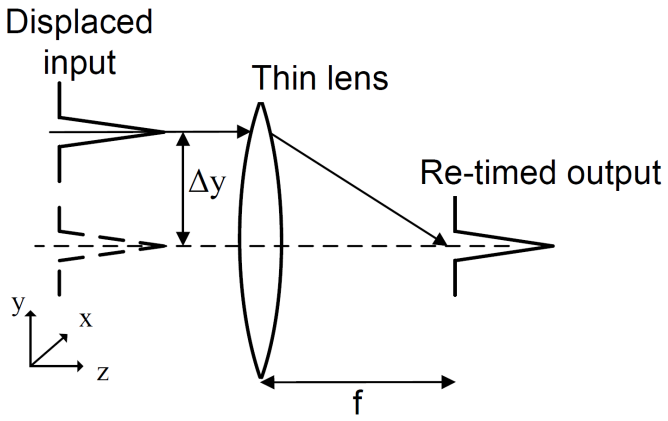


**Figure 3.4:** Schematic of object realignment by a thin lens.

After phase modulation the pulse is propagated in a dispersive medium with accumulated dispersion $D_{acc}$. At its output the waveform becomes (see also Eq. 3.18)

$$\begin{aligned} A_1(L,t) &= \int_{-\infty}^{+\infty} A_c(0,\tau)h_{\beta_2}(t-\tau)d\tau \\ &= \sqrt{\frac{i}{2\pi D_{acc}}}\int_{-\infty}^{+\infty} A_c(0,\tau)\exp(-\frac{i(t-\tau)^2}{2D_{acc}})d\tau \\ &= \sqrt{\frac{i}{2\pi D_{acc}}}\int_{-\infty}^{+\infty} A_0(0,\tau-\Delta t)\exp(\frac{iC\tau^2}{2})\exp(-\frac{i(t-\tau)^2}{2D_{acc}})d\tau \\ &= b\int_{-\infty}^{+\infty} A_0(0,\tau-\Delta t)\exp(i\tau^2(\frac{C}{2}-\frac{1}{2D_{acc}}))\exp(\frac{i\tau t}{D_{acc}})d\tau, \end{aligned} \tag{3.39}$$

where

$$b = \sqrt{\frac{i}{2\pi D_{acc}}}\exp(\frac{-it^2}{2D_{acc}}). \tag{3.40}$$

If the condition $C = 1/D_{acc}$ is fulfilled, and by performing the variable substitution $t/D_{acc} = \omega$ then:

$$\begin{aligned} A_1(L,t) &= b\int_{-\infty}^{+\infty} A_0(0,\tau-\Delta t)\exp(i\tau\omega)d\tau \\ &= b\cdot\exp(i\Delta t\omega)\cdot\tilde{A}_0(0,\omega)_{\omega=t/D_{acc}}. \end{aligned} \tag{3.41}$$

As in Section 3.3, the time domain output of the OFT system is proportional to the Fourier transform of the input, and realigned with the lens' axis. It has to be noticed that for a true re-timing that maintains the pulse shape, it is necessary that the pulse be the same as its Fourier transform pair, as is true for a Gaussian or a Sech pulse. However, regardless of the pulse shape, the detected output will still be re-timed. The last equation indicates that the time lens gives each temporal profile a phase shift ($\Delta\phi = \omega\Delta t$) proportional to its displacement compared to the optical axis of the lens. At the temporal focus, the initial time displacement is substituted by a frequency one.

## 3.6 Summary

The following chapter dealt with the mathematical analogies between the equations describing paraxial diffraction of space confined beams and propagation of optical pulses in dispersive media. The analogy does not extend only to diffraction, but can be applied to optical components as well, such as thin spatial lenses, whose equivalent temporal dual (time lens) is any process that can provide a quadratic phase modulation in the time domain. As in spatial optics a thin lens can be used as a Fourier transformation tool, then in temporal optics a time lens can be used to perform the same functionality. In fact, the combination of dispersion and quadratic phase modulation, gave rise to the implementation of the OFT technique, a very convenient bridge between temporal and spectral domains, resulting in frequency-to-time or time-to-frequency mapping. These techniques will be extensively used in the next chapters of this thesis.

# Chapter 4

# Flat-top pulse generation for increased tolerance to timing jitter and polarization variations

## 4.1 Introduction

For ultra-high-speed serial data communications reaching several hundred gigabits per second, data recognition and signal processing become limited by timing issues, such as generation of adequately narrow pulses, identifying sufficiently fast optical switches and obtaining low enough timing jitter on clock and data pulses. At high bit-rates especially the timing jitter becomes an important detrimental factor while being increasingly challenging to deal with [12, 98–101]. For this reason, introduction of a switching mechanism which is tolerant to timing jitter is highly desirable. In all-optical demultiplexing the switching mechanism is implemented by combining the OTDM data signal with a base rate control signal. In these systems the shape of the control pulse determines the shape of the switching window. To increase the tolerance to timing jitter in ultra-fast optical switches, flat-top pulses have been demonstrated to be very beneficial [101, 102].

Except for low timing jitter, polarization-independent (PI) operation is one of the most desired features of an optical demultiplexer, enabling it to process incoming optical data signals with arbitrary states of polarizations. In optical communication systems, the state of polarization of the received light is generally unknown, as it can change randomly over time due to e.g., varying birefringence of fibers, temperature fluctuations etc. This requires a polarization-independent operation of the receiver and of the other components of an optical network. For ultra-high-speed systems, nonlinear based switches have proven to be very beneficial due to their almost instantaneous response-time. But the nonlinear effects such as: XPM or FWM, which are used in ultra-high-speed all-optical demultiplexing, are inherently polarization dependent. This is the case also for the standard NOLM [69], since it is based on an XPM-induced phase shift. Different modification to the standard NOLM structure have been proposed in order to transform it into a PI device [103–105]. Other approaches for a PI nonlinear switching or wavelength conversion are based on a FWM approach [106, 107], [J-9, 10] [C-23, 30], or XPM-induced spectral broadening [108].

In the following sections we present the utilization of two different techniques used to generate flat-top pulses for all-optical signal processing. The chapter is organized as fol-

lows: Section 4.2 focuses on the utilization of the frequency-to-time OFT technique without the customary, yet cumbersome, active phase modulation in order to obtain narrow flat-top pulses. By using this technique, it is possible to generate a 1.6 ps flat-top pulse, and characterize it in a timing jitter tolerant demultiplexing experiment at 320 GBd. Numerical simulations based on a model derived from the space-time duality theory [76] show very good agreement with experimental results. On the other hand, Section 4.3 demonstrates the utilization of flat-top pulses generated in an interferometric long-period grating (LPG) pair, operating in partial destructive interference, for the realization of a polarization-independent NOLM (PI-NOLM). The operation principle of the PI-NOLM is based on the cancelation of the polarization-dependence of the XPM phase shift by careful use of the periodic power transfer function of the NOLM. This requires no structural modifications of the NOLM itself, and is achieved solely through adjustment of the power level and the polarization state of the control pulses. The concept is verified in a system experiment where a 640-GBd OTDM data signal, polarization-scrambled at high speed (∼113 kHz), is demultiplexed with error-free performance and low penalty.

## 4.2 Frequency-to-time conversion for flat-top pulse generation

Different approaches have been proposed for flat-top pulse generation, such as LPG filters [109], active mode locking and polarization rotation [110], electro-optic sinusoidal phase modulation [111], or super-structured fiber Bragg gratings (SSFBG) [112].

The following section describes how to use the frequency-to-time OFT technique without quadratic phase modulation (see Section 3.3.2) in order to obtain narrow flat-top pulses, which will be later used for all-optical signal processing in a FWM demultiplexing experiment.

### 4.2.1 Numerical Analysis

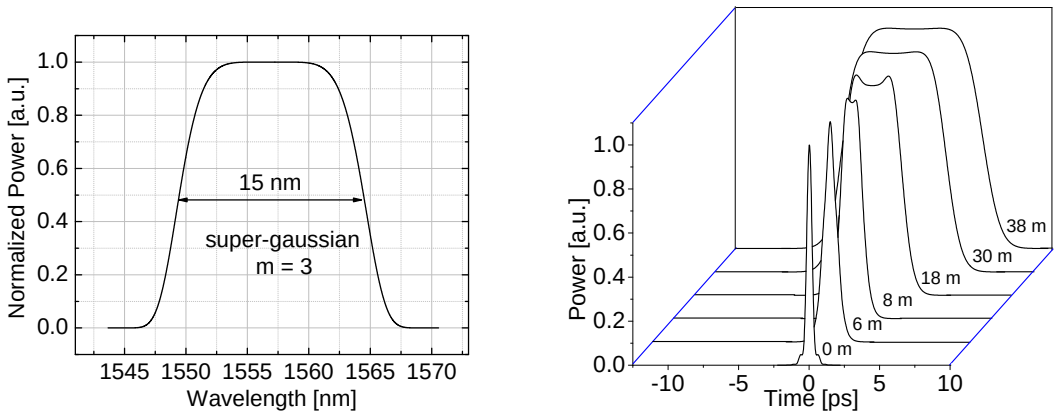


**Figure 4.1:** Simulation results of the evolution of a 500-fs FWHM sinc-like pulse with 15-nm wide third order super-Gaussian spectrum (a), when propagating in varying length of SMF, from 0 to 38 m (b).

Based on the theoretical analysis shown in the previous chapter (Section 3.3.2), the first step to generate a flat-top pulse by using the frequency-to-time OFT technique is to generate a sinc-like waveform in the time domain having a flat-top spectrum, and propagate it in a dispersive medium. Fig. 4.1 shows the intensity evolution of a pulse with a 15-nm wide third-order super-Gaussian[1] spectrum, when this is transmitted through different lengths of single-mode fiber (SMF). The group velocity dispersion (GVD) parameter for the SMF is D= $-17$ ps/(nm·km) or $\beta_2 = -21$ ps$^2$/km. For such a broad spectrum only short lengths of SMF are needed to see significant changes in the pulse shape. Due to the spectral width, the condition in Eq. (3.23) (Section 3.3.2) can be easily fulfilled for short lengths of SMF, leading to the generation of narrow flat-top pulses after only a few meters of propagation. The dispersion length in Fig. 4.1 varies from 0 to 38 m SMF. At 0 m dispersion, the pulse is in the transform limited plane (TL plane), meaning that it is not chirped, and has a sinc-like shape with ∼500-fs full-width at half maximum (FWHM). Based on (3.23) it can be found that after 38 m of propagation in SMF the initial narrow sinc-like pulse has turned into a perfect time-domain replica of the initial spectrum, with 9-ps FWHM (OFT plane). Even earlier, at 30 m propagation, the pulse is almost perfectly transformed (7.4-ps FWHM). Upon further propagation, the pulse will be in the far field and maintain its super-Gaussian shape, while simply growing broader. It is interesting to notice that after only 8 m of SMF, the pulse may not be perfectly transformed yet, but has a flat-topped appearance, and is 2-ps wide. Intercepting the pulse here, should thus provide a flat-top pulse suitable for ultra-high bit rate signal processing.

In this numerical simulation the effect of third-order dispersion (TOD) was not taken into consideration as the variation of the GVD in SMF is not very high and TOD's accumulated effect is very weak for short lengths of fiber.

### 4.2.2 Experimental validation

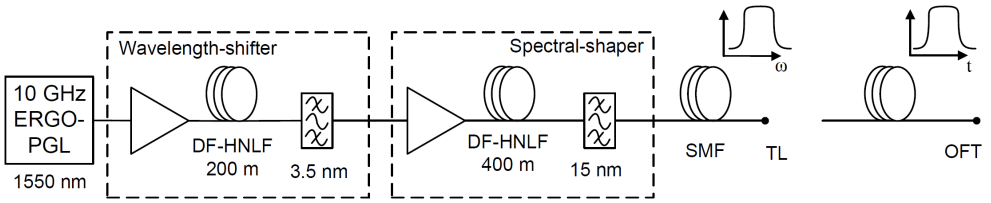


**Figure 4.2:** Experimental setup for generation of wavelength-tunable flat-top pulses from a broad flat-top spectrum.

Figure 4.2 shows the experimental set-up used to validate the numerical results and to generate narrow flat-top pulses used as control in a demultiplexing experiment. The output from an Erbium glass oscillator pulse-generating laser (ERGO-PGL) is injected into a wavelength-shifter based on 200-m dispersion-flattened highly-nonlinear fiber (DF-HNLF) followed by a 3.5-nm wide wavelength-tuneable optical bandpass filter (OBPF). The ERGO-PGL emits pulses at 10-GHz repetition rate centered at 1550 nm and with 1.5-ps FWHM. In the 200-m DF-HNLF, a supercontinuum is generated via SPM, and a section of it is filtered out by the 3.5 nm OBPF. This wavelength-shifted pulse train is injected into a second DF-HNLF, generating a second supercontinuum, which is filtered by a 15-nm third-order super-Gaussian

[1] A super-Gaussian $s(t)$ of order $m$, and $t_0 = 1/e$ width is $\propto \exp(-0.5(t/t_0)^{2m})$.

OBPF. Both the DF-HNLFs have nonlinear coefficient $\gamma$=10 $(\mathrm{W{\cdot}km})^{-1}$, dispersion D=–0.45 ps/(nm·km) at 1550 nm and dispersion slope S=0.006 ps/($\mathrm{nm}^2$·km). The tuning of the 3.5-nm OBPF determines the central wavelength of the flat-top spectrum at the output of the 15 nm filter, allowing for flexibility when allocating the wavelengths for the control and data signals. Transmitting this spectrum through 20-m SMF aligns all the spectral components, yielding the TL waveform, a sinc-like 500-fs wide pulse. It is from this TL-plane that the pulse will propagate into its frequency-to-time OFT shape, resembling it spectral intensity.

Figure 4.3 shows the spectrum generated at the output of the 15-nm filter (Fig. 4.2) and centered around 1556 nm. Fig. 4.4 shows the measured cross-correlation traces of the dispersed pulses, whose spectrum is shown in Fig. 4.3, after they are propagated in 16- and 19-m SMF after the TL-plane. The traces are generated by cross-correlating the flat-top pulse with a 500-fs narrow pulse. As it can be noticed there is a good agreement between the expected simulated and generated pulses. Fig. 4.5(a) shows the measured and simulated autocorrelation traces for two different lengths of dispersive fiber, respectively 8- and 19-m SMF. Fig. 4.5(b) shows the comparison between the FWHM of the measured and simulated autocorrelation traces for different dispersion lengths. As it can be seen the pulse evolution is in very good agreement with the simulated results.

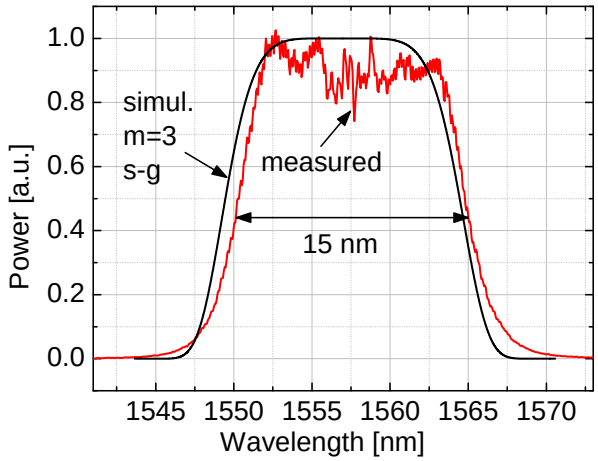


**Figure 4.3:** Comparison between the simulated and generated 15-nm wide third-order (m=3) super-Gaussian (s-g) spectrum. Note: linear scale.

The pulses shown in Fig. 4.4 have very broad spectrum (Fig. 4.3) and are in the middle of the C-band. In order for these pulses to be used as a control signal in an all-optical switch they have to be centered on the edges of the C-band in order not to overlap with the data spectrum. Fig. 4.6(a) shows an optimized 12-nm wide spectrum with a very flat-top part centered around 1536 nm, generated by tuning the 3.5 nm and the 15-nm bandpass filters shown in Fig. 4.2. As it can be seen the spectrum is narrower than the 15-nm case. This is due to the limited reach into the blue region of the supercontinuum generated at the output of the second DF-HNLF. However, this fact does not penalize the pulse evolution too much, as we are interested in intercepting the pulses when they start having a flat-top shape and when the condition in Eq. (3.23) is not fulfilled yet, because otherwise the pulses would be too broad. For this reason slightly narrower spectra work fine. The pulse corresponding to the 12-nm spectrum is measured before the OFT-plane at 10 m of propagation in SMF after the TL-plane, i.e., before it has evolved into an image of its own spectrum, and before it has broadened too much. Figure 4.6(b) shows the measured and fitted cross-correlation trace

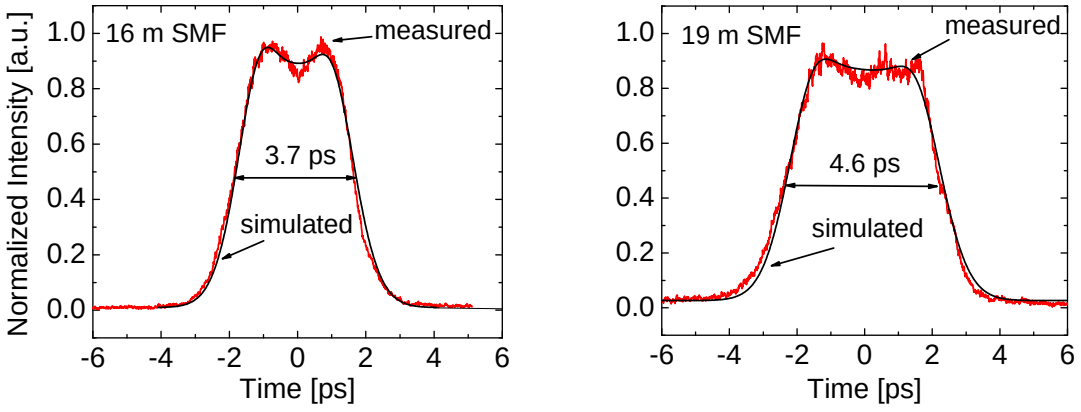


(a) (b)

**Figure 4.4:** Simulated and measured cross-correlation traces for flat-top pulses generated after propagating a narrow pulse with 15-nm wide third-order super-Gaussian spectrum in (a) 16-m SMF, (b) 19-m SMF.

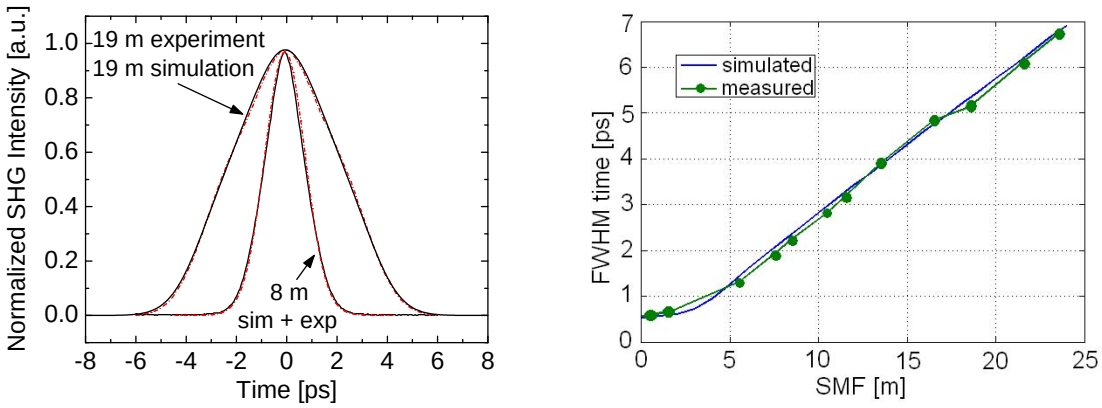


(a) (b)

**Figure 4.5:** (a) Comparison between simulated (dashed) and measured autocorrelation traces when propagating a arrow pulse with 15-nm wide third-order super-Gaussian spectrum in 8- and 19-m SMF; (b) Comparison between simulated and measured FWHM of autocorrelation traces for different propagation lengths of SMF.

between the flat-top pulse and a 500-fs sampling pulse. It can be noticed that the pulse has an upper part matching a 1.6-ps second-order super-Gaussian, but with wider tails. This is expected due to the fact that the pulse was intercepted in the early stage of its evolution when its shape is something in between a narrow sinc-like and a broader super-Gaussian.

### 4.2.3 Results and discussion

The pulses generated by the OFT technique are intrinsically accompanied by frequency chirp. This is true in both cases when they are generated with or without the presence of a time lens. As the dispersion itself is used to generate these flat-top pulses then the dispersion of the HNLF can further shape the pulses during the demultiplexing stage, when they are used as control signal. In order to avoid reshaping while demultiplexing, the length and dispersion of the HNLF are chosen to result in a very low accumulated dispersion ($D_{acc}^{(HNLF)}$). This can

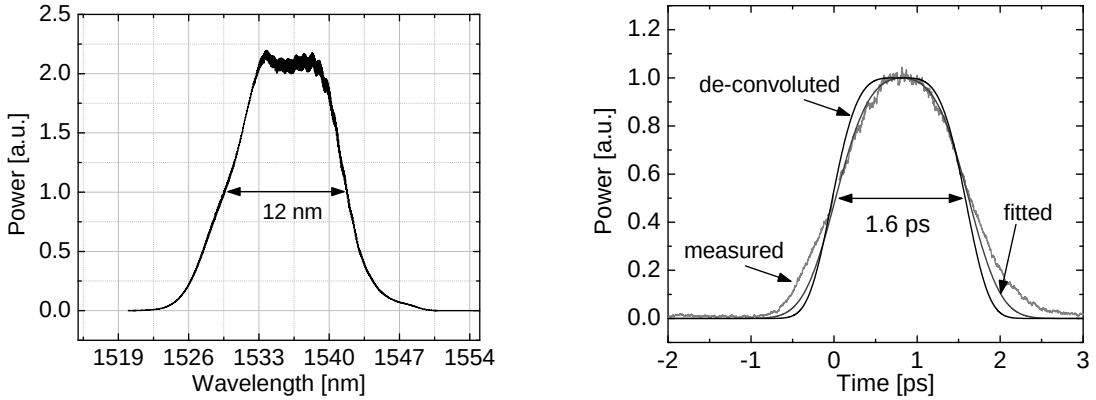


**Figure 4.6:** Experimental 1.6-ps FWHM pulse generated before OFT plane. (a) Flat-top spectrum 12-nm wide. (b) Cross-correlation trace between the flat-top pulse after 10 m of propagation and a sampling pulse of 500-fs width. Also shown is a de-convoluted waveform corresponding to 1.6-ps second-order (m=2) super-Gaussian and the fit of the measured trace when convoluted with the sampling pulse.

be achieved by choosing short lengths of HNLF[2] accompanied by low dispersion slope and positioning of the control signal close to the zero dispersion wavelength ($\lambda_0$) of the fiber. In this case the impact of broad pulse spectra and pulse pre-chirp will not have a significant impact on pulse reshaping.

A demultiplexing experiment, whose setup is shown in Fig. 4.7, is used to validate the quality of the generated 1.6-ps flat-top pulses seen in the previous section. A similar experiment was performed in [113] where it was shown the benefit of flat-top pulses over Gaussian ones when used as control signal in all-optical demultiplexing. In this case the Gaussian pulse gave evidently a worse performance in timing jitter mitigation. In Fig. 4.7 the OTDM transmitter consists of the same ERGO-PGL source emitting at 1550 nm, a Mach-Zehnder modulator (MZM) driven at 10 Gbit/s with a $2^7-1$ pseudo-random bit sequence (PRBS) for on-off keying (OOK) modulation, a pulse compressor, consisting of 400 m DF-HNLF, which compresses the data pulses down to 1 ps for 320-GBd operation, and a fiber-based optical multiplexer (OMUX). The OMUX is polarization and PRBS maintaining with a $(2^7-1)/2$ bits fiber delay in each OMUX stage. The resulting data pulses are 1.2-ps wide and are centered at 1552 nm. The demultiplexer is a 100-m long polarization-maintaining HNLF (PM-HNLF), with $\gamma$=10 (W·km)$^{-1}$, $\lambda_0$=1545 nm and S=0.025 ps/(nm$^2$·km), in which four-wave mixing between the OFT control pulses and the high-speed data signal takes place. The data signal was used as pump in the FWM process instead of the low rate control signal. This was done in order not to add additional amplification stages that would reshape the spectrum of the control signal.

The generated FWM product is selected by using a 0.98-nm wavelength-tunable OBPF centered at 1568 nm. In the pre-amplified receiver a variable optical attenuator (VOA) is used to vary the received power ($P_{rec}$) in order to perform a bit error ratio (BER) measurement. Figure 4.8(a) shows the BER vs. received power ($P_{rec}$) of the 160- and 320-Gbit/s OOK OTDM case. Error-free operation is readily obtained for bit rates up to 320 Gbit/s with excellent performance and less than 1-dB power penalty compared to the 10 Gbit/s back-

[2]However the HNLF should be long enough in order to have a good conversion efficiency in the demultiplexed signal.

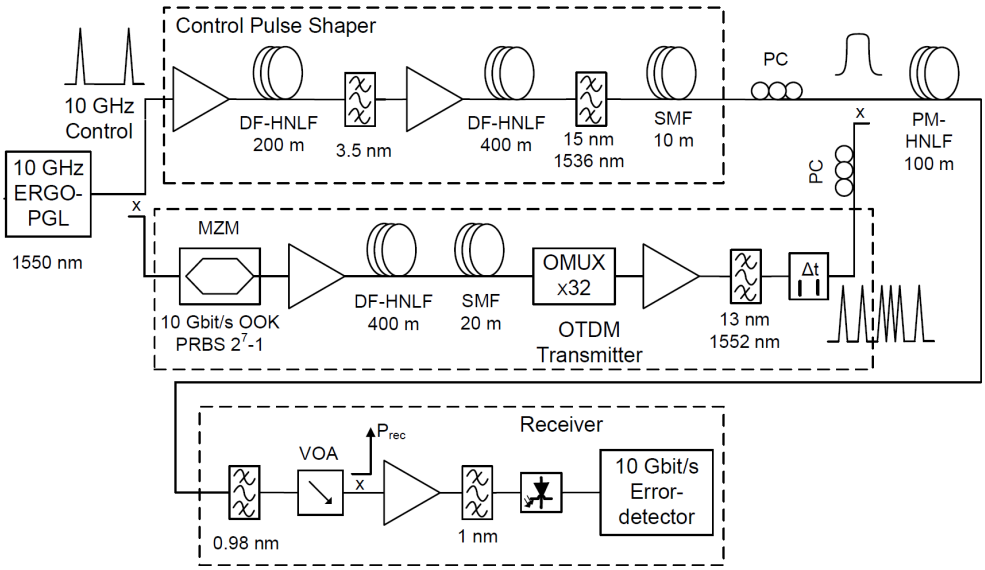


**Figure 4.7:** Setup for 320 Gbit/s OOK OTDM demultiplexing via FWM with 1.6-ps FWHM flat-top control pulses. ERGO-PGL: Erbium glass oscillating pulse-generating laser; DF-HNLF: dispersion-flattened highly-nonlinear fiber; PM-HNLF: polarization-maintaining HNLF; SMF: single-mode fiber; MZM: Mach-Zehnder modulator; PRBS: pseudo-random bit sequence; OMUX: optical multiplexer; PC: polarization controller; $\Delta t$: time delay line; VOA: variable optical attenuator; $P_{rec}$: received power.

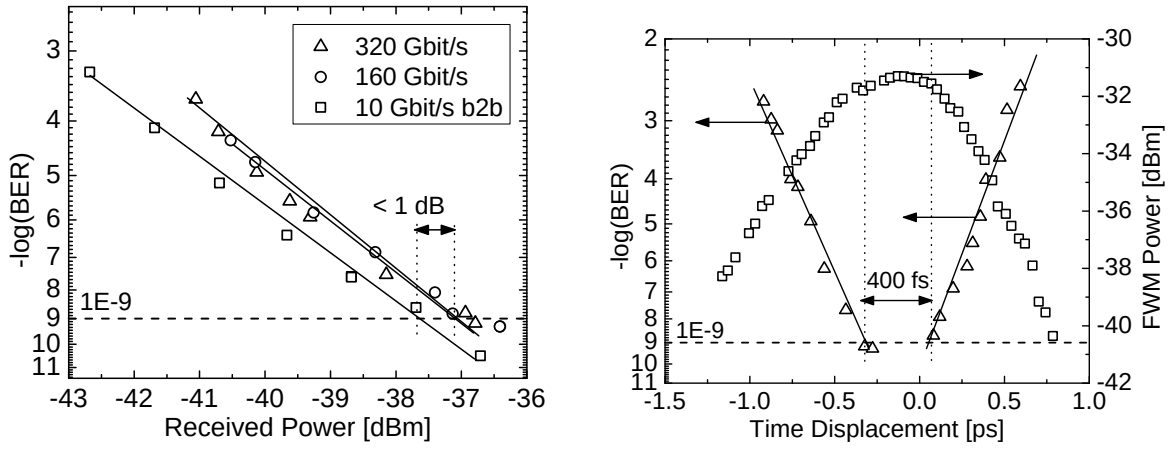


(a) (b)

**Figure 4.8:** Experimental BER measurements validating the quality of the flat-top pulses generated by the frequency-to-time OFT technique. (a) BER curve from a demultiplexed 160- and 320-Gbit/s OTDM signal. (b) Simultaneously measured timing tolerance and switched power for the 320-Gbit/s case.

to-back (b2b) case. Displacing the control pulse from the center position of a data pulse, by using the time delay $\Delta t$ in Fig. 4.7, enables the measurement of the timing tolerance of the demultiplexer. The power of the FWM product and the resulting BER are monitored simultaneously, effectively revealing the central part of the switching window (switched power of the FWM idler). As seen in Chapter 2 (Section 2.1.3), the idler is proportional to the complex conjugate of the probe and to the square of the pump field. Hence, the utilization of a square probe pulse will result into a flat switching window. As it can be seen in Fig. 4.8(b) this switching window has a very small slope on the top, over 400 fs, where the BER is $\leq 10^{-9}$. This is in good agreement with the previously mentioned work in [113] where the

authors could get a 500-fs switching window by using a flat-top pulse compared to a 150 fs switching window achieved with a 900-fs Gaussian pulse. In case the same Gaussian pulse had been used then an improvement factor of almost three in switching window size would have been achieved.

## 4.3 LPG-based flat-top pulse generation

LPG-based optical pulse shapers [109, 114, 115] have enabled the synthesis of flat-top optical pulses well in the picosecond and sub-picosecond range, i.e., with time widths as short as ∼700 fs [C-29]. These achievements have enabled the development of a range of nonlinear optical telecommunication data processing schemes enhanced by flat-top pulse shapers at unprecedented bit rates, namely up to 640 Gbit/s [101, 113, 116], [C-15]. Moreover the possibility of fabricating LPG pulse shapers with very low polarization sensitivities [116], [C-15] can be exploited to create polarization-independent OTDM demultiplexing systems [C-15].

The following sections give an overview of pulse shaping by the temporal differentiation technique. It is shown how to implement an optical differentiator via a single LPG or cascaded pairs of LPGs, and what are the conditions under which it is possible to generate flat-top pulses out of such devices. Finally, it is proved that by using a pair of polarization-independent LPGs inscribed in a commercial single-mode fiber it is possible to generate flat-top pulses suitable for 640-GBd OTDM polarization-independent demultiplexing.

### 4.3.1 Flat-top pulse shaping based on optical differentiation

The utilization of LPGs for flat-top pulse generation is based on a filtering scheme that employs optical temporal differentiation [114]. It can be proven that any desired temporal waveform can be synthesized by a linear superposition of a Gaussian-like pulse and a series of its time derivatives [117]. In fact a flat-top pulse generated by this technique can be approximated by only two terms of the series expansion, i.e., by a weighted combination of a Gaussian-like pulse and its first time-derivative. In the LPG-based implementation the weighting mechanism is achieved via frequency detuning between the input pulse and the differentiator's resonance [114].

The transfer function of a temporal differentiator, $\partial/\partial t$, is $H(\omega) = i\omega$. Hence, the mechanism of optical time differentiation [118, 119] can be realized using an optical filter that has a spectral transfer function proportional to $i(\omega - \omega_0)$, with $\omega_0$ being the zero-transmission frequency of the optical differentiator. Let $a(t)$ be the envelope of the input pulse to the optical differentiator. The envelope $b(t)$ after the differentiation process can be written as

$$b(t) \propto \frac{\partial a(t)}{\partial t} + i\Delta\omega\, a(t), \tag{4.1}$$

where $\Delta\omega = \omega_{in} - \omega_0$, with $\omega_{in}$ being the central wavelength of the input $a(t)$. By assuming that the input is transform limited, the temporal intensity profile of the signal at the optical differentiator output can be written as

$$|b(t)|^2 \propto \left|\frac{\partial a(t)}{\partial t}\right|^2 + \Delta\omega^2 |a(t)|^2. \tag{4.2}$$

As it can be seen, $|b(t)|^2$ is proportional to the intensity of the first derivative of the input $a(t)$ and to the intensity of the input itself weighted by $\Delta\omega^2$. Hence, it is possible to generate a pulse with a flat-top intensity profile ($|b(t)|^2$), by carefully adjusting the frequency shift between the resonance of the differentiator and the central frequency of the input signal. This is shown in Fig. 4.9, where a Gaussian input is transformed into its first derivative (Fig. 4.9(a)) for $\Delta\omega = 0$, a double-peaked pulse (Fig. 4.9(b)) for $\Delta\omega > 0$, and a flat-top pulse (Fig. 4.9(c)) for $\Delta\omega \gg 0$.

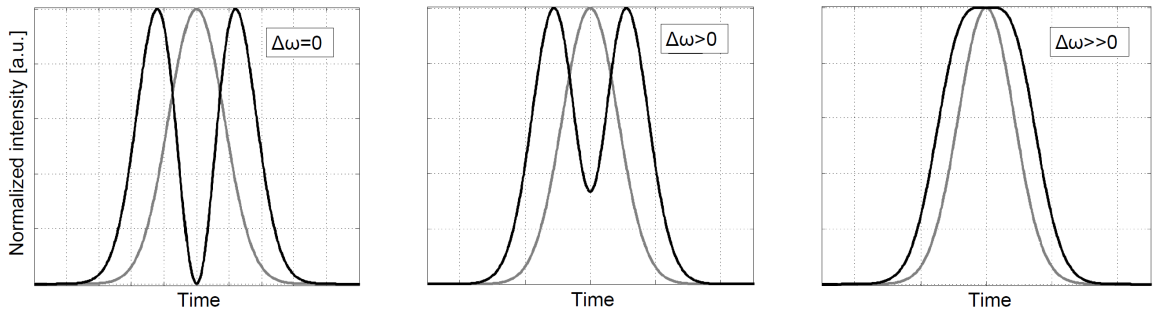


(a) (b) (c)

**Figure 4.9:** Simulation results showing the output pulse intensity of an optical time differentiator where a Gaussian input (light grey line), centered $\Delta\omega$ away from the resonance of the differentiator, is transformed into: (a) its first derivative for $\Delta\omega = 0$; (b) a double-peaked pulse for $\Delta\omega > 0$; (c) a flat-top pulse for $\Delta\omega \gg 0$.

The optical differentiation technique does not require precise control of the relation between the input pulse and the filter characteristics as long as the differentiator bandwidth is larger than the input's pulse one. This means that the same device can be used with different pulse sources emitting pulses of various durations and shapes. Depending on the input pulse characteristics, flat-top pulses with different peculiarities can be generated. This, of course, requires an adjustment of the wavelength tuning for each specific case. The resulting rise/fall edges and duration of the flat-top pulse will depend on the rise/fall and width of the initial pulse.

### 4.3.2 Optical differentiation based on a single LPG

As seen in the previous section, an optical differentiator is a linear device having a transfer function proportional to $i(\omega - \omega_0)$, which becomes 0 for $\omega = \omega_0$. The energy depletion at the central frequency $\omega_0$ implies an exact $\pi$ phase shift across $\omega_0$, and can be realized by complete energy transfer elsewhere. Specifically, in fiber optics, this can be achieved by resonant coupling of light between two modes of the optical fiber waveguide. Resonant light coupling is induced when light propagates in the two interacting modes with identical speeds, which is practically attainable e.g., by an increase or decrease of the light speed in one of the modes using a suitable phase diffraction grating [120]. In case of LPGs [121], the periodic variation of the refractive index along the direction of light propagation, induces resonant coupling between two co-propagating modes, one in the core and the other in the cladding of the hosting fiber. The term "*long*" refers to the diffraction grating period, which typically varies from tens to hundreds of micrometers, as opposed to short-period gratings (fiber Bragg gratings, FBGs), where the light is backscattered, resulting in coupling between modes traveling in opposite directions.

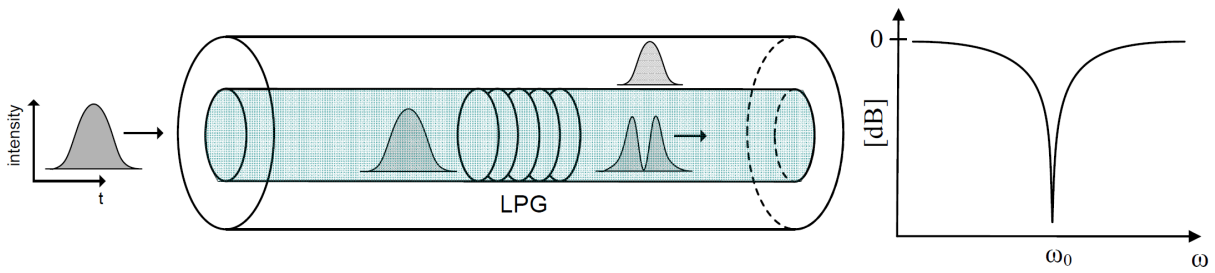


**Figure 4.10:** Single LPG used as an optical temporal differentiator, when the central frequency of the input is equal to the LPG resonance. On the right, it is shown the transfer function of an LPG with resonance at $\omega_0$.

Fig. 4.10 shows the utilization of a single LPG used as an optical temporal differentiator when $\omega_{in} = \omega_0$. The phase matching condition in order to achieve mode coupling between the core mode and the forward propagating cladding modes is given by

$$\beta_{01} - \beta_{cl}^{(n)} = 2\pi/\Lambda, \tag{4.3}$$

where $\beta_{01}$ and $\beta_{cl}^{(n)}$ are, respectively, the propagation constants of the core and the $n^{th}$-cladding mode, and $\Lambda$ is the periodicity of the grating. The fraction of power ($P_{cl}^{(n)}$) coupled into the $n^{th}$ cladding mode compared to the initial power ($P_{01}$) contained in the core mode is given by

$$\frac{P_{cl}^{(n)}(L)}{P_{01}(0)} = \frac{\sin^2[\kappa L\sqrt{1+(\delta/\kappa)^2}]}{1+(\delta/\kappa)^2}, \tag{4.4}$$

where $\delta$ is the detuning parameter

$$\delta = \frac{1}{2}\left[\beta_{01} - \beta_{cl}^{(n)} - \frac{2\pi}{\Lambda}\right], \tag{4.5}$$

$L$ is the grating length and $\kappa$ is the rate of the induced coupling per unit length between the core guided mode and cladding mode(s) [121]. To obtain efficient coupling between these modes, the period of the LPG must be properly adjusted to cause light diffraction from the core mode into the chosen cladding mode. Due to the different dispersion slopes of these two modes, the resonant coupling occurs only at a specific frequency $\omega_0$, referred to as the LPG resonance frequency. If the device is designed to exactly satisfy the condition $\kappa L = \pi/2$ then the grating induces complete energy coupling from the input guided core mode into the cladding mode at the resonance frequency. An optical fiber-based LPG specifically designed to provide 100% coupling between the fiber core mode and one of its cladding modes at the resonance frequency provides both the required $\pi$ phase shift and the transmission linear dependence that is necessary for time differentiation (assuming that the input optical signals are centered at the LPG resonance frequency) [118]. Such an LPG, coincidentally, has the required spectral linear response over a bandwidth as broad as several terahertz [119].

### 4.3.3 Optical differentiation based on an LPG pair

The optical differentiation technique can be achieved also in a Mach-Zehnder interferometric structure operated around any of its destructive interference fringes [122]. An all-fiber

implementation of this interferometric device can be created by serially inscribing a pair of similar LPGs on the same fiber [123].

The transfer function of a symmetric[3], unbalanced[4] interferometer can be written as [122]

$$H(\omega-\omega_0) \approx 1+\exp(i\omega\Delta t) = 1+\exp[i(\omega-\omega_0)\Delta t]\exp(i\omega_0\Delta t), \tag{4.6}$$

where $\Delta t$ is the relative time delay between the two interferometric arms. From the last equation it follows that, if the interferometer operates at a minimum transmission at the carrier frequency ($\omega_0$) then

$$\Delta t = \frac{\pi(2m+1)}{\omega_0}, \qquad \text{with } m \text{ integer.} \tag{4.7}$$

By substituting this value for $\Delta t$ in Eq. (4.6) we obtain

$$H(\omega-\omega_0) \approx 1-\exp(\frac{i\pi(2m+1)(\omega-\omega_0)}{\omega_0}). \tag{4.8}$$

The complex exponential of the last function can be approximated, in a narrow frequency interval around $\omega_0$, by the first term of the Taylor expansion:

$$\begin{aligned}\exp(\frac{i\pi(2m+1)(\omega-\omega_0)}{\omega_0}) &= \cos(\frac{\pi(2m+1)(\omega-\omega_0)}{\omega_0})+i\sin(\frac{\pi(2m+1)(\omega-\omega_0)}{\omega_0}) \\ &\approx 1+i\frac{\pi(2m+1)(\omega-\omega_0)}{\omega_0},\end{aligned} \tag{4.9}$$

resulting in

$$H(\omega-\omega_0) \approx -\frac{i(\omega-\omega_0)\pi(2m+1)}{\omega_0} = -i(\omega-\omega_0)\Delta t. \tag{4.10}$$

This is the transmission function required for optical temporal differentiation. The approximation shown in Eq. (4.10) holds for a narrow bandwidth around $\omega_0$, satisfying $\omega-\omega_0 \ll \pi/\Delta t$. In order to increase the differentiation bandwidth, the relative time delay should be decreased, but as it can be seen from Eq. 4.10 this would reduce the efficiency of the device as it would increase the loss.

As mentioned earlier, this unbalanced Mach-Zehnder interferometer can be created in a single fiber by using two cascaded LPGs as shown in Fig. 4.11. The first LPG couples 50% of the light into one of the cladding modes. This means that half of the light propagates in one of the cladding modes and half still in the core. Due to the different refractive indexes the light in the core mode accumulates a time delay $\Delta t$ compared to the cladding mode. At the second LPG the two modes are superimposed coherently. Due to the fact that both modes propagate in the same fiber and the co-propagation length is usually in the order of centimeters, any environmental fluctuation will perturb both modes in the same way, resulting in a very robust operation. This filter configuration will be used in the next sections for the generation of flat-top pulse which will be deployed in a polarization-independent NOLM (PI-NOLM) operation.

[3] 50% coupling/splitting ratio.

[4] different lengths for the two interfering paths.

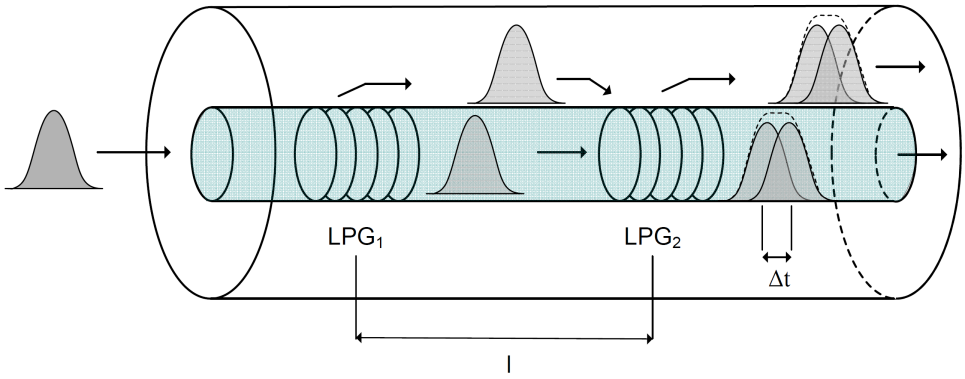


**Figure 4.11:** Schematics of the LPG-based common path interferometer for flat-top pulse shaping. The light is split by the first LPG, then propagates in the core and cladding modes with different speeds and is superimposed coherently using the second LPG. Due to the different propagation speed, the two modes (core and cladding) acquire a time delay equal to $\Delta t$.

### 4.3.4 Polarization-independent NOLM

Chapter 2 (Section 2.2) gave a short introduction on the NOLM operation and the XPM nonlinear effect on which it is based. It was mentioned that XPM is a polarization-dependent phenomenon. However, it is possible to elude its polarization-dependence and still realize a PI-NOLM by carefully adjusting its operation.

The principle for canceling the data polarization-dependence of the NOLM is based on the careful use of its periodic power transfer function without introduction of any structural modifications [25]. The operation principle is shown in Fig. 4.12 [25]. The polarization states of the involved signal are shown to the left: the control polarization is set to a linear state along the $y$-axis, and the data is in a random (elliptical) state with field-components $E_x$ and $E_y$ along the $x$- and $y$-axes, respectively. The XPM phase-shift $\Delta\phi_y$ induced by the control pulse on the parallel $E_y$-component is three times larger compared to the XPM phase-shift $\Delta\phi_x$ induced on the perpendicular component $E_x$. The power transfer function of the NOLM as a function of the phase-shift is shown to the right (Fig. 4.12). It is possible to find certain conditions under which the XPM phase-shifts of the two data-polarization components $E_y$ and $E_x$, $\Delta\phi_y$ and $\Delta\phi_x$=1/3$\Delta\phi_y$, respectively, give rise to equal transmissions $T_y$ and $T_x$. This will result in a polarization-independent (PI) switching operation and it occurs at $(\Delta\phi_x;\Delta\phi_y) = (\pi/2;3\pi/2)$ and $(\Delta\phi_x;\Delta\phi_y) = (\pi;3\pi)$. These conditions can be achieved by carefully adjusting the average control pulse power $P_{ctrl}$, since the XPM-phase shift depends on it. It is easy to understand that PI operation of the NOLM would benefit from the utilization of flat-top control pulses. This is related to the fact that a constant control pulse power would result in a constant phase shift along the data channel to be demultiplexed.

### 4.3.5 Experimental setup

Figure 4.13 shows the experimental setup for PI-NOLM operation using the cascaded LPG pair as pulse shaper [C-15], [J-2]. The pulse source is an ERGO-PGL running at 10 GHz and emitting 1.5-ps wide pulses centered at 1542 nm, which are used to create a supercontinuum in 400 m DF-HNLF. The output from the highly-nonlinear fiber is used to generate the control and data signal by using two OBPFs centered respectively at 1536- and 1555-nm.

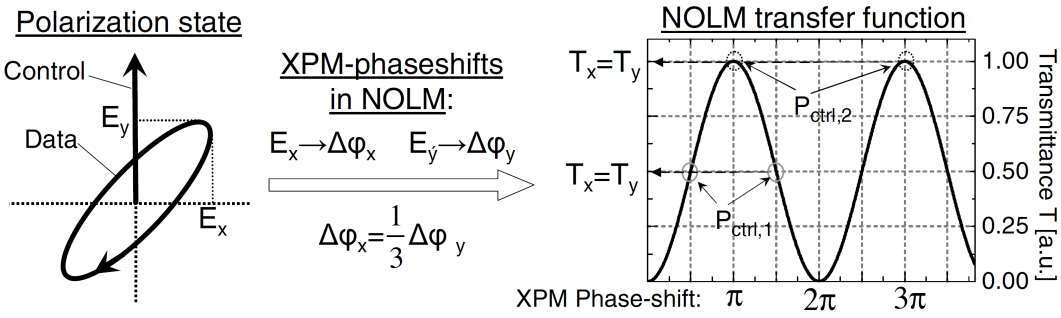


**Figure 4.12:** Operational principle of a polarization-independent NOLM [25].

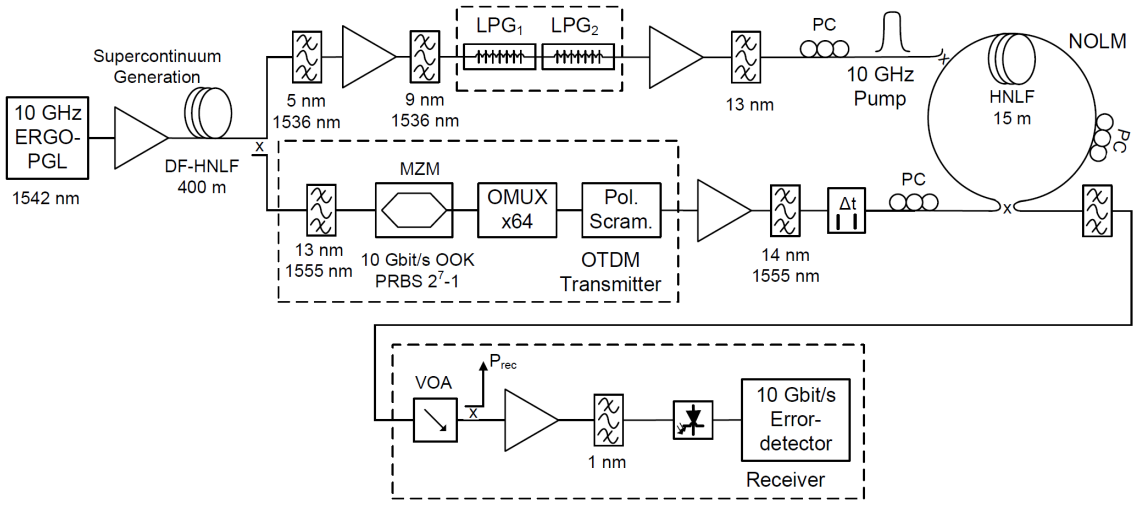


**Figure 4.13:** Setup for 640-GBd OOK OTDM demultiplexing in a polarization-independent NOLM implemented with 1.2-ps FWHM flat-top control pulses generated in a cascaded long period grating (LPG) pair. Pol. Scam.: polarization scrambler; NOLM: nonlinear optical loop mirror.

Due to the symmetric, unbalanced nature of the interferometer created at the output of the second LPG (Fig. 4.13), the recombined pulses from the two arms will interfere with each other, resulting in the spectral domain into a fringe interference patten as seen in the transfer function[5] in Fig. 4.14. The combined pulse intensity profile (after $LPG_2$) will depend on: 1) the time delay between the cladding and core modes; 2) the input pulse width and shape and 3) its central wavelength ($\lambda_{in}$) compared to the position of the fringes.

The pair of cascaded LPGs of Fig. 4.13, inscribed in a conventional telecommunication single-mode fiber, have a period of 387 $\mu$m and are spaced 28 mm apart. This leads to a time delay of 390 fs between the recombined cladding and core pulses. Fig. 4.15 shows the simulated output pulse intensity profiles based on the detuning of $\lambda_{in}$ compared to the fringes of the interferometric structure, when the input pulse is a 700-fs wide Gaussian (almost double the mode time delay). Figure 4.15 displays the fully destructive interference case (trace 1), with a central dip in the pulse's intensity profile and spectrum (the device is working as an optical differentiator), and the partially destructive interference case (traces 2 and 3), where the dip gets filled up to achieve a flat-top pulse. This pulse is formed by tuning the input's central wavelength to an offset <4 nm from the destructive interference wavelength (trace 3

[5]The LPG-pair transfer function has been measured by utilizing a broadband incoherent amplified spontaneous emission (ASE) source.

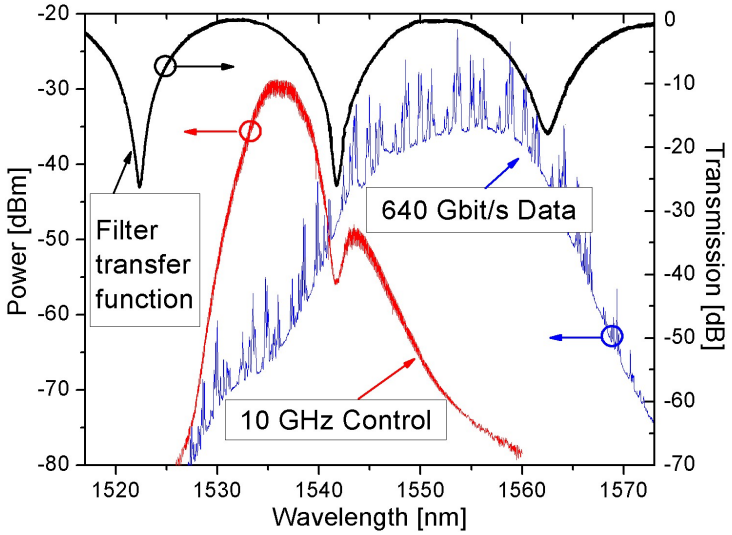


**Figure 4.14:** Transfer function of the LPG filter pair and control and data spectra.

in Fig. 4.15). This corresponds to a generated ∼1.2-ps flat-top pulse centered at 1536 nm, which is subsequently used as control in a NOLM demultiplexing experiment.

The HNLF in the NOLM has dispersion slope S=0.015 ps/(nm$^2$·km), zero dispersion at $\lambda_0$=1545 nm and nonlinear coefficient $\gamma$ =10.5 (W·km)$^{-1}$. The data signal to be demultiplexed is a single polarization, 640-GBd return-to-zero (RZ) OOK OTDM signal (PRBS $2^7$-1) centered at 1555 nm, with 410 fs wide pulses. The data is subsequently demultiplexed down to 10 Gbit/s for BER characterization. The spectra of data and control, as well as the LPG-pair transfer function are show in Fig. 4.14.

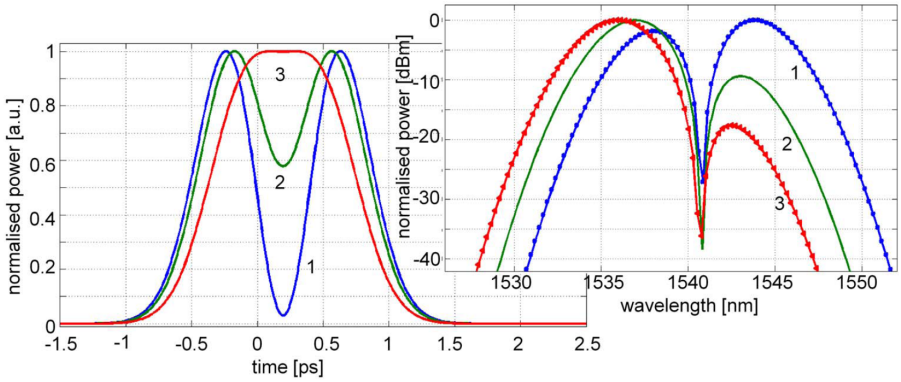


**Figure 4.15:** Traces in ascending order of pulse intensity profiles (left) and respective spectra (right) for detuning of $\lambda_{in}$ away from the interference fringe of a cascaded pair of LPGs.

### Fringe tuning by temperature variation

The position of the fringes in the interferometric LPG pair depends on many factors. One of them is the temperature of the fiber section where the fringes are inscribed. Figure 4.16 shows the position of the fringes when the LPG pair is heated from room temperature (∼ 25°C) to 56°C. In this case, when the temperature is increased the fringes shift by 2.4 nm towards longer wavelengths. This is a desired behavior, as it gives some flexibility in the wavelength allocation of the control signal.

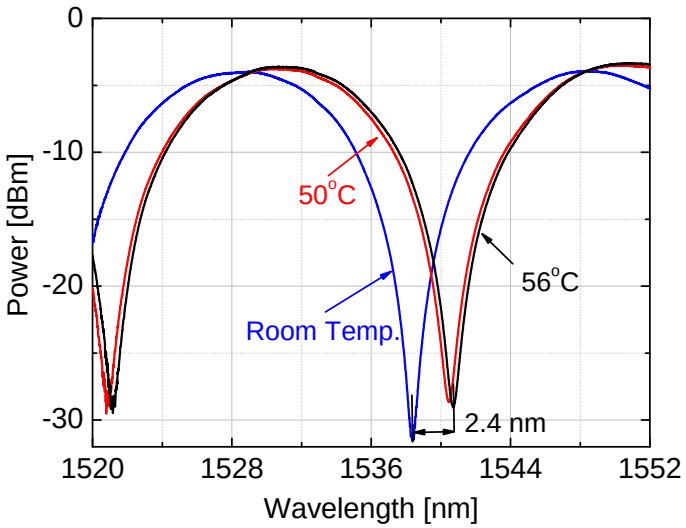


**Figure 4.16:** Fringes shift for different temperature values of the fiber section where the LPG-pair is inscribed.

### 4.3.6 Results and discussions

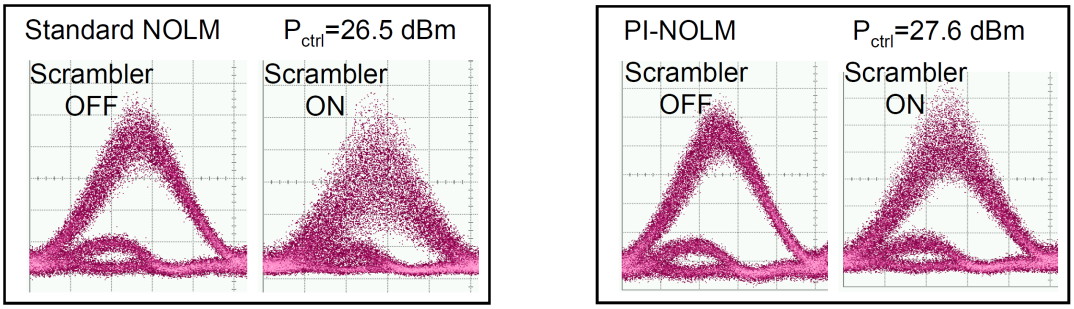


(a) (b)

**Figure 4.17:** Eye diagrams for the demultiplexed 10 Gbit/s signal for the: (a) Standard- and (b) PI-NOLM operations, with scrambler on and off.

The polarization state of the data signal is randomized at high speed (∼113 kHz) in a polarization scrambler. The standard NOLM operation (non-polarization insensitive operation) is reached for $P_{ctrl}$=26.5 dBm. When the scrambler is turned on the demultiplexed eye is severely deteriorated (Fig. 4.17(a)), independently on the polarization state of the control signal. When $P_{ctrl}$ is increased to 27.6 dBm and the control polarization is optimized then the NOLM starts working in PI mode. With the scrambler on, the eye remains open as seen in Fig. 4.17(b). By using a slow speed photodetector it is possible to measure a 0.7-dB residual polarization-dependence of the PI-NOLM operation when the scrambler is on (Fig. 4.18).

Fig. 4.19 shows the BER measurement for the standard and PI-NOLM operation. As it can be seen, when the scrambler is off the power sensitivity (at BER=$10^{-9}$) is the same for both cases. When the scrambler is turned on the standard NOLM exhibits an error floor above BER=$10^{-7}$. In contrast, the PI-NOLM shows just a power penalty of ∼1 dB. These measurements confirm the flat-top pulse quality and the PI operation of the NOLM.

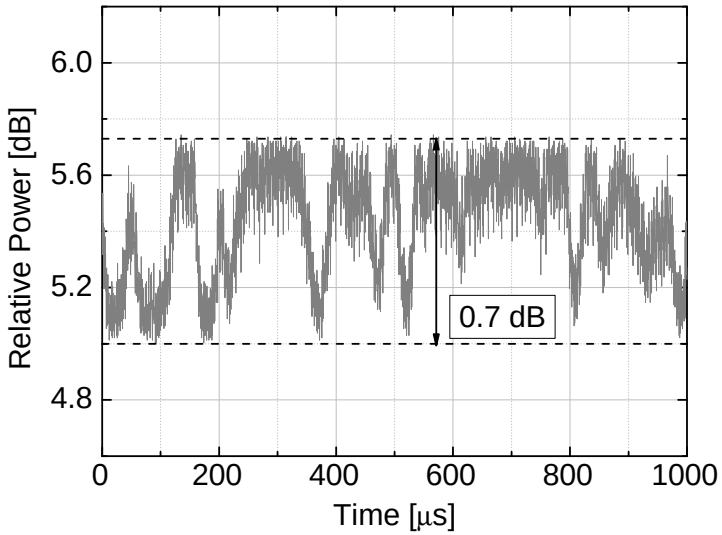


**Figure 4.18:** Power fluctuations of the residual polarization-dependence of the PI-NOLM operation measured using a slow photodiode.

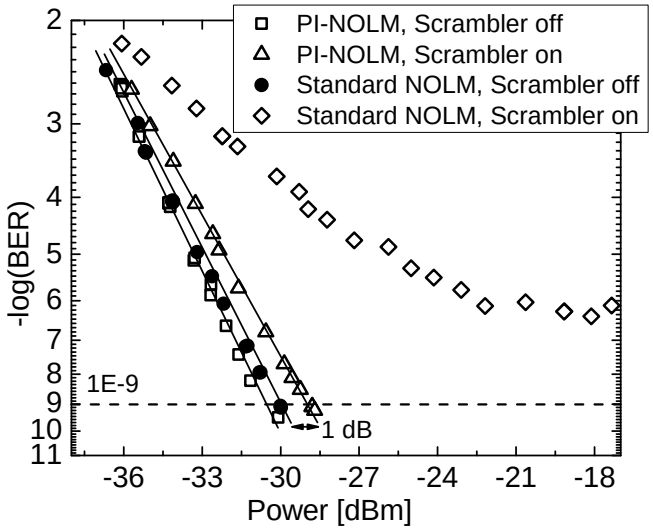


**Figure 4.19:** BER curves for the standard- and PI-NOLM operation.

## 4.4 Summary

This chapter showed the utilization of two different techniques for generation of flat-top pulses in the time domain and their application in nonlinear optical telecommunication data processing, particularly in demultiplexing of OTDM serial data using flat-top control pulses in FWM- or NOLM-based switches, at symbol rates up to 640 GBd.

Section 4.2 reported on the utilization of the frequency-to-time conversion OFT technique for generation of flat-top pulses used for timing jitter mitigation in an ultra-high speed optical switching experiment. The frequency-to-time conversion was implemented without the active phase modulation mechanism, but only by using the equivalent of the Fraunhofer far field condition applied to the time domain case. The generation of a 1.6-ps flat-top pulse, which is the shortest reported so far using this technique, was demonstrated. The pulses were thoroughly characterized both numerically and experimentally, and the shape and width was

in good accordance with the theoretical analysis. These flat-top pulses were successfully used in a 320-GBd demultiplexing experiment, showing a 400-fs timing tolerance and less than 1-dB power penalty compared to the back-to-back case.

Section 4.3 reported on the utilization of a pair of LPG filters in a cascaded configuration for generation of flat-top control pulses used in a polarization-insensitive NOLM demultiplexing experiment. The polarization-insensitive operation of the NOLM was achieved without changing its principle of operation but by just adjusting the control pulse's power and polarization. The quality of the control pulse was validated by error-free demultiplexing of a polarization scrambled 640-GBd OTDM signal, with only 0.7 dB penalty resulting from the scrambling process.

Both described techniques can be applied for the generation of even more complex pulse shapes of practical interest. E.g., triangular or parabolic waveforms, could be generated in the sub-picosecond regime using similar LPG or frequency-to-time OFT approaches, potentially enabling the implementation of other pulse shaping-enhanced telecommunication signal processing operations at unprecedented bit rates.

# Chapter 5

# OTDM-to-WDM conversion based on time-to-frequency OFT

## 5.1 Introduction

Serial-to-parallel conversion is one of the functionalities that might be necessary in future photonic networks, in which ultra-fast optical signals of any bit rate and modulation format will be transmitted and processed from end-to-end in the optical domain. Traditionally, OTDM has been utilized to push the serial data rate on a single wavelength far beyond electronic speeds. In combination with complex modulation formats and polarization multiplexing, up to 10.2 Tbit/s has been realized [C-12], [J-3]. At such speeds, at the receiver side in OTDM systems, each of the tributaries are traditionally demultiplexed in separate high-speed switches. Hence, the receiver complexity and power consumption essentially scale with the number of OTDM tributaries. On the other side, in the case of wavelength division multiplexing (WDM), each electrical data stream is allocated to an optical channel with its own central wavelength and each generated from a different laser. In contrast to OTDM, WDM channels can overlap in the time domain (parallel to each other) and at the receiver they can be selected by optical filtering.

A serial-to-parallel conversion would take advantage of the mature technology used in WDM systems for parallel channel extraction, and if such functionality would be performed on a single device it might lower the current OTDM switching energy. A number of schemes for demultiplexing all or several tributaries in a single switch by serial-to-parallel conversion have been proposed [124–126]. However, a true OTDM-to-WDM conversion is challenging, since it requires the converted tributary spectra to conform to the channel spacing of a WDM grid [127], hence requiring spectral compression of the low duty-cycle OTDM tributaries. In Section 3.4 it was demonstrated that the time-to-frequency OFT technique maps the time information of a given waveform into the spectral domain. In this case the OFT was implemented by dispersing the data signal and then quadratically phase modulating it. Parametric processes [128], such as FWM [37, 90, 91], second harmonic generation (SHG), SFG or DFG [80, 83, 89] can be used to apply the necessary quadratic phase modulation. In this case the OFT is implemented by dispersing the data signal followed by phase modulation based on a parametric process between the data pulses and linearly chirped pump pulses. F.x., in case of FWM, the time information of the OTDM signal is mapped onto the power spectrum of the idler generated in the FWM process, hence converting the time-interleaved OTDM tributaries to frequency interleaved WDM ones. At the same time, due to the OFT

properties (Section 3.4, Eq. (3.33)), the spectra of the converted tributaries are compressed as well. By doing so, in principle, more than half of all OTDM tributaries can be converted in a single OFT device, meaning that all tributaries can be simultaneously demultiplexed by conversion to dense WDM (DWDM) with only two parallel OFT devices [J-1].

The following chapter describes the utilization of the time-to-frequency conversion OFT technique for serial-to-parallel mapping, in a single step, of an OTDM signal into a DWDM grid. The chapter is organized as follows: Section 5.2 gives an overview of the implementation of the time-to-frequency OFT technique via FWM with linearly chirped pump pulses; Section 5.3 performs a numerical investigation of the OTDM-to-DWDM conversion process based on FWM, for different pump pulse shapes and spectral compressions [J-1]; Section 5.4 demonstrates the utilization of the OFT technique for serial-to-parallel mapping of a 320- and 640-GBd return-to-zero (RZ) OOK-modulated OTDM signal into a 100 GHz DWDM grid [C-13], [J-1]; Section 5.5 shows a converted 50 GHz grid and demonstrates that the OFT technique preserves the phase and amplitude information of the converted OTDM tributaries in case of complex-modulation formats such as quadrature phase-shift keying (QPSK) and 16-ary quadrature-amplitude modulation (16-QAM) [C-1]; Finally, Section 5.6 demonstrates that it is possible to achieve spectral compressions down to 25-GHz grids, allowing for more than half of the OTDM tributaries to be converted successfully [C-5], [J-4]. This means that with only two devices, all tributaries may be simultaneously demultiplexed/converted to DWDM. Section 5.6 shows also the successful implementation of the OFT technique not only in HNLFs but also in more compact nonlinear devices such as silicon nanowires. Even though the author was not the main responsible for the experimental work shown in the last section of this chapter (Section 5.6), he extensively contributed to the measurements and to the theoretical and numerical analysis as shown in Section 5.3.

## 5.2 Time-to-frequency OFT via FWM

Section 3.4 showed that it is possible to map the time profile of a waveform into the frequency domain, by firstly propagating the waveform in a medium with accumulated dispersion $D$ and subsequently quadratically phase modulating it with a linear chirp rate $C = 1/D$. If the waveform of our interest is not a single pulse but an entire OTDM signal, consisting of tributary channels spaced by a time interval $\Delta t$, then the result of the time-to-frequency OFT technique, would be a set of frequency multiplexed channels spaced by $\Delta\omega = \Delta t C$ (see Eq. (3.32) in Section 3.4). The chirp rate $C$, or equivalently the accumulated dispersion $D$, can be used to control the scale of the wavelength spacing (spectral compression), e.g., to match a particular DWDM grid.

As mentioned in Section 3.2.2, the quadratic phase modulation can be applied by different means, f.x., by electro-optical phase modulation (EOPM) or parametric processes. However an EOPM driven by a sinusoidal signal would not be the best choice due to its two main drawbacks. Firstly, the generated amount of chirp rate might not be adequate to achieve high compression ratios (see Section 6.2 for further details). Secondly, the required phase modulation should be applied over a relatively large time spans, in order to cover as many OTDM channels as possible. The sinusoidal signal driving the EOPM is approximately parabolic only 15% of its period around its maximum/minimum value, corresponding to 15 ps for a 10-GHz sine. All OTDM channels outside this range with see a nonlinear chirp rate or even one with the wrong sign. For these reasons a parametric implementation of the

time lens, such as via FWM, would suit better the serial-to-parallel conversion process.

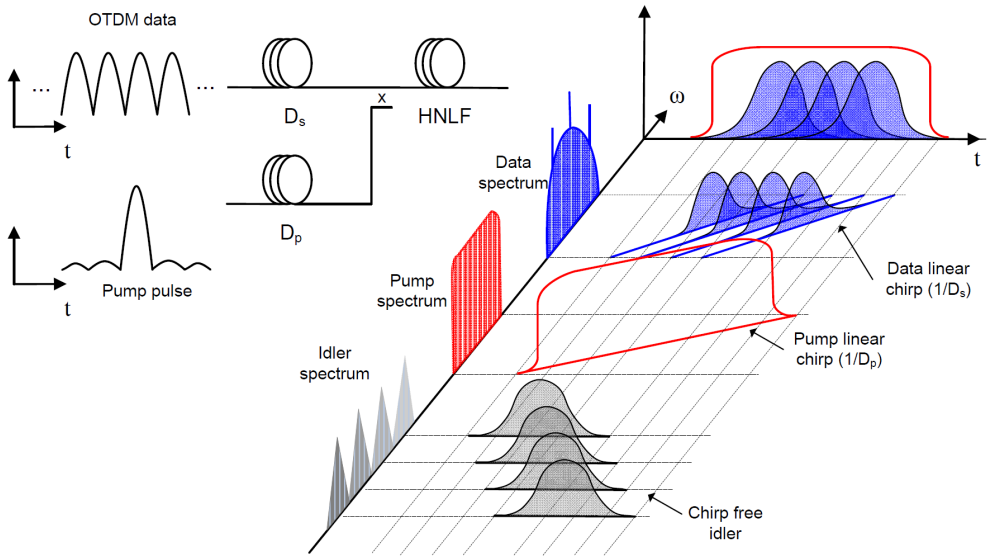


**Figure 5.1:** Time-to-frequency OFT for OTDM-to-DWDM conversion implemented via FWM. After dispersion ($D_s$), the OTDM signal is combined with linearly chirped pump pulses to generate a DWDM signal in the FWM idler. The right part of the figure shows the linear frequency chirp vs time for both pump and data signals.

The FWM-based quadratic phase modulation implementation is shown in Fig. 5.1. In this case, the dispersed waveform to be transformed acts as signal, $E_s(t)$, and the phase modulation is applied using linearly chirped pump pulses, $E_p(t)$, generated by propagation of transform limited pulses in a dispersive medium with accumulated dispersion $D_p$. While propagating through the dispersive medium, the pulses broaden and acquire a linear chirp, whose rate is $C_p = 1/D_p$. In the FWM process, the signal is converted to an idler, $E_i(t)$, which combines the phases of both pump and complex-conjugated signal ($E_i(t) \propto E_p^2(t)E_s^*(t)$) (see Section 2.1.3). As a result of the FWM process, the time information contained in the signal is mapped onto the power spectrum of the generated idler. Due to the idler's proportionality to the square of the pump field, the time-to-frequency mapping condition is true if

$$D_s = \frac{1}{2C_p} = \frac{D_p}{2}, \tag{5.1}$$

where $D_s$ is the signal's accumulated dispersion. As it can be seen from the last equation, the pump should be dispersed twice as much as the data signal in order to reach the optimal condition for time-to-frequency mapping.

To achieve an OTDM-to-WDM conversion by the above technique, the pump pulses must run at the repetition rate (base rate) of the OTDM tributaries in order to map each tributary bit to the same wavelength[1]. After the time-to-frequency OFT, the idler spectrum will resemble a wavelength grid were each channel is an OTDM converted tributary. This grid can be made to comply with recommendation ITU-T G.694.1 [127], which determines the optical frequencies to be used to identify DWDM channels for different frequency grids in the range 25–200 GHz.

It has to be noticed that the quadratic phase modulation is achieved over the temporal

[1]In the rest of this work the base rate will always be 10 GHz.

extension of the pump pulse, whose intensity profile determines the number of generated DWDM channels. The dispersed OTDM tributaries that are not fully covered by the pump pulse, will be distorted in the conversion process. The tributaries at the edges of the pump's bit slots (base rate bit slot), under the tails of the pump pulses, will suffer from lower conversion efficiency as well as a broadening of the DWDM channel spectrum, leading to reduced optical signal-to-noise ratio (OSNR) and DWDM inter-channel cross-talk. As it will be seen in the next section and as hinted in Fig. 5.1, the utilization of linearly chirped flat-top pump pulses extending to nearly the entire base-rate bit-slot can be used to successfully convert more then half of the OTDM tributaries in a single shot [J-1].

As a final remark: it has to be noticed that by changing the order of dispersion and quadratic phase modulation it is possible to achieve the opposite effect, parallel-to-serial conversion. In [C-4,7] a FWM-based time lens was used to transform a DWDM signal into an OTDM one, by firstly combining the DWDM channels with a linearly dispersed pump and then propagating the resulting idler into a dispersive medium.

## 5.3 Numerical analysis of time-to-frequency mapping

In this section, we are going to numerically investigate [129] the OTDM-to-DWDM conversion based on the OFT technique. Numerical simulations will examine the idler's shape and channel spacing based on shape and chirp of pump pulses, and signal dispersion. This analysis will help understand the limitations of the time-to-frequency OFT technique for serial-to-parallel conversion, and clarify which are the system requirements for the resulting idler to comply with a certain DWDM grid [127].

The OTDM signal is a 640-GHz unmodulated pulse train (64 tributaries at 10 GHz) having Gaussian-shaped pulses with 0.6 ps (40% duty cycle) FWHM. Pump and tributaries have the same repetition rate of 10 GHz. The HNLF used for the FWM process is 100-m long and has nonlinear coefficient $\gamma$=10 $(\mathrm{W{\cdot}km})^{-1}$. The FWM conversion efficiency is assumed to be uniform across the entire bandwidth of the signals (data, pump and idler) involved in the FWM process, and the phase mismatch is assumed to be zero. In these conditions the utilization of linearly chirped flat-top pump pulses would equalize the DWDM channels resulting from the OTDM-to-DWDM conversion process. As seen in Chapter 4 (Section 4.2), such pulses can be obtained by dispersing narrow sinc-like pulses having a broad flat-top spectrum. In this case the dispersion process maps the spectral profile into the time domain [C-33, J-11] (frequency-to-time mapping). The medium used to disperse the signal, and to linearly chirp the pump is dispersion compensating fiber (DCF) with $\beta_2$=148 $\mathrm{ps}^2$/km.

Figure 5.2(a) shows the data, pump and idler spectra at the output of the HNLF when the pump spectrum is a sixth order super-Gaussian with 10-nm FWHM. The pump is centered at 1550 nm, the data at 1565 nnm, and the resulting idler will be generated at 1535 nm. The data signal is dispersed in $L$=32 m DCF in order to achieve at the idler a channel frequency spacing $\Delta f=\Delta\tau/(2\pi\beta_2 L)$ of 50 GHz ($\Delta\tau$=1.56 ps: OTDM tributary spacing). This corresponds to a linear chirp $C$=0.21 $\mathrm{ps}^{-2}$, which can be achieved by dispersing the pump in 64 m DCF. Because of the flat intensity profile of the pump pulse, which broadens up to 74-ps FWHM, it is possible to have half of the tributaries (32 channels) mapped in the frequency domain, well equalized, and having <1.5 dB difference. With two of such OTDM-to-DWDM converters it should be possible to extract all 64 OTDM channels.

Higher compression ratios require higher pump and signal dispersion. This can be seen in

Fig. 5.2(b), where pump and data are dispersed in respectively, 128- and 64-m DCF in order to achieve a 25-GHz grid at the idler. As the required dispersion is twice as much compared to Fig. 5.2(a) then the spectral FWHM of the pump should be almost half of the previous case (5.2 nm), in order for the pump pulses to be flat, not interfere with each other and be 75 ps wide. A spectrally broader pump can not be used for such a high compression ratio as the broadened pump pulses would overlap with each other, resulting in distorted time-to-frequency mapping. Figure 5.2(b) shows also an open eye diagram of one of the converted tributaries. In order to get the eye diagram, the OTDM tributaries were OOK modulated and the desired channel was selected with a 0.16-nm 3-dB bandwidth optical bandpass filter (OBPF). The simultaneous mapping of all OTDM tributaries is possible, but this requires a high degree of spectral compression. This is related to the fact that most of the dispersed data pulses' energy should be covered by the pump. However, the data pulses, whose location is at the edges of the pump bit slot, will always have a worse conversion efficiency due to the fact that part of their energy leaks into the neighboring pump pulse slot. This means that a precise equalization of the resulting DWDM channels is hardly possible.

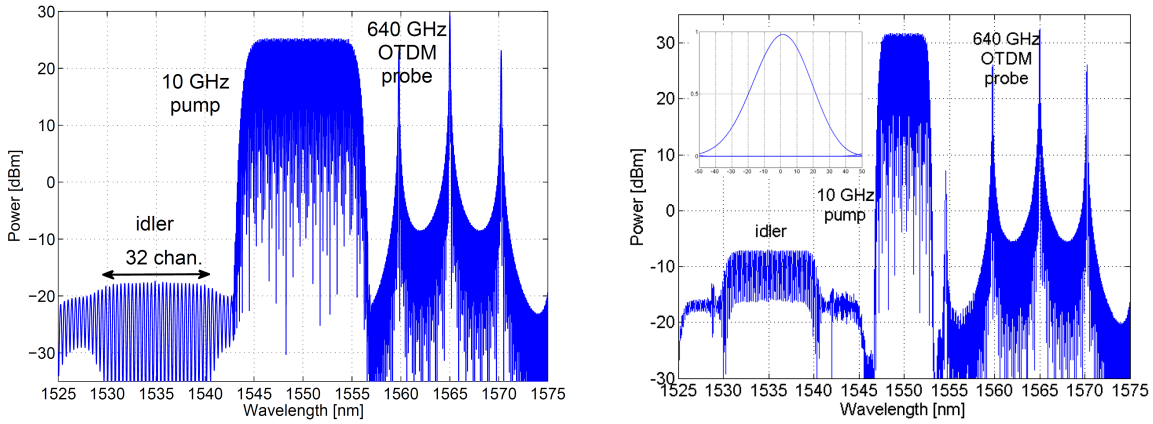


**Figure 5.2:** Simulated spectra at the output of the HNLF when flat-top, linearly chirped pump pulses are used for OTDM-to-DWDM conversion: (a) 50 GHz grid, (b) 25 GHz grid with eye diagram (inset) of one of the converted tributaries.

The utilization of Gaussian pump pulses would result in unequal power levels for the DWDM channels at the idler. This is related to the different pump intensity levels that various OTDM channels experience. This can be seen in Fig. 5.3, where pump (10 GHz, 0.5-ps FWHM Gaussian pulses) and signal are dispersed in respectively 32- and 16-m DCF, resulting in 0.8 nm (100 GHz) channel spacing. Figure 5.4 shows the idler for both 100- and 50-GHz (0.4 nm) spacing. In the later case, pump and signal are dispersed respectively in 64- and 32-m DCF. Because of the pump's spectral extension, and in order to avoid overlap between pump and idler spectra, the wavelength separation between pump and signal is made sufficiently larger compared to the previous cases. This means that the utilization of flat-top pump spectra not only generates linearly chirped flat-top pump pulses, which can equalize the DWDM idler but can also lower the pump interference in the frequency domain.

The deviation of both signal and pump chirp from the optimum value for a certain spectral compression would result in spectral distortions at the converted idler and consequently into time distortions for the selected DWDM channels. Figure 5.5 shows the eye diagrams for one of the OTDM tributaries when the dispersion of data and pump is separately increased by

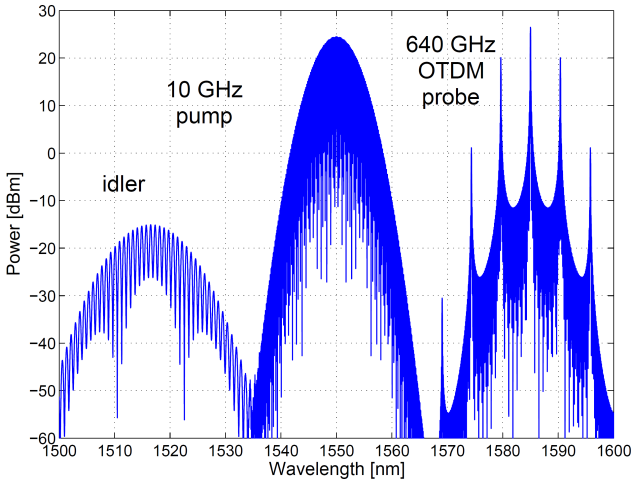


**Figure 5.3:** Simulated spectra at the output of the HNLF when Gaussian, linearly chirped pump pulses are used for OTDM-to-DWDM conversion, resulting in a 100 GHz grid.

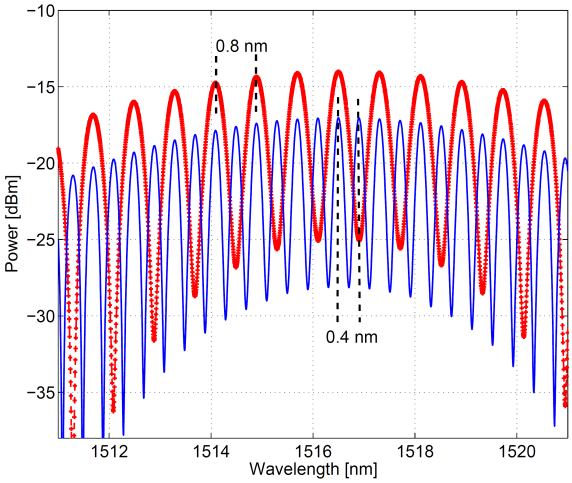


**Figure 5.4:** Simulated spectra at the output of the HNLF when Gaussian pump pulses are used for OTDM-to-DWDM conversion, in case of a 100 GHz (0.8 nm) and 50 GHz (0.4 nm) grid.

10% compared to the relative optimum case for 100-GHz grid shown in Fig. 5.4. Since the condition $C = 1/\beta_2 L$ is not fulfilled, then the pulses will have a residual phase component which induces some temporal shifts. The chosen DWDM channel corresponds to the OTDM tributary overlapping[2] in the time domain with the center of the pump pulse and it was selected with a 0.3-nm 3-dB bandwidth OBPF. As it can be seen, the dispersion deviation from the optimum value for any of the signals involved in the FWM process is enough to deteriorate the system's performance.

In some cases the effect of higher order dispersion terms can not be neglected and should be taken into consideration when studying pulse evolution. As mentioned in Chapter 3 (Section 3.3.3), the higher order terms of the Taylor expansion of the propagation constant ($\beta$) come mainly into play for ultrashort pulses, having a broad spectral content, and when the central wavelength is near to the zero dispersion wavelength of the fiber ($\lambda_0$). For wide spectra, the effect of third order dispersion (TOD) has to be taken in consideration. TOD repre-

[2]This OTDM tributary is always mapped to the same WDM channel, independently on the spectral compression factor.

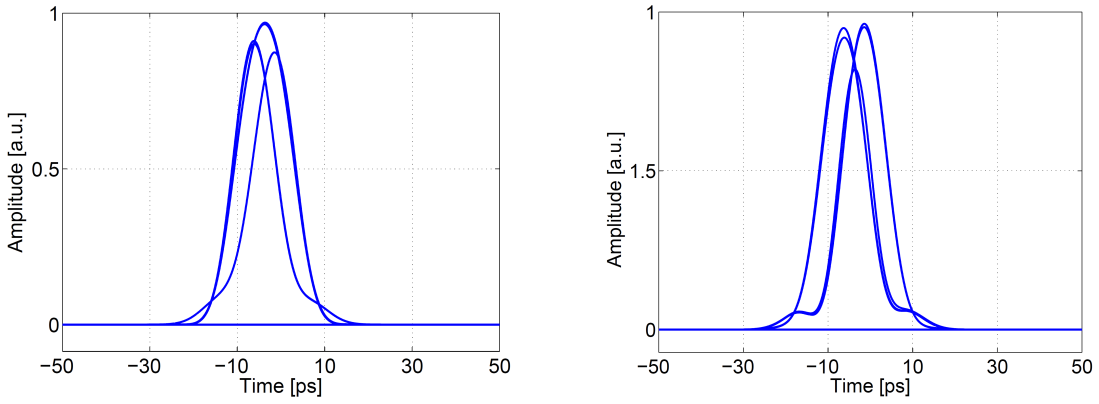


**Figure 5.5:** Distorted eye diagram when the dispersion of data (a) and pump (b) is independently increased by 10% compared to the relative optimum case for 100 GHz frequency spacing of Fig. 5.4.

sents an aberration factor, introducing distortions in the time-to-frequency mapping process. Figure 5.6 shows the effect of TOD for the 100-GHz spacing scenario of Fig. 5.4 but with $\beta_3$=1 ps$^3$/km and $\beta_3$=10 ps$^3$/km for both signal and pump dispersion fibers. $\beta_3$=1 ps$^3$/km is a typical value for commercially available DCF [130] and it does not introduce any distortion in the time-to-frequency mapping. Figure 5.6 shows also the eye diagrams when $\beta_3$=10 ps$^3$/km only for the pump (top) or only for the signal (bottom). Considerable abberations in the idler spectrum become visible when $\beta_3$ reaches or passes this value, for either one of the dispersion media.

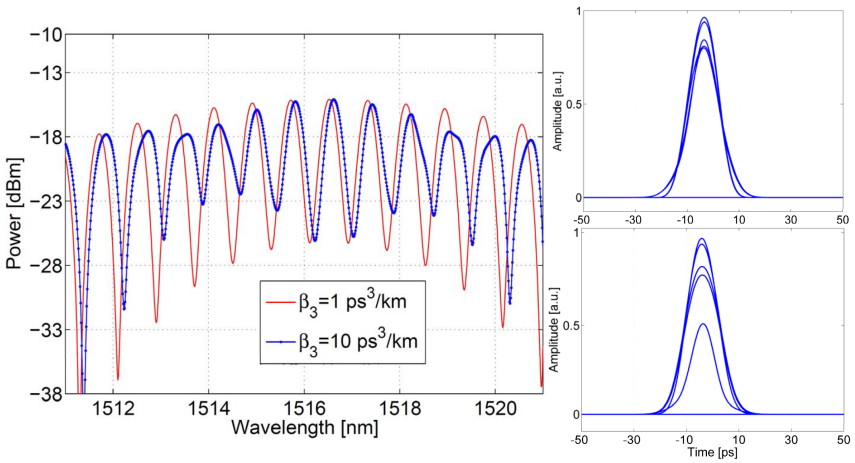


**Figure 5.6:** Simulated idler spectrum showing the effect of $\beta_3$=1 ps$^3$/km and 10 ps$^3$/km for both data and pump signals. Eye diagrams for $\beta_3$=10 ps$^3$/km only for: (top) pump dispersion, (bottom) data dispersion.

Time-to-frequency mapping can also be achieved for higher symbol rates, such as 1.28 TBd [131], [C-12]. This is shown in Fig. 5.7, where the pulses for both data and pump (at 10 GHz) are Gaussian with 0.3-ps FWHM. Because of the closer tributary position in the time domain, half of the dispersion fiber is required in order to achieve the same 100-GHz DWDM grid seen in Fig. 5.4. The resulting spectral compression can be seen in Fig. 5.7. Because of the closer spacing of the original OTDM tributaries, the extinction ratio between the DWDM channels is not as good as in the 640 GHz case (Fig. 5.7), generated from the terabaud signal

when every second pulse is suppressed. Despite this fact, it is possible to get an open eye (inset in Fig. 5.7) by filtering with a narrower filter (0.2-nm 3-dB bandwidth).

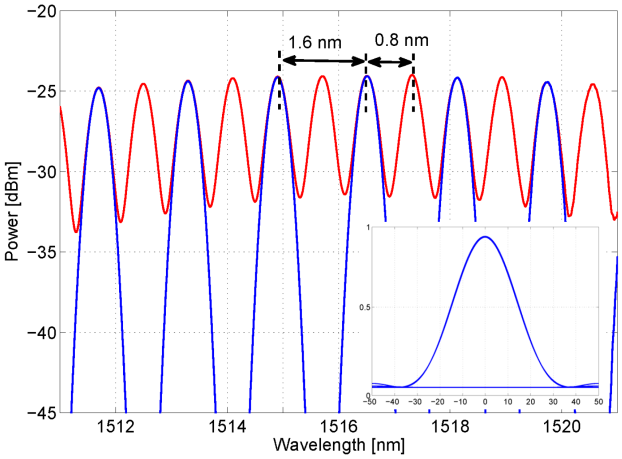


**Figure 5.7:** Simulated idler spectrum: 100-GHz (0.8 nm) and 200-GHz (1.6 nm) spacing for respectively 1.28-TBd and 640-GBd OTDM-to-WDM converter when pump and data are dispersed respectively in 16- and 8-m fiber with $\beta_2$=148 ps$^2$/km. Inset: eye diagram of one of the 10 Gbit/s tributaries converted from the 1.28 Tbit/s OTDM signal.

## 5.4 320- and 640-GBd RZ-OOK OTDM mapped to 100-GHz DWDM

The following section describes the experimental work on serial-to-parallel conversion of a 320- and 640-GBd RZ-OOK OTDM signal into a 100 GHz DWDM grid. In this case both data- and pump-pulses are Gaussian like. The main aim of this section is to prove the operational principle of the time-to-frequency OFT technique and to validate some of the numerical results shown in the previous section.

### 5.4.1 Experimental Setup

Figure 5.8 shows the schematics of the experimental setup used to perform the OTDM-to-DWDM conversion. The same setup is used to test the principle on both 320- and 640-GBd OTDM systems, except for some small details concerning optical bandpass filtering and power levels. The pulse source is an ERGO-PGL emitting ∼1.5-ps FWHM pulses with 10 GHz repetition rate and centered at 1542 nm. The ERGO-PGL output is amplified and its spectrum is broadened via SPM in a 400 m dispersion-flattened HNLF (DF-HNLF), having dispersion D=–0.45 ps/(nm·km), dispersion slope S=0.006 ps/(nm$^2$·km) at 1550 nm, and nonlinear coefficient $\gamma$=10 (W·km)$^{-1}$. Both data and pump spectra are carved out of the SPM-induced broad spectrum. The pump pulses for the FWM process are filtered at 1545 nm by using a 5-nm OBPF for the 320-GBd case or a 13-nm OBPF for the 640-GBd case. The 10-GHz pulse train for the data signal is obtained by filtering the supercontinuum at 1557 nm with a 13-nm OBPF for both cases. The data pulses are OOK encoded with a 10 Gbit/s, $2^7$-1 PRBS pattern, in a Mach-Zehnder modulator (MZM), and then are optically time division multiplexed up to 320- or 640-GBd by using a passive fiber-based delay-line

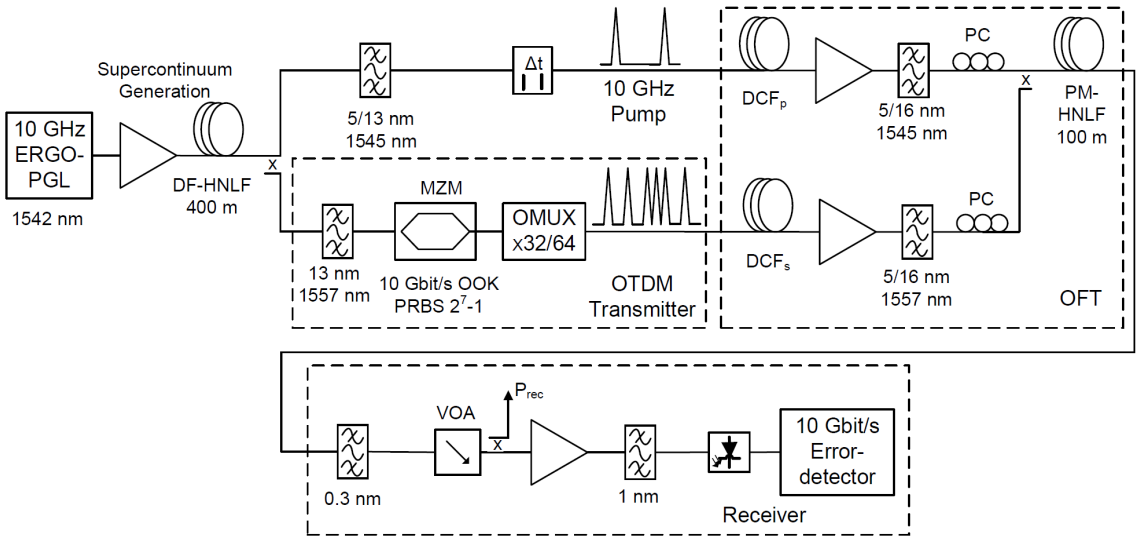


**Figure 5.8:** Experimental setup for OTDM-to-DWDM conversion of 320- and 640-GBd RZ-OOK OTDM systems: ERGO-PGL: Erbium glass oscillating pulse-generating laser; DF-HNLF: dispersion-flattened highly-nonlinear fiber; MZM: Mach-Zehnder modulator; OMUX: optical time-division multiplexer; DCF: dispersion-compensating fiber; PC: polarization controller; PM-HNLF: polarization-maintaining HNLF; VOA: variable optical attenuator; $P_{rec}$: received power. In the optical filters nomenclature the "/" character conceptually divides the filter used for the 320- or 640-Gbit/s OTDM data setup cases.

optical multiplexer (OMUX).

After generation, both data and pump signals are injected into the time-to-frequency OFT block. This is composed of different lengths of DCF in which both signals are dispersed before being amplified and injected into a polarization-maintaining HNLF (PM-HNLF) in which the FWM-idler (OFT product) is generated. The PM-HNLF is 100-m long, with zero dispersion wavelength $\lambda_0$=1545 nm, dispersion slope S=0.025 ps/(nm$^2$·km) and nonlinear coefficient $\gamma$=10 (W·km)$^{-1}$. At the PM-HNLF output, a narrow 0.3-nm wavelength-tuneable OBPF, whose transfer function is shown in Fig. 5.11(a), extracts the converted 10 Gbit/s tributaries centered at different wavelengths in the idler signal. The time delay, $\Delta t$ (Fig. 5.8) is used to change the position between the center of the pump pulse and the OTDM channels, hence shifting their mapped positions in the frequency domain. The filtered tributaries are sent into a 10 Gbit/s pre-amplified receiver for bit-error ratio (BER) evaluation. The receiver and the PRBS generator are synchronized to the same clock signal, which is used to drive the ERGO-PGL.

### 5.4.2 320 GBd case

Firstly, the OTDM-to-DWDM (serial-to-parallel) conversion scheme was applied to a 320-GBd RZ-OOK OTDM signal [C-13]. This was done in order to see the bell shaped spectrum envelope of the idler resulting from Gaussian pump pulses, as previously seen in Section 5.3. Before dispersion, both data and pump pulses were Gaussian-like with 1.3-ps FWHM. The dispersive fiber used was 20-m DCF (DCF$_s$) for the data and 48-m DCF (DCF$_p$) for the pump. The pump pulses at the input of the PM-HNLF were thus broadened up to 17.5 ps FWHM. The average powers at the input of the PM-HNLF were 20.3 dBm for the pump and 2.6 dBm for the 320 Gbit/s data. Figure 5.9(a) shows the resulting spectrum at the output of the PM-HNLF. As it can be seen the tributaries are successfully mapped to different

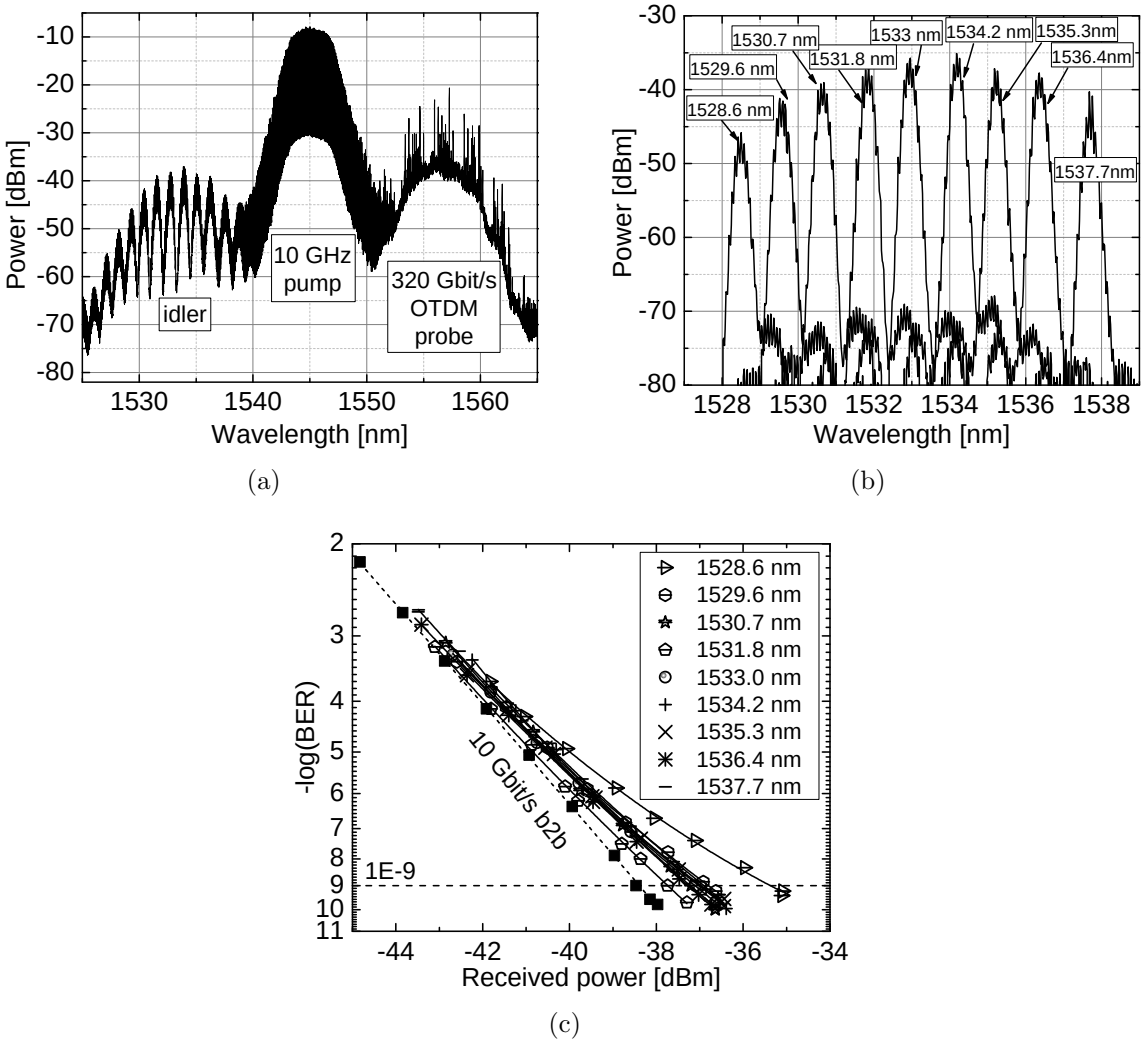


**Figure 5.9:** System performance of 320 Gbit/s OTDM-to-WDM conversion: (a) output spectrum of PM-HNLF, (b) 10 Gbit/s tributaries extracted at different wavelengths (resolution 0.01 nm), (c) BER curves of nine 10 Gbit/s tributaries from 1528.6 nm to 1537.7 nm and the reference back-to-back (b2b) case extracted at 1557 nm.

wavelengths with ∼1.1 nm spacing. As expected the idler power spectrum has a Gaussian shaped envelope due to the Gaussian shape of the dispersed pump pulses. Nine different 10 Gbit/s tributaries from 1528.6 nm to 1537.7 nm were extracted using the 0.3-nm OBPF as shown in Fig. 5.9(b). The corresponding BER curves are shown in Fig. 5.9(c). The performance is error-free (BER=$10^{-9}$) for all channels, with a penalty of <1.6 dB compared to the 10 Gbit/s back-to-back (b2b) reference, extracted at the MZM output using the same 0.3-nm OBPF centered at 1557 nm. Only the 1528.6 nm tributary exhibits a larger penalty of 3.0 dB, attributed to a 10-dB lower conversion efficiency compared to the central tributaries.

### 5.4.3 640 GBd case

The OTDM-to-WDM conversion scheme was successfully performed also on a 640-GBd RZ-OOK OTDM system. The experimental setup is the same as the one shown in Fig. 5.8. The average input powers into the PM-HNLF were 24 dBm for the pump and –2.5 dBm for

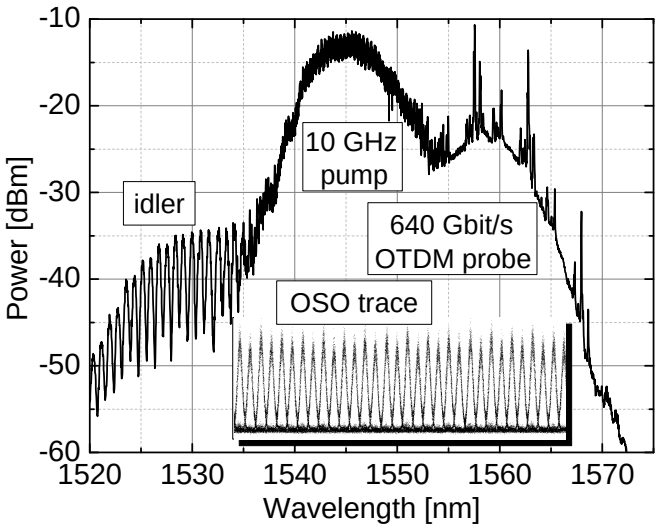


**Figure 5.10:** Spectrum at the output of the PM-HNLF, for 100 GHz spacing of the idler channels. Inset: Optical sampling oscilloscope (OSO) trace of the 640 Gbit/s original data signal.

the data signal. Before being dispersed, the FWHM of the transform limited pulses were: 600 fs for the 640-Gbit/s data signal, and 490 fs for the 10-GHz pump. Figure 5.10 shows the output spectrum of the PM-HNLF, where a tributary channel spacing of 100 GHz is achieved. The idler signal contains 19 tributaries mapped to different wavelengths in the range 1520–1535 nm. In this case the 640 Gbit/s OTDM data and 10 GHz pump were dispersed in 15- and 36-m DCF (Fig. 5.11(a)). As it can be noticed the simulated result shown in Fig. 5.4 is similar to the measured one in Fig. 5.11(a), where in both cases the resulting DWDM channel-spacing is 100 GHz. The only difference is the DCF lengths used to disperse the data and linearly chirp the pump. This is related to the dispersion of the various extra optical components present in the setup and to the different pieces of DCF fibers, with presumably different characteristics, used in the experiment. It is possible to increase the spectral compression rate, by increasing the amount of DCF used to disperse pump and data. This was seen in Section 5.3 and it is confirmed in Fig. 5.11(b). In this case data and pump were dispersed respectively in 23- and 48-m DCF, resulting in 0.55 nm (69 GHz) channel spacing of the converted tributaries.

It should be noted that the wavelength positions of the individual DWDM channels are shifted when changing the relative timing between pump and OTDM signal at the input to the FWM medium, but the envelope of the DWDM spectrum is unchanged. By changing the time delay between pump and data it is possible to adjust the idler shown in Fig. 5.11(a) to the wavelength grid for 100-GHz DWDM as specified in [127]. Smaller channel spacing is possible, e.g., for 50 GHz systems, but in this case a narrower OBPF is required in order to select the desired tributary channel. The eight tributaries from 1527.8- to 1533.6-nm were extracted by tuning the 0.3-nm OBPF, whose transfer function is shown in Fig. 5.11(a). The resulting spectra are shown in Fig. 5.12 and the corresponding BER curves in Fig. 5.13. For the best tributary the performance is error-free with penalty <2.5 dB compared to the 10 Gbit/s b2b reference at 1557 nm, extracted the same way as in the 320-Gbit/s case. As it can be seen, the tributaries centered at the longer wavelengths have a worse sensitivity. This is attributed to the closer presence of the pump spectrum. To verify the integrity of the entire 640 Gbit/s OTDM signal, each tributary is extracted by keeping the 0.3-nm OBPF fixed at 1529.5 nm

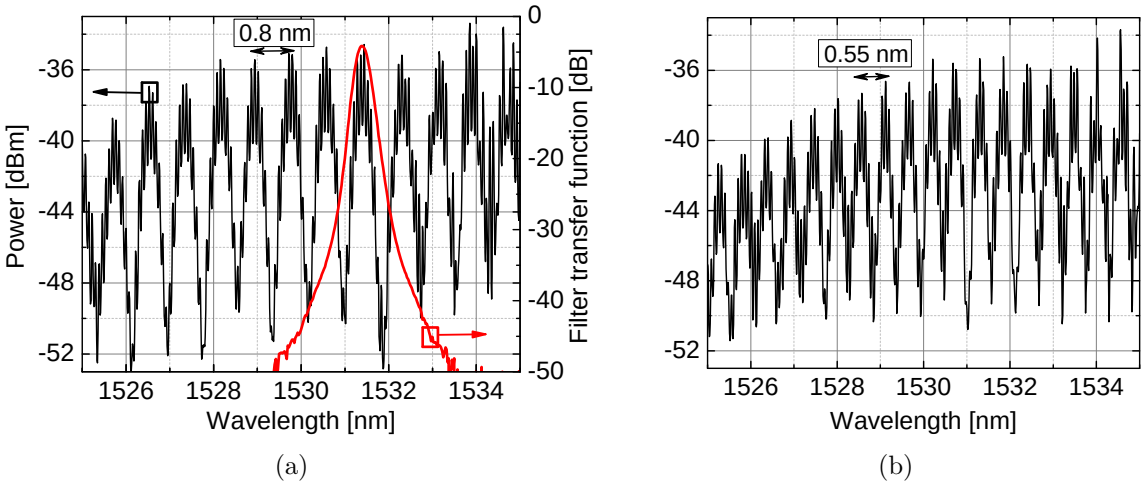


(a) (b)

**Figure 5.11:** Idler spectra (at the output of the PM-HNLF) when the 640 Gbit/s OTDM data and the 10 GHz pump are dispersed respectively in: (a) 15- and 36-m DCF, and (b) 23- and 48-m DCF (resolution 0.05 nm). (a) also shows the transfer function of the 0.3-nm OBPF.

and by tuning the time delay ($\Delta t$) to extract each tributary. All 64 tributaries have error-free performance with a sensitivity variation of 3.2 dB as shown in Fig. 5.13. Temperature fluctuations in the fibers before combination of the pump and OTDM signals caused slight variations in their relative timing, but these shifts were continuously compensated by small manual readjustments of the variable time-delay $\Delta t$ shown in Fig. 5.8. Similarly, temperature fluctuations in the fibre-based OMUX stages resulted in small temporal variations of the OTDM tributary spacing, which converted into small DWDM channel spacing variations.

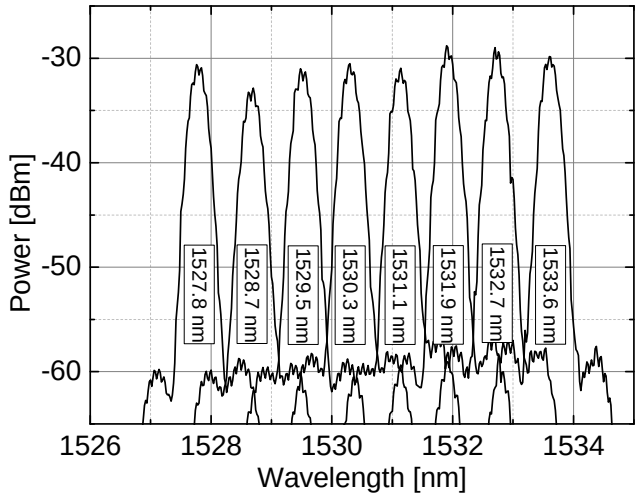


**Figure 5.12:** Spectra of the 10 Gbit/s tributaries extracted at different wavelengths by using the 0.3-nm OBPF, whose transfer function is shown in Fig. 5.11(a).

Finally, it can be noticed that due to the narrow channel spacing and optical window used, DWDM systems require well controlled, cooled lasers to prohibit drift outside of a given DWDM optical channel. A reliable grid at 25 GHz would require the network lasers to maintain accuracy over time and environmental drifts of at least ±0.02 nm[3] or even

[3]In the context of time-to-frequency mapping of a 640-GBd OTDM signal to a 25-GHz grid, a frequency

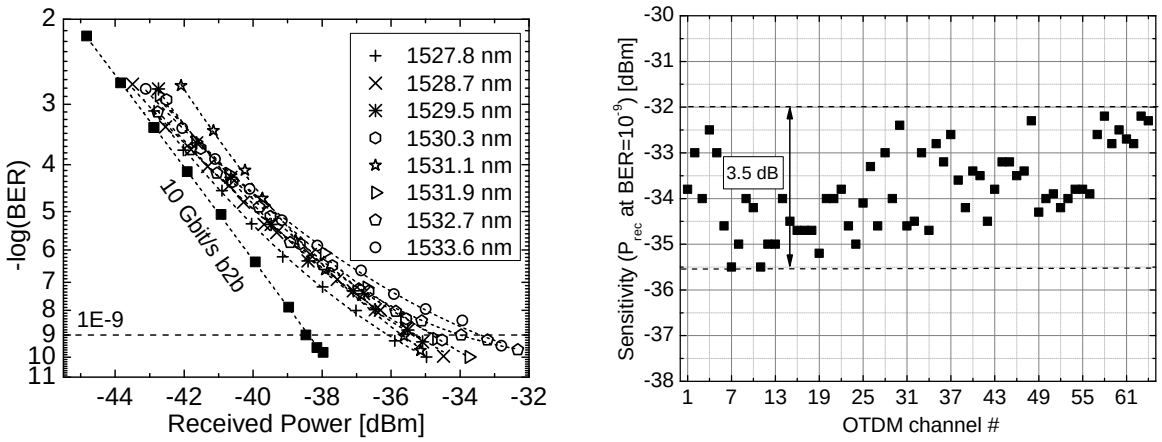


(a) (b)

**Figure 5.13:** (a) BER measurement for the 10 Gbit/s tributaries, resulted from OTDM-to-DWDM conversion, extracted at different wavelengths. (b) Sensitivity of all the 64 OTDM channels, measured by scanning the OTDM signal in the time domain and keeping the 0.3-nm OBPF fixed at 1529.5 nm.

better. Such lasers are not easily available. But with the time-domain OFT technique implementation of serial-to-parallel conversion, what is required is the right compression, and the stability of the OTDM signal against time drifts. Once these requirements are achieved then the right wavelength allocation at the demultiplexer can be obtained by just changing the relative time delay between pump and OTDM signal, possibly controlled by a feedback mechanism.

### 5.4.4 System performance in non-optimum data dispersion

In case of single-channel demultiplexing via FWM (Section 4.2), NOLM (Section 4.3), etc., if the dispersion of the control and/or data signal has not been fully optimized then the control pulse will switch energy from the neighboring OTDM channels, which results in inter-channel crosstalk. A similar phenomenon happens also in the time-to-frequency OFT case. If the data accumulated dispersion ($D_{acc}$) and pump linear-chirp ($C$) are not optimized then the condition $C = 1/D_{acc}$ does not hold any longer, resulting in a distorted time-to-frequency mapping.

In order to investigate the sensitivity of the system in case of non-optimal dispersion conditions, the pump dispersion is kept at 36-m DCF and the data dispersion is changed by adding some extra lengths of single-mode fiber (SMF) or DCF to the optimal value of 15-m DCF (640 Gbit/s case). This was done by adding respectively 5-, 10- or 12-m SMF, or 1- or 2-m DCF. This would correspond to lowering the data dispersion by 4.7-, 9.5- or 11.4-% in case of additional SMF[4] or increasing it by 6.6- or 13.3-% in case of additional DCF. As it can be seen from Fig. 5.14, the WDM nature of the idler signal disappears when the dispersion imbalance increases. The deterioration of the system's performance is also confirmed in Fig. 5.15. Here are shown the BER curves of the extracted 10 Gbit/s tributaries using the 0.3-nm OBPF centered at 1529.5 nm. As it can be seen, the tolerance

stability of ±0.02 nm would require a timing jitter of the OTDM system of ±160 fs.

[4] 7 m SMF are supposed to compensate for 1 m DCF.

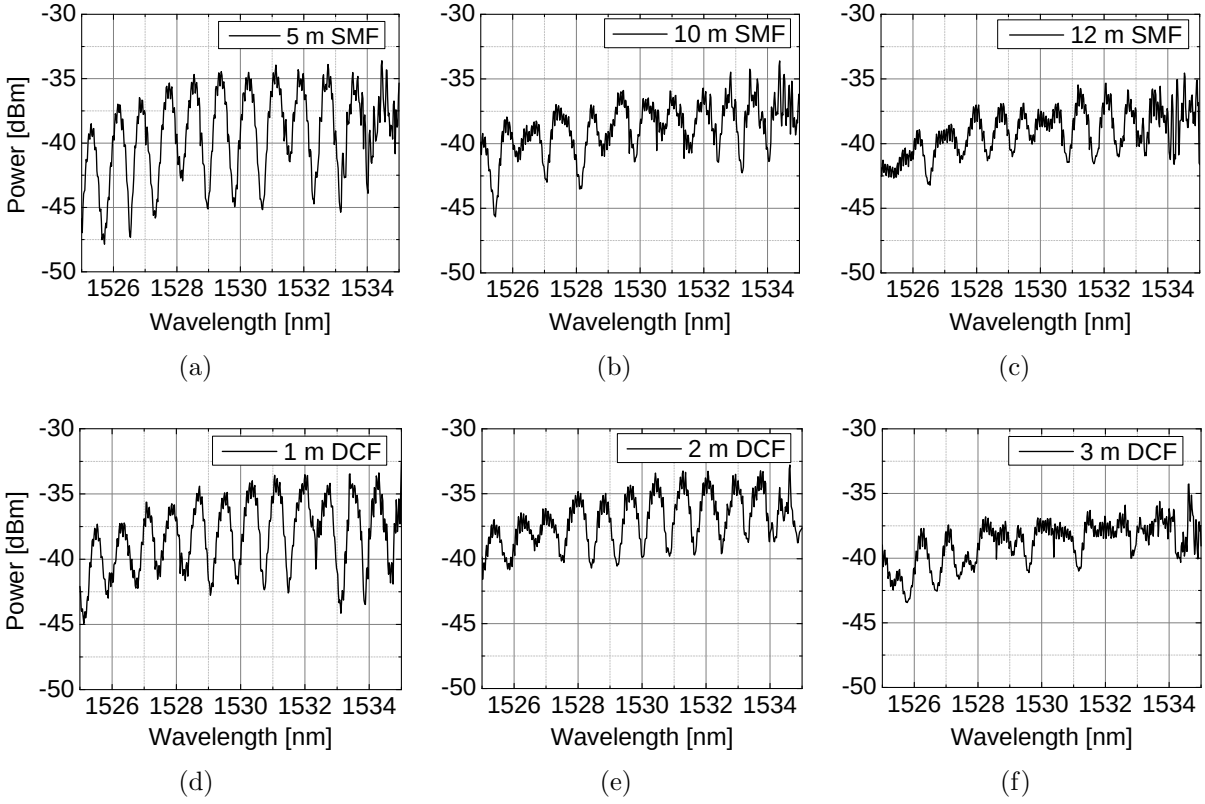


**Figure 5.14:** Idler spectra in case the dispersion of the 640-Gbit/s signal is changed from the optimal value of 15-m DCF, by adding: 5-, 10- or 12-m SMF (a), (b) and (c) or 1-, 2- or 3-m DCF (d), (e) and (f). The pump dispersion was kept at 36-m DCF.

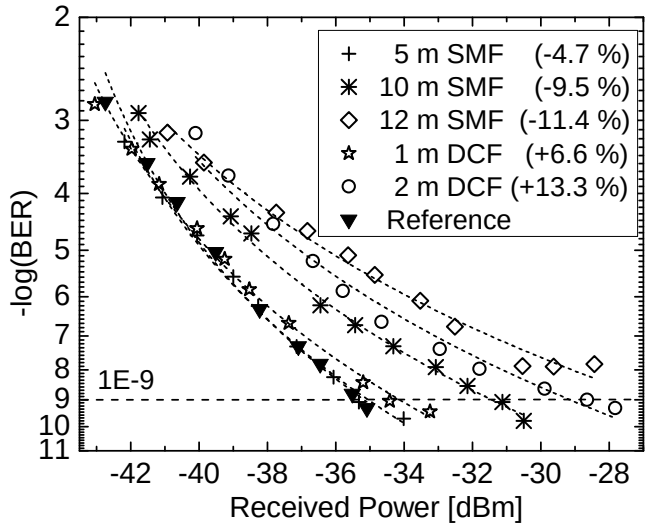


**Figure 5.15:** BER in case the 640-Gbit/s signal dispersion is changed from the optimal (*Reference* curve) value of 15-m DCF. The deviation is expressed both in terms of dispersion percentage variation and amount and type of fiber added. The pump dispersion was kept at 36-m DCF.

of the system to extra dispersion is in the order of ±1 m DCF ($\sim \pm 7\%$). As the dispersion imbalance increases the BER curve starts having an error-floor (12-m SMF trace) resulting from cross-talk interference between neighboring channels.

## 5.5 640-GBd RZ-QPSK and 16-QAM OTDM mapped to 50-GHz DWDM

The implementation of time-to-frequency mapping via FWM can also be used for serial-to-parallel conversion of an OTDM signal having tributaries with advanced-modulation formats, such as $n$-phase-shift keying ($n$-PSK), $n$-QAM etc. This is related to: 1) the FWM process is transparent to the data modulation format and 2) the OFT technique preserves the amplitude and phase information of each converted waveform (Section 3.4). Advanced modulation formats need a coherent receiver in order to be detected [132] (see also App.1). However, as in the OOK case, due to the high speed of our OTDM data, first the tributaries have to be demultiplexed and then they can be demodulated in the coherent receiver. By applying the time-to-frequency OFT technique, once the OTDM tributaries are mapped into the frequency domain, and are individually selected via passive filtering they can be demodulated in a heterodyne coherent receiver using a continuous-wave (CW) laser as local oscillator (LO) [133]. For more information on the time-domain implementation of the coherent receiver please refer to App.1. In Chapter 7 we will see a different technique based on a coherent receiver implemented via a pulsed local oscillator, which performs simultaneously demultiplexing and demodulation of the desired OTDM tributary.

In the following section we demonstrate the utilization of the OFT technique for single step conversion of several 10-GBd tributaries of a 64×10-GBd OTDM signal encoded with complex modulation formats onto a 50-GHz (0.4 nm) DWDM grid. The data signal is generated with RZ-QPSK modulation, and RZ 16-QAM. Again, the time-to-frequency OFT is performed via dispersion followed by phase modulation using linearly chirped pump pulses in a FWM process. The time-to-frequency conversion results in spectral compression which maps the different OTDM tributaries into separate DWDM channels and preserves the phase and amplitude information encoded on them. Differently from the previous section, the resulting 10-GBd DWDM channels are demodulated in a coherent heterodyne receiver using a CW laser as local oscillator (LO). The resulting DWDM channels are found to be error-free assuming 7 % hard-decision forward error correction (FEC) coding [134].

### 5.5.1 Experimental setup

As mentioned in the previous sections, by changing the data accumulated dispersion $D_s$ and pump linear chirp $C_p$ it is possible to control the amount of spectral compression that can be achieved at the transformed signal. Here, the parameters are chosen such that a 640 GBd tributary spacing of $\Delta\tau$=1.56 ps is mapped into a DWDM spacing of $\Delta f$=50 GHz (0.4 nm).

Figure 5.16 shows the experimental setup. It is composed of the OTDM transmitter, the OFT block for serial-to-parallel conversion and the coherent receiver. At the transmitter side, an ERGO-PGL produces a train of pulses having 1.2-ps FWHM, 10 GHz repetition rate and center wavelength at 1550 nm. The pulses are amplified to 21.5 dBm and injected into a 250-m long DF-HNLF with attenuation $\alpha$=0.78 dB/km, dispersion D=–0.49 ps/(nm·km), slope S=0.0061 ps/(nm$^2$·km) at 1550 nm and nonlinear coefficient $\gamma$=10 (W·km)$^{-1}$. The optical spectrum at the output of the DF-HNLF is broadened due to SPM, resulting in a wide supercontinuum exceeding 40 nm. The broad spectrum is used to generate both data and pump for the FWM process. The pump spectrum is carved out of the supercontinuum by a 10-nm wide flat-top OBPF centered at 1546 nm. To obtain data modulation the

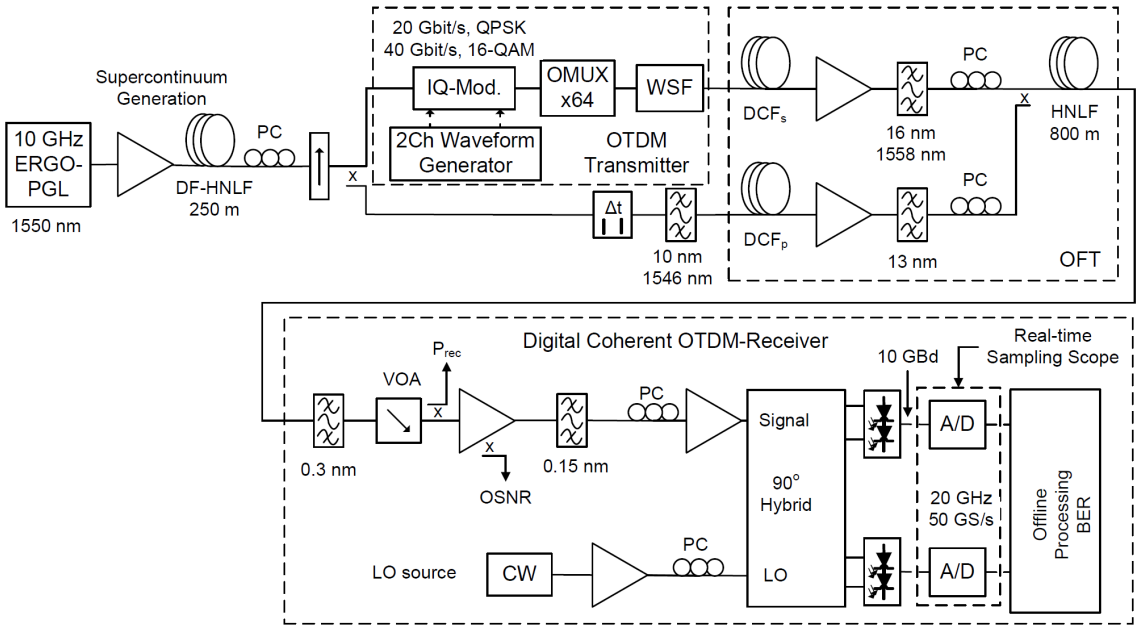


**Figure 5.16:** Experimental setup for OTDM-to-WDM conversion of 640-GBd OTDM systems with advanced modulation formats. IQ-Mod: in-phase quadrature modulator; WSF: wave-shaping filter; CW: continuous wave; LO: local oscillator; OSNR: optical signal-to-noise ratio; A/D: analog-to-digital converter.

supercontinuum is injected in an in-phase and quadrature modulator (IQ-Mod.). The IQ modulator is driven by a two-channel arbitrary waveform generator which is programmed to generate QPSK or 16-QAM modulation (De Bruijn sequence of $2^{15}$ before symbol mapping) resulting in respectively a 20- or 40-Gbit/s data signal. This signal is time interleaved up to 640 GBd in a fiber-based delay line multiplexer (OMUX). At the output of the OMUX stage, the supercontinuum is filtered by a wave-shaping filter (WSF), Finisar Waveshaper 4000S, in order to generate Gaussian-like pulses of 600-fs duration centered at 1558 nm. The WSF is based on a programmable liquid crystal on silicon (LCoS) grid that can control both the amplitude and phase of an input waveform as a function of frequency. The signal is then launched into the time-to-frequency OFT block.

The data path of the OFT block consists of dispersion compensating fiber (DCF$_s$ in Fig. 5.16) used to compensate 244-m SMF. DCF$_p$ (Fig. 5.16), equivalent to 501-m SMF, is used to linearly chirp the pump pulses. It has to be noticed that the total dispersion of both data and pump before entering the nonlinear medium for FWM does not depend only on the used DCFs, but also on the various other components in the setup through which the signals propagate. For this reason the WSF, is not only used for amplitude filtering, but also to fine tune the amount of dispersion on the OTDM signal in order to comply with the OFT requirements. The phase profile of the WSF was optimized based on the DWDM spectrum after FWM. Once dispersed, data and pump are injected into 800-m HNLF for the FWM process. The used HNLF has D=0.18 ps/(nm·km), S=0.018 ps/(nm$^2$·km) at 1550 nm and $\gamma$=10 (W·km)$^{-1}$. At the output of the HNLF a tunable 0.3-nm OBPF is used to select the desired DWDM channel from the FWM idler. This 10 GBd channel is sent to the coherent receiver for demodulation and BER characterization.

The data path of the pre-amplified receiver consists of a variable optical attenuator (VOA) to vary the received signal power and OSNR, two erbium-doped fiber amplifiers (EDFA), a 90°-hybrid, two balanced photo-detectors (BPD), two analog-to-digital converters (A/D, 50-

GS/s real-time sampling oscilloscope with 20 GHz bandwidth) and a computer for offline processing and BER measurement. A tunable CW laser is used as LO. The optical input powers into the 90°-hybrid are 12 dBm for the data signal and 14 dBm for the LO. The data is recovered by a conventional digital signal processing block comprising resampling, relative carrier frequency offset compensation (data signal with respect to LO) and blind adaptive equalization. After pre-convergence of the equalizer using the constant modulus algorithm, it was switched to a decision-directed least-mean square filter error criterion.

### 5.5.2 Results and discussions

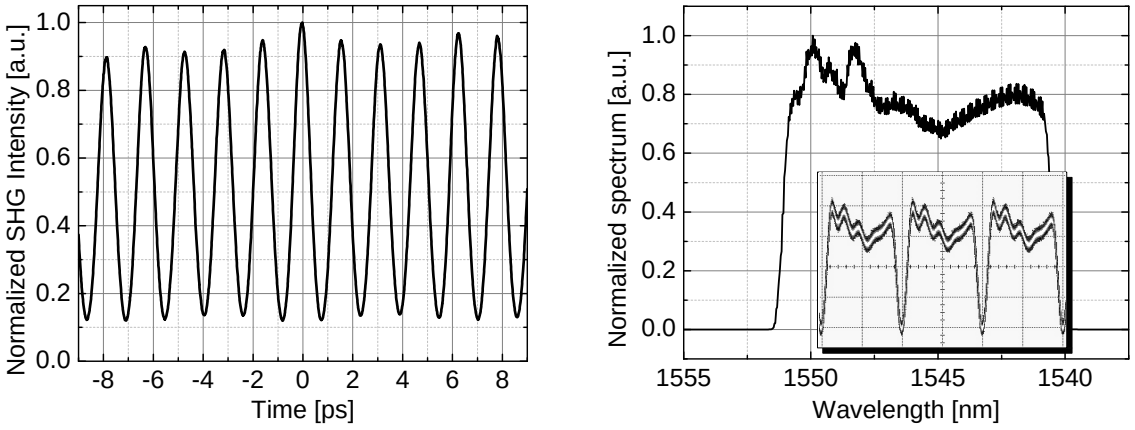


(a) (b)

**Figure 5.17:** (a) Autocorrelation trace of the 640-GBd RZ-QPSK OTDM signal before entering the time-to-frequency OFT block. (b) Frequency-to-time mapping of the pump spectrum in the time domain after propagation in $DCF_p$.

Figure 5.17(a) shows the autocorrelation trace of the 640-GBd RZ-QPSK signal at the input of the OFT system, when the data pulses are transform limited. Figure 5.17(b) shows the normalized pump spectrum in a linear scale. The transform limited pulse corresponding to this spectrum has a sinc-like shape. However, as seen in Chapter 4 (Section 4.2), this pulse is transformed into a flat-top one due to its propagation in a dispersive medium such as the DCF used for linearly chirping the pump. Due to frequency-to-time mapping, the pump pulse intensity, at the input of the HNLF used for the FWM process, will resemble the shape of its spectral envelope. This can be seen in the inset of Fig. 5.17(b), where is shown the trace of an electrical oscilloscope consisting of three pump pulses at 10 GHz repetition rate, measured at the input of the HNLF. As it can be seen the pulse resembles the shape of the pump spectrum. Unfortunately, as the spectrum is carved out of a supercontinuum, its shape is not as flat as desired. In the next section we will see that the utilization of a second WSF (absent at the time of this experiment), can help to improve the spectral shape and hence the resulting pulse quality, and idler equalization.
Figure 5.18(a), 5.18(b)and 5.18(c) show the spectra at the output of the HNLF in case of 160-, 320- and 640-GBd RZ-QPSK OTDM data signals. A zoom-in on the idler spectrum for the 320- and 640-GBd cases is shown in Fig. 5.18(d). More than 17 tributaries are time-to-frequency mapped in case of 320-GBd OTDM signal, with a grid spacing of 100 GHz, and more than 35 tributaries are mapped in case of 640 GBd, with a grid spacing of 50 GHz

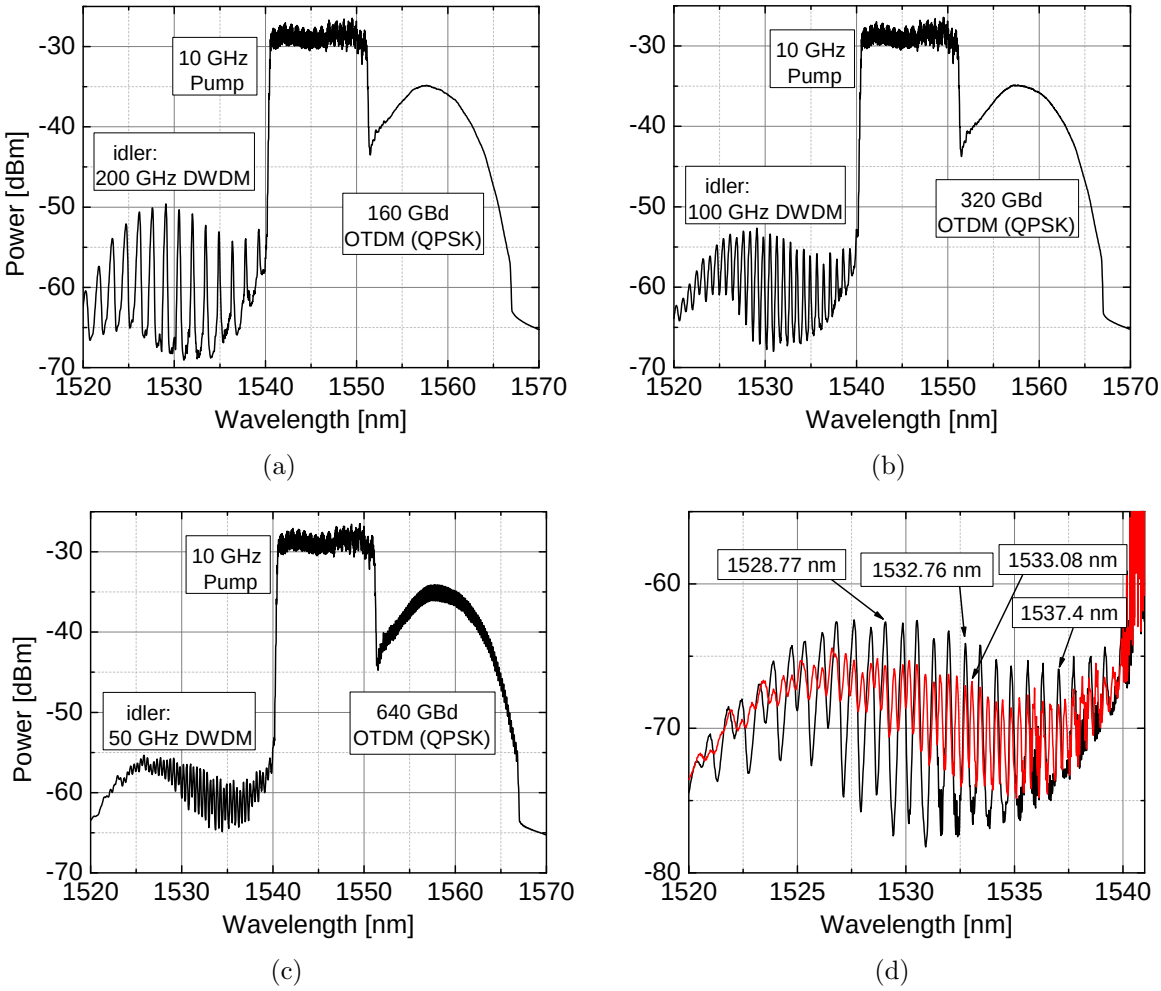


**Figure 5.18:** (a), (b) and (c) spectra at HNLF output in case of 160-, 320-, and 640-GBd RZ-QPSK. (d) Zoom-in on the DWDM idler for both 320- and 640-GBd.

(range 1527.5–1540 nm).

Figure 5.19(a)) shows the BER vs. OSNR curve of the 10-GBd converted tributary centered at 1533.5 nm. The performance is compared with three back-to-back (b2b) curves measured for a 10-GBd RZ and a 10-GBd non-return to zero (NRZ) QPSK signal centered at the selected idler channel and data-signal wavelengths (1558 nm). The three b2b curves were measured in order to confirm the wavelength independence of the receiver and the modulation quality of the RZ pulses. As it can be seen, there is negligible penalty in case of 160- and 320-GBd OTDM signals. However, the performance of the system is worse at 640-GBd. This is related to inter-symbol interference caused by the walk-off in the FWM-HNLF between pump and data. This can be seen also in the width of the converted idler spectrum in Fig. 5.18(d). Due to walk-off the spectra are broader than expected.

To verify the integrity of the entire OTDM signal, each tributary is extracted by keeping the 0.3-nm OBPF fixed to 1533.5 nm and by changing the time delay $\Delta t$ (Fig. 5.16) between pump and OTDM tributaries. This results in a frequency scan of the tributaries at the FWM idler. Figure 5.19(b) shows the measured OSNR in order to reach a BER=$10^{-3}$ for all the OTDM tributaries in case of 160-, 320- and 640-GBd RZ-QPSK OTDM. As it can be seen the required OSNR and its variation per channel is higher in case of 640-GBd. Figure 5.19(c)

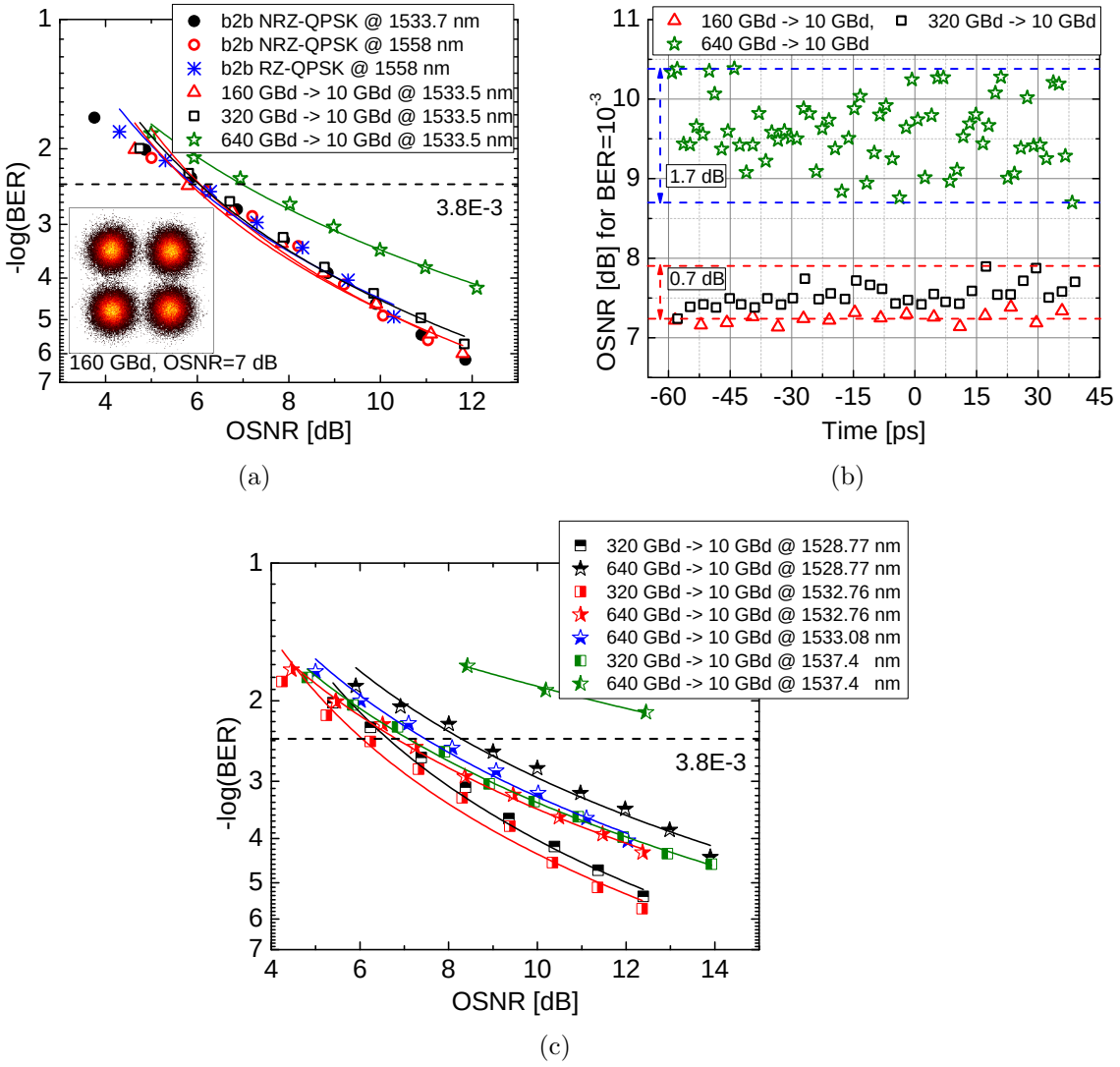


**Figure 5.19:** (a) BER curves for one converted 10-GBd tributary at 1533.5 nm in case of 160-, 320- and 640-GBd RZ-QPSK OTDM. Inset: Constellation for one 10-GBd channel out of a converted 160-GBd OTDM QPSK signal at 7-dB received OSNR (BER=$10^{-3}$). (b) Time scan of all tributaries with required OSNR for BER=$10^{-3}$ (c) BER performance for various DWDM channels.

shows the BER performance for different DWDM channels measured by keeping $\Delta t$ fixed and by tuning the 0.3-nm OBPF and the wavelength of the LO. Compared to the central DWDM channels, the ones closer to the pump have a worse BER performance due to interference with residual pump light.

Finally, the time-to-frequency OFT technique is tested also in case of 16-QAM data modulation. Figure 5.20 shows the BER curve for the converted 10-GBd tributary centered at 1530.4 nm in case of 160- and 320-GBd RZ 16-QAM OTDM. The curves are compared to the back-to-back cases for 10-GBd RZ and NRZ 16-QAM (at the data and idler wavelengths). Both BER curves are below the $3.8{\cdot}10^{-3}$ threshold value for 7% overhead FEC. This confirms the fact that the time-to-frequency OFT technique preserves the phase and amplitude information encoded on the converted OTDM tributaries. At 640-GBd the system did not comply with FEC specifications. This is related to the walk-off between pump and data signal, due to the HNLF length used for the FWM process. An improved performance

is expected in case of an HNLF with lower or absent walk-off.

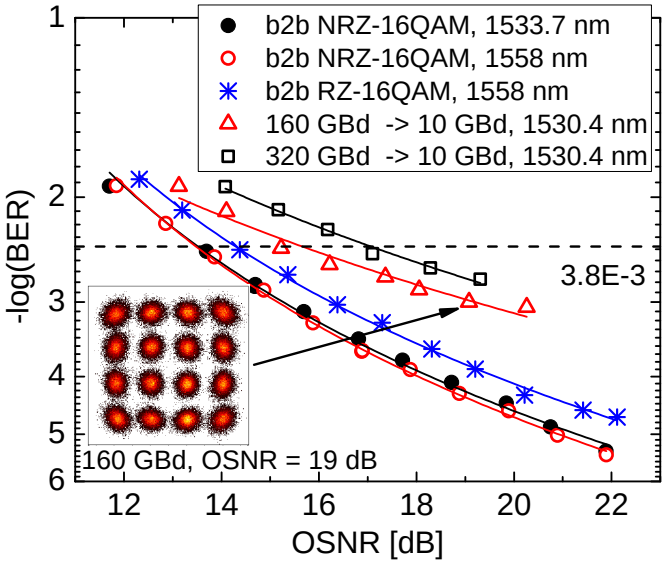


**Figure 5.20:** BER curves for the converted 10-GBd tributary at 1530.4 nm in case of 160- and 320-GBd RZ 16-QAM OTDM. Inset: Constellation for one 10-GBd channel out of a converted 160-GBd OTDM 16-QAM signal at 19-dB received OSNR (BER=$10^{-3}$).

## 5.6 640-GBd RZ-OOK and DPSK OTDM mapped to 25-GHz DWDM

A numerical analysis in Section 5.3 showed that it is possible to use a maximum of two time-to-frequency OFT blocks in order to convert and extract all the OTDM tributaries independently on the signal rate and data modulation. This is confirmed experimentally, in the following section. It is demonstrated that by using enough compression and a single OFT block it is possible to extract, error-free and with low penalty, more than half of the OTDM tributaries of a 640-GBd OTDM signal. It is also shown that this can be achieved not only in HNLF, as demonstrated until now, but also in more compact nonlinear devices such as silicon nanowires [37, 135, 136]. Lately, nonlinear silicon photonics is attracting considerable interest due to its complementary metal-oxide-semiconductor (CMOS) compatibility, integration potential with electronics, low cost and broad operation bandwidth [137, 138]

The experimental results shown below are taken from [C-5] and [J-4], in which a more detailed analysis can be found.

### 5.6.1 Experimental Setup

Figure 5.21 shows the experimental setup used for converting a 640-GBd OTDM signal into a 25-GHz spaced DWDM signal. The pump and OTDM data are obtained from two different 10-GHz ERGO-PGLs emitting 1.5-ps FWHM pulses at 1557- and 1542-nm, respectively. In both cases, the ERGO-PGLs output pulses undergo spectral broadening via SPM in DF-HNLFs with normal dispersion.

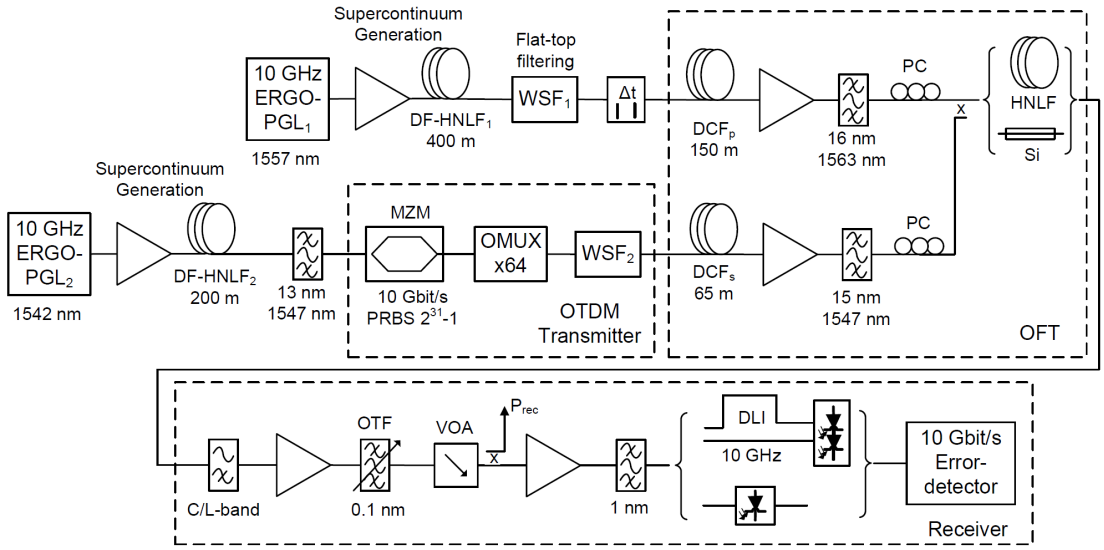


**Figure 5.21:** Experimental setup for OTDM-to-WDM conversion, performed in HNLF or silicon nanowire, of 640-GBd RZ-OOK and DPSK OTDM signals.

To obtain the pump pulses, the output spectrum of DF-HNLF$_1$ is filtered using a programable WSF (Finisar Waveshaper 4000S). The WSF$_1$ is programmed to generate a $5^{th}$ order super-Gaussian spectrum of 5.3-nm 3-dB bandwidth centered at 1563 nm, as shown in Fig. 5.22(a). To obtain the data signal, the output spectrum of DF-HNLF$_2$ is pre-filtered at 1547 nm with a 13-nm OBPF. The resulting pulses are data-modulated with a 10-Gbit/s $2^{31}$-1 PRBS pattern in a push-pull MZM to obtain either OOK modulation (Section 5.6.2) or differential phase-shift keying (DPSK) format (Section 5.6.3). The 10-Gbit/s pulses are subsequently multiplexed to 640 Gbit/s single polarization OTDM using passive fiber-based delay-line multiplexer stages (OMUX). A second wave-shaping filter (WSF$_2$) is used to shape the data spectrum into a Gaussian one with 6.1-nm 3-dB bandwidth centered at 1547 nm. The resulting gaussian pulses are nearly transform-limited with 615-fs FWHM.

After generation, the pump and data signal enter the time-to-frequency OFT block for OTDM-to-DWDM conversion. As part of the OFT process the data pulses are dispersed in 65-m DCF (OFT block in Fig. 5.21). As mentioned in Section 5.3 it is desirable to have a flat pump pulse profile in order to equalize the DWDM FWM-idler resulting from the OFT process. In this experiment, the pump pulses at the WSF$_1$ output are propagated through 150-m DCF (OFT block, Fig. 5.21), resulting in a linearly chirped flat-top waveform of ∼83-ps FWHM. Figure 5.22(b) and 5.22(c) show the pulse shape traces measured respectively with an optical sampling oscilloscope (OSO) and electrical sampling oscilloscope (after 50-GHz photodetector). It has to be noticed that the total dispersion of both data and pump, before entering the nonlinear medium for FWM purposes, does not depend only on the amount of used DCFs in the OFT block, but also on the various other components in the setup through which the signals propagate. For this reason both WSFs, are not only used for amplitude filtering, but also to fine tune the amount of dispersion on both pump and signal. The phase profile of the WSFs was optimized based on the DWDM spectrum after FWM. After propagation in the dispersive media (DCF$_s$ and DCF$_p$), both pump and data signals are amplified, filtered, and combined using a 3 dB coupler before undergoing FWM in either the HNLF or silicon nanowire. In both cases the average input power to the nonlinear medium was 22.0 dBm for the pump and 12.6 dBm for the OTDM signal. Because

of the pump and probe wavelength centering the generated idler results in the L-band.

After the FWM process, the DWDM idler is isolated from the pump and signal using a C/L-band splitter and is amplified in an L-band EDFA. The individual DWDM channels are extracted using an optical tunable filter (OTF) (Santec, model OTF-350). The OTF filter transfer function, Fig. 5.23(b), has a 3-dB bandwidth of 0.14 nm. After filter extraction by the OTF, the BER performance of each DWDM channel is measured in a 10-Gbit/s pre-amplified receiver. In the case of DPSK, a 1-bit delay-line interferometer (DLI) and balanced photo-detectors (BPD) are employed. In the case of OOK, single-ended photo-detection is used. A 10 GHz synthesizer is used to synchronize the ERGO-PGLs, the PRBS pattern generator, and the receiver.

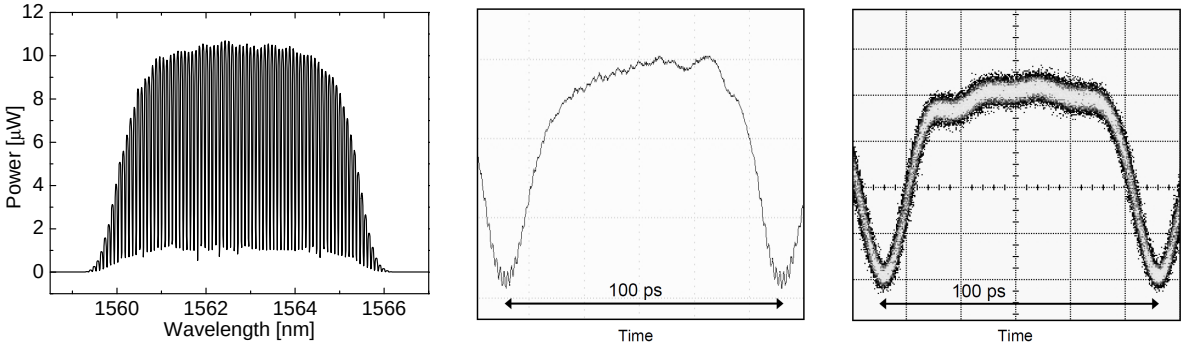


**Figure 5.22:** Characterization of the 10 GHz pump pulse: (a) Optical spectrum, res. 0.01 nm. Pump's temporal shape at input to the nonlinear medium measured using (b) optical oscilloscope and (c) electrical oscilloscope.

### 5.6.2 OFT in HNLF

Figure 5.23 shows the results for the conversion of 640 Gbit/s OTDM-OOK to a 25-GHz DWDM grid in an HNLF. The used fiber is 50-m long and has a non-linear coefficient $\gamma$=10 $(\mathrm{W{\cdot}km})^{-1}$, zero-dispersion wavelength at ∼1565 nm and dispersion slope of 0.02 $\mathrm{ps/(nm^2{\cdot}km)}$. The spectrum at the output of the HNLF (after FWM) is shown in Fig. 5.23(a). The FWM conversion efficiency is -24 dB. Fig. 5.23(b) shows a zoom-in on the DWDM spectrum, together with the transfer function of the OTF. A total of 43 consecutive channels extracted by tuning the OTF central wavelength have an error-free performance (BER$< 10^{-9}$). The BER curves of selected DWDM channels are shown in Fig. 5.23(c). Figure 5.23(d) shows the entire DWDM spectrum and the sensitivities (received power ($P_{rec}$) for BER=$10^{-9}$ ) of the 43 error-free channels. The 10 Gbit/s reference curve shown in Fig. 5.23(c) is measured on a 50% RZ-OOK signal, obtained from a 1579 nm CW laser followed by the 10 Gbit/s MZM and a 10 GHz Mach-Zehnder interferometer (MZI) pulse carver. As expected, the best performance is obtained for the central channels originating from OTDM tributaries fully overlapped by the flat-top pump pulse, while the performance deteriorates for channels towards the sides of the DWDM spectrum originating from tributaries crossing the tails of the pump pulse. The majority of the DWDM channels from ∼1575 nm to ∼1581 nm exhibit similar performance, which is attributed to the flat-top pump pulse allowing for a linear chirp and uniform conversion efficiency over a broad time-span of ∼83 ps. In particular, the 32

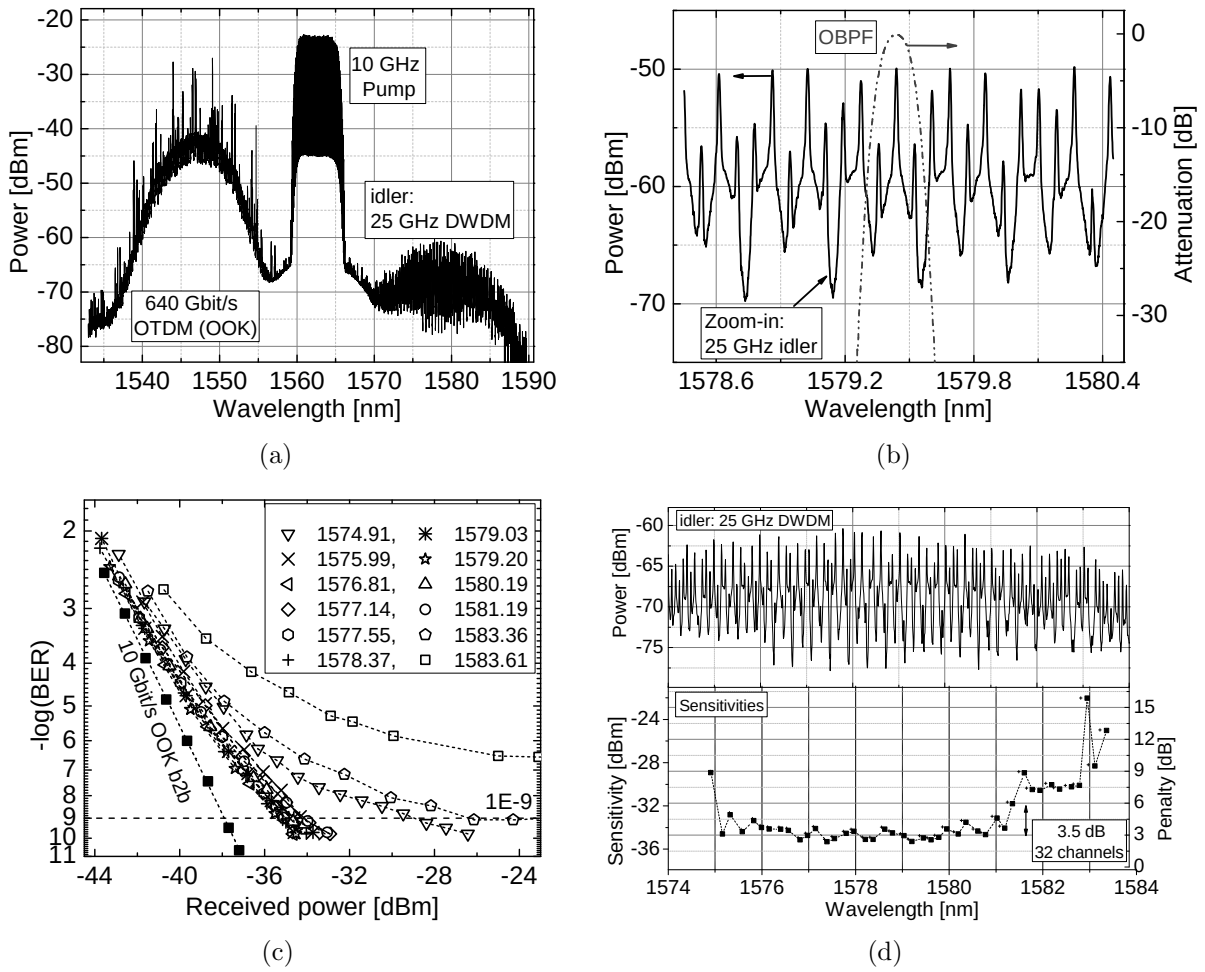


**Figure 5.23:** Results for HNLF case: (a) Output spectrum of HNLF, (b) zoom-in on idler DWDM spectrum with plot of OTF transfer function, res. 0.01 nm, (c) 10 Gbit/s OOK BER curves for selected DWDM channels, (d) DWDM spectrum (above) and sensitivity of each DWDM channel (required $P_{rec}$ for BER=$10^{-9}$) (below).

channels (half of all tributaries) ranging from 1575.2 nm to 1581.4 nm have power penalties ranging from 2.5 to 6 dB difference compared to the 10 Gbit/s reference. Figure 5.23(c) shows BER curves of various DWDM channels within this group. A large penalty is, instead, observed for the lateral channels, such as 1574.9 nm and 1583.36 nm (Fig. 5.23(c)), which is primarily attributed to the expected DWDM inter-channel cross-talk in this part of the DWDM spectrum. The BER curve (Fig. 5.23(c)) of even further channels (compared to the central wavelength of the idler), such as 1583.61 nm, exhibits an error floor above BER=$10^{-7}$.

As a final comments, it has to be noted that the pump pulse employed in this experiment still deviates from an ideal uniform flat-top shape with steep edges. By considering a flat FWM gain, a pump pulse closer to the ideal flat-top should result in a more uniform DWDM spectrum envelope (Section 5.3) and uniform BER performances compared to the results obtained in the present demonstration.

### 5.6.3 OFT in silicon nanowires

The same experiment described in the previous section can be performed in more compact nonlinear optical components such as in silicon nanowires. The setup is similar to Fig. 5.21 where the HNLF is substituted with the silicon nanowire, the data format is changed to DPSK and the 10 Gbit/s receiver is preceded by a delay-line interferometer of 1 bit delay. The rest of the components and power levels are unchanged.

Figure 5.24 shows a sketch of the silicon nanowire together with some scanning electron micrograph pictures. The device is a dispersion-engineered, 3.6-mm long silicon waveguide. The main waveguide section is ∼3-mm long and has a cross section of 450×24 nm$^2$ while the tapering sections are each ∼0.3 mm long and their width is inversely tapered from 450 to 20 nm. This enables coupling between the silicon waveguide and the larger polymer waveguide (SU8-2005) into which the whole silicon structure is embedded. The cross section (3.4×3.4 $\mu$m$^2$) of the polymer waveguide matches the tapered access fibers, reducing the fiber coupling loss to 1.5-dB per facet. The device has a silicon-on-insulator (SOI) structure, with the silicon waveguide placed on a $SiO_2$/Si substrate. The measured propagation loss is 4.3 dB/cm and the fiber-to-fiber loss of the device is 4.5 dB. A FWM conversion bandwidth of more than 12 THz has been measured for this nanowire when using a CW pump in the C-band. The thresholds for significant two-photon absorption (TPA) and free carrier absorption occur at an input peak power of ∼39 dBm and ∼45 dBm, respectively. Below these power levels, the ultra-fast Kerr effect dominates and the silicon nanowire can be employed for FWM-based signal processing without significant patterning effects influencing the high operation bandwidth [137].

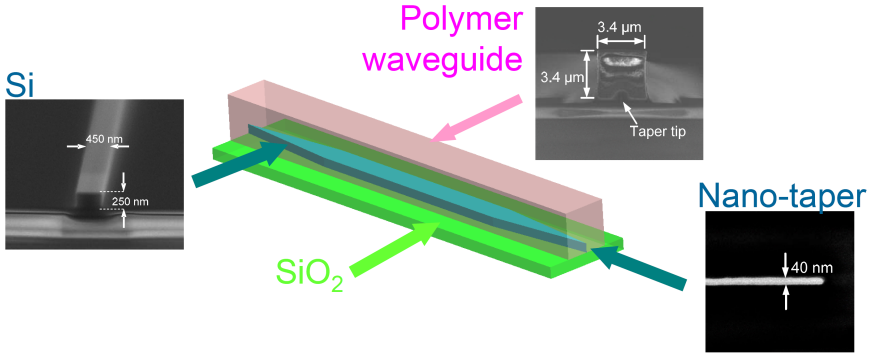


**Figure 5.24:** Schematic drawing of the nano-engineered silicon nanowire and scanning electron micrograph pictures of the sample.

Figure 5.25 shows the experimental result of OTDM-to-DWDM conversion in case of silicon nanowire. The resulting spectra from the FWM process are shown in Fig. 5.25(a). The conversion efficiency of the FWM process is –32 dB, which is lower compared to the HNLF case (Fig. 5.23(a)). The resulting lower OSNR in the DWDM signal and the lower OSNR requirement for DPSK forced us to use DPSK modulation instead of OOK as used in the HNLF case. For BER evaluation, the DWDM channels are held fixed by maintaining a constant relative pump-OTDM timing, and each DWDM channel is extracted by tuning the OTF. Figure 5.25(b) shows the BER curves of selected DWDM channels. The 10 Gbit/s reference curve in Fig. 5.25(b) is measured on a 50% RZ-DPSK signal, obtained from a 1579 nm CW laser followed by the 10 Gbit/s MZM and a 10 GHz MZI pulse carver. A total of 42 consecutive DWDM channels have a BER performance below the FEC limit of $3.8{\cdot}10^{-3}$.

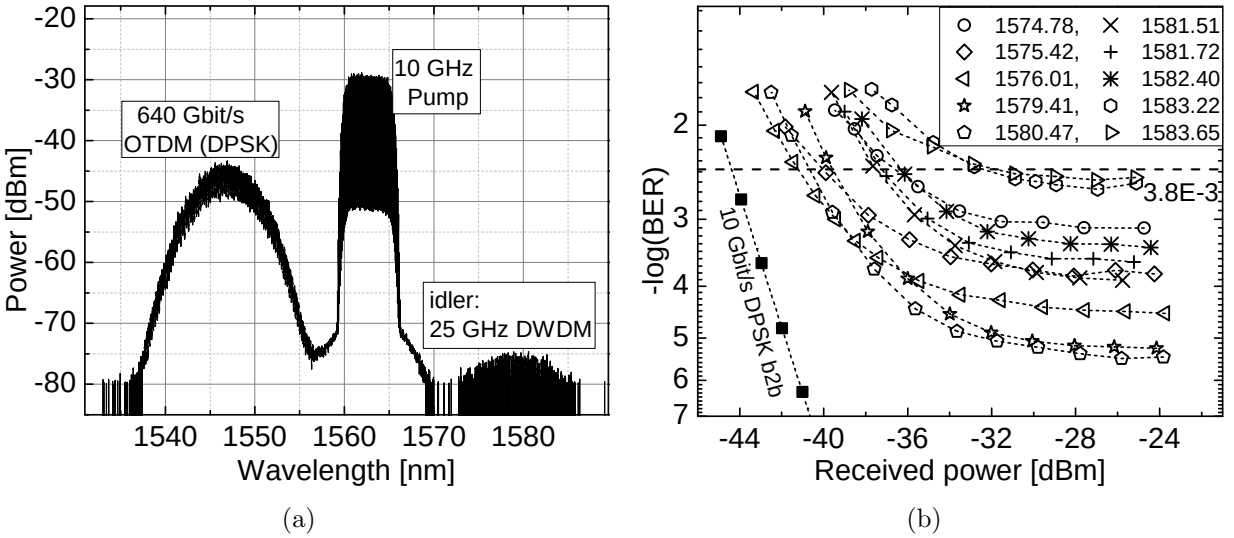


**Figure 5.25:** Results for silicon nanowire: (a) Output spectrum of silicon nanowire, (b) 10 Gbit/s DPSK BER curves for selected DWDM channels.

As expected, the best performance is obtained for the center channels originating from OTDM tributaries fully overlapped by the flat-top pump pulse, while the performance deteriorates for channels towards the sides of the DWDM spectrum originating from tributaries crossing the tails of the pump pulse. For example, the channel centered at 1579.41 nm is among the best performing ones, with a BER below $10^{-5}$. On the other hand, the edge DWDM channels do not achieve a BER below the FEC limit. The observed error-floor for all channels is attributed to an OSNR limitation resulting from the low conversion efficiency of the FWM process. This limits the BER value to $10^{-5}$ at the best. However, we expect that significantly better results can be obtained using silicon waveguides with lower propagation loss and therefore higher conversion efficiency [137]. Indeed, the propagation loss of 4.3 dB of our sample is relatively high compared to the state-of-the-art loss of $\sim$1 dB [135]. The use of such silicon nanowires are expected to yield significantly improved BER performance for this OTDM-to-DWDM conversion technique.

## 5.7 Summary

This chapter described a novel scheme for serial (OTDM) to parallel (DWDM) signal conversion, base on the OFT technique. The conversion process is based on time-to-frequency mapping implemented by a FWM process between the dispersed OTDM data and linearly chirped pump pulses. The OFT implementation results in spectral compression enabling the OTDM tributaries to be converted directly onto a DWDM grid. The serial-to-parallel conversion was successfully demonstrated for up to 640-GBd OTDM signals, reaching DWDM grids ranging from 100 GHz down to 25 GHz spacing. The converted DWDM spectra were compliant with ITU-T specifications in terms of wavelength spacing and allocation. Numerical simulations show scalability to even higher bit rates (e.g. in the terabaud regime). The conversion process is independent on tributary data modulation and channel spacing can be controlled by manipulating the amount of data dispersion and pump linear-chirp. The wavelength allocation of the various WDM channels can be controlled by changing the time

delay between pump and data signal.

It was demonstrated that the FWM based implementation of the serial-to-parallel conversion process preserves the modulation format of the OTDM tributaries. This was shown for 640-GBd RZ-QPSK and 320-GBd RZ 16-QAM. The OFT operational principle was demonstrated both in HNLF and silicon nanowires. It was shown that by using the right linearly-chirped flat-top pump pulses, it is possible to convert more than half of the OTDM tributaries. This means that the OFT technique could result in a simplified OTDM receiver which can demultiplex all tributaries using only two time-to-frequency OFT devices. This can not only enable a significant reduction in the complexity of an OTDM receiver, but due to its simplicity and symbol-rate scalability it could enable ultra-high speed serial data communication systems with potentially moderate energy requirements. Due to the ability of converting several OTDM tributaries simultaneously on a single device, the OFT serial-to-parallel converter should be able to bring down the required switching energy per bit.

# Chapter 6

# All-optical re-timing and synchronization

## 6.1 Introduction

The demand for full 10 Gbit/s Ethernet (10 GE) services, with expectations of lower cost and reliable optical 10 Gbit/s links, creates a need for design of ultra-high throughput optically transparent switches/routers with Tbit/s interfaces that will aggregate traffic from several lower bit rate links. OTDM technology can be a possible solution to this aggregation problem due to its high capacity and serial nature. However, interfacing between Ethernet protocol and OTDM systems faces a number of challenges, such as packet length variation (64–1518 bytes), non return-to-zero (NRZ) to return-to-zero (RZ) format conversion, asynchronous data arrival, and repetition rate variations. Due to the asynchronous nature of Ethernet packets and the synchronous one of TDM systems, the Ethernet packets in each link have to be synchronized to a master clock in the Terabit Ethernet (TE) interfaces and then time-division multiplexed into a serial Tbit/s data stream. For an asynchronous Ethernet network-link with a nominal line rate of 10 Gbit/s, the frequency-variation of data packets (data frames) must be within ±100 ppm. This means that up to 1 MHz frequency offset in repetition rate between transmitted data packets and receiver clocks must be tolerated [139]. As data packets may come from various origins, a desired feature of a network node would be the ability to synchronize the arriving data packets to a local master clock [140–142].

The following chapter describes the utilization of the time lens for synchronization of an incoming packet to a certain master clock. The problem is transformed into a re-timing issue between the lens and the input signal. In our system the time lens is implemented via an electro-optical phase modulator with sinusoidal phase modulation which approximates the quadratic phase within a small range. The chapter is organized as follows: Section 6.2 gives an introduction to the utilization of an electro-optical phase modulator (EOPM) for implementing the all-optical re-timer; Section 6.3 concentrates on some experimental results on re-timing of different packet lengths up to 12144 bits (corresponding to the longest Ethernet packet) to a local clock corresponding to the base rate of an OTDM signal, when the two signals' frequencies differ by 200 kHz (±20 ppm) [C-22,24,27,28]; Section 6.4 describes a possible way of simultaneously performing NRZ-to-RZ format conversion and frame synchronization, for multiplexing 10 Gbit/s Ethernet packets into a Tbit/s OTDM signal [J-7, C-14,16,19].

## 6.2 Retiming via electro-optical phase modulator

In Section 3.5 it was proven that the utilization of a time lens and dispersive element could be used to eliminate temporal drifts, or displacements, present in the input object. This is made possible by the Fourier transform capabilities of the lens itself, and the fact that time drifts do not change the spectral envelope of the signal but only its phase. Like in the spatial case, the output image at the back focal plane of the time lens corresponds to the Fourier transform of the input object and this image would result synchronized to the temporal axis of the time lens itself.

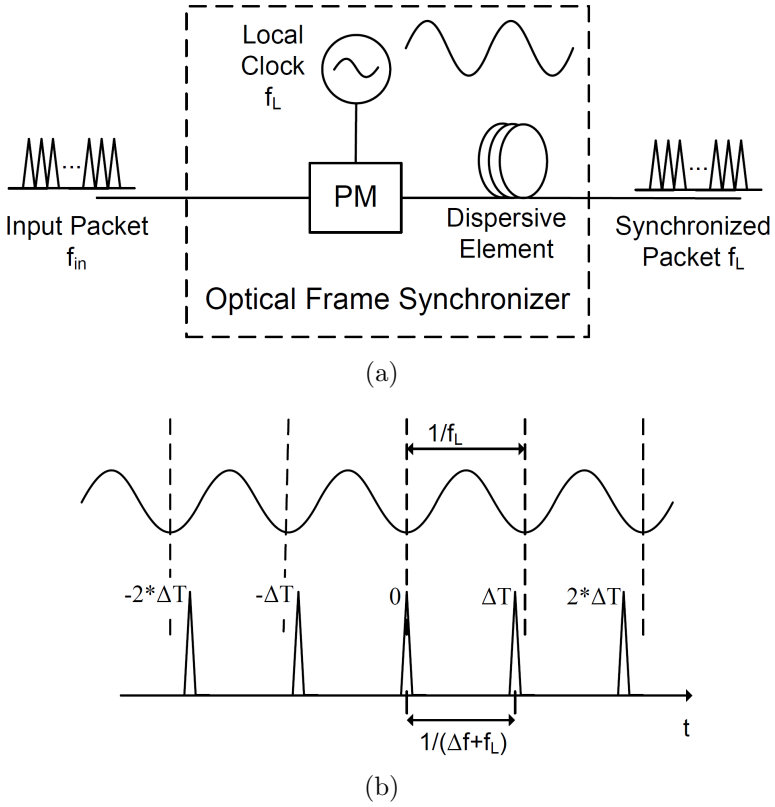


**Figure 6.1:** (a) Optical frame synchronizer realized with a phase modulator (PM) driven by a sinusoidal signal (frequency $f_L$) and a dispersive element. The input packet with repetition rate $f_{in}$ gets re-timed and synchronized to the local frequency $f_L$; (b) Operation principle of the optical frame synchronizer; the time displacements ($n \times \Delta T$, $n = \ldots$-1, 0, 1, $\ldots$) between the sinusoidal minima and the pulses' peaks are transformed into frequency displacements of the re-timed pulses.

As mentioned in Section 3.2.2 a time lens is any mechanism that can apply a quadratic phase modulation on an incoming optical signal. In the previous chapter such mechanism was performed via FWM with linearly chirped pump pulses. However, a simpler method is based on the utilization of an EOPM driven by a sinusoidal electrical signal. Fig. 6.1 shows the basic principle of re-timing via EOPM. The input optical frame with repetition rate $f_{in} = f_L + \Delta f$ is launched into the phase modulator which is driven by a local clock with frequency $f_L$. The phase imposed by the phase modulator can be expressed as [143]

$$\phi(t) = \pi \frac{V_{pp}}{V_\pi} \cos(\omega_L t) = \pi \frac{V_{pp}}{V_\pi} \cos(2\pi f_L t), \tag{6.1}$$

with $V_{pp}$ and $V_\pi$ being respectively the peak-to-peak driving voltage and the necessary voltage to achieve a $\pi$ phase shift. A Taylor expansion of $\cos(\omega_L t)$, confined only to the first term, results in

$$\phi(t) \approx -\pi \frac{V_{pp}}{4V_\pi} \omega_L^2 t^2. \tag{6.2}$$

By using the same variable definition as in Section 3.5, then the linear chirp rate can be written as $C = -\pi\omega_L^2 V_{pp}/2V_\pi$. Based on the results of Section 3.5, the dispersive element following the electro-optic time lens should have an accumulated dispersion $D_{acc} = -2V_\pi/(\pi\omega_L^2 V_{pp})$ in order for the image to resemble the input's Fourier transform and the waveform in the time domain to be synchronized with the driving signal at $f_L$. Therefore, it is possible to use the time lens to remove the timing difference between the local clock and the input frequency, and consequently synchronize the input packet with the local frequency $f_L$.

The input pulse aligned with the minimum of the parabolic clock (approximated with a sinusoidal clock) will not be displaced and will always be on the axis of the time lens. The other pulses will see a negative or positive frequency chirp depending on their position compared to the maximum (or minimum) of the sinusoidal driving signal.

## 6.3 Experimental setup

Fig. 6.2 shows the experimental setup for the optical frame synchronizer based on a time lens. It is composed of a 10 Gbit/s optical frame generator, an optical frame synchronizer block and a 10 Gbit/s receiver. The ERGO-PGL produces optical pulses centered at 1549 nm and with 1.5-ps FWHM. The pulse train is generated at $f_{in}$=9.9535 GHz, which is the frequency of the transmitter RF-synthesizer. The laser spectrum is filtered with a 0.33-nm optical bandpass filter and the pulses are broadened to 13 ps. The broadened pulses are OOK modulated in a Mach-Zehnder modulator with a 10 Gbit/s PRBS ($2^7$-1) sequence. The modulated RZ-OOK signal is passed through an intensity modulator (IM) driven by a square electrical pulse-train with 50 kHz repetition rate. The IM is used to carve out frames/packets from the data modulated continuous stream. The packet length can be adjusted by changing the square electrical signal driving the IM. In the experiment, we used two different packet lengths: a shorter one of 640 bytes (5120 bits) and a longer one of 1518 bytes (12144 bits). After generation, the 10-Gbit/s optical frames were sent into the optical frame synchronizer, composed of a phase modulator (PM), driven by a local RF clock ($f_L$=9.9537 GHz), and followed by 6-km SMF used as dispersive element. The phase modulator was driven by 28 dBm RF signal power, which led to $2.7\pi$ phase shift. In the 10-Gbit/s receiver, the synchronized optical packet was measured by an oscilloscope and an error analyzer, both triggered by the new local clock frequency. As it can be seen, $|\Delta f|$=200 kHz. This complies with 10 GE wide area networks (WAN) requirements, whose nominal transmission rate can vary with up to ±20 ppm , i.e. ±200 kHz frequency offset between transmitter and receiver must be tolerated [144].

### 6.3.1 Results and discussion

Fig. 6.3 shows the RF spectra of the original and synchronized frames of 5120 bits (Fig. 6.3(a)) and 12144 bits (Fig. 6.3(b)). The 50 kHz spacing peaks are due to the frame repetition rate.

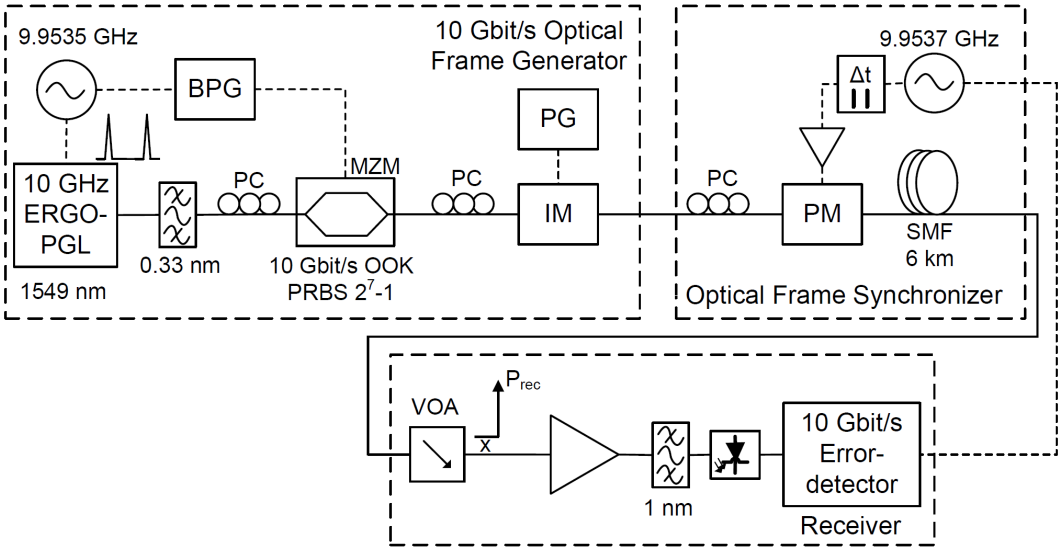


**Figure 6.2:** Experimental setup for the time-lens based optical frame synchronizer. ERGO-PGL: Erbium glass oscillating pulse-generating laser; BPG: bit patten generator; MZM: Mach-Zehnder modulator; PRBS: pseudo-random bit sequence; PG: pulse generator; IM: intensity modulator; PC: polarization controller; Δt: variable time delay; PM: phase modulator; SMF: single-mode fiber; VOA: variable optical attenuator; $P_{rec}$: received power.

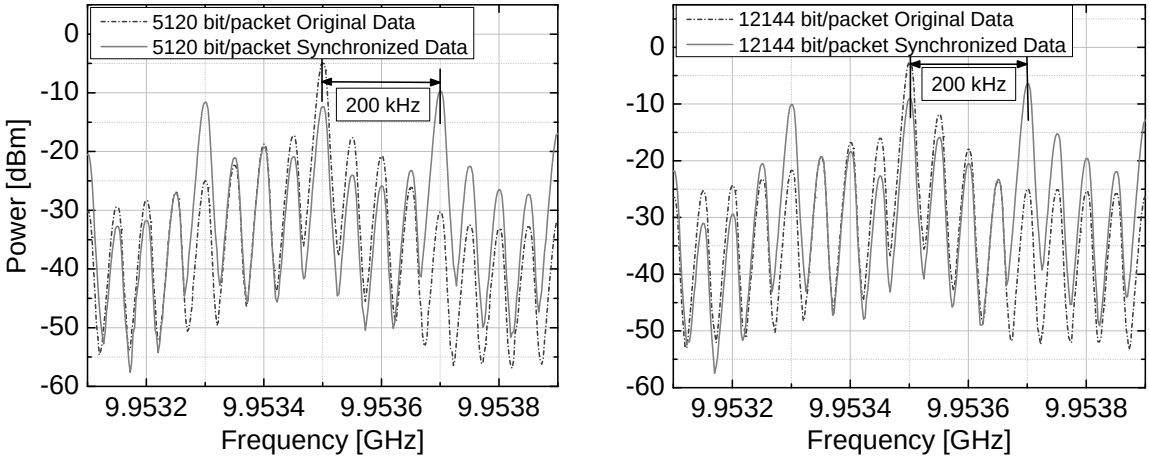


**Figure 6.3:** (a) RF spectrum of original data and synchronized data for the 5120 bits frame; (b) RF spectrum of original data and synchronized data for the 12144 bits frame.

For both packet lengths it is possible to clearly see that the maximum frequency peak of the synchronized signal has been adjusted to the local frequency of 9.9537 GHz. Fig. 6.4 shows the BER measurements for both frames. In order to perform error counting measurements the error-detector was operating in burst mode and it was triggered by the local clock. As it can be noticed, the synchronized frame of 5120 bits has only 0.7-dB penalty compared to the back-to-back case. Instead the synchronized packet of 12144 bits shows a penalty of 1.2 dB. This is related to the frame length and the fact that the edge bits are out of the quadratic phase approximation of the modulator. The nonlinear chirp that these bits experience can not be compensated by the subsequent SMF. Of course, this penalty could be reduced if a

proper quadratic phase modulation was to be applied. Fig. 6.5 shows the eye diagrams for the synchronized frame of 5210 bits. The synchronized eye could be displayed only if the oscilloscope was triggered by the local clock. From Fig. 6.5(a), it can be noticed that the unsynchronized eye can not be displayed.

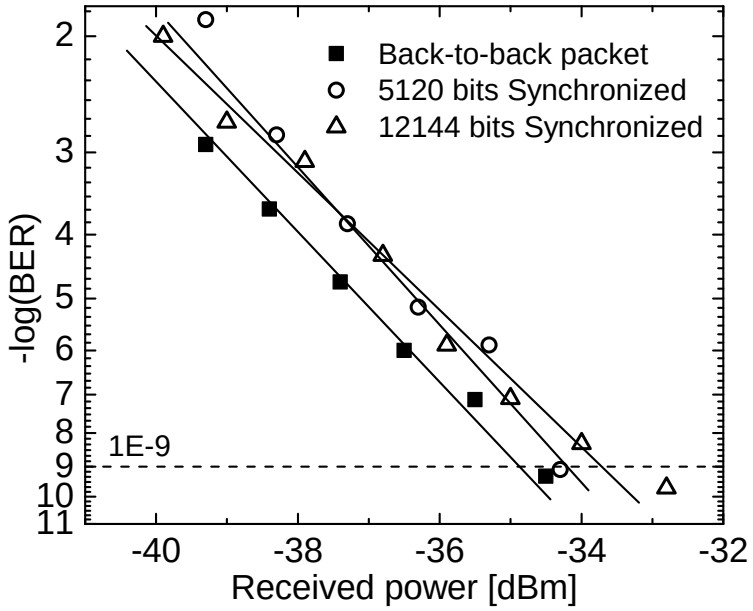


**Figure 6.4:** BER measurements for the back-to-back packet and the synchronized ones for 5120 bits and 12144 bits.

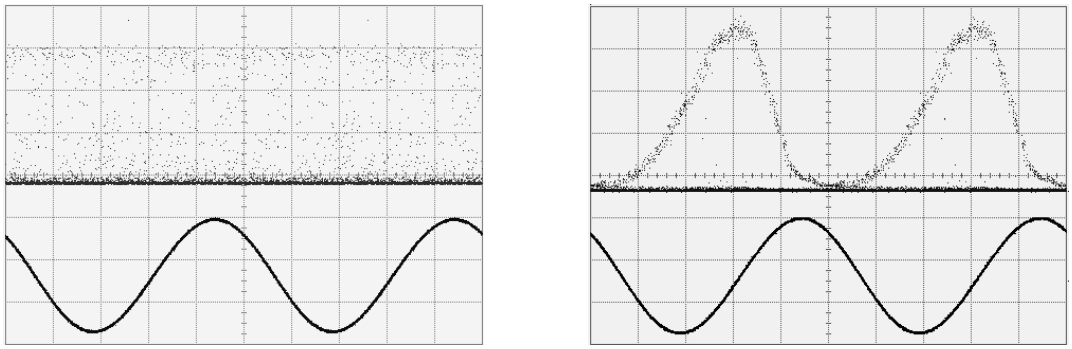

(a) (b)

**Figure 6.5:** (a) Eye diagram of the input packet without synchronization; (b) Eye diagram of the synchronized packet of 5120 bits. The electrical oscilloscope is triggred by the local clock.

## 6.4 Integration with OTDM systems

As mentioned in Section 3.5, the re-timing process is based on the fact that the entities to be synchronized are RZ optical pulses. However 10 GE commercial systems generate data having an NRZ format. Thus, an integration of these systems with Tbit/s OTDM ones would require format transformation (NRZ-to-RZ conversion) and pulse compression down to few hundred femtoseconds. In [C-8,J-5] the NRZ ethernet package is simultaneously

synchronized and converted into an RZ packet, then further pulse compressed to a FWHM of 400 fs. After compression the pulses are multiplexed by time interleaving with a serial 1.28-Tbit/s signal including a vacant time slot, thus forming a 1.29-Tbit/s time-division multiplexed serial signal. The frequency difference ($\Delta f$) between the OTDM tributary and the initial ethernet data is 200 kHz. Fig. 6.6 shows the setup used in this experiment and a possible implementation for integration of NRZ ethernet frames with OTDM systems. To be noticed the extra MZM modulator placed in the synchronizer. This is used to remove the part of the waveform subject to nonlinear chirp or having a linear chirp but with the wrong sign resulting from the negative intensity part of the sinusoidal driving signal. The error-free performance of the synchronization and multiplexing blocks is confirmed at the OTDM receiver, where the ethernet frame is demultiplexed and analyzed.

The main drawback of this technique is the fact that by mapping the spectrum in the time domain, the time displacement is transformed into a frequency displacement. This means that the synchronized pulses will not have all the same central wavelength. As the frequency shift depends linearly on the time displacement, then the lateral pulses of a given frame will be the ones that will suffer more form this phenomenon.

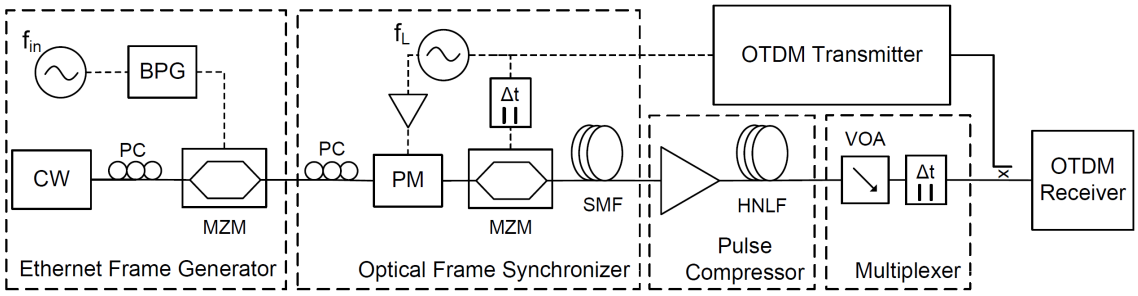


**Figure 6.6:** Experimental setup for the time-lens based optical frame synchronizer for NRZ ethernet frames and their integration with OTDM systems. CW: continuous wave laser; BPG: bit patten generator; MZM: Mach-Zehnder modulator; PC: polarization controller; PM: phase modulator; SMF: single-mode fiber; HNLF: highly nonlinear fiber; VOA: variable optical attenuator; $\Delta t$: variable time delay.

## 6.5 Summary

This chapter demonstrated the utilization of the space-time duality for re-timing and synchronization of optical packets with up to 12144 bits. The principle relies on the fact that temporal shifts do not distort the spectral envelope and it is based on the ability of a time lens to perform a Fourier transformation of the input signal by eliminating the misalignment between the incoming data signal and the lens' temporal axis. The implementation of the time lens was based on an electro-optical phase modulator driven by a sinusoidal electrical signal. The packet was synchronized to a local clock, whose frequency differed by 200 kHz ($\pm$20 ppm) from the input frames repetition rate. The performance of the synchronized packets was error-free and with low penalty. No extra clock recovery from the input packet signal was performed. Finally, it was shown the possibility of integration of the optical frame synchronize with OTDM systems, in order to reach up to 1.29 Tbit/s.

# Chapter 7

# High-capacity coherent OTDM systems

## 7.1 Introduction

In general, the increase in single-channel data rate transmission is achieved by increasing the symbol rate and/or the use of advanced modulation formats in which a larger number of bits is encoded per symbol [132]. The first transmission system demonstration at 1.28 Tbit/s was reported in the year 2000 [11]. By using polarization-multiplexing (PolMux), OOK modulation and a 640 GBd symbol rate, it was possible to generate a terabit signal and transmit it through 70 km of fiber. The utilization of PolMux with differential quadrature phase-shift keying (DQPSK) on the same symbol rate doubled the total bit rate to 2.56 Tbit/s and increased the transmission distance to 160 km [12]. Doubling of the capacity (5.1 Tbit/s) was enabled by multilevel formats like 16-QAM and the transition from direct detection to digital coherent detection. This was shown in a back-to-back experiment at 640 GBd [14]. Recently, this experiment was extended and transmission of 640-GBd PolMux 16-QAM over 80 km [C-6] was reported. The first attempt to increase the symbol rate to 1.28 TBd and combine it with DQPSK and PolMux in a back-to-back experiment was reported in [13]. The transmission of such a high symbol rate was first shown though for single-polarization DPSK signals over 50 km in [145].

The combination of sub-picosecond pulses, advanced modulation formats (e.g. 16-QAM), polarization multiplexing and digital coherent receivers, allowed the generation and transmission of 10.2 Tbit/s [C-12], which is the highest serial data rate so far. The utilization of an OTDM-coherent receiver for demultiplexing and demodulation reduced the bandwidth requirements for the optical-to-electrical conversion and the analog-to-digital converters (A/D) due to the reduced rate of the demultiplexed data signal.

The following chapter presents the latest results of 5.1-Tbit/s and 10.2-Tbit/s with 16-QAM modulation at symbol rates of 640 GBd and 1.28 TBd with transmission over 80- and 29-km dispersion-managed fiber (DMF), respectively. The chapter is organized as follows: Section 7.2 gives a brief introduction to the principle of synchronous coherent demultiplexing; Section 7.3 focuses on the realization of the 5.1-Tbit/s OTDM transmission experiment while in Section 7.4 the experiment is extended to 10.2 Tbit/s, which represents the present speed-record for serial transmission in a single-wavelength channel.

## 7.2 Basic principle: OTDM coherent receiver

In the previous chapter, Section 5.5, we demonstrated the utilization of the OFT technique for demultiplexing, via time-to-frequency conversion, of an OTDM signal with advanced modulation formats (QPSK and 16-QAM). The OTDM signal was mapped to the frequency domain via FWM with a chirped pulsed pump. After demultiplexing via filtering, the DWDM signal was demodulated in a coherent receiver by using a CW laser having the same central wavelength as the desired channel. However the utilization of a CW laser as a local oscillator is not mandatory and this section focuses on the implementation of an OTDM coherent receiver based on a single pulsed local oscillator.

For digital coherent receivers, as well as in the direct-detection (DD) case, the electronic components such as analog-to-digital converters, limit the maximum speed of the receiver, which is not compatible with the symbol rates that can be generated by the OTDM technique [C-12]. Currently, a maximum symbol rate of 56 GBd was demonstrated [146] using a conventional digital coherent receiver with a CW-LO. But for higher symbol rates, the use of a fast optical demultiplexer is necessary. The utilization of coherent detection with OTDM data offers several advantages, including compatibility with spectrally efficient modulation formats, high sensitivities and simultaneous demultiplexing and demodulation of ultra-high speed data signals. In Section 5.5 we used a CW-LO in order to demodulate the 10-GBd OTDM converted tributaries. But this does not mean that the local oscillator has to be a continuous wave. By substituting the CW-LO with a pulsed LO, whose pulse train overlaps with only one of the OTDM tributaries, then it is possible to perform high-speed demultiplexing and demodulation at the same time. Time-division demultiplexing by using a pulsed LO in a coherent optical receiver was introduced in [147], [148]. Such principle was later demonstrated for synchronous digital [147] coherent demultiplexing and demodulation in a digital coherent receiver [149].

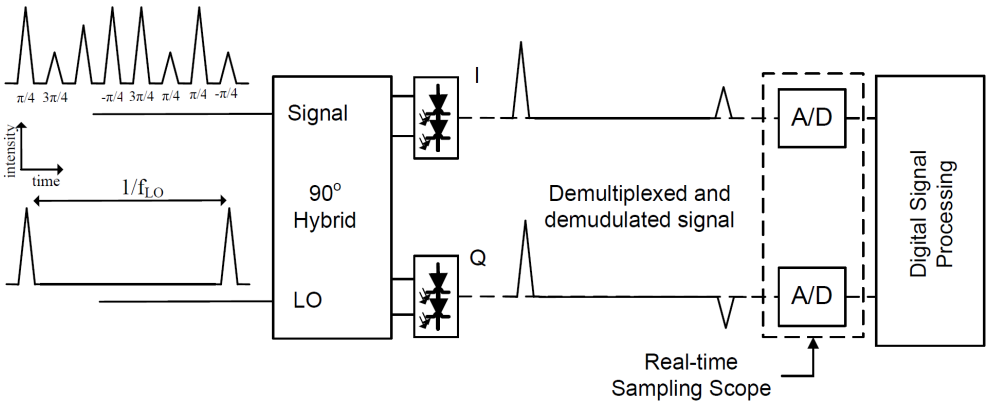


**Figure 7.1:** Principle of synchronous digital coherent demultiplexing of a single polarization RZ 16-QAM signal. The phase of the different symbols is indicated under the symbol. The demultiplexing is shown for one tributary signal.

Figure 7.1 shows the basic principle of synchronous digital coherent demultiplexing and demodulation of a single-polarization OTDM signal. In the shown case the data is an RZ 16-QAM signal, where one out of eight tributaries is extracted at a given moment. A simultaneous demultiplexing of all OTDM tributaries would require several of such configurations in parallel, i.e., eight for the chosen example. This means that 64 and 128 of these demultiplexers would be necessary (per polarization state) in order to parallelize the reception of

all OTDM tributaries for the experiments shown in Section 7.3 and 7.4. Like in the digital coherent receiver shown in App.1 (Fig. 4), the data and LO are sent into a 90° optical hybrid, and the in-phase (I) and quadrature (Q) outputs are detected by high-speed balanced photodetectors. The generated electrical data streams are sampled via A/D converters before digital signal processing. The presence of a pulsed LO in the hybrid ensures that only one tributary is switched at a time[1]. In its absence the signal would be canceled out at the balanced photodetectors. Since the signal is demodulated only in the presence of an LO pulse, this means that the receiver performs a demultiplexing function as well. Moreover, the temporal resolution of the demultiplexing process is given by the LO pulse width. This should be broad enough to cover an entire symbol slot of the OTDM data signal and not too broad in order to switching energy from the neighboring tributaries.

In Fig. 7.1 the LO pulse repetition rate ($f_{LO}$) is one eighth of the signal's symbol rate. This requires the pulse LO to be synchronized to the base rate of the incoming data signal. For this reason a clock recovery mechanism is necessary in order to lock the LO pulse source. The principle can be interpreted as synchronous optical sampling with one sample per bit. This, however, does not allow electronic compensation of distortions [150]. Hence e.g. chromatic dispersion (CD) needs to be compensated optically, before the 90° optical hybrid.

In the following sections we will describe, base on the principle shown in Fig. 7.1, the demultiplexing and demodulation process of an RZ 16-QAM OTDM signal with symbol rate up to 1.28 TBd.

## 7.3 Transmission of a 5.1-Tbit/s serial data signal

The following section describes the generation, transmission and reception of a 5.1-Tbit/s serial data signal, generated by the combination of a 640 GBd OTDM signal with 16-QAM modulation format and polarization multiplexing.

### 7.3.1 Experimental setup

Figure 7.2 shows the experimental setup. It includes the 5.1-Tbit/s transmitter, the 80-km dispersion-managed fiber (DMF) and the digital coherent receiver. The light source is an ERGO-PGL generating a pulse train having 1.2-ps FWHM, 10-GHz (STM-64) repetition rate and central wavelength at 1550 nm. The pulses generated from the laser need to be compressed down to half of their original width in order to be multiplexed up to 640 GBd. This is achieved by SPM-induced spectral broadening in an HNLF with subsequent chirp compensation. The 1.2-ps pulses from the ERGO-PGL (Fig. 7.2) are amplified to 21.5 dBm and injected into a 250-m long, dispersion-flattened germanium-doped silica HNLF with attenuation $\alpha$=0.78 dB/km, dispersion D=–0.49 ps/(nm·km), dispersion slope S=0.0061 ps/(nm$^2$·km) at 1550 nm and nonlinear coefficient $\gamma$=10 (W·km)$^{-1}$. The optical spectrum is broadened due to SPM, resulting in a broad supercontinuum exceeding 40 nm. The initial laser spectrum and the SPM-generated supercontinuum are shown in Fig. 7.3(a). The supercontinuum is offset filtered by a 20-nm broad square optical bandpass filter (OBPF) centered at 1555 nm and is subsequently modulated in an in-phase-quadrature modulator (IQ-Mod.).

The IQ modulator (model AVANEX DQ40) is driven by a two-channel arbitrary waveform generator (model Tektronix AWG7122B) which was programmed to generate a 16-QAM

[1]The LO pulses behaves as time gates.

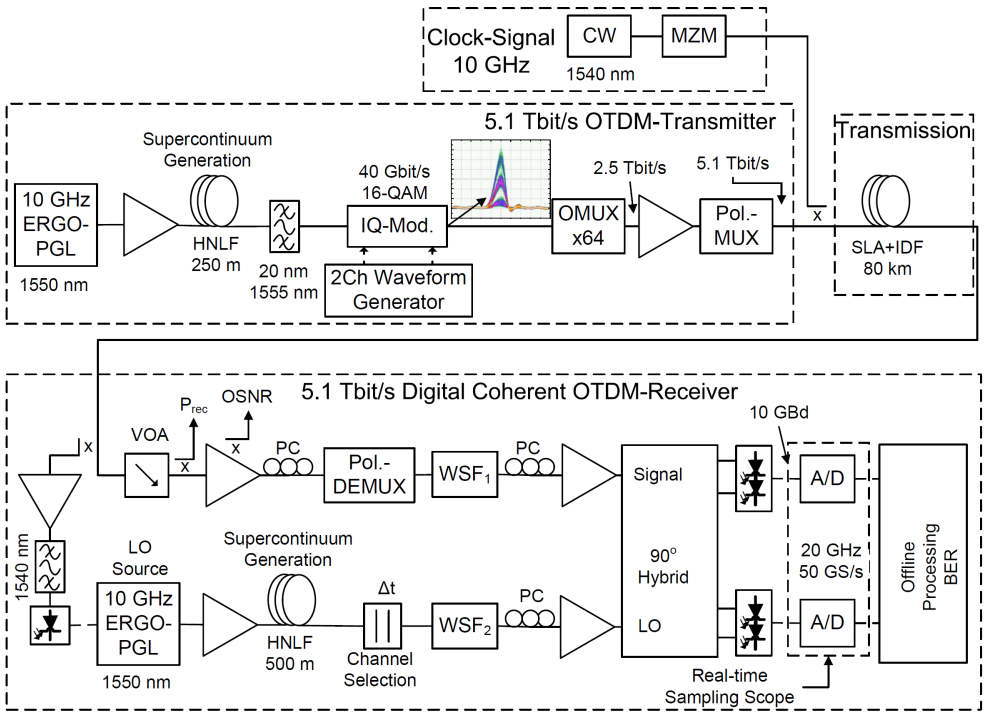


**Figure 7.2:** Schematic depiction of the experimental setup for 5.1-Tbit/s generation, transmission and detection: ERGO-PGL: Erbium glass oscillating pulse generating laser, DF-HNLF: dispersion-flattened highly-nonlinear fiber, IQ-Mod: in-phase quadrature modulator, OMUX: optical time-division multiplexer, PolMUX: polarization multiplexer, CW: continuous wave, MZM: Mach-Zehnder modulator, SLA: super large area fiber, IDF: inverse dispersion fiber, VOA: variable optical attenuator, LO: local oscillator, $P_{rec}$: received power, OSNR: optical signal-to-noise ratio, PC: polarization controller, Pol.-DEMUX: polarization demultiplexer, WSF: wave-shaping filter, A/D: analog-to-digital converter, BER: bit-error ratio.

($2^{15}$ De Bruijn sequence before symbol mapping) resulting in an optical 40-Gbit/s (10 GBd single polarization) data signal. This data signal is optically time division multiplexed in a fiber-based delay line optical multiplexer (OMUX), up to 64 times, resulting in a data rate of 2.5 Tbit/s (640 GBd single polarization). At the last stage of the transmitter, the signal passes through a polarization multiplexer (PolMUX), based on a polarization beam-splitter for separating the signal in two branches. The two orthogonally polarized signals are subsequently decorrelated via a fiber delay in one branch and then recombined using a polarization-maintaining coupler. The combination of 16-QAM and 128-fold dual-polarization OTDM results in the total serial data capacity of 5.1-Tbit/s (640 GBd per polarization). After generation, the optical signal-to-noise ratio (OSNR) of the 5.1-Tbit/s signal, measured at the output of the transmitter, was 46 dB.

The signal is launched into an 80-km transmission link together with a 10-GHz clock signal[2] at 1540 nm. The 80-km DMF link (Ultrawave$^{TM}$) consisted of 55.7 km super large area (SLA) fiber with D=20 ps/(nm·km) and S=0.06 ps/(nm$^2$·km), and 23.5 km inverse dispersion fiber (IDF) with D=–47.8 ps/(nm·km) and S=–0.15 ps/(nm$^2$·km). The link had a differential group delay (DGD) of 0.3 ps and a total loss of 17.6 dB. The polarization state of the data signal was aligned with the principal polarization axes of the fiber in order to

[2]The transmission of the clock signal was necessary as a 640-GBd optical clock recovery mechanism was not available at the time of the experiment.

mitigate degrading effects that result from polarization mode dispersion (PMD).

In the pre-amplified receiver the 10-GHz transmitted clock is extracted via a 10-dB coupler and a 1.2-nm 3-dB bandwidth OBPF. The extracted clock is detected by an optical 10-GHz receiver and then used to synchronize a second ERGO-PGL, which is used as LO in the coherent receiver. The LO ERGO-PGL produces 10-GHz (STM-64) pulses with 1.8-ps FWHM and is centered at 1550 nm. As in the transmitter case, the LO pulses are too broad to be used for demultiplexing a single 10-GBd tributary out of the 640 GBd OTDM signal. For this reason the LO is amplified to 23.4 dBm and injected in a 500-m long HNLF having the same properties as the one used to generate the supercontinuum at the transmitter. The broad spectrum resulting from SPM is subsequently reshaped by a liquid crystal on silicon (LCoS) wave-shaping filter (WSF, Finisar WaveShaper 4000S). A tunable time-delay is used to align the LO pulses with one of the 64 TDM tributaries, which allows the demultiplexer to extract one 10 GBd tributary at a time. By using the tunable time-delay, all tributaries can be selected and subsequently characterized.

The data path of the pre-amplified receiver consists of a variable optical attenuator (VOA) to vary the received signal power and OSNR, two erbium-doped fiber amplifiers (EDFA), a polarization demultiplexer (polarization beam splitter in combination with a polarization controller at its input), a second WSF, a 90°-hybrid, two balanced photo detectors (BPD), two A/Ds (50-GS/s real-time sampling oscilloscope with 20-GHz bandwidth, model Tektronix DPO72004) and a personal computer for offline BER measurement. The average optical input powers into the 90°-hybrid were 15 dBm for the data signal and 12 dBm for the LO. The data was recovered by a conventional digital signal processing block for single-polarization signals and included: resampling to an integer number of samples per symbol, correction of the 90°-hybrid phase error and imbalance by using the Gram-Schmidt orthogonalization, fast Fourier transforms based frequency-offset compensation (data signal with respect to LO), clock-recovery and blind adaptive equalization (finite-impulse response filter). After pre-convergence of the equalizer using the constant modulus algorithm, the error criterion was switched to a decision-directed least-mean square filter [151, 152].

### 7.3.2 Results and discussion

Figure 7.3(b) shows the transmitted spectrum including the 10-GHz clock at 1540 nm and the 20-nm data spectrum, carved out from the broad supercontinuum shown in Fig. 7.3(a). For optimum system performance, the supercontinua generated at the transmitter and LO have to be transformed to achieve the shortest possible pulses on the BPDs. In our setup, this transformation is accomplished by the dispersion of the fiber components, the residual dispersion of the fiber link and fine tuning of the spectral amplitude and phase profile of the two WSF (signal and LO path).

Figure 7.3(c) shows the optical spectra of the 10-GHz LO and the 5.1-Tbit/s 16-QAM data signal at the input of the 90°-hybrid, i.e. after spectral reshaping in the WSFs. Both spectra are Gaussian with 6-nm FWHM and centered at 1555 nm. The residual phase profile of the DMF link as shown in Fig. 7.3(c) was compensated by the phase shaping ability of the WSF[3] in the data path inside the coherent receiver (see Fig. 7.2). This allowed precise compensation of the residual dispersion of the link up to the fourth order dispersion ($\beta_2$, $\beta_3$

[3]The phase shaping ability of the WSF was used to compensate also for the residual dispersion of the optical components and other shorter fibers present in the setup.

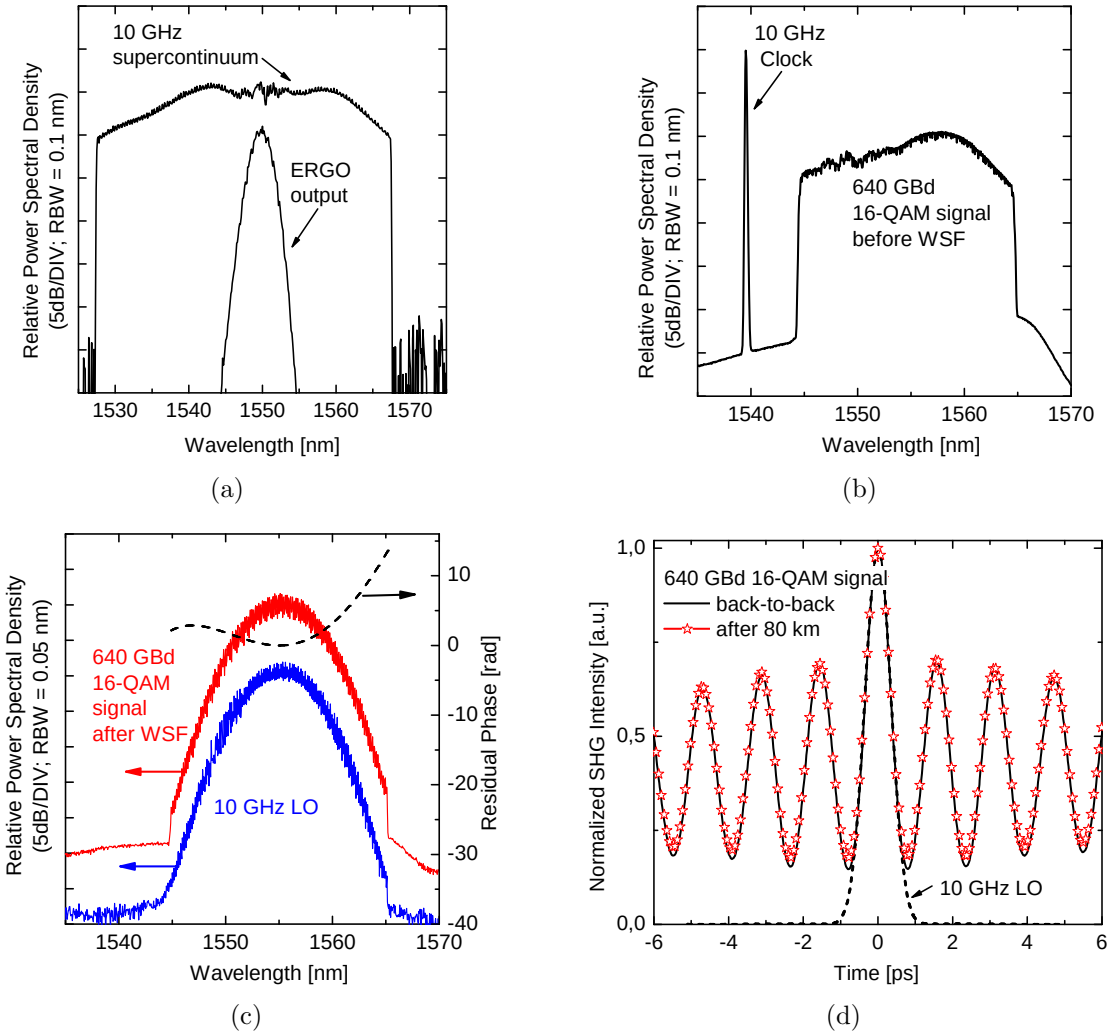


**Figure 7.3:** (a) Optical spectra at the output of the ERGO-PGL and the 10-GHz supercontinuum. (b) Transmitted optical spectrum including 10-GHz clock and 5.1-Tbit/s data signal. (c) Optical spectra of the compressed and filtered 10-GHz LO pulses and the 640-GBd 16-QAM data signal measured at the input of the 90°-hybrid as well as the residual phase profile of the 80-km transmission link. (d) Autocorrelation traces of the compressed 10-GHz LO pulse train (dashed) as well as the modulated and optically multiplexed 640-GBd RZ-16-QAM data signal (solid black line: back-to-back, red stars: after 80-km transmission.

and $\beta_4$) and thus allowed to minimize pulse broadening due to chromatic dispersion (CD). Additionally, the data polarization was aligned with the principal axes of the link to minimize pulse broadening due to PMD. For the single polarization 640-GBd data signal the measured degree of polarization (DOP) after transmission over 80-km DMF was found to be 98%. After full dispersion compensation and spectral reshaping, as described above, autocorrelation measurements (Fig. 7.3(d)) yielded pulse widths of 580-fs FWHM at the BPDs for both, the LO and data signal pulses, assuming Gaussian shapes in the time domain. Besides the compressed 10-GHz LO pulses, Fig. 7.3(d) shows also the autocorrelation traces of the 640-GBd 16-QAM data signal (single polarization) for the back-to-back case and after 80-km transmission. The traces show negligible pulse broadening due to transmission, indicating proper CD compensation and mitigation of PMD.

Figure 7.4(a) and Fig. 7.4(c) show the BER as a function of OSNR and received opti-

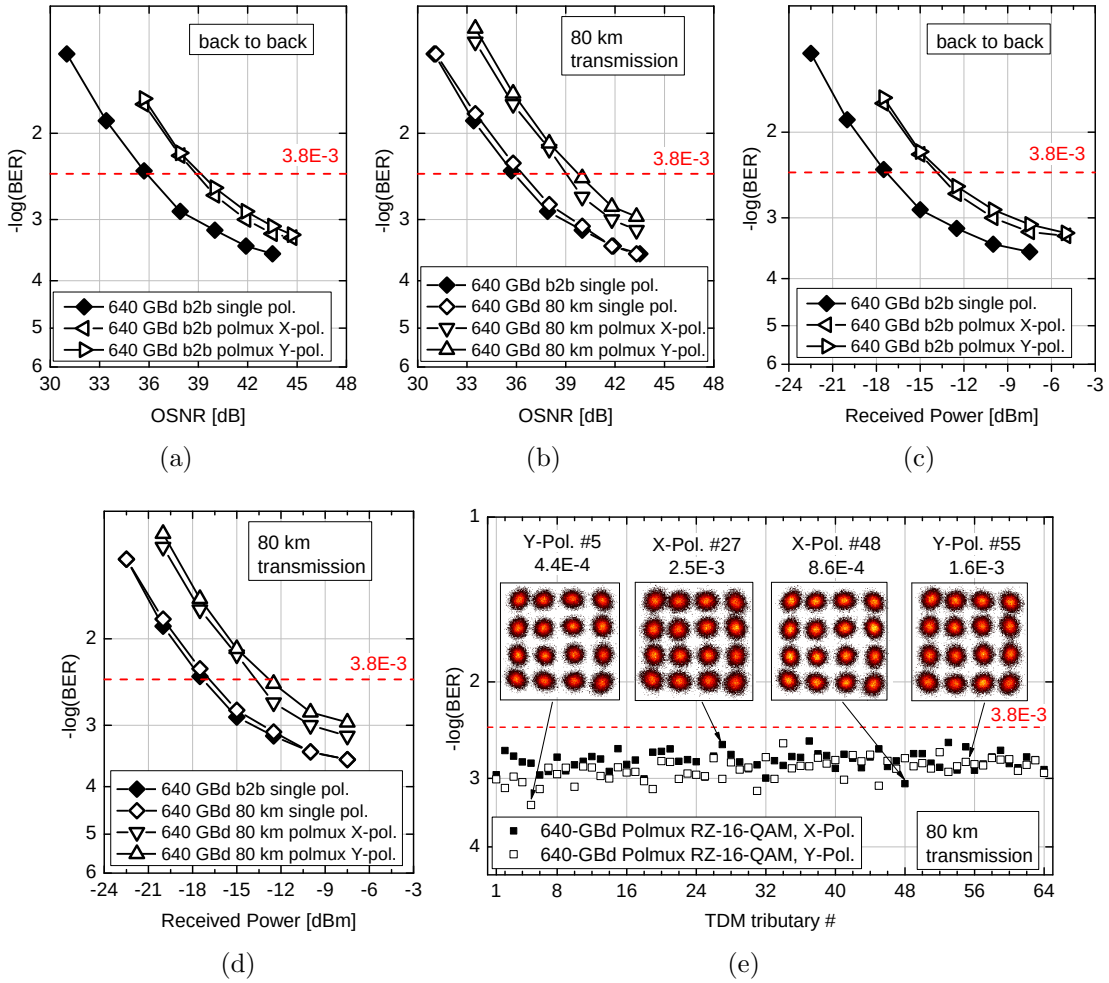


**Figure 7.4:** 5.1-Tbit/s BER measurements. (a), (c) Back-to-back BER for one TDM tributary of the 640-GBd single polarization (2.5 Tbit/s) data signal and after polarization multiplexing (5.1 Tbit/s). (b), (d) BER for one TDM tributary after 80-km transmission. (e) BER for all 128 tributaries (X- and Y-polarization) of the 5.1-Tbit/s data signal after 80-km transmission. The insets show constellation diagrams with BER values for selected tributaries.

cal power (excluding the power in the transmitted clock signal) for the back-to-back case for one of the OTDM tributaries. The required OSNR for a BER=$3.8{\cdot}10^{-3}$ was 36 dB (at -17.5 dBm received power) for the single polarization and 40 dB (at -13.7 dBm) for the polarization multiplexed signal[4]. Figure 7.4(b) and Fig. 7.4(d) show the BER performance of one OTDM-tributary after 80-km transmission. The input power into the 80-km DMF span was 12.5 dBm. Due to the high symbol rate of the data signal this power did not induce a significant nonlinear penalty for the transmission. As it can be seen, Fig. 7.4(a) and Fig. 7.4(b) show an error-floor at a BER=$10^{-4}$. Although the required OSNR values were close to the maximum available transmitter OSNR of 46 dB, the observed error-floor is attributed mainly to the timing jitter between the two ERGOs used as data and LO sources. In fact the measured jitter for the data ERGO-PGL was 69 fs, and for the LO ERGO-PGL was 72 fs. There is no such error-floor when using the same laser for both signals (Section 7.4,

[4]Note the fact that the OSNR values were measured before spectral shaping of the data signal in the WSF.

Fig. 7.7(a) and Fig. 7.7(b)).

By changing the time delay between the LO pulses and the data signal it is possible to demultiplex and characterize all tributaries. Figure 7.4(e) shows the measured BER for all 128 OTDM tributaries (both polarizations: X-Pol., Y-Pol.) after 80-km transmission at an OSNR of 43.3 dB. All tributaries perform below the BER limit of $3.8{\cdot}10^{-3}$ for hard decision FEC with 7% overhead, thus representing error-free transmission of 4.8-Tbit/s net data rate. Fig. 7.4(e) shows also, for selected tributaries, the constellation diagrams with the corresponding BER values. Each constellation consists of about 200000 symbols.

The experimental results showed excellent performance in back-to-back and after transmission, which proves the high degree of phase coherence of the compressed pulses. The supercontinuum generated at the output of the 200 m HNLF (data path in Fig. 7.2) was broad enough to generate even narrower pulses which enabled a doubling in symbol rate up to 1.28 TBd as will be described in the following section.

## 7.4 Demonstration of 10.2-Tbit/s serial data signal

### 7.4.1 Experimental setup

Figure 7.5 shows the experimental setup for generation, transmission and detection of a 10.2-Tbit/s serial data signal. The setup is similar to the one shown in Fig. 7.2, with just minor modifications. Compared to the previous experiment, an extra multiplexing stage was added in order to reach a multiplication factor of 128. The bandwidth of the OBPF after the supercontinuum generation was increased to 30 nm in order to generate narrower optical pulses, suitable for 1.28 TBd. The maximum OSNR available at the transmitter output, including PolMUX, was 48 dB.

Compared to the previous section, the transmission link was reduced to 29 km, consisting of 19-km SLA and 10-km IDF. The total loss of the link was 10.1 dB and its DGD was equal to 0.3 ps. Similarly to the previous experiment (Section 7.3), the polarization state of the data signal was aligned with the principal polarization axes of the transmission fiber. This ensured a DOP of 98% for the data signal after transmission.

In the digital coherent receiver, both the amplitude and phase profiles of the WSFs' transfer functions were calculated in order to recover the shortest possible pulses for the data signal and LO on the BPDs. As it can be seen in Fig. 7.5 the pulsed LO for the receiver in the 10.2-Tbit/s experiment was derived from the transmitter supercontinuum. This avoided detrimental effects originating from the relative timing-jitter between two separate ERGOs.

### 7.4.2 Results and discussion

Figure 7.6(a) shows the optical spectra of the 10-GHz LO pulses and the 10.2-Tbit/s 16-QAM signal at the input of the 90°-hybrid. Both spectra are Gaussian-like and have the same FWHM. Figure 7.6(a) shows also the residual phase profile of the 29-km DMF link. The compensation of the link residual dispersion was performed via the WSF in the receiver data path and comprised dispersion compensation up to the fourth order ($\beta_4$). Figure 7.6(b) shows the autocorrelation traces of the compressed 10-GHz LO pulses and the 1.28-TBd 16-QAM signal (back-to-back and after 29-km transmission). The width of the deconvoluted LO pulse (Gaussian-like) is 300 fs. The utilization of such narrow pulses makes it difficult

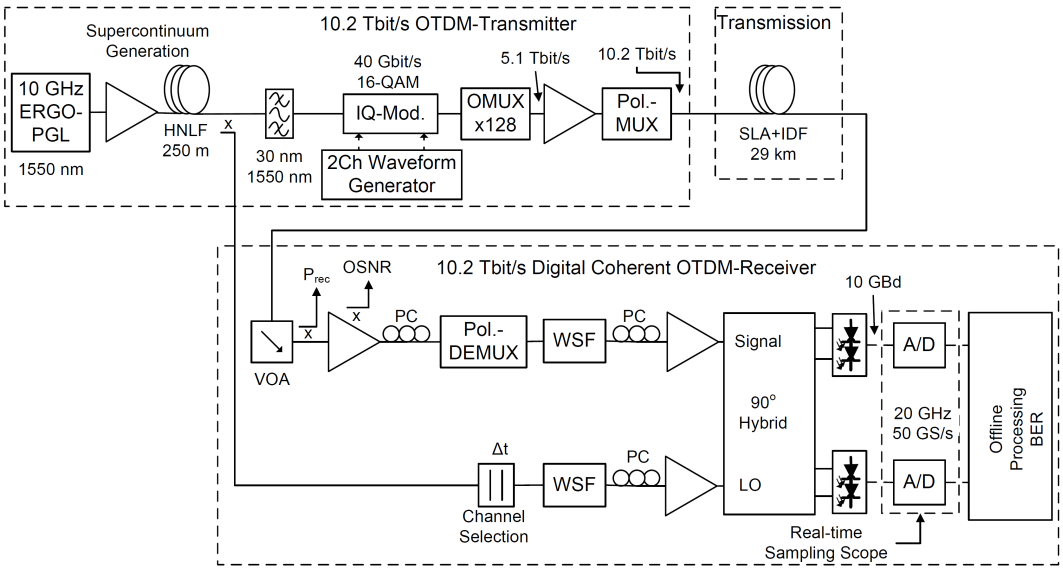


**Figure 7.5:** Schematic depiction of the experimental 10.2-Tbit/s setup. Refer to Fig. 7.2 for clarifications on the acronyms.

to accurately adjust the OMUX stages in terms of time delay and tributary amplitudes, in order to achieve a well equalized OTDM signal. This is a prerequisite for small variations of the BER performace of the individual TDM-channels. Despite this fact, the autocorrelation trace shown in Fig. 7.6(b) is a good indicator of the precise time interleaving achieved for the OTDM tributaries. This is confirmed also by a time-domain scan over all 128 tributaries of one polarization state of the 1.28-TBd data signal as shown in Fig. 7.6(c). In the plot a 25-ps section is enlarged from the 100-ps inset. The plot shows the sum of the variances of the in-phase and quadrature components of the demodulated data signal as a function of the relative time delay between the data signal and LO pulses. The scan was performed by changing the LO delay (used for TDM-channel selection in the BER measurements) in steps of 0.04 ps. The resulting waveform shown in Fig. 7.6(c) represents the convolution of the data signal with the LO pulses. Due to the utilization of 300-fs short LO pulses, this time-domain scan provides a high-resolution mapping of the average intensity waveform of the 1.28 TBd data signal. The scan over all tributaries demonstrates the well adjusted OMUX stages in terms of time delay and amplitude.

Figure 7.7 shows the BER measurements for the of back-to-back and transmission cases. Figure 7.7(a) and 7.7(c) show the back-to-back BER versus OSNR and received power for an arbitrarily selected TDM tributary. The required OSNR for BER=$3.8{\cdot}10^{-3}$ was ∼39 dB (at a received power of -14.3 dBm) for the single polarization case and 42 dB (at a received power of -10.5 dBm) for the polarization multiplexed (PolMUX) signal. As expected there is a 3-dB increase in OSNR sensitivity when moving to twice the symbol rate (1.28 TBd per polarization), compared to the previous experiment described in Section 7.3. To be noticed the fact that in contrast to Fig. 7.4 there is no corresponding error-floor evident at a BER of $10^{-4}$ in Fig. 7.7. This is due to the use of LO pulses which were derived from the same laser source as the data signal.

In order to test the transmission performance, the 10.2-Tbit/s signal was sent through 29-km DMF (15-dBm input power). The autocorrelation trace in Fig. 7.6(b) shows negligible pulse broadening due to transmission. Figure 7.7(b) and 7.7(d) show the measured BER for

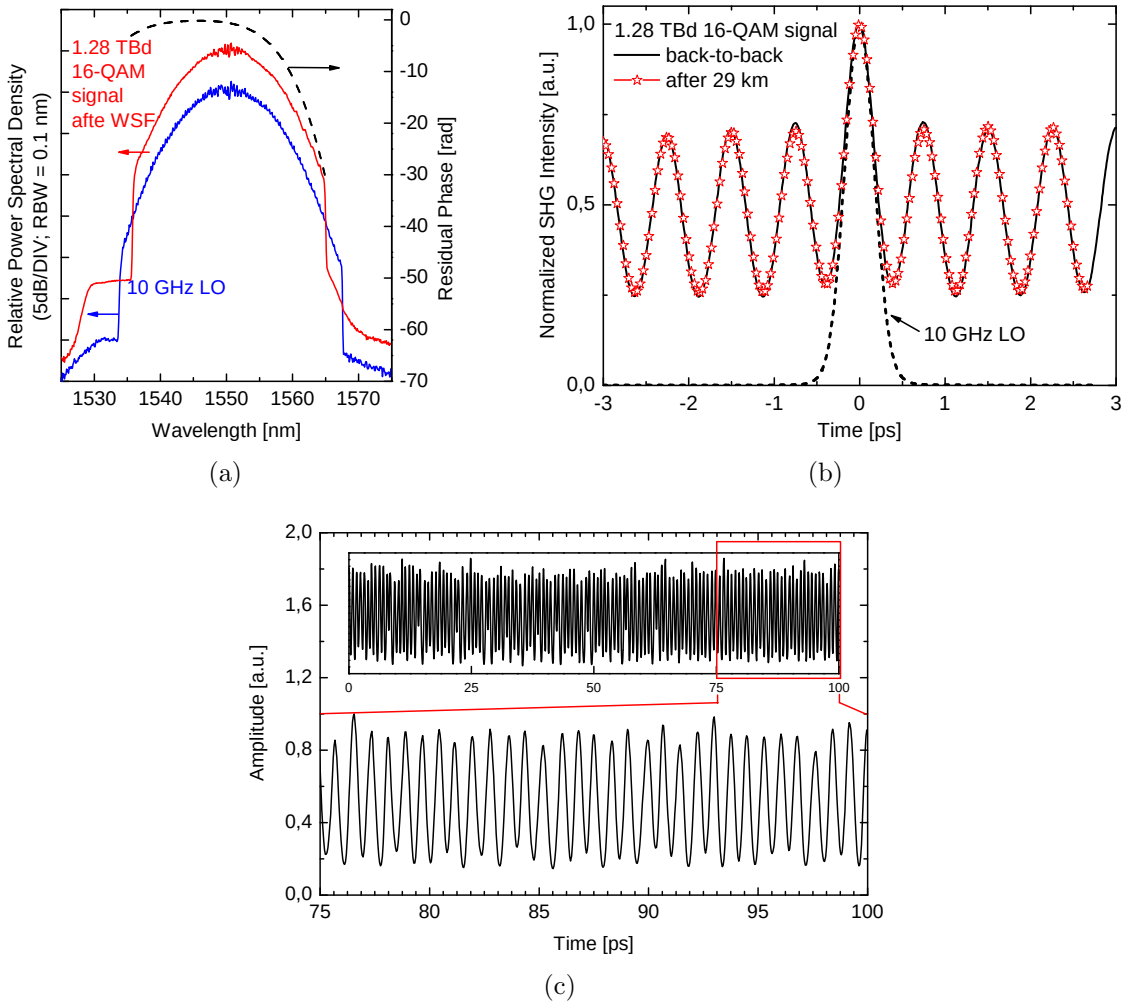


**Figure 7.6:** (a) Optical spectra of the compressed and filtered 10-GHz LO pulses and the 1.28-TBd 16-QAM data signal measured at the input of the 90°-hybrid as well as the residual phase profile of the 29-km transmission link. (b) Autocorrelation traces of the compressed 10-GHz LO pulse train (dashed) as well as the modulated and optically multiplexed 1.28-TBd RZ-16-QAM data signal (solid black line: back-to-back, red stars: after 29-km transmission) (c) Time-domain scan over 128 tributaries of the 1.28-TBd signal (single polarization).

one of the TDM tributaries. For the single-polarization signal no penalty was observed compared to the back-to-back performance, indicating no degradation by transmission. For the polarization multiplexed signal a penalty of about 3 dB was observed compared to the back-to-back PolMUX performance. We attribute this mainly to PMD in the setup. Nevertheless, a BER below the FEC threshold was reached for both polarization states of the investigated tributary.

Finally, in order to check the quality of all the TDM tributaries we scan the time delay between the data signal and the LO, in the back-to-back configuration (Fig. 7.7(e)). The BER of all 256 tributaries (both polarizations: X-Pol., Y-Pol.) were measured for the 10.2-Tbit/s signal at a received OSNR of 48 dB. Considering the BER limit of $3.8{\cdot}10^{-3}$ for hard-decision FEC with 7% overhead, all tributaries perform error-free, thus achieving an error-free serial single-channel net data rate of 9.5 Tbit/s. Fig. 7.7(e) shows also some examples of constellation diagrams for selected tributaries. Each constellation consists of

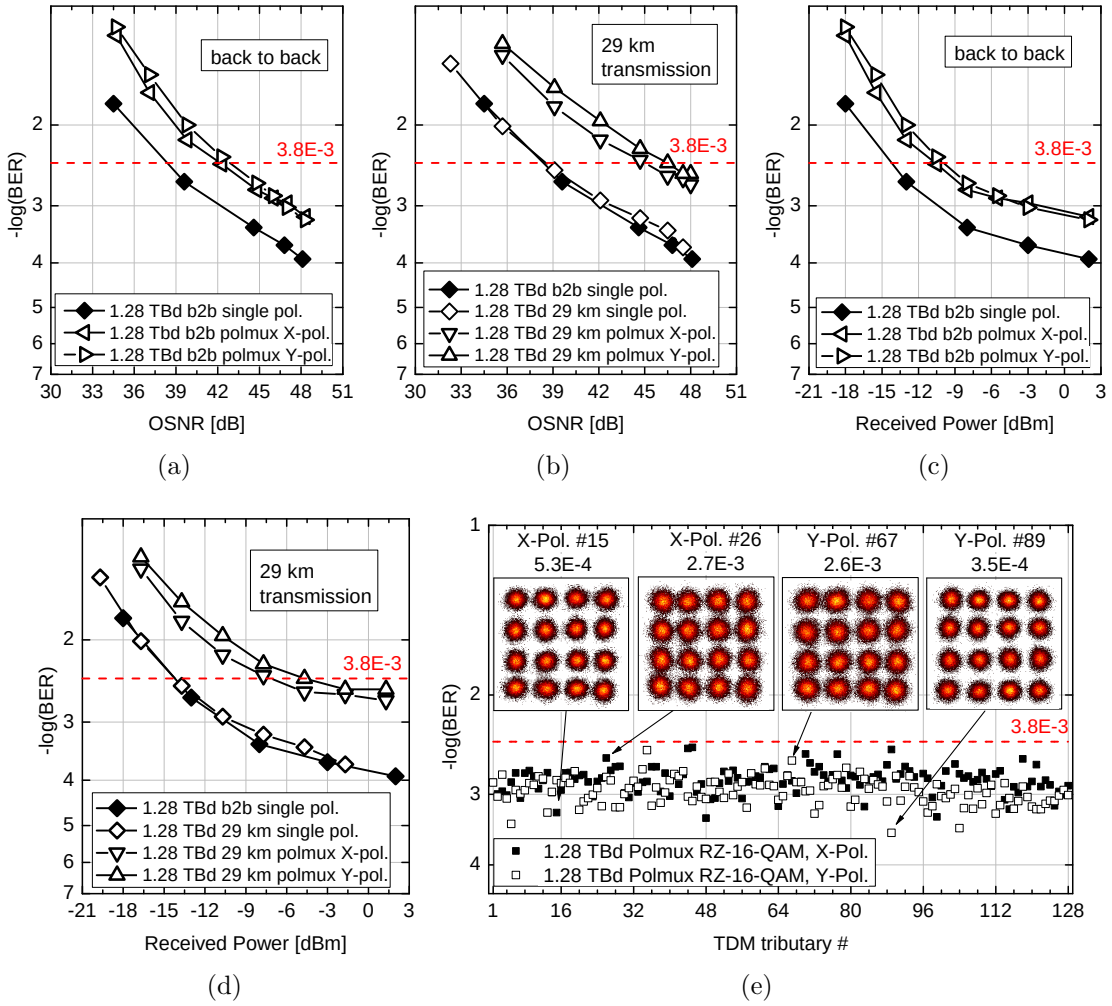


**Figure 7.7:** 10.2-Tbit/s BER measurements. (a), (c) Back-to-back BER for one TDM tributary of the 1.28-TBd single polarization (5.1 Tbit/s) data signal and after polarization multiplexing (10.2 Tbit/s). (b), (d) BER for one TDM tributary after 29-km transmission. (e) BER for all 256 tributaries (X- and Y-polarization) of the 10.2-Tbit/s data signal in back-to-back configuration. The insets show constellation diagrams with BER values for selected tributaries.

about 200000 symbols.

## 7.5 Summary

This chapter presented the combination of OTDM technology with advanced modulation formats for generation and transmission of record-high serial data rates over a single-wavelength channel. We managed to generate sub-picosecond Gaussian pulses with widths as short as 300 fs and succeeded inapplying 16-QAM in combination with up to 128-fold OTDM to reach a symbol rate of 1.28 TBd per polarization. The utilization of a pulsed local oscillator at the coherent receiver, allowed demultiplexing and demodulation of the high-speed serial data signals with a temporal resolution which is only limited by the LO pulse width. Due to the high coherence of the compressed pulses, we were able to use arbitrary pulses from the compressed pulse trains for modulation and demodulation. We used the amplitude and

phase shaping abilities of a wave-shaping filter in order to mitigate the spectral distortions induced by amplification and pulse broadening due to chromatic dispersion. We managed to compensate not only for GVD but also for higher order dispersion terms up to $\beta_4$.

We succeeded to experimentally demonstrate the transmission of 5.1 Tbit/s (640 GBd) serial-data over 80-km dispersion managed fiber (DMF) and 10.2 Tbit/s (1.28 TBd) over 29-km DMF. In the first experiment, the BER of all 128 OTDM-tributaries (both polarizations) were below the hard-decision FEC-threshold of $3.8{\cdot}10^{-3}$. This corresponds to an error-free net data rate of 4.8 Tbit/s. In the second experiment (10.2 Tbit/s), we checked the BER of all 256 TDM-tributaries (both polarizations) in the back-to-back configuration. They were all found to be below the FEC-threshold, corresponding to an error-free net data rate of 9.5 Tbit/s. Negligible pulse broadening was found after transmitting the signal through 29-km DMF. This resulted in a BER below the FEC limit for arbitrary selected tributaries.

# Chapter 8

# Conclusion

This thesis has demonstrated different all-optical signal processing functionalities for serial symbol rates up to 1.28 TBd. The utilization of the frequency-to-time and time-to-frequency OFT technique allowed the generation of flat-top pulses and the conversion of OTDM signals into parallel DWDM grids compliant with ITU-T specifications. On the other hand, the utilization of advanced modulation formats in combination with terabaud symbol rates and polarization multiplexing enabled the generation, transmission and reception of 10.2 Tbit/s OTDM. The results and conclusions are summarized in more detail below.

## 8.1 Summary

### Frequency-to-time OFT-based pulse shaping

To our knowledge, it is the first time that the frequency-to-time OFT technique has been used for the purpose of pulse shaping in the time domain. This technique is based on the duality between spatial optical systems and temporal ones. We investigated its utilization for generation of optical pulses with flat-top intensity profiles in the picosecond regime. The frequency-to-time conversion was implemented without the active phase modulation mechanism, but only by using the equivalent of the Fraunhofer far-field condition applied to the time domain case. The generation of a 1.6-ps flat-top pulse, which is the shortest reported so far using this technique, was demonstrated. The quality of the pulses was investigated in a FWM-based demultiplexing experiment at 320 GBd. The flat-top pulses showed good qualities in mitigating the deteriorations caused by the timing jitter induced in the system. The timing tolerance given by these pulses was a flat-switching window of 400 fs, and the power penalty was less than 1 dB compared to the back-to-back case. The theoretical and experimental results suggest that this technique is a powerful tool for pulse shaping purposes, and can be applied for generation of even more complex pulse shapes, such as triangular or parabolic ones, which can be of practical interest for nonlinear signal processing operations. Finally it has to be noticed that the dispersion mechanism used to reshape the intensity profile of the optical pulses, provides an additional linear chirp which was later used in the more complex scheme of serial-to-parallel conversion based on FWM.

## LPG based pulse shaping

The second technique used for generation of flat-top control pulses was based on the utilization of a pair of LPG filters inscribed in the same single-mode fiber (cascaded configuration), forming a symmetric unbalanced interferometer. For the first time, we presented results on the utilization of these flat-top pulses for error-free, low penalty, polarization-independent demultiplexing in a NOLM of a polarization-scrambled 640-GBd OTDM signal. The polarization-insensitive operation of the NOLM was achieved without changing its principle of operation but by just adjusting the control pulse's power and polarization.

## Serial-to-parallel conversion

The novel scheme, proposed in this thesis, for OTDM-to-DWDM conversion is based on the time-to-frequency OFT technique implemented via a FWM process between dispersed OTDM data and linearly chirped pump pulses. The conversion process was analyzed both numerically and experimentally, with good agreements between the two techniques. The serial-to-parallel conversion was successfully demonstrated for up to 640-GBd OTDM signals, reaching down to 25 GHz DWDM grids, which allows the simultaneous demultiplexing by passive optical filtering of more than half of the converted OTDM tributaries. It was demonstrated that the conversion process is independent on tributary data modulation and that channel spacing can be controlled by manipulating the amount of data dispersion and pump linear-chirp. At the same time tributary wavelength-allocation can be modified by changing the time delay between the pump and data signal. Except for enabling a significant reduction of the complexity of the OTDM receiver, due to its simplicity and symbol-rate scalability, the time-to-frequency OFT can enable ultra-high speed serial data communication systems with potentially moderate energy requirements.

## Re-timing and synchronization via time lensing

It was demonstrated the utilization of the space-time duality for re-timing and synchronization of optical packets with up to 12144 bits. The principle relies on the fact that temporal shifts do not distort the spectral envelope and it is based on the ability of a time lens to perform a Fourier transformation of the input signal by eliminating the misalignment between the incoming data signal and the lens' temporal axis. The implementation of the time lens was based on an electro-optical phase modulator driven by a sinusoidal electrical signal. The packet was synchronized to a local clock, whose frequency differed by 200 kHz ($\pm$20 ppm) from the input frames repetition rate. The performance of the synchronized packets was error-free and with low penalty. No extra clock recovery from the input packet signal was performed. Finally, it was shown the possibility of integration of the optical frame synchronize with OTDM systems, in order to reach up to 1.29 Tbit/s.

## High-capacity coherent OTDM

The record-high 10.2 Tbit/s serial bit rate was generated using 16-QAM modulation and 128-fold OTDM on a symbol rate of 1.28 TBd per polarization. The excellent properties of the 300 fs compressed pulses enabled the first demonstration of the successful use of 16-QAM modulation at such high symbol rate. The BER performance of all 256 tributaries

(both polarizations) was found to be below the hard-decision FEC-threshold ($3.8{\cdot}10^{-3}$) in the back-to-back configuration. This translates to an error-free net data rate of 9.5 Tbit/s. The transmission of the signal over 29-km DMF resulted in negligible pulse broadening and a BER below the FEC limit for arbitrarily selected tributaries. For the 10.2 Tbit/s experiment the signal pulses and the LO-pulses were derived from the same laser source (homodyne detection) since the relative timing jitter between the two sources limited the performance. The utilization of two independent laser sources for the signal- and LO-pulses resulted in a symbol rate of 640 GBd corresponding to a serial line rate of 5.1 Tbit/s. The BER of all 128 OTDM tributaries (both polarizations) was found to be below the hard decision FEC threshold after transmission over 80-km DMF corresponding to an error-free net data rate of 4.8 Tbit/s.

## 8.2 Outlook

The following gives a brief outlook and some suggestion for future work on two of the main topics discussed in this thesis, respectively all-optical signal processing and integration of OTDM systems with the Ethernet protocol.

### All-optical signal processing

Caulfield wrote in 1998 on the perspectives in optical computing [153] and he discussed the competition between optics (space optics) and electronics, arguing that there were three different evolutionary stages; first"ignorance and underestimation" of electronics then "awakening and fear inferiority" and now "realistic acceptance that optical computing and electronics are eternal partners" [154]. A similar discussion can be applied to all-optical signal processing as well, where, as seen in the rest of this projet, we shift from space to the time domain and recreate the same analogy. The goal of all-optical signal processing is not to substitute the role of electronics but to improve the systems performance and add functionalities in the optical domain, there where electronics can do very little or nothing at all. Compared to all-optical signal processing electronics is more mature, better funded, and has the advantage that electrons are easier to manipulate than photons. However this does not mean that there are no areas or applications where optics is superior compared to electronics. Just to mention some of them: 1) Due to the nonlinear Kerr effect, optics can process signals down to few tens of femtoseconds. 2) Optics can handle continuous data streams, while electronics by definition are digital. This can be seen in processes such as wavelength conversion, dispersion compensation, all-optical sampling etc; 3) While parallelism in electronics require the parallelization of entire systems and components, optics is parallel by nature. This is true for the time-to-frequency OFT technique, where the time lens implemented via the FWM effect can concurrently perform a Fourier transform of more than half of the OTDM channels; 4) It might be true that a single electronic operation (depending how these are defined) could be less energy consuming compared to an optical one. However, due to their large number, electronic operation require in total more energy than optical ones. In order for all-optical signal processing to become more attractive, some of its limitations, such as polarization dependence, have to be mitigated or used in a more advantageous way. In this thesis, this approach was taken with chromatic dispersion, which is usually seen as a detrimental factor in OTDM systems. However, it was possible to turn it into a desirable effect for implementing

serial-to-parallel conversion.

It is still an open question on when and how all-optical signal processing will have a higher presence outside the research environment. However, we believe it will eventually come more into focus as future applications will shape the Internet into a large photonic network.

## Integration of OTDM and Ethernet protocol

It falls out of the scope of this thesis to discuss the overall advantages and disadvantages of OTDM systems, and the role that it might play, alone or in conjunction with other technologies, in future communication systems. The actual trend in the telecommunication industry is to adopt more consolidated and mature technologies, such as WDM systems, when increasing the systems' bandwidth. In fact, the decision of IEEE P802.3ba Task Force to break with the traditional 10× hops in speed has influenced the debate on the data rate of next generation Ethernet, speculating that 400 GE might be the next step, instead of 1 TE. Already at 100 GE, the Task Force has broken the serial nature of the Ethernet protocol, by defining the 100 GE as a combination of four 25 Gbit/s lanes at different wavelengths. Based on [17] this was done as there was no other better suggestion at the time. However this does not mean that a serial 100 GE approach is impossible or un-efficient. On the other side the integration of higher OTDM rates with the Ethernet protocol might need some fundamental restructuring of the protocol itself (which is already happening) in order to fit the physical implementations and technological impairments.

# List of Acronyms

**A/D:** Analog–to–Digital Converter

**ASE:** Amplified Spontaneous Emission

**BER:** Bit–Error Ratio

**BPD:** Balanced Photo Detector

**CD:** Chromatic Dispersion

**CW:** Continuous Wave

**DCF:** Dispersion Compensating Fiber

**DD:** Direct Detection

**DDF:** Dispersion Decreasing Fiber

**DFF:** Dispersion Flattened Fiber

**DFG:** Difference Frequency Generation

**DF–HNLF:** Dispersion Flattened Highly Nonlinear Fiber

**DGD:** Differential Group Delay

**DLI:** Delay–Line Interferometer

**DMF:** Dispersion Managed Fiber

**DOP:** Degree of Polarization

**DPSK:** Differential Phase Shift Keying

**DSF:** Dispersion Shifted Fiber

**DWDM:** Dense Wavelength Division Multiplexing

**EDFA:** Erbium Doped Fiber Amplifier

**EOPM:** Electro-Optical Phase Modulator

**ERGO–PGL:** Erbium Glass Oscillator Pulse Generating Laser

**FBG:** Fiber Bragg Grating

**FWHM:** Full Width at Half Maximum

**FWM:** Four Wave Mixing

**GBd:** Giga Baud

**GVD:** Group Velocity Dispersion

**HNLF:** Highly Nonlinear Fiber

**IDF:** Inverse Dispersion Fiber

**IM:** Intensity Modulator

**IQ-Mod:** In-phase-Quadrature Modulator

**ISI:** Inter Symbol Interference

**LCFG:** Linearly Chirped Fiber Bragg Gratings

**LCIC:** Linearly Chirped Intermodal Couplers

**LCoS:** Liquid Crystal on Silicon

**LPG:** Long Period Grating

**LO:** Local Oscillator

**NRZ:** Non–Return to Zero

**OBPF:** Optical Bandpass Filter

**OFT:** Optical Fourier Transform

**OMUX:** Optical Multiplexer

**OOK:** On–Off Keying

**OSNR:** Optical Signal to Noise Ratio

**OSO:** Optical Sampling Oscilloscope

**OTDM:** Optical Time Division Multiplexing

**OTF:** Optical Tunable Filter

**PM:** Phase Modulator

**PMD:** Polarization Mode Dispersion

**PolMUX:** Polarization Multiplexing

**QAM:** Quadrature Amplitude Modulation

**QPSK:** Quadrature Phase Shift Keying

**RF:** Radio Frequency

**RZ:** Return to Zero

**SC:** Supercontinuum

**SFG:** Sum Frequency Generation

**SHG:** Second Harmonic Generation

**SLA:** Super Large Area Fiber

**SMF:** Single Mode Fiber

**SOI:** Silicon on Insulator

**SPM:** Self-Phase Modulation

**SSFBG:** Super Structured Fiber Bragg Grating

**TBd:** Tera Baud

**TDM:** Time Division Multiplexing

**TOD:** Third Order Dispersion

**TPA:** Two Photon Absorbtion

**TL:** Transform Limited

**VOA:** Variable Optical Attenuator

**WAN:** Wide Area Network

**WDM:** Wavelength Division Multiplexing

**WSF:** Wave Shaping Filter

# Bibliography


[1] *Cisco Visual Networking Index-Forecast and Methodology, 2007–2012*, Cisco white paper, 2008.

[2] (2010) German internet exchange DE-CIX, Frankfurt. [Online]. Available: http://www.de-cix.de/content/network/Traffic-Statistics.html

[3] L. Xu, S. Zhang, F. Yaman, T. Wang, G. Liao, K. C. A. Singla, A. Singh, K. Ramachandran, and Y. Zhang, "All-Optical Switching Data Center Network Supporting 100Gbps Upgrade and Mixed-Line-Rate Interoperability," in *Optical Fiber Communication Conference, OFC 2011*, Los Angeles, California, USA, Mar. 2011, paper PDPA5.

[4] J. Yu, Z. Dong, X. Xiao, Y. Xin, S. Shi, C. Ge, W. Zhou, N. Chi, and Y. Shao, "Generation, Transmission and Coherent Detection of 11.2 Tb/s (112x100Gb/s) Single Source Optical OFDM Superchannel," in *Optical Fiber Communication Conference, OFC 2011*, Los Angeles, California, USA, Mar. 2011, paper PDPA6.

[5] D. Qian, M.-F. Huang, E. Ip, Y.-K. Huang, Y. Shao, J. Hu, and T. Wang, "101.7-Tb/s (370x294-Gb/s) PDM-128QAM-OFDM Transmission over 3x55-km SSMF using Pilot-based Phase Noise Mitigation," in *Optical Fiber Communication Conference, OFC 2011*, Los Angeles, California, USA, Mar. 2011, paper PDPB5.

[6] Y. Yung, S. Alam, Z. Li, A. Dhar, D. Giles, I. Giles, J. Sahu, L. Gruner-Nielsen, F. Poletti, and D. J. Richardson, "First demonstration of multimode amplifier for spatial division multiplexed transmission systems," in *European Conference on Optical Communication, ECOC 2011*, Geneva, Switzerland, Sep. 2011, paper Th.13.K.4.

[7] J. Sakaguchi, Y. Awaji, N. Wada, A. Kanno, T. Kawanichi, T. Hayashi, T. Taru, T. Kobayashi, and M. Watanabe, "109-Tb/s (7x97x172-Gb/s SDM/WDM/PDM) QPSK transmission through 16.8-km homogeneous multi-core fiber," in *Optical Fiber Communication Conference, OFC 2011*, Los Angeles, California, USA, Mar. 2011, paper PDPB6.

[8] B. Zhu, T. F. Taunay, M. Fishteyn, X. Liu, S. Chandrasekhar, M. F. Yan, J. M. Fini, E. M. Monberg, F. V. Dimarcello, K. Abedin, P. W. Wisk, D. W. Peckham, and P. Dziedzie, "Space-, Wavelenth-, Polarization-Division Multiplexing Transmission of 56-Tb/s over a 76.8-km Seven-Core Fiber," in *Optical Fiber Communication Conference, OFC 2011*, Los Angeles, California, USA, Mar. 2011, paper PDPB7.

[9] S. Chandrasekhar, A. H. Gnauck, X. Liu, P. J. Winzer, Y. Pan, E. C. Burrows, B. Zhu, T. F. Taunay, M. Fishteyn, M. F. Yan, J. M. Fini, E. M. Monberg, and F. V. Dimarcello, "WDM/SDM Transmission of 10x128-Gb/s PDM-QPSK over 2688-km 7-Core

Fiber with a per-Fiber Net Aggregate Spectral-Efficiency Distance Product of 40,320 km·b/s/Hz," in *European Conference on Optical Communication, ECOC 2011*, Geneva, Switzerland, Sep. 2011, paper Th.13.C.4.

[10] R. S. Tucker, G. Eisenstein, and S. K. Korotky, "Optical Time-Division Multiplexing for very high bit–rate transmission," *J. Lightw. Technol.*, vol. 6, no. 11, pp. 1737–17 489, Nov. 1988.

[11] M. Nakazawa, T. Yamamoto, and K. R. Tamura, "1.28 Tbit/s-70 km OTDM transmission using third- and fourth-order simultaneous dispersion compensation with a phase modulator," *Electron. Lett.*, vol. 36, no. 24, pp. 2027–2029, Nov. 2000.

[12] H. G. Weber, S. Ferber, M. Kroh, C. Schmidt-Langhorst, R. Ludwig, V. Marembert, C. Boerner, F. Futami, S. Watanabe, and C. Schubert, "Single channel 1.28 Tbit/s and 2.56 Tbit/s DQPSK transmission," *Electron. Lett.*, vol. 42, no. 3, pp. 178–179, Feb. 2006.

[13] H. C. H. Mulvad, M. Galili, L. K. Oxenløwe, H. Hu, A. T. Clausen, J. B. Jensen, C. Peucheret, and P. Jeppesen, "Demonstration of 5.1 Tbit/s data capacity on a single-wavelength channel," *Opt. Express*, vol. 18, no. 2, pp. 1438–1443, Jan. 2010.

[14] C. Schmidt-Langhorst, R. Ludwig, D.-D. Groß, L. Molle, M. Seimetz, R. Freund, and C. Schubert, "Generation and coherent time-division demultiplexing of up to 5.1 Tb/s single-channel 8-PSK and 16-QAM signals," in *Optical Fiber Communication Conference, OFC 2009*, San Diego, California, USA, Mar. 2009, paper PDPC6.

[15] J. D'Ambrosia, "40 Gigabit Ethernet and 100 Gigabit Ethernet: The Development of a Flexinble Architecture," IEEE Commun. Mag., Mar. 2009.

[16] J. Roese, R.-P. Braun, M. Tomizawa, and O. Ishidas, "Optical Transport Network Evolving with 100 Gigabit Ethernet," *IEEE Commun. Mag.*, vol. 48, no. 3, pp. s28–s33, Mar. 2010.

[17] J. D'Ambrosia, "100 Gigabit Ethernet and Beyond," *IEEE Commun. Mag.*, vol. 48, no. 3, pp. s6–s13, Mar. 2010.

[18] HECTO Project. [Online]. Available: http://www.ict.kth.se/MAP/FMI/Hecto/Hecto.php

[19] GIBON Project. [Online]. Available: http://www.ist-gibon.eu/project.htm

[20] A. D. Ellis, J. K. Lucek, D. Pitcher, D. G. Moodie, and D. Cotter, "Full 10x10 Gbit/s OTDM generation and demultiplexing using electro absorpsion modulators," *Electro. Lett.*, vol. 34, no. 18, pp. 1688–1690, 1998.

[21] V. Kaman, Y.-J. Chiu, T. Liljeberg, S. Z. Zhang, and J. E. Bowers, "Integrated tandem travelling-wave Electroabsorpsion modulators for >100 Gbit/s OTDM applications," *IEEE Photon. Technol. Lett.*, vol. 12, no. 11, pp. 1471–1473, Nov. 2000.

[22] R. Ludwig, S. Diez, E. Erhardt, L. Kuller, W. Pieper, and H. G. Weber, "A tunable femtosecond modelocked semiconductor laser for applications in OTDM systems," *IEICE Transac. Electron.*, vol. E81C, no. 2, pp. 140–145, 1998.

[23] L. Krainer, R. Pascotta, G. J. Spühler, I. Klimov, C. Y. Teisset, and K. J. Weingarten, "Tunable picosecond pulse-generating laser with repetition rate exceeding 10 GHz," *Electro. Lett.*, vol. 38, no. 5, pp. 225–227, Feb. 2002.

[24] G. P. Agrawal, *Nonlinear Fiber Optics*, 4th ed. Academic Press, 2007.

[25] H. C. M. Mulvad, M. Galili, L. K. Oxenløwe, A. T. Clausen, L. G.-Nielsen, and P. Jeppesen, "Polarization-Independent High–Speed Switching in a Standard Non-Linear Optical Loop Mirror," in *Optical Fiber Communication Conference, OFC 2008*, San Diego, California, USA, Mar. 2008, paper OMN3.

[26] A. M. Weiner, "Femtosecond optical pulse shaping and processing," *Prog. Quant. Electr.*, vol. 19, no. 3, pp. 161–237, 1995.

[27] T. Otani, T. Miyajaki, and S. Yamamoto, "Optical 3R regenerator using wavelength converters based on electroabsorption modulator for all-optical network applications," *IEEE Photon. Technol. Lett.*, vol. 12, no. 4, pp. 431–433, Apr. 2000.

[28] F. Parmigiani, P. Petropoulos, M. Ibsen, and D. J. Richardson, "All-optical pulse reshaping and retiming systems incorporating pulse shaping fiber Bragg grating," *J. Lightw. Technol.*, vol. 24, no. 1, pp. 357–364, Jan. 2006.

[29] F. Parmigiani, C. Finot, K. Mukasa, M. Ibsen, M. A. F. Roelens, P. Petropoulos, and D. J. Richardson, "Ultra-flat SPM-broadened spectra in a highly nonlinear fiber using parabolic pulses formed in a fiber Bragg grating," *Opt. Express*, vol. 14, no. 17, pp. 7617–7622, Aug. 2006.

[30] N. Bloembergen, *Nonlinear Optics*, 1st ed. Benjamin Reading, 1977.

[31] Y. R. Shen, *Principles of Nonlinear Optics*, 1st ed. Wiley, 1984.

[32] P. N. Butcher and D. N. Cotter, *The Elements of Nonlinear Optics*, 1st ed. Cambridge University Press, 1990.

[33] R. W. Boyd, *Nonlinear Optics*, 2nd ed. Academic Press, 2003.

[34] A. M. Weiner, *Ultrafast Optics*, 1st ed. Wiley, 2009.

[35] S. Yamashita and M. Tani, "Cancellation of Spectral Spread in SBS-Suppressed Fiber Wavelength Converters Using a Single Phase Modulator," *IEEE Photon. Technol. Lett.*, vol. 16, no. 9, pp. 2096–2098, Sep. 2004.

[36] B. P.-P. Kuo, E. Myslivets, N. Alic, and S. Radic, "Wavelength Multicasting via Frequency Comb Generation in a Bandwidth-Enhanced Fiber Optical Parametric Mixer," *J. Lightw. Technol.*, vol. 29, no. 23, pp. 3515–3522, Dec. 2011.

[37] R. Salem, M. A. Foster, A. C. Turner, D. F. Geraghty, M. Lipson, and A. L. Gaeta, "Optical time lens based on four-wave mixing on a silicon chip," *Opt. Lett.*, vol. 33, no. 10, pp. 1047–1049, May 2008.

[38] T. Richter, R. Elschner, A. Gandhe, and C. Schubert, "Parametric Amplification of 112 Gbit/s Polarization Multiplexed DQPSK Signals in a Fiber Loop Configuration," in *Optical Fiber Communication Conference, OFC 2011*, Los Angeles, California, USA, Mar. 2011, paper OThC4.

[39] F. Parmigiani, R. Slavik, J. Kakande, C. Lundstrom, M. Sjodin, P. Andrekson, R. Weerasuriya, S. Sygletos, A. D. Ellis, L. Gruner-Nielsen, D. Jakobsen, S. Herstrom, R. Phelan, J. O'Gorman, A. Bogris, D. Syvridis, S. Dasgupta, P. Petropoulos, and D. J. Richardson, "All-optical phase regeneration of 40Gbit/s DPSK signals in a black-box phase sensitive amplifier," in *Optical Fiber Communication Conference, OFC 2010*, San Diego, California, USA, Mar. 2010, paper PDPC3.

[40] R. H. Stolen, J. E. Bjorkholm, and A. Ashkin, "Phase-matched three-wave mixing in silica fiber optical waveguides," *Appl. Phys. Lett.*, vol. 24, no. 7, pp. 308–311, Apr. 1974.

[41] R. H. Stolen, "Phase-Matched-Stimulated Four-Photon Mixing in Silica-Fiber Waveguides," *IEEE J. Quantum Electron.*, vol. QE-11, no. 3.

[42] G. Sagnac, "Interference of two beams which have described the same circuit in opposite directions," *Comptes Rendus Hebdomadaires des Seances de l'Academie des Sciences*, vol. 150, pp. 1737–1739, Dec. 1910.

[43] M. Jinno, "Effects of Group Velocity Dispersion on Self/Cross Phase Modulation in a Nonlinear Sagnac Interferometer Switch," *J. Lightw. Technol.*, vol. 10, no. 8, pp. 1167–1178, Aug. 1992.

[44] N. Doran and D. Wood, "Nonlinear-optical loop mirror," *Opt. Lett.*, vol. 13, no. 1, pp. 56–58, Jan. 1988.

[45] K. Blow, N. Doran, B. Nayar, and B. Nelson, "Two-wavelength operation of the nonlinear fiber loop mirror," *Opt. Lett.*, vol. 15, no. 4, pp. 248–250, Feb. 1990.

[46] K. J. Blow, N. J. Doran, and B. P. Nelson, "Demonstration of the nonlinear fibre loop mirror as an ultrafast all-optical demultiplexer," *Electron. Lett.*, vol. 26, no. 14, pp. 962–964, Jul. 1990.

[47] M. Jinno and T. Matsumoto, "Nonlinear Sagnac interferometer switch and its applications," *IEEE J. Quantum Electron.*, vol. 28, no. 4, pp. 875–882, Apr. 1992.

[48] M. Jinno, "Effects of Crosstalk and Timing Jitter on All-Optical Time-Division Demultiplexing Using a Nonlinear Fiber Sagnac Interferometer Switch," *IEEE J. Quantum Electron.*, vol. 30, no. 12, pp. 2842–2853, Dec. 1994.

[49] N. Finlayson, B. Nayar, and N. Doran, "Switch inversion and polarization sensitivity of the nonlinear-optical loop mirror," *Opt. Lett.*, vol. 17, no. 2, pp. 112–114, Jan. 1992.

[50] A. Bogoni, M. Scaffardi, P. Ghelfi, and L. Poti, "Nonlinear optical loop mirrors: investigation solution and experimental validation for undesirable counterpropagating effects in all-optical signal processing," *IEEE J. Sel. Topics Quantum Electron.*, vol. 10, no. 5, pp. 1115–1123, Oct. 2004.

[51] A. T. Clausen, H. N. Poulsen, L. K. Oxenløwe, A. I. Siahlo, J. Seoane, and P. Jeppesen, "Pulse source requirements for OTDM systems," in *The 16th Annual Meeting of the IEEE Lasers and Electro-Optics Society, LEOS 2003*, vol. 1, San Diego USA, pp. 382–383.

[52] A. M. Weiner and J. P. Heritage, "Picosecond and femtosecond Fourier pulse shape synthesis," *Rev. Phys. Appl.*, vol. 22, no. 12, pp. 1619–1628, 1987.

[53] W. Tomlinson, R. Stolen, and C. Shank, "Compression of optical pulses chirped by self–phase modulation in fibers," *J. Opt. Soc. Am. B*, vol. 1, no. 2, pp. 139–149, Apr. 1984.

[54] S. Taccheo and P. Vavassori, "Dispersion-flattened fiber for effcient supercontinuum generation," in *Optical Fiber Communication Conference, OFC 2002*, Anaheim, California, USA, Mar. 2002, paper ThY5.

[55] Y. Yang, C. Lou, H. Zhou, J. Wang, and Y. Gao, "Simple pulse compression scheme based on filtering self-phase modulation-broadened spectrum and its application in an optical time-division multiplexing system," *Appl. Opt.*, vol. 45, no. 28, pp. 7524–7528, Oct. 2006.

[56] T. Morioka, H. Takara, S. Kawanishi, O. Kamatani, K. Takiguchi, K. Uchiyama, M. Saruwatari, H. Takahashi, M. Yamada, T. Kanamori, and H. Ono, "1 Tbit/s (100 Gbitx10 channel) OTDM/WDM transmission using a single supercontinuum WDM source," *Electron. Lett.*, vol. 32, no. 10, pp. 906–907, May 1996.

[57] N. J. Doran and K. J. Blow, "Solitons in Optical Communications," *IEEE J. Quantum Electron.*, vol. QE–19, no. 12, pp. 1883–1888, Dec. 1983.

[58] N. J. Smith and N. J. Doran, "Picosecond soliton propagation using nonlinear optical loop mirrors as intensity filters," *Electron. Lett.*, vol. 30, no. 13, pp. 1084–1085, Jun. 1994.

[59] L. J. Richardson, W. Forysiak, and N. J. Doran, "Dispersion-managed soliton propagation in short-period dispersion maps," *Opt. Lett.*, vol. 25, no. 14, pp. 1010–1012, Jul. 2000.

[60] K. A. Ahmed, K. C. Chan, and H. F. Liu, "Femtosecond pulse generation from semiconductor lasers using the soliton-effect compression technique," *IEEE J. Sel. Topics Quantum Electron.*, vol. 1, no. 2, pp. 592–600, Jun. 1995.

[61] L. Chusseau and E. Devalaque, "250-fs optical pulse generation by simultaneous soliton compression and shaping in a nonlinear optical loop mirror including a weak attenuation," *Opt. Lett.*, vol. 19, no. 10, pp. 734–736, Apr. 1994.

[62] K. Tamura and M. Nakazawa, "Spectral-smoothing and pedestal reduction of wavelength tunable quasi-adiabatically compressed femtosecond solitons using a dispersion-flattened dispersion-imbalanced loop mirror," *IEEE Photon. Technol. Lett.*, vol. 11, no. 2, pp. 230–232, Feb. 1999.

[63] K. Smith and L. F. Mollenauer, "Experimental observation of adiabatic compression and expanssion of soliton pulses over long fiber paths," *Opt. Lett.*, vol. 14, no. 14, pp. 751–753, Jul. 1989.

[64] S. V. Chernikov and P. V. Mamyshev, "Femtosecond soliton propagation in fibers with slowly decreasing dispersion," *J. Opt. Soc. Amer. B*, vol. 8, no. 8, pp. 1633–1641, Aug. 1991.

[65] S. V. Chernikov, E. M. Dianov, D. J. Richardson, and D. N. Payne, "Soliton pulse compression in dispersion decreasing fiber," *Opt. Lett.*, vol. 18, no. 7, pp. 476–478, Apr. 1993.

[66] M. Schell, D. Bimberg, V. A. Bogatyrjov, E. M. Dianov, A. S. Kurkov, V. A. Semenov, and A. A. Sysoliatin, "540 fs light pulses at 1.5 $\mu$m with variable repetition rate using a tunable twin guide laser and soliton compression in a dispersion decreasing fiber," *IEEE Photon. Technol. Lett.*, vol. 6, pp. 1191–1193, Oct. 1994.

[67] M. Pelusi and H.-F. Liu, "Higher order soliton pulse compression in dispersion-decreasing optical fibers," *IEEE J. Quantum Electron.*, vol. 33, no. 8, pp. 1430–1439, Aug. 1997.

[68] M. Nakazawa, E. Yoshida, H. Kubota, and Y. Kimura, "Generation of a 170 fs, 10 Ghz transform-limited pulse train at 1.55 $\mu$m using a dispersion-decreasing, erbium-doped active soliton compressor," *Electron. Lett.*, vol. 30, no. 24, pp. 2038–2040, Nov. 1994.

[69] M. Nakazawa, E. Yoshida, T. Yamamoto, E. Yamada, and A. Sahara, "TDM single channel 640 Gbit/s transmission experiment over 60 km using 400 fs pulse train and walk-off free, dispersion flattened nonlinear optical loop mirror," *Electron. Lett.*, vol. 34, no. 9, pp. 907–908, Apr. 1998.

[70] F. L. Pedrotti and L. S. Pedrotti, *Introduction to Optics*, 2nd ed. Pentics–Hall, 1993.

[71] M. T. Kauffman, W. C. Banyal, A. A. Godil, and D. M. Bloom, "Time-to-frequency converter for measuring picosecond optical pulses," *Appl. Phys. Lett.*, vol. 64, no. 3, pp. 270–272, Jan. 1994.

[72] A. W. Lohmann and D. Mendlovic, "Temporal filtering with time lenses," *Appl. Opt.*, vol. 31, no. 29, pp. 6212–6219, Oct. 1992.

[73] M. T. Kauffman, A. A. Godil, B. A. Auld, W. C. Banyai, and D. M. Bloom, "Applications of time lens optical systems," *Electron. Lett.*, vol. 39, no. 3, pp. 268–269, Feb. 1993.

[74] A. A. Godil, B. A. Auld, , and D. M. Bloom, "Picosecond time-lenses," *IEEE J. Quantum Electron.*, vol. 30, no. 3, pp. 827–837, Mar. 1994.

[75] A. Papoulis, "Pulse compression, fiber communications, and diffraction: A unified approach," *J. Opt. Soc. Amer. A, Opt. Image Sci.*, vol. 11, no. 1, pp. 3–13, Jan. 1994.

[76] B. H. Kolner, "Space-Time Duality and the Theory of Temporal Imaging," *IEEE J. Quantum Electron.*, vol. 30, no. 8, pp. 1951–1963, Aug. 1994.

[77] X. Yang, "Implementation of time lenses and optical temporal processors," *Opt. Commun.*, vol. 116, no. 1, pp. 193–207, Feb. 1995.

[78] P. Naulleau and E. Leith, "Stretch, time lenses and incoherent time imaging," *Appl. Opt.*, vol. 34, no. 20, pp. 4119–4128, Jul. 1995.

[79] V. B. Yurchenko, "Improving the accuracy of a time lens," *J. Opt. Soc. Amer. B, Opt. Phys.*, vol. 14, no. 11, pp. 2921–2924, Nov. 1997.

[80] C. V. Bennett and B. H. Kolner, "Upconversion time microscope demonstrating 103x magnification of femtosecond waveforms," *Opt. Lett.*, vol. 24, no. 11, pp. 783–785, Jun. 1999.

[81] K. N. Berger, B. Levit, S. Atkins, and B. Fischer, "Time-lens-based spectral analysis of optical pulses by electrooptic phase modulation," *Electro. Lett.*, vol. 36, no. 19, pp. 1644–1646, Sep. 2000.

[82] L. K. Mouradian, F. Louradour, V. Messager, A. Barthelemy, , and C. Froehly, "Spectro-temporal imaging of femtosecond events," *IEEE J. Quantum Electron.*, vol. 36, no. 7, p. 795801, Jul. 2000.

[83] C. V. Benett, R. P. Scott, and B. H. Kolner, "Temporal magnification and reversal of 100 Gb/s optical data with an up-conversion time microscope," *Appl. Phys. Lett.*, vol. 65, no. 20, pp. 2513–2515, Nov. 1994.

[84] T. Hirooka and M. Nakazawa, "Optical Adaptive Equalization of High-Speed Signals Using Time-Domain Optical Fourier Transformation," *J. Lightw. Technol.*, vol. 24, no. 7, pp. 2530–2540, Jul. 2006.

[85] P. J. Almeida, P. Petropoulos, B. C. Thomsen, M. Ibsen, and D. J. Richardson, "All-optical packet compression based on time-to-wavelength conversion," *IEEE Photon. Technol. Lett.*, vol. 16, no. 7, pp. 1688–1690, Jul. 2004.

[86] J. Azaña, N. K. Berger, and B. Fischer, "Simplified Temporal Imaging Systems for Optical Waveforms," *IEEE Photon. Technol. Lett.*, vol. 17, no. 1, pp. 94–96, Jan. 2005.

[87] J. Azaña and M. A. Muriel, "Fiber Optics and Optical Communications-Technique for multiplying the repetition rates of periodic trains of pulses by means of a temporal self-imaging effect in chirped fiber gratings," *Opt. Lett.*, vol. 24, no. 23, pp. 1672–1674, Dec. 1999.

[88] T. Ng, F. Parmigiani, M. Ibsen, Z. Zhang, P. Petropoulos, and D. J. Richardson, "Compensation of Linear Distorsion by Using XPM With Parabolic Pulses as a Time Lens," *IEEE Photon. Technol. Lett.*, vol. 20, no. 13, pp. 1097–1099, Jul. 2008.

[89] E. Arons, E. N. Leith, A.-C. Tien, and R. Wagner, "High-resolution optical chirped pulse gating," *Appl. Opt.*, vol. 36, no. 12, pp. 2603–2608, Apr. 1997.

[90] Y. Okawachi, R. Salem, M. A. Foster, A. C. Turner-Foster, M. Lipson, and A. L. Gaeta, "100x Frequency Magnification Using a Time-Lens-Based Spectral Imaging System," in *Conference on Lasers and Electro–Optics, CLEO 2009*, 2009, paper CWB4.

[91] ——, "High-resolution spectroscopy using a frequency magnifier," *Opt. Express*, vol. 17, no. 7, pp. 5691–5697, Mar. 2009.

[92] J. W. Goodman, *Introduction to Fourier Optics*, 2nd ed. McGraw–Hill, 1996.

[93] J. Azaña, "Time-to-frequency conversion using a single time lens," *Opt. Commun.*, vol. 217, no. 1, pp. 205–209, Jan. 2003.

[94] J. Azaña and M. A. Muriel, "Real-Time Optical Spectrum Analysis Based on the Time-Space Duality in Chirped Fiber Gratings," *IEEE J. Quantum Electron.*, vol. 36, no. 5, pp. 517–526, May 2000.

[95] J. U. Jeon, H. K. Seo, and Y. T.Lee, "Wide-band High Negative Dispersion-Flattened Fiber," in *European Conference on Optical Communication, ECOC 2002*, Copenhagen, Denmark, Sep. 2002, paper P1.35.

[96] J. Azaña, M. A. Muriel, and A. Carballar, "Real-Time Fourier Transformation based on Fiber Gratings," *Opt. Lett.*, vol. 24, no. 1, pp. 1–3, May 1999.

[97] J. Azaña and M. A. Muriel, "Temporal Talbot Effect in Fiber Gratings and its Applications," *Appl. Opt.*, vol. 38, no. 32, pp. 6700–6704, Nov. 1999.

[98] T. Yamamoto, E. Yoshida, and M. Nakazawa, "Ultrafast nonlinear optical loop mirror for demultiplexing 640 Gbit/s TDM signals," *Electron. Lett.*, vol. 34, no. 10, pp. 1013–1014, May 1998.

[99] S. Watanabe, "Optical signal processing using nonlinear fibers," *J. Opt. Fiber Commun. Reports*, vol. 3, no. 1, pp. 1–24, 2006.

[100] E. Tangdiongga, Y. Liu, H. de Waardt, G. D. Khoe, A. M. J. Koonen, H. J. S. Dorren, X. Shu, and I. Bennion, "All-optical demultiplexing of 640 to 40 Gbits/s using filtered chirp of a semiconductor optical amplifier," *Opt. Lett.*, vol. 32, no. 7, pp. 835–837, Apr. 2007.

[101] L. K. Oxenløwe, R. Slavík, M. Galili, H. C. M. Mulvad, A. T. Clausen, Y. Park, J. Azaña, and P. Jeppesen, "640 Gbit/s Timing Jitter Tolerant Data Processing Using a Long-Period Fiber Grating-based Flat-Top Pulse Shaper," *IEEE J. Sel. Topics Quantum Electron.*, vol. 14, no. 3, pp. 566–572, May 2008.

[102] F. Parmigiani, L. K. Oxenløwe, M. Galili, M. Ibsen, D. Zibar, P. Petropoulos, D. Richardson, A. T. Clausen, and P. Jeppesen, "All-optical 160 Gbit/s RZ data retiming system incorporating a pulse shaping fibre Bragg grating," in *European Conference on Optical Communication, ECOC 2007*, Berlin, Germany, Sep. 2007.

[103] K. Uchiyama, S. Kawanishi, H. Takara, T. Morioka, and M. Saruwatari, "100 Gbit/s to 6.3 Gbit/s demultiplexing experiment using polarization-independent nonlinear optical loop mirror," *Electron. Lett.*, vol. 30, no. 11, pp. 873–875, Mar. 1994.

[104] B.-E. Olsson and P. A. Andrekson, "Polarization Independent Demultiplexing in a Polarization Diversity Nonlinear Optical Loop Mirror," *IEEE Photon. Technol. Lett.*, vol. 9, no. 6, pp. 764–766, Jun. 1997.

[105] T. Sakamoto, H. C. Lim, and K. Kikuchi, "All-optical polarization-insensitive time-division demultiplexer using a nonlinear optical loop mirror with a pair of short polarization-maintaining fibers," *IEEE Photon. Technol. Lett.*, vol. 14, no. 12, pp. 1737–1739, Dec. 2002.

[106] T. Morioka, S. Kawanishi, K. Uchiyama, H. Takara, and M. Saruwatari, "Polarization-independent 100 Gbit/s all-optical demultiplexer using four-wave mixing in a polarization-maintaining fiber loop," *Electron. Lett.*, vol. 30, no. 7, pp. 591–592, Mar. 1994.

[107] T. Sakamoto, K. Seo, K. Taira, N. S. Moon, and K. Kikuchi, "Polarization-insensitive all-optical time-division demultiplexing using a fiber four-wave mixer with a peak-holding optical phase-locked loop," *IEEE Photon. Technol. Lett.*, vol. 16, no. 2, pp. 563–565, Feb. 2004.

[108] R. Salem, A. S. Lenihan, G. M. Carter, and T. E. Murphy, "160-Gb/s Polarization-Independent Optical Demultiplexing in 2-m Nonlinear fiber," *IEEE Photon. Technol. Lett.*, vol. 18, no. 21, pp. 2245–2247, Nov. 2006.

[109] R. Slavík, Y. Park, and J. Azaña, "Long-Period Fiber-Grating-Based Filter for Generation of Picosecond and Sub-Picosecond Transform-Limited Flat-Top Pulses," *IEEE Photon. Technol. Lett.*, vol. 20, no. 10, pp. 806–808, May 2008.

[110] W. F. Xiaohui, L. Chao, Y. H. Tam, and H. S. Wang, "Flat-top pulse generation based on the combined action of active mode locking and nonlinear polarization rotation," in *Conference on Lasers and Electro–Optics, CLEO/QELS 2008*, 2008, paper JTuA91.

[111] K. N. Berger, B. Levit, B. Fischer, and J. Azaña, "Picosecond flat-top pulse generation by low-bandwidth electro-optic sinusoidal phase modulation," *Opt. Lett.*, vol. 33, no. 2, pp. 125–127, Jan. 2008.

[112] P. Petropoulos, M. Ibsen, A. D. Ellis, and D. J. Richardson, "Rectangular pulse generation based on pulse reshaping using a superstructured fiber Bragg grating," *J. Lightw. Technol.*, vol. 19, no. 5, pp. 746–752, May 2001.

[113] R. Slavík, L. Oxenløwe, M. Galili, H. C. H. Mulvad, Y. Park, J. Azaña, and P. Jeppesen, "Demultiplexing of 320-Gb/t OTDM Data Using Flat-Top Pulses," *IEEE Photon. Technol. Lett.*, vol. 19, no. 22, pp. 1855–1857, Nov. 2007.

[114] Y. Park, M. Kulishov, R. Slavík, and J. Azaña, "Picosecond and sub-picosecond flat-top pulse generation using uniform long-period fiber grating," *Opt. Express*, vol. 14, no. 26, pp. 12 671–12 678, Dec. 2006.

[115] R. Slavík, Y. Park, and J. Azaña, "Tunable dispersion-tolerant picosecond flat-top waveform generation using an optical differentiator," *Opt. Express*, vol. 15, no. 11, pp. 6717–6726, May 2007.

[116] L. K. Oxenløwe, M. Galili, H. C. M. Mulvad, R. Slavík, A. T. Clausen, and P. Jeppesen, "Polarisation-independent sub-picosecond flat-top pulse generation for ultra-fast 640 Gbit/s gating," in *Optical Fiber Communication Conference, OFC 2009*, San Diego, California, USA, Mar. 2009, paper OWS5.

[117] M. H. Asghari and J. Azaña, "Proposal and analysis of a reconfigurable pulse shaping technique based on multi-arm optical differentiators," *Opt. Comm.*, vol. 281, no. 18, pp. 4581–4588, May 2008.

[118] M. Kulishov and J. Azaña, "Long-period fiber gratings as ultrafast optical differentiators," *Opt. Lett.*, vol. 30, no. 20, pp. 2700–2702, Oct. 2005.

[119] R. Slavík, Y. Park, M. Kulishov, R. Morandotti, and J. Azaña, "Ultrafast all-optical differentiators," *Opt. Express*, vol. 14, no. 22, pp. 10 699–10 707, Oct. 2006.

[120] R. Kashyap, *Fiber Bragg Gratings*, 2nd ed. Academic Press, 2009.

[121] A. M. Vengsarkar, P. J. Lemaire, J. B. Judkins, V. Bhatia, T. Erdogan, and J. E. Sipe, "Long-period fiber gratings as band-rejection filters," *J. Lightw. Technol.*, vol. 14, no. 1, pp. 58–65, Jan. 1996.

[122] Y. Park, J. Azaña, and R. Slavík, "Ultrafast all-optical first and higher-order differentiators based on interferometers," *Opt. Lett.*, vol. 32, no. 6, pp. 710–712, Mar. 2007.

[123] R. Slavík, Y. Park, D. Krčmařík, and J. Azaña, "Stable all-fiber photonic temporal differentiator using a long-period fiber grating interferometer," *Opt. Comm.*, vol. 282, no. 12, pp. 2339–2342, Feb. 2009.

[124] K. Uchiyama, H. Takara, K. Mori, and T. Morioka, "160 Gbit/s all-optical time-division demultiplexing utilising modified multiple-output OTDM demultiplexer (MOXIC)," *Electron. Lett.*, vol. 38, no. 20, pp. 1190–1191, Sep. 2002.

[125] C.-S. Brès, A. O. J. Wiberg, B. P.-P. Kuo, J. M. C.-Boggio, C. F. Marki, N. Alic, and S. Radic, "Single-gate 320-to-8x40 Gb/s demultiplexing," in *Optical Fiber Communication Conference, OFC 2009*, San Diego, California, USA, Mar. 2009, paper PDPA4.

[126] S. Liu, K. J. Lee, F. Parmigiani, M. Ibsen, P. Petropoulos, D. Richardson, and K. Gallo, "OTDM to WDM Format Conversion Based on Cascaded SHG/DFG in a Single PPLN Waveguide," in *Optical Fiber Communication Conference, OFC 2010*, San Diego, California, USA, Mar. 2010, paper OWF4.

[127] *ITU-T G.694.1: Spectral grids for WDM applications: DWDM frequency grid.*, ITU-T, May 2002.

[128] C. V. Benett and B. H. Kolner, "Principles of Parametric Temporal Imaging-Part I: System Configurations," *IEEE J. Quantum Electron.*, vol. 36, no. 4, pp. 430–437, Apr. 2000.

[129] G. Bosco, A. Carena, V. Curri, R. Gaudino, P. Poggiolini, and S. Benedetto, "Suppression of Spurious Tones induced by the Split-Step Method in fiber Systems Simulation," *IEEE Photon. Technol. Lett.*, vol. 12, no. 5, pp. 489–491, May 2000.

[130] L. G. Nielsen, M. Wandel, P. Kristensen, C. Jørgensen, L. V. Jørgensen, B. Edvold, B. Pálsdóttir, and D. Jakobsen, "Dispersion–Compensating Fibers," *J. Lightw. Technol.*, vol. 23, no. 11, pp. 3566–3579, Nov. 2005.

[131] H. C. H. Mulvad, L. K. Oxenløwe, M. Galili, A. T.Clausen, L. Nielsen, and P. Jeppesen, "1.28 Tbit/s single-polarisation serial OOK optical data generation and demultiplexing," *Electron. Lett.*, vol. 45, no. 5, pp. 280–281, Feb. 2009.

[132] P. J. Winzer and R.-J. Essiambre, "Advanced Modulation Formats for High-Capacity Optical Transport Networks," *J. Lightw. Technol.*, vol. 24, no. 12, pp. 4711–4728, Dec. 2006.

[133] M. Seimetz, *High-Order Modulation for Optical Fiber Transmission.* Heidelberg Springer: Optical Sciences, 2009.

[134] Y. Cai, "Performance and Limits of FEC and Modulation Formats in Optical Fiber Communications," in *The 19th Annual Meeting of the IEEE Lasers and Electro-Optics Society, LEOS 2006*, Oct. 2003, paper WH1.

[135] M. A. Foster, A. C. Turner, R. Salem, M. Lipson, and A. L. Gaeta, "Broad-band continuous-wave parametric wavelength conversion in silicon nanowaveguides," *Opt. Express*, vol. 15, no. 20, pp. 12 949–12 958, Oct. 2007.

[136] M. A. Foster, R. Salem, D. F. Geraghty, A. C. Turner-Foster, M. Lipson, and A. L. Gaeta, "Silicon-chip-based ultrafast optical oscilloscope," *Nature*, vol. 456, no. 7218, pp. 81–84, Nov. 2008.

[137] H. Hu, H. Ji, M. Galili, M. Pu, C. Peucheret, H. C. H. Mulvad, K. Yvind, J. M. Hvam, P. Jeppesen, and L. K. Oxenløwe, "Ultra-high-speed wavelength conversion in a silicon photonic chip," *Opt. Express*, vol. 19, no. 21, pp. 19 886–19 894, Oct. 2011.

[138] H. Ji, M. Pu, H. Hu, M. Galili, L. K. Oxenløwe, K. Yvind, J. M. Hvam, and P. Jeppesen, "Optical waveform sampling and error-free demultiplexing of 1.28 Tb/s serial data in a nanoengineered silicon waveguide," *J. Lightw. Technol.*, vol. 29, no. 4, pp. 426–431, Sep. 2011.

[139] *802.3ae-Amendments, Parameters for 10 Gb/s Operation*, IEEE, 2002.

[140] J. Harrison, K. Blow, and A. Poustie, "All-optical bit-level retiming and jitter suppression," *Opt. Commun.*, vol. 240, no. 1, pp. 221–226, Jun. 2004.

[141] X. Huang, P. Ye, M. Zhang, and L. Wang, "A novel self-synchronization scheme for all-optical packet networks," *IEEE Photon. Technol. Lett.*, vol. 17, no. 3, pp. 645–647, Mar. 2005.

[142] D. Petrantonakis, D. Apostolopoulos, O. Zouraraki, D. Tsiokos, P. Bakopoulos, and H. Avramopoulos, "Packet-level synchronization scheme for optical packet switched network nodes," *Opt. Express*, vol. 14, no. 26, pp. 12 665–12 669, Dec. 2006.

[143] J. v. Howe and C. Xu, "Ultrafast Optical Signal Processing Based Upon SpaceTime Dualities," *J. Lightw. Technol.*, vol. 24, no. 7, pp. 2649–2662, Jul. 2006.

[144] C. Meirosu, P. Golonka, A. Hirstius, S. Stancu, B. Dobinson, E. Radius, A. Antony, F. Dijkstra, J. Blom, and C. de Laat, "Native 10 Gigabit Ethernet experiments over long distances," *Future Gener. Comput. Syst.*, vol. 21, no. 4, pp. 457–468, Nov. 2006.

[145] H. Hu, M. Galili, L. K. Oxenløwe, J. Xu, H. C. H. Mulvad, C. Peucheret, A. T. Clausen, and P. Jeppesen, "Error-free transmission of serial 1.28 Tbaud RZ-DPSK signal," in *European Conference on Optical Communication, ECOC 2010*, Torino, Italy, Sep. 2010, paper P4.18.

[146] G. Raybon, P. J. Winzer, A. A. Adamiecki, A. H. Gnauck, A. Konczykowska, and F. Jorge, "All-ETDM 80-Gbaud (160-Gb/s) QPSK Generation and Coherent Detection," *IEEE Photon. Technol. Lett.*, vol. 23, no. 22, pp. 1667–1669, Nov. 2011.

[147] F. Ito, "Interferometric demultiplexing experiment using linear coherent correlation with modulated local oscillator," *Electron. Lett.*, vol. 32, no. 1, pp. 14–15, Jan. 1996.

[148] ——, "Demultiplexed Detection of Ultrafast Optical Signal Using Interferometric Cross-Correlation Technique," *J. Lightw. Technol.*, vol. 15, no. 6, pp. 930–937, Jun. 1997.

[149] C. Zhang, Y. Mori, K. Igarashi, K. Katoh, and K. Kikuchi, "Ultrafast operation of digital coherent receivers using their time-division demultiplexing function," *J. Lightw. Technol.*, vol. 27, no. 3, pp. 224–232, Feb. 2009.

[150] E. M. Ip and J. M. Kahn, "Digital equalization of chromatic dispersion and polarization mode dispersion," *J. Lightw. Technol.*, vol. 25, no. 8, pp. 2033–2043, Aug. 2007.

[151] S. J. Savory, "Digital Coherent Optical Receivers: Algorithms and Subsystems," *IEEE J. Sel. Topics Quantum Electron.*, vol. 16, no. 5, pp. 1164–1179, Sep. 2010.

[152] E. M. Ip and J. M. Kahn, "Fiber Impairment Compensation Using Coherent Detection and Digital Signal Processing," *J. Lightw. Technol.*, vol. 28, no. 4, pp. 502–519, Feb. 2010.

[153] H. J. Caulfield, "Perspectives in optical computing," *Computer*, vol. 31, no. 2, pp. 22–25, Aug. 1998.

[154] P. Ambs, "Optical Computing: A 60-Year Adventure," *Advanc. Opt. Commun.*, vol. 2010, pp. 1–15, Feb. 2010.

[155] B. Nebendahl and B. Szafraniec, *Agilent Metrology of Advanced Optical Modulation Formats*, Agilent Technologies, Apr. 2009. [Online]. Available: http://cp.literature.agilent.com/litweb/pdf/5990-3748EN.pdf

[156] D. S. Millar and S. J. Savory, "Blind adaptive equalization of polarization-switched QPSK modulation," *Opt. Express*, vol. 19, no. 9, pp. 8533–8538, Apr. 2011.

[157] D. S. Millar, D. Lavery, S. Makovejs, C. Behrens, B. C. Thomsen, P. Bayvel, and S. J. Savory, "Generation and long-haul transmission of polarization-switched QPSK at 42.9 Gb/s," *Opt. Express*, vol. 19, no. 10, pp. 9296–9302, Apr. 2011.

# .1 Coherent detection of optical advanced modulation formats

The fundamental methods of encoding digital information onto an optical carrier are identical to the methods that have been developed and are widely used in the radio frequency (RF) and wireless world [155]. The only difference between the optical and wireless domain resides in the frequency of the deployed carrier. While in radio transmission the carrier frequencies spans from kHz to few GHz, in case of optical communications they are in the range of ∼200 THz.

The term "complex" or "advanced" when applied to modulation formats refers to the fact that information is no longer encoded only on the amplitude of the carrier but also on its phase and sometimes on its polarization state. Such schemes span from simpler (only two symbols) phase modulation formats like binary phase shift keying (BPSK) to more advance quadrature-amplitude modulation (QAM) where the number of symbols can be as high as 1024. A combination of 2-ary polarization-shift keying and quadrature phase-shift keying (QPSK) in each polarization (PS-QPSK) further increases the modulation complexity into a four dimensional space [156,157]. While complex or advanced modulation formats are widely used in the RF and wireless world, on-off keying (OOK), the simplest of digital modulation formats, is highly deployed in the optical domain. However, despite its popularity and the simplicity of generation and detection, the OOK format suffers from various problems. The large bandwidth that OOK signals occupy not only limits the number of channels, but results in low spectral efficiency and poor tolerance to chromatic dispersion (CD) and polarization mode dispersion (PMD).

## .1.1 Types of detection

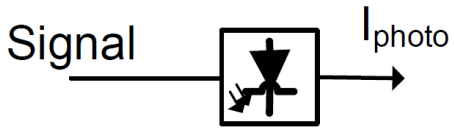


**Figure 1:** Direct detection of the optical signal $S$.

Direct detection of OOK modulation format request only power detection of the optical signal. This can be done in a photodiode (Fig. 1) that converts optical power into electrical current. Let the optical signal ($S$), entering the photodetector, to be described as

$$S = A_S \cdot \exp(i\omega_S t + i\phi_S), \tag{1}$$

where $\omega_S$ represents the angular frequency, $\phi_S$ the phase, and $A_S$ the amplitude of the signal. The photo-current ($I_{photo}$) generated at the photodiode is proportional to the product of the signal $S$ and its complex conjugate $S^*$ and can be described by the following equation:

$$\begin{aligned} I_{photo} &\propto S \cdot S^* \\ &= [A_S \cdot \exp(i\omega_S t) \cdot \exp(i\phi_S)] \cdot [A_S \cdot \exp(-i\omega_S t) \cdot \exp(-i\phi_S)] \\ &= A_S^2. \end{aligned} \tag{2}$$

Equation (2) shows that the phase information of the signal is lost due to direct detection. Hence, advanced modulation formats can not be detected directly in a photodiode, but require a detection technique that provides a measurement of the phase information $\phi_S$. Since it is not possible to directly measure the rapidly changing phase of an optical carrier, the measuring technique must rely on a relative measurement with respect to some phase reference.

There are two basic ways to obtain the reference for a phase measurement. The first one relies on the utilization of a time delayed version of the signal itself. As usually the interest is focussed on the phase changes over time, it is possible to use a delayed portion of the signal itself as a phase reference in a delay-line interferometer (DLI) configuration. The second method uses a second laser source that acts as a local oscillator (LO) similarly to RF systems. In this case, it is the LO that serves as a phase reference signal.

Once a phase reference is available, it is possible to convert the phase difference between the signal and the phase reference into power, and then by using conventional detection methods, to convert power into electrical current. Due to the square-law at the detector, a linear superposition of the optical signal $S$ and a reference signal $R$ (amplitude $A_R$, phase $\phi_R$ and angular frequency $\omega_R$) on a photodiode (Fig. 2) leads to

$$\begin{aligned} I_{photo} &\propto (S+R)\cdot(S+R)^* \\ &= [A_S\cdot\exp(i\omega_S t+i\phi_S)+A_R\cdot\exp(i\omega_R t+i\phi_R)]\cdot[\ldots]^* \\ &= A_S^2+A_R^2+2A_SA_R\cos(\Delta\phi+\Delta\omega t). \end{aligned} \tag{3}$$

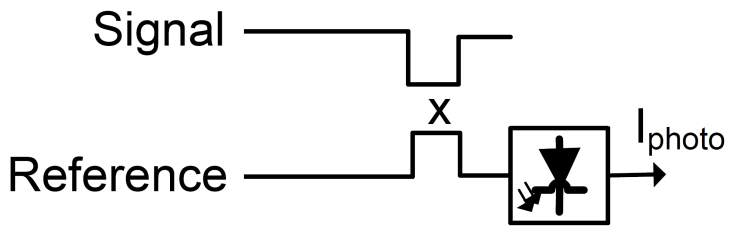


**Figure 2:** Linear superposition of a an optical signal $S$ and a reference $R$ on a photodiode.

The resulting photocurrent ($I_{photo}$) in Eq. (3), depends on the amplitude and phase of both signals, $S$ and $R$. The phase (frequency) difference term ($\Delta\omega t$) is called the beat term or the heterodyne term. It results from the "beating" (mixing) of the optical signals at the square-law detector, and disappears if $\omega_S$ is equal to $\omega_R$. This represents the homodyne case, and is always true in case of the utilization of a delayed version of the signal as reference (self-beating). From Eq. (3), it can also be noticed that the utilization of an external LO offers a better signal-to-noise ratio compared to self-beating. This is related to the fact that usually the signal has gone through different stages of attenuation, reshaping and amplification before reaching the receiver. Hence, it suffers from OSNR limitations, which on the other hand are easy to overcome by having a separate LO with high quality.

## .1.2 Balanced receivers

It can be seen form Eq. (2) and (3) that direct detection of the superposition of the modulated signal ($S$) and reference ($R$) contains terms that do not depend on the relative phase difference, but on the power of the signal and reference ($A_S^2$ and $A_R^2$). The utilization of a

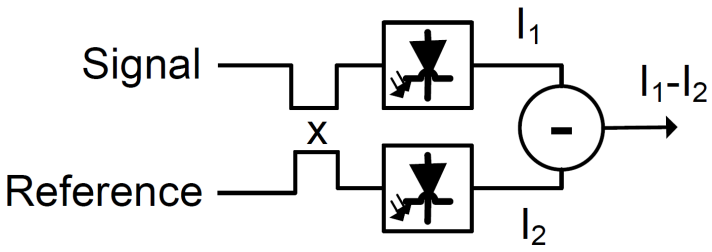


**Figure 3:** Balanced coherent receiver.

balanced receiver, as the one shown in Fig. 3, which subtracts the currents generated at the photodetectors, makes it possible to remove these terms:

$$\begin{aligned} I_1 - I_2 &\propto [(S+R)\cdot(S+R)^*] - [(S-R)\cdot(S-R)^*] \\ &= 4A_S A_R \cos(\Delta\phi + \Delta\omega t). \end{aligned} \tag{4}$$

As it can be seen, by subtracting current $I_1$ and $I_2$ the power terms are eliminated and the beat term is preserved. The preservation of the beat term and its multiplication by a factor of two (compared to Eq. (3)) is related to the properties of the optical coupler, that divides equally the power levels but creates a $\pi$ phase shifts between optical waves exiting its two output arms. Hence, after subtraction the beat term doubles.

## .1.3 Coherent receiver and time domain detection

As shown in Eq. (4), the difference between the photodiode currents $(I_1 - I_2)$ depends on the cosine of the phase- and frequency-difference between signal and reference. Due to the periodicity of the cosine function, only phase differences between 0 and $\pi$ can be uniquely resolved. This degree of freedom is sufficient for binary modulation formats like BPSK, but does not work for higher ones such as $n$-level phase shift keying ($n$-PSK), or $n$-QAM. In these cases, an additional beating product generated with a reference signal having a $\pi/2$ phase shift is needed. This allows creation of the quadrature signal and a full $2\pi$ phase coverage

$$\begin{aligned} Q_1 - Q_2 &\propto [(S+i\cdot R)\cdot(S+i\cdot R)^*] - [(S-i\cdot R)\cdot(S-i\cdot R)^*] \\ &= 4A_S A_R \sin(\Delta\phi + \Delta\omega t). \end{aligned} \tag{5}$$

Intuitively, the new term will depend on the sine of the phase- and frequency-difference. By using both terms (sine and cosine) it is possible to have a full phase coverage from 0 to $2\pi$. Additionally, it is even possible to distinguish phase information from amplitude ones:

$$\begin{aligned} A_S A_R &\propto \sqrt{(I_1 - I_2)^2 + (Q_1 - Q_2)^2} \\ \Delta\omega t + \Delta\phi &\propto \arctan\left(\frac{Q_1 - Q_2}{I_1 - I_2}\right). \end{aligned} \tag{6}$$

Figure 4 shows the implementation of a coherent receiver for a polarization–multiplexed signal, in which the information is encoded not only on the phase and amplitude of the fields but also on the two orthogonal states of polarization. For this type of signals the phase and

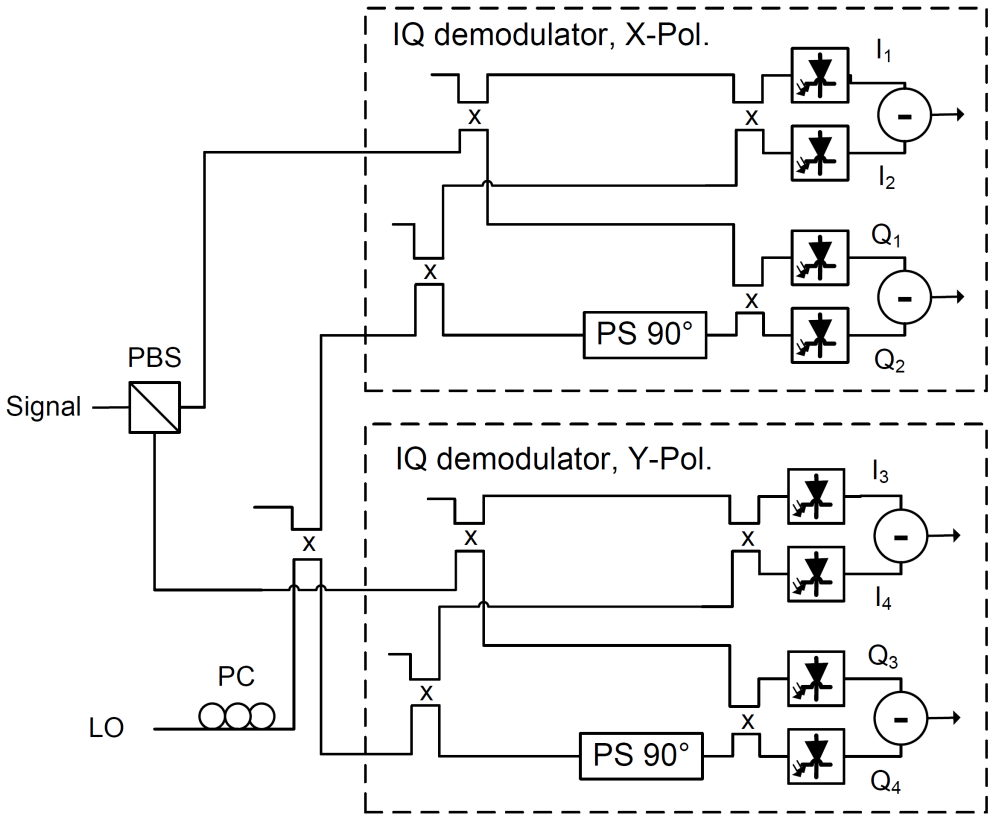


**Figure 4:** Basic principle for coherent detection of polarization multiplexed signals. PBS: polarization beam splitter.

amplitude information must be measured for both polarization states (polarization resolved measurement).

The signals generated at the balanced detectors in Fig. 4 (both polarizations) oscillate at an angular frequency $\Delta\omega = \omega_S - \omega_R$. This results in a rotation of the constellation diagram, which is relatively slow compared to the typical symbol rates of the modulated signal. By observing the constellation and its behavior, it is possible to distinguish between the symbols and their slow rotation. For this reason an electronic post-processing is necessary in order to estimate the carrier frequency $\Delta\omega$. The tolerance of the post processing algorithms depends on the modulation format and on the signal rates.